EXPERIMENTAL INVESTIGATION OF VARIED THRUSTER BODY BIAS ON ELECTRON BEHAVIOR IN THE NEAR-FIELD OF A MAGNETICALLY SHIELDED HALL THRUSTER

A Dissertation
Presented to
The Academic Faculty

By

Naia I. Butler-Craig

In Partial Fulfillment
of the Requirements for the Degree
Doctor of Philosophy in the
Georgia Institute of Technology College of Engineering
Daniel Guggenheim School of Aerospace Engineering

Georgia Institute of Technology
May 2026

EXPERIMENTAL INVESTIGATION OF VARIED THRUSTER BODY BIAS ON ELECTRON BEHAVIOR IN THE NEAR-FIELD OF A MAGNETICALLY SHIELDED HALL THRUSTER

Approved by:

Dr. Mitchell L. R. Walker, Advisor
School of Aerospace Engineering
Georgia Institute of Technology

Dr. Kentaro Hara
Department of Aeronautics and Astronautics
Stanford University

Dr. Sedina Tsikata
School of Aerospace Engineering
Georgia Institute of Technology

Dr. George Williams
Electric Propulsion Group
NASA Glenn Research Center

Dr. Wenting Sun
School of Aerospace Engineering
Georgia Institute of Technology

Date Approved: February 26, 2026

To God, my village, and myself.

ACKNOWLEDGEMENTS

I'd like to acknowledge God, first and foremost, for giving me the passion to start and the fortitude to finish this degree. God, you have sustained me mentally, emotionally, and physically through not just this rigorous degree but all the obstacles that piled up along the way. I commit everything I do to you and thank you for establishing my plans. Thank you for letting me a living testimony of James 1:12. Second, I must acknowledge my parents, Sharon Denise-Lashay Butler and Clayton Orlando Craig. I wear your last names like a badge, and we all should wear the title of Dr. Butler-Craig like one, too. This is our achievement, and I am nothing and no one without you two. Words can't begin to express my gratitude for everything you've done and continue to do for me. Mom, thank you for always being a prayer warrior, listening ear and guide as I navigated the challenges in this journey. Dad, thank you for everything you did and continue to do to take things off my plate so I could focus. To the rest of my family who always shared encouragement, never lost faith in me, and understood my absence over these 10.5 years, thank you. Periodically coming home to your love was like gassing up before a long trip. I felt replenished to go forth and get this thing done. To my lab mates, thank you for being the family you have been to me. I would not be here without our collective teamwork. All of you taught me so much and I am honored to have been on the brilliant and resilient team that is HPEPL. Jean Luis, aka the Thomson sensei, thank you for teaching me everything I know! I am grateful for your selflessness in how you shared your brilliance and

provided guidance to your younger lab mates. You paved the way for us to do interesting investigations and complete our studies. You were also a great leader and better friend. I owe you! David, thank you for being my intro into this lab! Your guidance and support in those early years was invaluable and I am forever grateful. Chhavi, thank you for being an amazing example to look to while in this lab! Your story, work, and commitment inspired me so much and seeing you defend gave me motivation to keep going! Arega, you are such a powerful and inspiring person! Thank you for always looking out for me, your kindness, and for being the reason I got to explore my love for cathodes. Julian, I sincerely enjoyed being your Thomson team teammate! I am very grateful to have worked with and learned from a mind like yours. Thanks for always being willing to share your ideas and be a sounding board! Richeek, you're going to do great things, and you were an awesome and dedicated Thomson teammate! Muhannad, you were a highlight of my lab experience! Not only were you like my twin and hilarious, but I'll always appreciate and be inspired by how you stand by your values. Thank you for being a wonderful friend. Kiss Bucci for me! Adrian, thank you for your kindness and support over the years. You were always available to lend a helping hand regardless of how busy you were and that meant the world. Jacob, the same goes for you! Your kindness and willingness to help or support was incredible and I'm so grateful for all the ways you showed up for me over the years. Will, it was honor to walk with you. I have always not only admired your intelligence and work ethic but the kindness you showed to everyone in spite the stress we were always under. Janice, it's been great watching you from undergrad to now! I know you'll continue to conquer the field. My relationship with you all ended up being a highlight of my experience in graduate school. You saw me and were there at my absolute worst, so we are locked in for life as far as I'm concerned! To Ebise, Devin and the other new graduate and undergraduate students to come – I know you're all going to do wonderful work there! I will be watching all of you as you continue to do remarkable things in your careers. To Professor Walker, thank you for your guidance, patience, and expertise throughout this process. The graduate school learning curve was extremely steep for me, but your individualized advising approach helped to smooth the path forward. I am grateful for the way you met me where I was, challenged me to grow, and trusted me to find my own footing as a researcher. The lessons I learned under your mentorship extend far beyond the lab and will shape the rest of my career. Thank you to the host of mentors that shared words of support, guidance and encouragement along way. Your words helped carry me through the challenges that I faced. To Jeremy^2, Jim French, and the entire AE machine shop, thank you for being the gears that kept this whole thing turning. You enable so many PhDs with your engineering excellence, patience, and kindness during some of the most stressful stretches a graduate student can face. You saved me more times than I can count, and this dissertation quite literally would not exist without your craftsmanship and generosity. To the AE school staff, thank you for the behind-the-scenes work that made everything possible. From making sure equipment got ordered and delivered, to ensuring I got paid on time, to navigating the countless administrative puzzles that come with doctoral research, you

kept the wheels moving so I could focus on the science. Your care and competence do not go unnoticed, and I am deeply grateful.

TABLE OF CONTENTS

LIST OF TABLES

LIST OF FIGURES

LIST OF SYMBOLS AND ABBREVIATIONS

A	amplitude of oscillation
A_s	surface area
b_J	Placzek- Teller coefficient
B_g	rotational energy constant
D_g	centrifugal distortion constant
$\Delta\emptyset$	potential difference
c	speed of light
c_p	pressure coefficient
e	elementary charge
η	intensified photoelectron
ϵ_J	energy mode
E_i	incident laser energy
f_i	breathing mode frequency
g_J	degeneracy
h	Planck's constant
I_e	electron current
I_i	ion current
I_g	nuclear spin quantum number
J	energy level
k_B	Boltzmann constant
λ_i	incident wavelength
$\lambda_{J'}$	Raman shifted wavelength
L	length of probe volume
$L_{ion/accel}$	ionization/acceleration region length
m_i	ion mass
m_e	electron mass
n_g	gas number density

n_o local plasma density

n_J population in J

$\Delta\Omega$ solid angle of collection

φ_f floating potential

p_g gas pressure

P_λ^R Raman scattering signal

P_λ^T Thomson scattering signal

Q_g rotational partition function

ρ depolarization ratio

σ_{IF} instrument function

T_e electron temperature

T_g gas temperature

τ full-width half maximum

θ_{kio} angle between incident radiation propagation direction and scattering observation

θ_{eiz} angle between incident radiation polarization and z axis

v_{ion} ion velocity

v_n neutral velocity

ζ polarization angle between incident and scattered radiation

$\frac{\partial\sigma^R}{\partial\Omega}$ Raman scattering cross section

$\frac{\gamma^2}{\epsilon_o{}^2}$ anisotropy of molecular polarizability tensor

SUMMARY

This dissertation answers a focused question: does varying the thruster body bias affect electron behavior in the near-field of a magnetically-shielded Hall effect thruster (HET)? The answer is yes, and the effect is both spatially distributed and circuit dependent. The investigation employs a two-phase experimental campaign on the 9-kW H9 thruster. Phase I uses the inner front pole cover (IFPC), electrically isolated from the thruster body, as a current probe while the body bias is scanned from 0.5 to 2.0 V relative to ground at the 300 V, 20 A operating condition. Phase II uses spatially-resolved laser Thomson scattering (LTS) at 150 V, 40 A to measure electron density, temperature, and radial drift velocity at fifteen locations spanning the near-field from the cathode centerline to the channel centerline under three boundary conditions: floating, cathode-tied, and +2 V relative to ground. Four principal findings emerge. First, electrons are strongly magnetized throughout the measurement domain under all configurations, which validates magnetized-transport assumptions and has a direct experimental consequence: because the anomalous transport term in the electron momentum equation is non-negligible in this regime, electron pressure cannot serve as a reliable proxy for electrostatic potential. At several measurement locations the sign of the pressure gradient is inconsistent with the measured radial drift direction, demonstrating that direct measurement of electron properties, rather than pressure-based inference, is required to characterize near-field electron pathways. Second, body bias systematically and linearly modulates collected electron current; body and IFPC currents exhibit a monotonic

response (slopes of −0.088 and −0.020 A/V, respectively). Third, the spatial distribution of electron density undergoes a configuration-dependent inversion that directly reflects each circuit topology: the cathode-tied configuration sustains elevated density at the cathode centerline but the lowest density at the channel centerline, while the +2 V configuration produces the opposite, providing macroscopic evidence for the proposed circuit-topology interpretation. Fourth, electron temperature and radial drift velocity provide supplementary kinematic evidence: the +2 V configuration shows the lowest electron temperature at the inner-pole region, consistent with the positively biased surface acting as an energy-selective filter that preferentially absorbs high-energy electrons, and the time-averaged drift trends correlate with the configuration-dependent breathing-mode oscillation amplitudes observed in the discharge current. Beyond the physical findings, the work yields practical guidance for configuration selection. The floating configuration is mechanically simplest and draws zero body current, but its self-consistent potential drifts with plasma conditions and can become strongly ion-attractive at higher discharge voltages, raising erosion risk. The cathode-tied configuration provides a well-defined, low-magnitude body current and is the heritage choice for flight, but its lower channel-centerline density could result in lower ionization efficiency measured in this region. The ground-relative (+2 V) configuration offers the most stable voltage boundary, but completes its circuit through the facility walls, which is not representative of the space environment. Together, these results provide novel, direct experimental evidence for configuration-dependent electron pathways in the near-field of a magnetically-shielded

HET and clarify the role of thruster body electrical boundary conditions in shaping electron transport, with implications for both flight configuration selection and the interpretation of ground-based test data.

CHAPTER 1: INTRODUCTION

This chapter establishes the motivation and scope of the present work. Section 1.1 provides the problem context, describing the role of electric propulsion in modern spacecraft and the outstanding challenge of inner front pole cover erosion in magnetically shielded Hall effect thrusters. Section 1.2 presents the thesis question, experimental objectives, and an outline of the dissertation structure.

1.1 Motivation and Problem Context

Electric propulsion (EP) has emerged as a key technology for modern space exploration and satellite operations, offering high specific impulse and efficient fuel utilization compared to traditional chemical propulsion. Among EP devices, Hall effect thrusters (HETs) are widely employed due to their robustness and efficiency. However, the long-term durability of HETs remains a critical challenge, particularly for magnetically-shielded configurations. While magnetic shielding extends thruster lifetime by mitigating the ion-induced erosion of the acceleration channel walls that limits the life of traditional HETs, it introduces a new life-limiting mechanism: inner front pole cover (IFPC) erosion. In the case of metallic inner front pole cover materials in thrusters with center-mounted cathode geometries, the IFPC can experience significant plasma interaction, leading to erosion that impacts overall thruster longevity. Sputtering from ion bombardment is the accepted cause of wear on the IFPC, however, the mechanisms driving ion bombardment are still not fully understood. Some mechanisms for IFPC erosion are hypothesized to be:

1. radial electrostatic fields driven by electron pressure gradients, accelerating discharge channel ions to the IFPC surface [1];
2. bombardment of ions born from the edge of the discharge channel and cathode plasmas, or an undetected, low-density, high-energy (>150 eV) population of ions [24];
3. anomalous ion heating due to plasma waves near the pole that energize local ions to energies beyond what is expected from classical acceleration and heating [2].

Using laser Thomson scattering (LTS), Betancourt et al. measured a local electron pressure drop relative to the channel centerline and inferred that if collisional and magnetic effects in the electron momentum equation could be neglected, the local potential would also be at a minimum at the inner front pole, thus providing an electrostatic field capable of driving beam ions into the IFPC [1]. Jorns et al. utilized laser induced fluorescence and surface-mounted probes to characterize the flux and energy distribution of ions incident at the inner pole and concluded that 10-25% of the calculated erosion at the inner pole is a result of a bulk population of ions originating from the cathode plasma and edge of the discharge channel beam. The rest of the calculated erosion is postulated to be a result of a separate, undetected, and low-density population of high-energy (> 150 eV) ions [24]. Finally, Roberts et al. claimed that inner front pole erosion is a result of azimuthally accelerated and heated cathode ions driven by experimentally observed anti-drift plasma waves.

Of the three proposed mechanisms, this dissertation builds upon mechanism 2: the electrostatic potential pathways. The selection of the cathode-tied electrical configuration as the baseline flight configuration 3, in part due to its observed mitigation of IFPC erosion, suggests that the local electric field structure near the IFPC is sensitive to the thruster body electrical boundary condition. Because this is an electrical change rather than a geometric or material one, it motivates investigation of the erosion mechanism most directly tied to the plasma environment. In the electron momentum equation, the electron pressure gradient is a contributing term to the local electric field. Characterizing how electron properties redistribute in response to electrical configuration changes is therefore a necessary step toward understanding the erosion-driving mechanisms at the IFPC. This mechanism presents the most direct opportunity to investigate the relationship between a controllable boundary condition at the IFPC and the response of the near-field plasma through the redistribution of electrons. Electron pathways as inferred from the spatial pressure distribution may not fully characterize the electric field landscape experienced by ions since the near field is characterized by collisional and magnetic effects. However, electron pressure lends critical insight into the plasma's internal force balance.

Radial electron flux measurements are relevant to understanding electron pathways to the IFPC surface for several reasons. First, in magnetically-shielded HETs, the magnetic field topology near the pole features field lines that extend radially outward from the IFPC before turning downstream into the plume [4]. Electrons following these field lines or undergoing cross-field transport would exhibit radial motion as they approach or depart from the pole surface. Second, the proposed erosion mechanism [1] involves radial electric fields that develop due to electron pressure gradients between the channel plasma and the low-density region in front of the IFPC [5]. These radial fields can drive ion acceleration toward the pole, and understanding the electron flux that creates these pressure gradients is essential to characterizing this phenomenon. Additionally, the radial electron drift velocity provides insight into electron flow toward or away from the IFPC. This has implications on whether the local sheath structure is electron attracting or repelling under varied body bias conditions [31, 6].

Both axial and radial ion fluxes contribute to IFPC erosion, however, understanding the radial contribution is motivated by observed erosion characteristics as seen in Figure 1. These recent observations of circumferential radial striations on the IFPC surfaces provide evidence that radial ion transport mechanisms contribute to erosion. Notably, these striations exhibit minimal sensitivity to background pressure variations from 5-12 μTorr-Xe, which is unexpected if beam divergence were the primary cause, as increased background pressure shifts the acceleration region upstream [7] and would be expected to reduce beam divergence angles and thus the angle of incidence on the IFPC. The expectation would be that if the angle of incidence is small, less ions would be incident on the IFPC thus reducing erosion. But because that was not the result, it begs the question of what mechanism is driving ion bombardment on the IFPC?

Figure 1: Photo of the NGHT-1X, a magnetically-shielded Hall-effect thruster, after 873 hours of operation during long-duration wear testing. Adapted from reference [8]

1.2 Thesis Question, Objectives, and Outline

1.2.1 Thesis Question

As used in this work, the term "electron pathways" refers to the routes by which electrons transport and close current in the near-field region of the thruster. The available current closure routes depend on the electrical boundary conditions imposed on the thruster body and facility walls. Variations in thruster body potential alter these routes, redirecting electron current through the body, along the plume, or to grounded facility surfaces. Spatially resolved electron density and pressure measurements serve as proxies for identifying these pathways, as regions of elevated density or pressure gradients indicate preferential transport routes. However, these scalar quantities do not fully resolve the directional or transient character of the electron current, and thus represent an indirect inference of the underlying current closure mechanisms.

This thesis investigates the influence of controlled thruster body bias relative to ground on the local electron pathways at the inner front pole of a magnetically-shielded HET and answers the following thesis question.

Does varying the thruster body bias affect the electron behavior in the near-field of a magnetically-shielded Hall effect thruster?

1.2.2 Thesis Objectives

These electron pathways are inferred by their response to variations in thruster body bias as observed through two key diagnostics.

1. The magnitude and polarity of current collected by witness plates on the IFPC, measured in Phase I, indicating whether electrons or ions dominate the net flux to the surface.

2. The spatial redistribution of electron density, temperature, and the resulting electron pressure in front of the IFPC, measured in Phase II at 2-3 key bias conditions, which reflects changes in force imbalances that cause electrons to move.

1.2.2.1 Phase I

Phase I was meant to include the use of witness plates fastened to the metallic IFPC and held at the same potentials as the thruster body to measure current collected to their surfaces across a range of thruster body biases relative to ground. The collected current measurements as a result of variable thruster body bias in Phase I were expected to provide insight into the dominant particle flux to the IFPC under the convention that a positive current suggests net ion collection, while a negative current indicates electron collection. From this, it can be inferred how the local surface potential relative to the bulk plasma is altered and changes the direction of electron pathways to the surface. Inflection points or sharp transitions in the witness plate current curve as a function of thruster body bias were also meant to highlight bias conditions that dramatically alter near-surface behavior and thus offer an additional condition at which electron properties can be investigated in Phase II. However, as discussed in Section 4.2, practical implementation of this discrete witness plate concept encountered significant engineering and thermal constraints, which ultimately required revising the experimental approach adopted in Phase I.

1.2.2.2 Phase II

In phase II, laser Thomson scattering (LTS) is employed to obtain spatially resolved measurements of electron density, temperature, and resultant electron pressure in the near field. The spatial redistribution of pressure, calculated at two to three key thruster body biases in Phase II, reflects how electrons reorganize under different boundary conditions. Although individual electron trajectories are not directly tracked, the body bias-induced spatial restructuring of the electron population provides insight into how electron pathways vary in response to changing boundary conditions.

1.2.3 Thesis Outline

This thesis is structured as follows: Chapter 2 provides a review of relevant background literature, including an overview of HETs, beginning with an overview of EP, ground testing with the objective of simulating spaceflight environment and electrical conditions, description of fundamental plasma physics principles, predictive modeling critical to EP research, and electron property estimation using LTS. Chapter 3 addresses the first step in answering the central thesis question: Does the thruster body bias measurably alter near-field electron properties beyond experimental uncertainty? The chapter begins with a brief survey of relevant literature on facility effects, with particular focus on how the electrical configuration of the thruster body influences key plasma diagnostics. The preliminary experiment presented here outlines the methodology and results of a diagnostic campaign designed to evaluate bias effects along the cathode centerline.

Findings from this study demonstrate that variations in thruster body bias produce measurable changes in near-field electron density and temperature, confirming that the body potential has an appreciable influence on electron behavior in this region. Finally, Chapter 4 presents the experimental test plan to investigate and answer the thesis question as described in Section 1.2.2.

CHAPTER 2: BACKGROUND

This chapter provides foundational context for the research by first introducing the role of EP in modern spacecraft systems. It then discusses the challenges of ground-based EP testing, particularly the need to simulate spaceflight-relevant conditions, such as background pressure and electrical boundary configurations, within vacuum facilities. A review of fundamental plasma physics principles is included to establish the theoretical basis for understanding thruster behavior, followed by a discussion of the role of predictive modeling in bridging experimental data with flight scenarios. The chapter then introduces LTS as a non-intrusive diagnostic tool for measuring electron properties, which are critical to evaluating local plasma behavior. Finally, a brief literature survey highlights recent findings on the influence of the thruster.

2.1 Overview of Electric Propulsion

EP is a class of advanced spacecraft propulsion technologies that use electromagnetic or electrostatic forces to accelerate a propellant to high velocities. Unlike traditional chemical propulsion, EP systems rely on electricity, typically generated by solar panels, to ionize and accelerate propellant particles. This results in significantly higher specific impulse, I_{sp}, and better propellant efficiency, making EP ideal for long-duration missions and satellite station-keeping applications [9].

EP systems are broadly categorized into three main types.

1. Electrothermal propulsion: Uses electrically generated heat to thermally accelerate the propellant, e.g., resistojets and arcjets.
2. Electrostatic propulsion: Accelerates ions using electrostatic fields, e.g., ion engines, HETs.
3. Electromagnetic propulsion: Employs electromagnetic fields to accelerate plasma, e.g., magnetoplasmadynamic thrusters.

2.1.1 History of Electric Propulsion

EP has revolutionized space exploration by providing high-efficiency propulsion systems suitable for long-duration missions. A detailed history of EP, noting the background and developments up to the 1950s, can be found in Choueiri [10]. Additionally, other works provide a comprehensive overview of EP history across various nations, such as the "History of Hall thruster Development in the USSR" by Kim et al. [11], which highlights the Soviet Union's pioneering contributions to the practical deployment of HETs, and Patterson et al. provide a history of EP, particularly at NASA Glenn Research Center [12].

In summary, the concept of EP was first proposed individually by both Goddard in 1906 [13] and Tsiolkovsky in 1911 [14]. Practical experimentation began in the mid-20th century, driven by the need for efficient propulsion systems for long-duration space missions. The Soviet Union led the way with the first operational use of HETs on the Meteor-series satellites in the 1960s and 1970s. Meanwhile, the United States pursued the development of ion thrusters, achieving a significant milestone with NASA’s Space Electric Rocket Test (SERT-1) in 1964, the first in-space demonstration of ion propulsion.

Both technologies matured significantly over the following decades. By the late 1990s, EP systems had become integral to space exploration, exemplified by missions such as Deep Space 1 (1998), which used ion propulsion for precise maneuvering.

Key milestones in EP development:

- 1964: NASA's Space Electric Rocket Test (SERT-1) mission marked the first successful demonstration of ion propulsion in space, using cesium and mercury ion engines [15].
- 1971: The Soviet Union successfully used HETs on its Meteor satellites, showcasing the operational viability of these devices [11].
- 1998: NASA’s Deep Space 1 mission utilized a xenon-powered ion engine, marking a significant milestone in the integration of EP into deep-space missions [16].

Among the various EP technologies, HETs – a subset of electrostatic propulsion – have emerged as a cornerstone due to their balance of efficiency and thrust-to-power ratio.

HETs gained prominence for their reliability in satellite station-keeping and orbit adjustments. Their simplicity and robustness have made them one of the most widely used EP systems in both commercial and scientific applications.

2.1.2 Overview of HETs

HETs are a prominent type of EP system used on spacecraft. The key components of an HET include the anode, an externally mounted cathode, discharge channel, and magnetic poles. They operate on the principle of a crossed-field discharge, where an electric field is imposed perpendicular to a magnetic field. The electric field accelerates ions axially, while the magnetic field confines and controls electron motion to sustain efficient ionization of the propellant, typically xenon or krypton. Figure 2 illustrates standard HET operation and is adapted from Ref. 17. Neutral propellant is injected near the anode, where electrons from the cathode ionize it, creating a plasma. The electric field then accelerates these ions out of the thruster at high velocity, generating thrust. Electrons from the cathode neutralize the ion beam to maintain charge neutrality. [9]

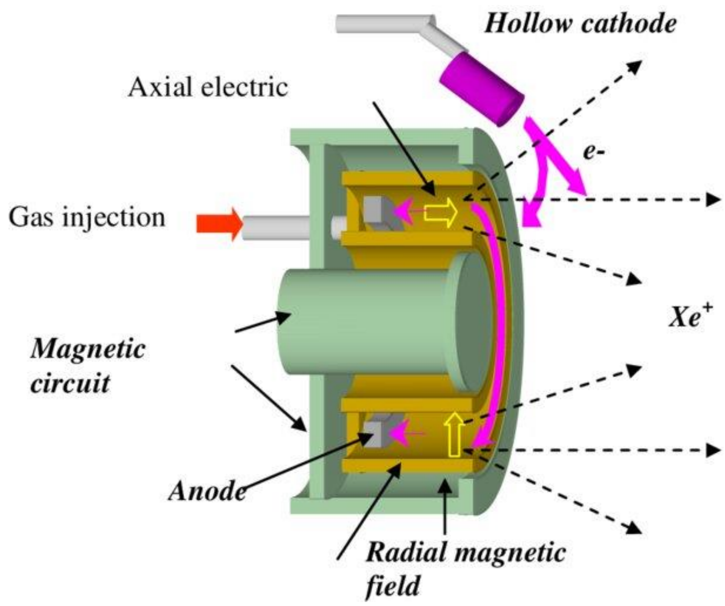

Figure 2: HET operational diagram with an externally mounted cathode. Reproduced from Dudeck et al. [17]

This axial electric field plays a significant role in defining the thruster's performance, as it governs ion acceleration, thrust generation, and efficiency. To quantify these effects, we use the fundamental electrostatic relationships that determine thrust, specific impulse, and efficiency, η. To quantify these effects, we can define the fundamental electrostatic relationships that determine thrust, T, I_{sp}, and η. Thrust is produced by the electrostatic acceleration of ions, given by,

$$T = \dot{m}v_e \quad \text{Equation 1}$$

,

where $\dot{m}$ is the mass flow rate of the propellant (primarily through the anode), and v_e is the ion exhaust velocity [9]. The ion velocity is determined by the kinetic energy ($m_i v_e^2/2$) gained as the ion is accelerated through an electric potential ($e\phi$), Equating these expressions gives an ion exhaust velocity of,

$$\frac{1}{2} m_i v_e^2 = e\emptyset \qquad \text{Equation 2}$$

$$v_e = \sqrt{\frac{2e\emptyset}{m_i}} \qquad \text{Equation 3}$$

where m_i is the ion mass, e is the elementary charge ($e = 1.602 \times 10^{-19}$ C), and ϕ is the potential drop across the discharge channel [18]. Specific impulse, I_{sp}, is a measure of how efficiently the thruster uses propellant. It is defined as the thrust per unit weight flow rate of propellant

$$I_{sp} = \frac{T}{\dot{m} g_e} = \frac{v_e}{g_e}. \qquad \text{Equation 4}$$

A high specific impulse is indicative of a high propellant efficiency, meaning greater impulse per unit of propellant consumed. The thruster efficiency, η, accounts for effectively the input power supplied to the thruster is converted into useful kinetic energy of the ions,

$$\eta = \frac{\text{Output Power (ion kinetic)}}{\text{Input Power}} = \frac{\frac{1}{2}\dot{m} v_e^2}{P_d} = \frac{T^2}{2\dot{m} P_d} \qquad \text{Equation 5}$$

where P_d is the discharge power supplied to the thruster. A higher efficiency indicates more of the electrical power supplied to the thruster is converted into ion kinetic energy rather than being lost to inefficiencies like Joule heating, and sputtering.

HETs are broadly categorized into two main types based on their channel designs: Stationary Plasma Thrusters (SPTs) and Thrusters with Anode Layers (TALs) [19]. Both share the fundamental principle of utilizing perpendicular electric and magnetic fields for the acceleration of ions and confinement of electrons, but their structural differences lead to differences in operations – specifically by shortening or lengthening the electric field region where the ion acceleration occurs [9]. SPTs are most widely used and feature a dielectric discharge channel material with low secondary electron emission coefficients and sputtering yields, such as boron nitride (BN). Collisions of electrons and ions with the dielectric walls keep the electron temperature low in the discharge plasma through the generation of low-energy secondary electrons, thereby extending the electric field region responsible for ion acceleration [20]. TALs, in contrast, compress this acceleration zone by employing a metallic discharge channel instead of a dielectric one. Without energy-reducing exchange processes for electrons, their temperature is allowed to increase without limit as they travel to the anode. As the electron temperature rises, the plasma potential increases more sharply near the anode, concentrating ion generation and acceleration within a narrow region near the anode [20]. For the work outlined in this dissertation, the HETs under investigation are of the SPT type.

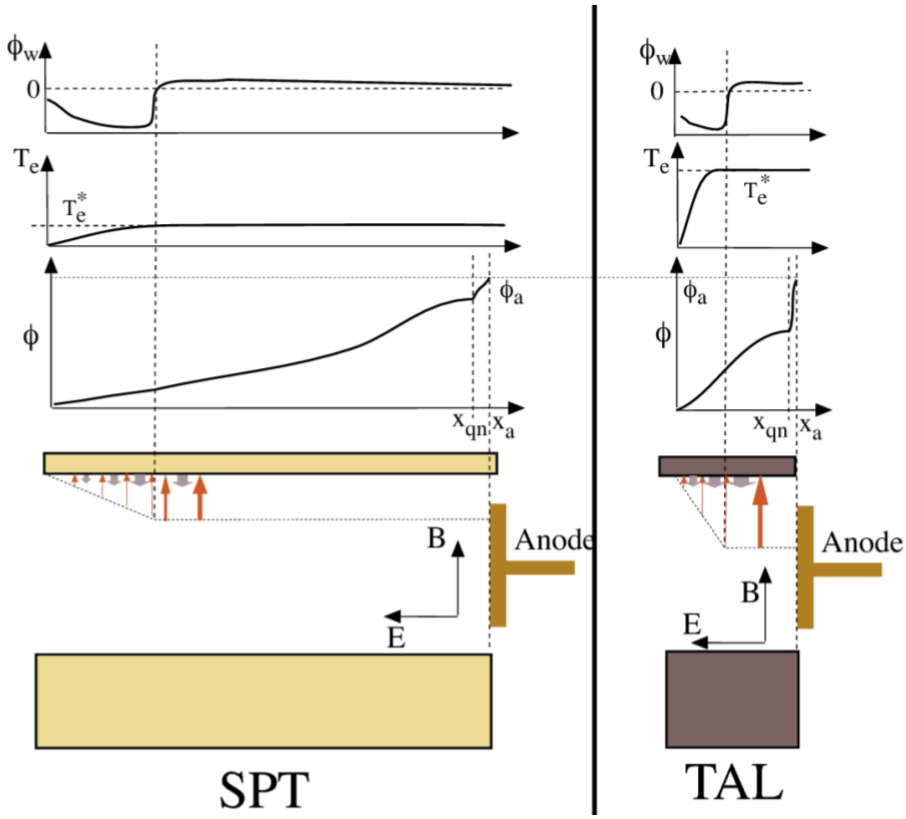

Figure 3: SPT (left) and TAL (right) type HETs and their subsequent electron temperature, potential, and wall potential profiles. The photo was adapted with permission from Choueiri [21].

Further distinctions within the HETs arise from advancements in magnetic field design. These refinements have led to the development of unshielded and magnetically-shielded SPT HETs.

2.1.2.1 Magnetic Shielding in HETs

A significant advancement in HET technology is the development of magnetically shielding. Traditional HETs face a major challenge due to erosion of the discharge channel, caused by energetic ions bombarding the walls. This erosion not only limits the operational lifespan of the thruster but also introduces performance variability over time. Magnetic shielding addresses this issue by altering the magnetic field topology to prevent ions from reaching the channel walls, thereby extending thruster life [22].

In a magnetically-shielded HET, the magnetic field lines are designed to minimize ion bombardment on the discharge channel walls. This is achieved by extending the magnetic field lines near the discharge channel walls deep into the anode region of the thruster. As a result, low electron temperature and high plasma potential are maintained along the entirety of the discharge chamber walls, which results in local ion energies below the sputtering threshold of the wall material [23]. While this innovation reduces channel erosion to negligible levels, it causes the acceleration region to shift downstream. As a result, potential gradients at the edge of the beam are produced that result in greater divergence of energetic ions that now can bombard the inner front pole and other downstream surfaces, leading to erosion in these areas, thus creating a new life-limiting mechanism [24, 25]. However, the location and rate of erosion of the inner front pole are more predictable than discharge channel erosion and can be mitigated through material selection and geometry optimization of the pole surfaces [26].

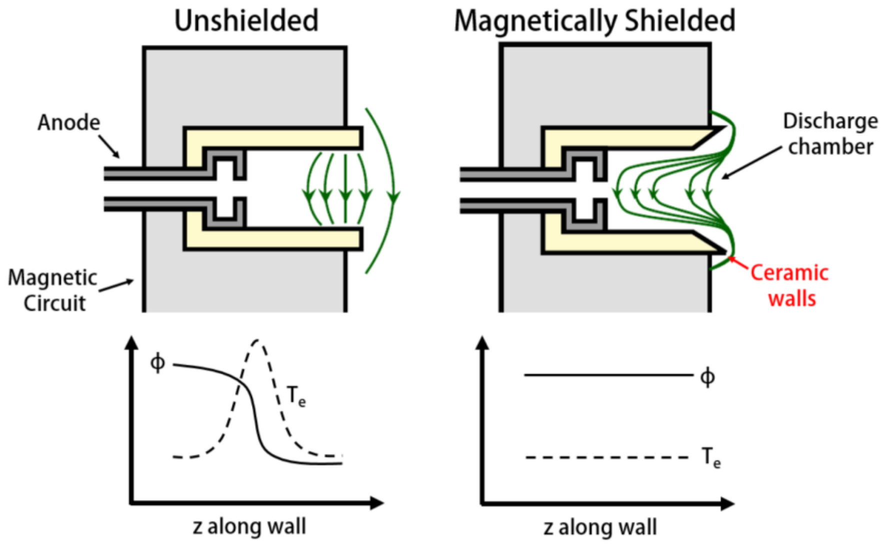

Figure 4: Unshielded and magnetically-shielded potential profile comparison adapted from [27] with permission.

While significant advancements have been made in the design and operation of HETs, challenges remain in understanding the detailed electron dynamics in the near-field region of the thruster. Specifically, the interaction of the thruster body with the plasma, and how this affects electron mobility and current pathways, has not been fully understood, especially in the context of varying thruster body bias and surface sheath characteristics.

2.2 Ground Testing in EP

Ground testing in EP refers to the experimental evaluation of EP systems conducted in terrestrial facilities designed to replicate the space environment. These tests are key to understanding the behavior, performance, and reliability of EP systems before they are deployed on spacecraft. By simulating operational conditions in controlled environments, researchers can characterize performance, investigate plasma behavior, and validate numerical models. However, facility effects and limitations inherent to ground-based setups often pose challenges for accurately replicating the in-space environment.

The features of ground-based testing are vacuum chambers, propellant flow, diagnostics, and instrumentation. Vacuum chambers are necessary to replicate the ultralow pressures the spacecraft is to encounter in space, typically less than 10^{-6} Torr [9]. Vacuum chambers used to test EP systems are often equipped with cryogenic pumps capable of high pumping speeds to maintain low pressures despite potentially high thruster flow rates. Propellant is fed to the thruster through intricate piping systems and precision flow controllers that aim to minimize propellant contamination from air and to evaluate performance at specific flow rates with high resolution. Probe and laser diagnostics are employed to measure key plasma properties and are operated in such a way to minimize perturbations because of their presence in the plasma and influences that may provide inaccurate data.

Facility effects include, but are not limited to, background pressure effects, chamber material sputtering deposition, and electrical effects. Background pressure effects, for instance, have been investigated in depth in previous studies seeking to understand elevated pressure effects on acceleration-region dynamics [46]. Studies in the last decade have identified a facility interaction, outside of the thoroughly investigated pressure effects, that involves the electrical interaction of the conducting vacuum facility with the HET plume [28,29]. The electrical configuration of the thruster, or how the thruster electrodes and chassis are connected, plays a major role in this. Peterson et al. in Ref. [30] completed detailed performance maps of NASA's 12.5-kW Hall Effect Rocket with Magnetic Shielding (HERMeS) Technology Demonstration Unit-1 (TDU-1) with the thruster in several ground-based electrical configurations. The study aimed to assess the best electrical configuration to conduct development and qualification testing for flight missions. An additional facet of the study was varying the exit plane boundary condition between a dielectric and conducting surface. This was employed using dielectric and conducting pole covers. While grounding the thruster body by electrically connecting it to the conducting vacuum chamber yielded the highest performance in this study, this configuration was not ideal since it created a low-resistance electron pathway through the conducting chamber, allowing electrons to recombine with plume ions at the chamber walls, which is a condition not representative of the space environment [29]. Peterson et al. confirmed this with a measurement of 10% of the discharge current flowing through the thruster body to ground in this configuration [30].

Butler-Craig et al. aimed to enhance the understanding of thruster body electrical configurations by incorporating measurements of near-field electron properties [52]. By quantifying electron properties downstream of the cathode centerline, their work laid the groundwork for investigating and characterizing electron pathways to current-collecting surfaces of the thruster. This is the basis of the effort detailed in this work, which will also investigate the role of thruster sheaths in influencing these pathways, contributing to a deeper understanding of electron mobility and current collection in this critical region.

2.3 Fundamental Plasma Physics

Plasma, often referred to as the fourth state of matter, is a quasi-neutral ensemble of charged particles that exhibits collective behavior. In the context of HETs, understanding plasma behavior is critical for predicting thruster performance and lifetime. Plasma dynamics are governed by several fundamental principles and equations, such as the continuity equation, momentum conservation, energy conservation, and Maxwell's equations. Key plasma parameters, such as Debye length, plasma frequency, and sheath formation, play crucial roles in the behavior of plasma in EP devices. [9]

2.3.1 Key Plasma Parameters

In HETs, key plasma parameters such as electron density, ne, electron temperature, T_e , and ion temperature, T_i, are typically characterized by specific values that define the operational regime of these devices. A fundamental scale in plasma physics is the Debye length, λ_D, which determines the thickness of the sheath by quantifying the distance over which electric fields are effectively screened. Additionally, the plasma frequency, ω_{pe}, representing the characteristic oscillation frequency of electrons, along with other essential plasma parameters, plays a crucial role in governing the dynamic behavior of the plasma and its interactions within the thruster environment.

2.3.2 Governing Equations

Maxwell's equations govern the electric and magnetic fields in HET plasmas. In the case of a vacuum that contains charges and currents, Maxwell's equations are [31, 9]

$$\nabla \cdot E = \frac{\rho}{\varepsilon_o} \qquad \text{Equation Go}$$

$$\nabla \times E = -\frac{\partial B}{\partial t} \qquad \text{Equation 6}$$

$$\nabla \cdot B = 0 \qquad \text{Equation 7}$$

$$\nabla \times B = \mu_o \left(J + \varepsilon_o \frac{\partial E}{\partial t} \right) \qquad \text{Equation 8}$$

where ρ is the charge density, **J** is the current density in the plasma, and ε_o, and $\mu_o$are the permittivity and permeability of free space, respectively.

2.3.3 Single particle motions

The motion of a charged particle in a plasma is fundamentally governed by the Lorentz force law, expressed as

$$F = q(E + v \times B) \qquad \text{Equation 9}$$

Where q is the charge of the particle, E is the electric field, B is the magnetic field, and v is the velocity of the particle. This force results in a combination of acceleration along the electric field and a deflection by the magnetic field, leading to characteristic helical trajectories. When the electric field is absent or aligned with the magnetic field, the particle undergoes uniform circular motion, gyration around the magnetic field lines. The frequency of this circular motion, known as the cyclotron frequency, is given by [31]

$$\omega_c = \frac{qB}{m}, \qquad \text{Equation 10}$$

where m is the mass of the particle, and the corresponding radius of the circular motion (the Larmor or gyroradius) is

$$r_L = \frac{v_\perp}{\omega_c} \qquad \text{Equation 11}$$

with $v_\perp$ representing the component of the velocity perpendicular to B.

In realistic plasma environments, such as those found in operating HETs, the electromagnetic fields are often spatially inhomogeneous and time-varying. Under the assumption that these fields change slowly compared to the particle's gyration, one can invoke the guiding center approximation. This approximation allows the particle's complex motion to be decomposed into a rapid gyration around a slowly drifting center, known as the guiding center. Among the most significant drift motions is the E×B drift, given by

$$v_{E\times B} = \frac{E\times B}{|B|^2}, \qquad \text{Equation 12}$$

which is independent of the particle's charge and mass. Other important drift phenomena include the gradient-B drift and curvature drift, which arise in non-uniform magnetic fields and contribute to the overall transport and confinement properties of the plasma.

2.4 Sheath Basics

The plasma sheath is a non-neutral boundary layer that forms at the interface between a plasma and a material surface. Its formation is driven by the higher thermal velocities of electrons compared to ions, which causes electrons to escape to the wall more readily, leaving behind a net positive charge in the bulk plasma. This charge imbalance creates a strong electric field that establishes a steep potential drop across the sheath, typically over a distance on the order of the Debye length, defined as,

$$\lambda_D = \sqrt{\frac{\epsilon_0 k_B T_e}{n_e e^2}}.. \qquad \text{Equation 13}$$

The spatial variation of the electric potential $\phi(x)$ within the sheath is governed by Poisson's equation,

$$\frac{d^2\phi}{dx^2} = \frac{-\rho(x)}{\epsilon_0}, \qquad \text{Equation 14}$$

with $\rho(x) = e(n_i - n_e)$ representing the net charge density, where n_i is the ion density. Under the assumption that electrons obey a Boltzmann distribution, their density can be expressed as

$$n_e(x) = n_{e0} \exp\left(\frac{e\phi(x)}{k_B T_e}\right), \qquad \text{Equation 15}$$

where n_{e0} is the electron density in the quasi-neutral plasma.

A key requirement for the formation of a stable, ion-attracting, electron-repelling sheath is provided by the Bohm criterion, which states that ions must enter the sheath with a velocity at least equal to the ion acoustic speed,

$$v_i \geq c_s = \sqrt{\frac{k_B T_e}{m_i}}, \qquad \text{Equation 16}$$

where m_i is the ion mass [31]. This condition ensures that ions have sufficient kinetic energy to overcome the potential barrier and sustain a continuous ion flux toward the wall.

The potential drop across the sheath is critical because it directly affects ion acceleration and, consequently, the energy and flux of ions impacting surfaces. This has a significant impact on phenomena such as sputtering and erosion. In cases where the current density is limited by space charge, the Child-Langmuir law provides a relation for the ion current density, J, in a planar geometry,

$$J = \frac{4\epsilon_0}{9} \sqrt{\frac{2e}{m_i}} \frac{(\phi_p - \phi_w)^{3/2}}{d^2}, \qquad \text{Equation 17}$$

where ϕ_p is the plasma potential, ϕ_w is the wall potential, and d is the effective thickness of the sheath [32].

2.5 Predictive Modeling in EP

Predictive modeling is essential for advancing EP systems because it enables the investigation of complex plasma phenomena without relying exclusively on costly and time-consuming experiments. It facilitates iterative design improvements, reducing reliance on expensive and time-consuming ground tests. Additionally, predictive models offer critical insights into plasma behavior in regions that are challenging or inaccessible to standard diagnostic probes. For HETs, accurate models of the plasma environment are necessary to predict performance under various operating conditions. However, existing models have limitations when it comes to the complex interactions between the thruster body, magnetic field, and plasma.

Predictive modeling of HET plasma dynamics involves solving nonlinear, coupled partial differential equations (PDEs) that describe the behavior of electrons, ions, and neutral atoms based on governing equations outlined in Chapter 2. There are also several assumptions necessary to simplify these equations for their application to HET plasma dynamics [33]. Existing HET simulation frameworks can be broadly categorized into fluid, kinetic/particle-in-cell (PIC), and hybrid models.

Fluid models are based on fluid equations for electrons, ions and neutrals. These models can be formulated under either quasineutral or nonneutral assumptions [34]. The key assumption used for HET fluid models is the drift-diffusion approximation 35. Assuming quasineutrality indicates nearly equal ion and electron densities throughout the plasma. The electric field is obtained from a continuity equation for total current. Particle species in fluid models are modeled as follows,

- Electrons are modeled using continuity, momentum, and energy equations. The freedom to specify anisotropic EVDFs along surfaces such as magnetic field lines or channel walls allows for improved accuracy in predicting transport properties.
- Ions are treated as cold fluids or with a prescribed temperature, depending on the level of model fidelity. Continuity and momentum equations describe ion motion, including acceleration by the electric field.
- Neutrals are often described using simplified fluid equations, given their limited interaction with the plasma [33].

Kinetic models like Kinetic PIC Direct Simulation Monte Carlo (DSMC) model [36, 37], are the most detailed simulation frameworks, treating all species (electrons, ions, and neutrals) as discrete particles. Grid-based direct kinetic (DK) methods also fall under the kinetic modeling category[38]. While this is advantageous as fewer assumptions are needed, this advantage comes at great computational cost.

Hybrid models combine the strengths of kinetic and fluid approaches by treating electrons as a fluid and heavy species (ions and neutrals) as discrete particles. These models do the following,

- Represent ions as discrete particles, allowing for resolution of ionization and acceleration processes.
- Include sub-models for key effects like charge exchange (CEX) collisions, where neutral atoms interact with ions to produce new ionized particles.
- Track changes in particle properties, such as ion density and velocity, across the domain.

Hybrid models are computationally less intensive than fully kinetic simulations while maintaining a higher degree of fidelity than fluid models [33]. One example is the quasi-one-dimensional hybrid PIC model known as HPHall, originally developed by Fife [39]. Another notable example is Hall2De [40], a two-dimensional axisymmetric code developed at JPL, which also has the capability to be operated as a hybrid model. This model has also been applied to simulate wall erosion and thruster lifetime. However, one of its disadvantages is its reliance on the quasineutrality and Maxwellian electron energy distribution function (EEDF) assumptions that inhibit wall sheath modeling [41].

2.6 Laser Thomson Scattering Fundamentals

2.6.1 Overview of Light Scattering in Plasmas

Light scattering phenomena are typically categorized as elastic or inelastic, with key examples including Rayleigh, Thomson, Raman, and Compton scattering. The phenomenon is described as an electromagnetic wave interacting with a particle, such as a free electron, atom, or molecule, redirecting it away from its original propagation path. In elastic scattering, such as Rayleigh or Thomson scattering, the frequency of the scattered photon remains the same, while in inelastic processes like Raman and Compton scattering, the scattered photon's frequency is shifted to higher or lower values.

Rayleigh scattering arises when the scattering centers, e.g., molecules are much smaller than the wavelength of light, resulting in an elastic process with no change in photon frequency. Raman scattering is an inelastic process in which the scattered photon emerges at a shifted frequency due to changes in the internal vibrational or rotational energy modes of the molecules, thus offering insights into molecular structure and temperature. Compton scattering, relevant at high photon energies, also involves inelastic photon-electron collisions, but the energy shifts can be significant, reflecting relativistic effects and electron recoil.

Thomson scattering refers to the elastic scattering of electromagnetic radiation by free electrons as described by classical electromagnetism. It is a low-energy, non-relativistic, limit of Compton scattering, meaning the photon energy is well below the electron rest mass energy ($m_e c^2 \cong 511$ keV), so recoil and quantum effects can be neglected. In essence, an electromagnetic wave exerts an oscillatory force on the electron since the electron's charge, e, interacts with the incident electric field. [42, 43]

LTS is a diagnostic technique that exploits the elastic scattering of laser light by free electrons in a plasma to provide direct, highly resolved measurements of key plasma parameters. In a typical LTS experiment, a laser beam is directed into the plasma and its interaction with the various plasma species causes a fraction of the incident light to be scattered. The measured scattered power per unit wavelength, $P_{\lambda,i}(\lambda)$, from an individual species ii can be modeled as,

$$P_{\lambda,i}(\lambda) = P_0 n_i f \frac{d\sigma_i}{d\Omega} L\Delta\Omega S_{\lambda,i}(\lambda), \qquad \text{Equation 18}$$

Where P_0 is the incident laser power, n_i is the density of species i, f represents the efficiency of the optics and detector, $\frac{d\sigma_i}{d\Omega}$ is the differential scattering cross-section, L is the length of the detection volume along the laser path, and $\Delta\Omega S_{\lambda,i}(\lambda)$ denotes the spectral density of scattered photons over a solid angle $\Delta\Omega$ [44].

In the plasma, free electrons are of particular interest because their low mass allows them to respond quickly to the incident electromagnetic field. As the laser light interacts with the electrons, the scattered photons experience Doppler shifts due to the electrons' thermal motion, which is described by a Maxwellian velocity distribution. This thermal motion leads to a Gaussian broadening of the scattered spectrum, where the width of the profile directly reflects the electron temperature.

Furthermore, the overall scattering behavior is influenced by the scattering parameter α, which compares the scale of electron oscillations within a Debye sphere to the laser wavelength. Depending on whether $\alpha \ll 1$ (incoherent scattering) or $\alpha \gg 1$ (coherent, or collective, scattering), the LTS spectrum can display either a simple broadened profile or distinct satellite peaks corresponding to plasma waves. This versatility allows LTS not only to yield simultaneous measurements of electron density and temperature but also to probe the electron energy distribution function (EEDF) without assuming local thermodynamic equilibrium [45, 82]. The scattering in this work is only concerned with incoherent scattering.

To ensure that the absolute electron density measurements obtained from LTS are accurate, however, the detection system must be carefully calibrated. This calibration is achieved through Laser Raman Scattering (LRS), which leverages the inelastic scattering of monochromatic laser light by polyatomic molecules which is primarily the diatomic species in air. LRS provides a means to determine the transmission efficiency of the detection branch by comparing known scattering cross-sections and synthetic Raman spectra with experimental measurements. In the following section, we describe the calibration procedure using rotational Raman scattering, detailing the derivation of key equations and the methodology used to ensure that the LTS measurements yield reliable, absolute density values.

2.6.1.1 Optical Diagnostics in EP

Optical diagnostics have become vital tools for advancing the understanding of HET plasma dynamics. These non-invasive methods provide high spatial and temporal resolution, enabling detailed characterization of plasma properties such as electron temperature, density, and ion velocity. By offering insights into plasma dynamics and behavior in regions inaccessible to probes, optical diagnostics play a critical role in validating predictive models and optimizing thruster performance. Key laser-based methods include Laser-Induced Fluorescence (LIF), Two-Photon Absorption Laser-Induced Fluorescence (TALIF), and Laser Thomson Scattering (LTS), while Optical Emission Spectroscopy (OES) is a passive technique that collects light naturally emitted by the plasma without requiring a laser source.

2.6.1.1.1 Laser Induced Fluorescence (LIF)

LIF is a widely utilized technique for measuring velocity distribution functions within HET plasmas. By tuning a laser to specific electronic transitions of ions or neutral atoms, researchers can induce fluorescence and analyze the emitted light to determine velocities and densities. LIF allows for studying ion dynamics in the near field as a function of various variables, including background pressure which is crucial for characterizing ground test facility effects and acceleration region migration and consequently, thruster operation [46]. Time-resolved LIF has also been applied to measure the perturbation of the ion velocity distribution function (IVDF) to study ion heating by lower hybrid waves in the near-pole region of a magnetically-shielded thruster [47].

2.6.1.1.2 Two-Photon Absorption Laser-Induced Fluorescence (TALIF)

TALIF builds upon LIF by allowing the excitation of ground-state neutrals through the simultaneous absorption of two photons. This method is particularly effective for detecting neutral xenon or krypton atoms in HETs. This is an extremely necessary effort for characterizing how neutral particle interactions affect life-limiting mechanisms in HETs. CEX collisions are of particular interest to the EP community as slow ions and fast neutrals for many reasons but most importantly because of their ability to erode channel walls among other thruster surfaces [48].

2.6.1.1.3 Optical Emission Spectroscopy (OES)

OES leverages the analysis of naturally emitted light from excited species within the plasma to infer properties such as electron temperature, density, and species composition. While OES is less invasive and simpler to implement than laser-based methods, it typically provides line-of-sight integrated data, which can complicate spatial resolution. Interesting applications of OES relevant to channel erosions were executed by Williams et al. on the high-power NASA-300M and NASA-457Mv2 thrusters. By leveraging excited xenon states to normalize emission spectra of ground state boron as a function of thruster operating condition, the authors were able to capture the overall trend in channel erosion of these thrusters [49].

2.6.1.1.4 Laser Thomson Scattering (LTS)

LTS provides direct measurements of electron temperature, T_e, and density, n_e, by analyzing the scattering of laser photons off free electrons in the plasma. This diagnostic has proven invaluable in studying near-field regions of HETs [50, 51, 52] where traditional Langmuir probes are less desirable due to theoretical limitations and practical challenges because of their perturbative nature. Langmuir probes are particularly unreliable in these regions because high-energy particles can damage or excessively heat the probes, leading to significant errors in the measurement of electron properties [53].

Recent LTS studies by Roberts et al. [54] have reported electron temperatures in HET near-field plasmas that exceed values of electron temperature predicted by earlier fluid codes based on near-field probe measurements by a factor of up to 2.5. Betancourt et al. [55] also revealed that magnetic field lines, previously assumed to be isothermal in conventional HET models, exhibit non-isothermal behavior. This discovery challenges a long-standing assumption in HET physics and has prompted further investigations into advanced heat flux models that are able to produce results like those measured in previous experiments [56]. These findings highlight discrepancies between theoretical models and experimental observations, providing critical motivation for refining existing models.

2.6.2 Calibration with Rotational Raman Scattering

As stated, before the LTS spectra can be analyzed to estimate electron properties, specifically the absolute electron number density, an intensity calibration using laser Raman scattering (LRS) is necessary to determine the transmission efficiency of the detection branch. LRS is the inelastic scattering of monochromatic laser light by polyatomic molecules, resulting in a shift in energy corresponding to the internal energy modes of the molecule. LRS is particularly valuable for studying molecular vibrational and rotational energy levels. When a photon interacts with a molecule, it can transit through a virtual state and emerge at a frequency different from the original if the molecule either gains or loses energy. For rotational Raman scattering, the selection rules for the possible transitions in the rotational quantum number, J, often involve $\Delta J = \pm 2$ for diatomic molecules. The (+) sign indicates that the molecule is transitioning to a higher energy level, thus gaining energy and decreasing photon frequency, otherwise called a Stokes transition. Whereas the (-) indicates a transition to a lower energy level, where there is a loss of energy and an increase in frequency, and is called an anti-Stokes transition.

Raman calibration ensures accurate density measurements by using known scattering cross-sections from diatomic molecules in air. The synthetic Raman spectrum is compared with experimental measurements to calibrate optical and detection efficiencies.

2.6.2.1 Equations and Derivations

This calibration is conducted by comparing the calculated synthetic spectra of the rotational Raman spectra of air at representative pressures with the experimental measurements. The agreement between the two provides for a more accurate estimation of the calibration coefficient. The expression corresponding to the synthetic Raman spectra of air assumed to comprise 79% nitrogen and 21% oxygen is given by Equation 19, [82, 57].

$$C = \eta \frac{\lambda_i}{hc} \Delta\Omega L E_i n_g,$$

$$P_\lambda^R(x^R, \theta^R) = C(T_g, p_g) \times \left[\gamma_{N_2}\left[\sum_J \frac{\partial\sigma^R}{\partial\Omega_{J'}}\right]_{N_2} + \gamma_{O_2}\left[\sum_J \frac{\partial\sigma^R}{\partial\Omega_{J'}}\right]_{O_2}\right] S_\lambda^R(\lambda_{J'}, \tau)$$

Equation 19

$\gamma_{N_2} = 0.79$ and $\gamma_{O_2} = 0.21$

Where P_λ^R is the expected Raman signal in photon counts per nm. The parameters extracted and fitted to are $x^R = [T_g, \tau, \eta, \lambda_i]$. The $S_\lambda^R(\lambda_{J'}, \tau)$ term is the spectral redistribution function and is given by Equation **20** where it is assumed that the only relevant source of spectral redistribution is due to the instrument function as Doppler and pressure broadening are negligible [82].

$$S^R(\lambda_{J'}, \tau) = \frac{1}{\sqrt{2\pi}\sigma_{IF}(\tau)} \exp\left[-\frac{1}{2}\left(\frac{\lambda_i - \lambda_{J'}}{\sigma_{IF}(\tau)}\right)^2\right] \qquad \text{Equation 20}$$

Where the Gaussian instrument function width σ_{IF} is a function of the full-width half maximum, τ and is given by

$$\sigma_{IF}(\tau) = \frac{\tau}{2\sqrt{2\log(2)}} \qquad \text{Equation 21}$$

The $\sum_J \frac{\partial\sigma^R}{\partial\Omega_{J'}}$ terms are the rotational Raman scattering cross sections for each of the gases and is comprised of the sum of the Stokes and anti-Stokes cross sections, $\frac{\partial\sigma^R}{\partial\Omega} = \sum_J \frac{\partial\sigma^R}{\partial\Omega_{Stokes}} + \sum_J \frac{\partial\sigma^R}{\partial\Omega_{Santi-tokes}}$. In Raman scattering, re-emitted or scattered photons can either be higher (anti-Stokes) or lower (Stokes) energy than the incident photon. The rotational selection rules dictate which rotational transitions are allowed when the molecule absorbs or emits a photon. For diatomic molecules, only J to J ± 2 transitions are authorized [58]. The Stokes and anti-Stokes cross-sections are functions of the perpendicular scattering cross-section, $\frac{\partial\sigma^{\perp}}{\partial\Omega_{J'}}$, through the following expression [82],

$$\frac{\partial\sigma}{\partial\Omega_{J'}} = \frac{n_J}{n_g}\{(1-\rho)\cos^2(\zeta)[1-\cos^2(\theta_{kio})\sin^2(\theta_{eiz})]+\rho\}\frac{\partial\sigma^{\perp}}{\partial\Omega_{J'}} \quad \text{Equation 22}$$

Where the perpendicular scattering cross section is given by [82],

$$\frac{\partial\sigma^{\perp}}{\partial\Omega_{J'}} = \frac{64\pi^4\gamma^2 b_{J'}}{45\,\epsilon_0^2\lambda_{J'}^4} \quad \text{Equation 23}$$

$\frac{n_J}{n_g}$ is the population fraction and is given by [82],

$$\frac{n_J}{n_g} = \frac{1}{Q_g} g_j(2J+1)\exp\left[\frac{\epsilon_J(J)}{k_B T_g}\right] \quad \text{Equation 24}$$

Q_g is the rotational partition function, ϵ_J is the rotational energy mode, p_g is the pressure of the gas via the ideal gas law, $b_{J'}$ is the Placzek-Teller coefficient, and λ_j is the scattered wavelengths [82],

$$Q_g = \frac{(2I_g+1)^2 k_B T_g}{2B_g hc} \quad \text{Equation 25}$$

$$\epsilon_J(J) = hc[B_g J(J+1) - D_g J^2(J+1)^2] \quad \text{Equation 26}$$

$$p_g = n_g k_B T_g \quad \text{Equation 27}$$

$$b_{J'} = \frac{3(2J+1\pm1)(2J+1\pm3)}{8(2J+1)(2J+1\pm2)} \quad \text{Equation 28}$$

$$\lambda_{J'}(J) = \lambda_i \pm \lambda_i^{\,2} B_g(4J + 2 \pm 4) \qquad \text{Equation 29}$$

2.6.2.2 Raman Calibration Procedure

Figure 5 shows an example of a Raman scattering spectrum. The black "+" symbols represent the experimental data, while the dashed red line corresponds to the expression shown in Equation 19 to which the experimental Raman data is fit. The green boxes illustrate the rejection measurements that are usually intense and centered around the interrogation laser wavelength as they are affected by light redistribution at the stray light peak. However, as is evident in the plot, the BNF filtering effectively attenuated stray light at 532 nm while permitting the Stokes and anti-Stokes transitions to be clearly distinguishable.

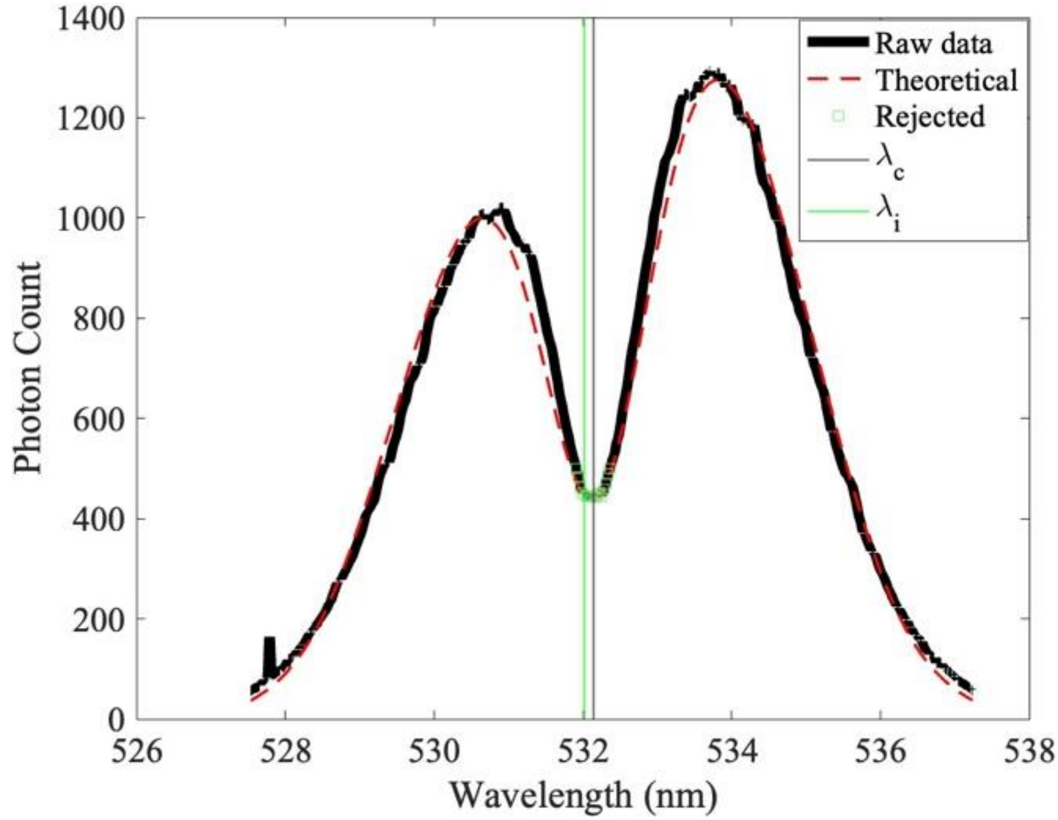

Figure 5: Example of a Raman scattering spectrum on air used for calibration, where λ_i denotes the incident laser wavelength and λ_c denotes the center wavelength of the resultant spectrum

2.6.3 Incoherent Thomson Scattering

2.6.3.1 Fitting Procedure for Electron Properties

To estimate the electron properties from LTS spectra, the experimental data is fit to the expression Equation 30 for the total Thomson scattered spectrum power, P_λ^T, that is a function of the wavelength of the scattered light. The scattering spectrum's redistribution is primarily influenced by wavelength shifts due to the relative motion or velocity of the scattering electrons with respect to the reference or incident wavelength. The shape of the distribution, governed by the Thomson spectral redistribution function, denoted by $S_k(\lambda)$, is related to the electron velocity distribution function, which is assumed to be Maxwellian if the electrons are in thermal equilibrium [82].

$$P_\lambda^T(x^T, \theta^T) = \eta \frac{\lambda_i}{hc} \Delta\Omega L E_i n_e \frac{\partial \sigma^T}{\partial \Omega} S_{k,\lambda}^T(x^T, \lambda_i) \qquad \text{Equation 30}$$

Where the fitted to and parameters extracted are $x^T = [T_e, n_e, v_d]$, and $\theta^T = [\eta, \lambda_i]$. The spectral redistribution function for a Maxwellian plasma is given by,

$$S_{k,\lambda}^T = \frac{1}{\sqrt{2\pi} k_\sigma \sigma_T} \exp\left[-\frac{1}{2}\left(\frac{\omega_i - \omega - k_\sigma v_d}{k_\sigma \sigma_T}\right)^2 \right] \qquad \text{Equation 31}$$

The error of each of the extracted parameters is estimated from the 95% confidence bounds obtained from the Curve Fitting Toolbox in MATLAB.

2.6.3.2 Signal Isolation Methods

Each acquisition was comprised of some combination of frame and on-ccd accumulations that totaled 1500 shots. The grounded configuration scans were acquired with 30 on-ccd accumulations and 50 frames, while the tied and floating configurations were acquired with 25 on-ccd accumulations and 60 frames. The motivation here was to minimize the noise on the detector relative to the raw Thomson signal. To isolate the scattered spectrum due only to Thomson scattering, four spectra were acquired at each axial location. The first is the raw spectra ("A") with both the laser and thruster on. The second is the emission spectra ("B") acquired with the laser off while the thruster is on to capture the plasma emission from the thruster. The third is the reflection spectra ("C") acquired with the laser on while the thruster is off to capture the stray light reflections of the interrogation beam off reflective surfaces in the chamber. Finally, the background ("D") with both the laser and thruster off is used to capture and subtract the detector noise. The resultant Thomson signal is given by,

$$\text{Resultant Thomson Signal} = A - (B + C - D). \qquad \text{Equation 32}$$

See Figure 7 for all four spectra and the resultant Thomson signal on which all measurements were performed. The green boxes in Figure 6 represent the width of the rejected region, which was estimated as a fixed multiple of the inferred FWHM of the distribution and varied arbitrarily between data sets. Figure 7 shows an example of the raw, emission, reflection, and background spectra that are input into Equation 32 to give the spectra used for analysis, denoted as the "Thomson" spectra.

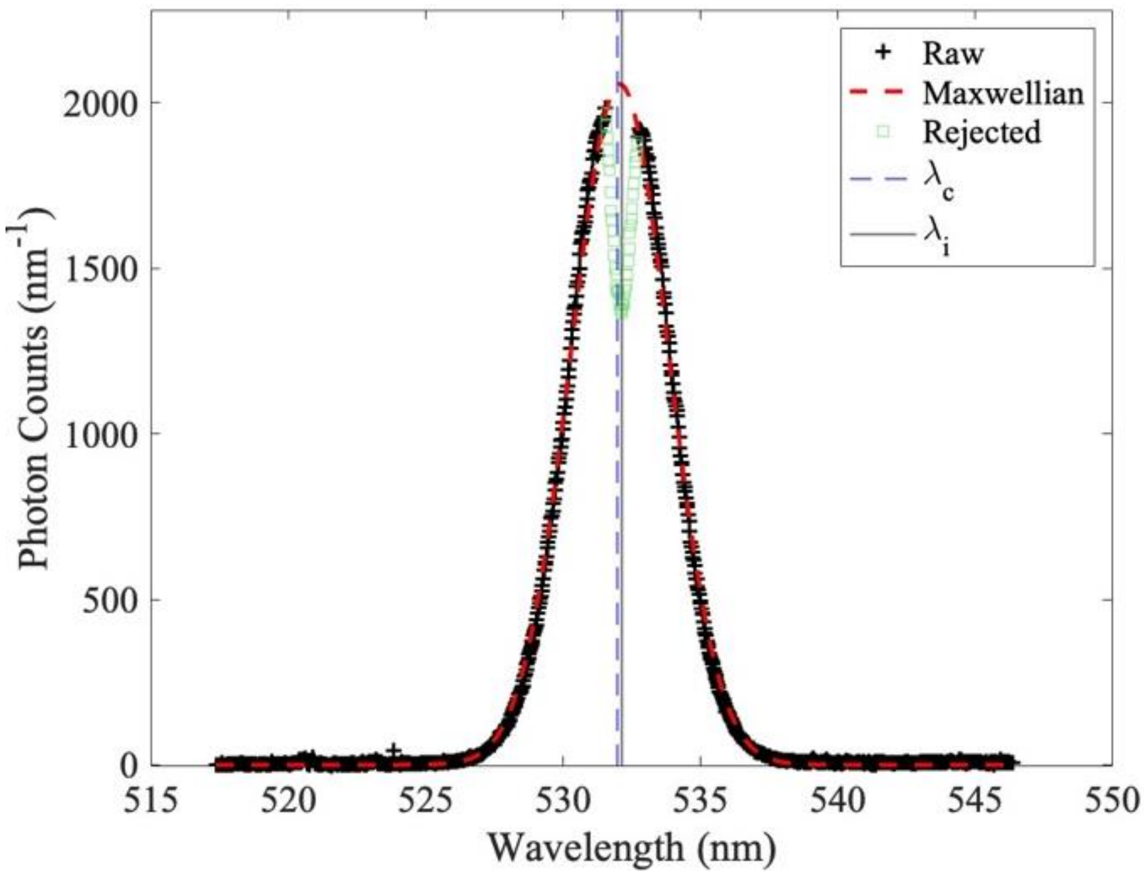

Figure 6: Example of processed LTS spectra, photon as a function of wavelength.

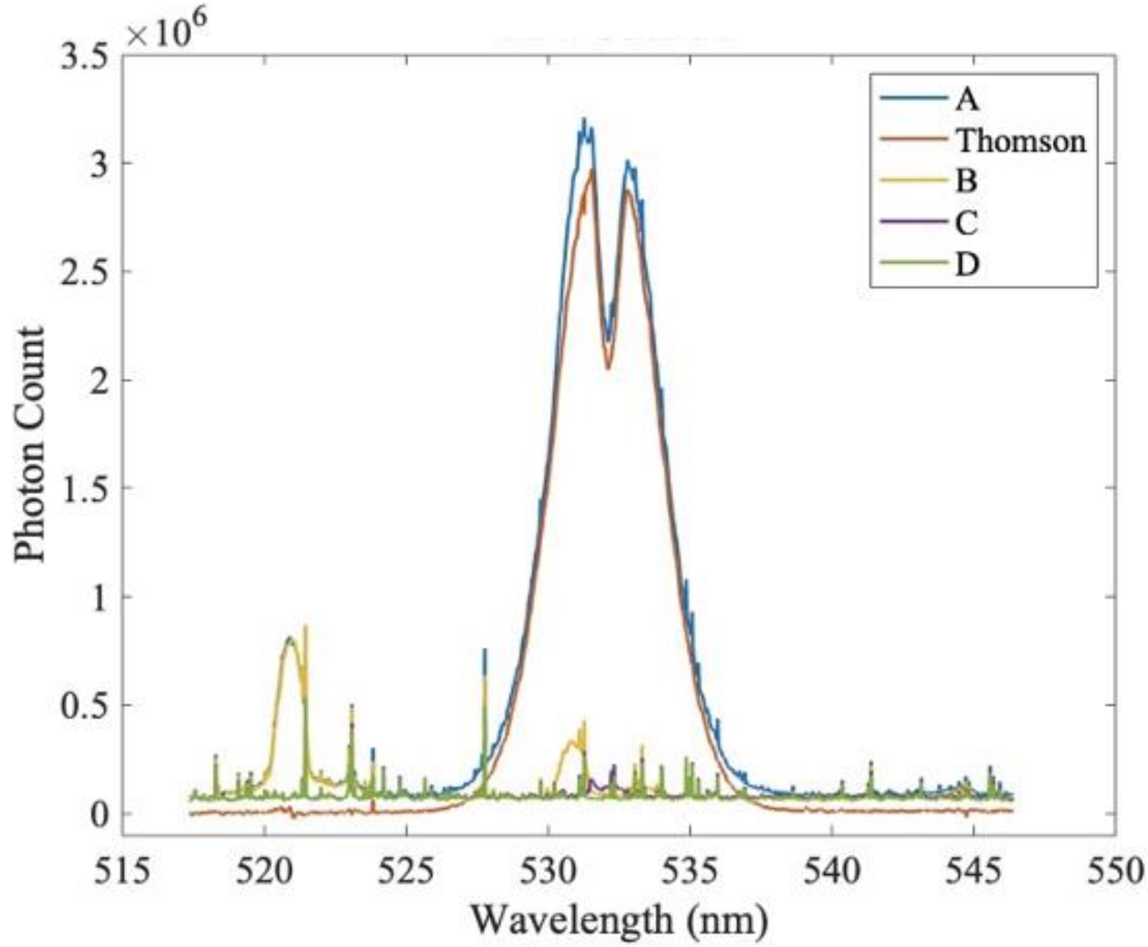

Figure 7: Example of raw spectra A, B, C, and D, that were input into Equation 32 to obtain the resultant Thomson spectra.

2.6.3.3 Data Processing Techniques

The following is a discussion about how the rejection region of the raw Thomson spectra was determined. Thomson scattering spectra are contaminated by intense elastic scatter centered at the laser line wavelength λ_0, which must be excluded from the fit to avoid biasing the extracted electron properties. This is usually referred to as “Stray Light”. Previous analyses employed an arbitrarily defined exclusion factor C_σ representing a fixed multiple of the spectral distribution's inferred FWHM based on the observed peaks. However, this approach lacked efficiency and introduced variability between datasets that could not be reliably quantified.

To improve consistency and repeatability, an automatic exclusion factor determination algorithm was implemented for all Phase II LTS analyses. The procedure operates as follows:

1. Within a pre-defined wavelength window around the laser line, approximately 530–535 nm, the algorithm identifies the two dominant spectral peaks corresponding to the Thomson-scattered signal on either side of the elastic scatter region which is rejected by the Bragg Notch Filters [Section 3.2.3].
2. The local minimum between the two identified peaks is located.

3. The wavelength distance between the laser line center λ_0 and the local minimum location is measured and recorded as the "half-width" of the exclusion region: $\Delta\lambda_{exclusion} = |\lambda_{valley} - \lambda_0|$.
4. To generalize the exclusion region definition across different spectral conditions and electron temperatures, the measured half-width is normalized by the instrumental width, σ_{IF}, to define a dimensionless exclusion factor: $\xi = \frac{\Delta\lambda_{exclusion}}{\sigma_{IF}}$.
5. The spectral region, $\lambda_0 - \xi \cdot \sigma_{IF}$, $\lambda_0 + \xi \cdot \sigma_{IF}$, is excluded from the nonlinear least-squares fitting routine (but labeled as green boxes), ensuring that only the remaining Thomson-scattered spectra inform the parameter extraction.

This automatic algorithm was validated by confirming repeatability across multiple acquisitions at the same plasma condition and by verifying that the extracted electron properties converged to physically consistent values. Figure 8 illustrates the automatic exclusion factor determination, showing the identified peaks, valley location, and resulting exclusion region, which is the data between the left and right peaks. The algorithm successfully identified exclusion regions that aligned with visual inspection while removing the subjectivity that could contaminate the results from the analysis workflow.

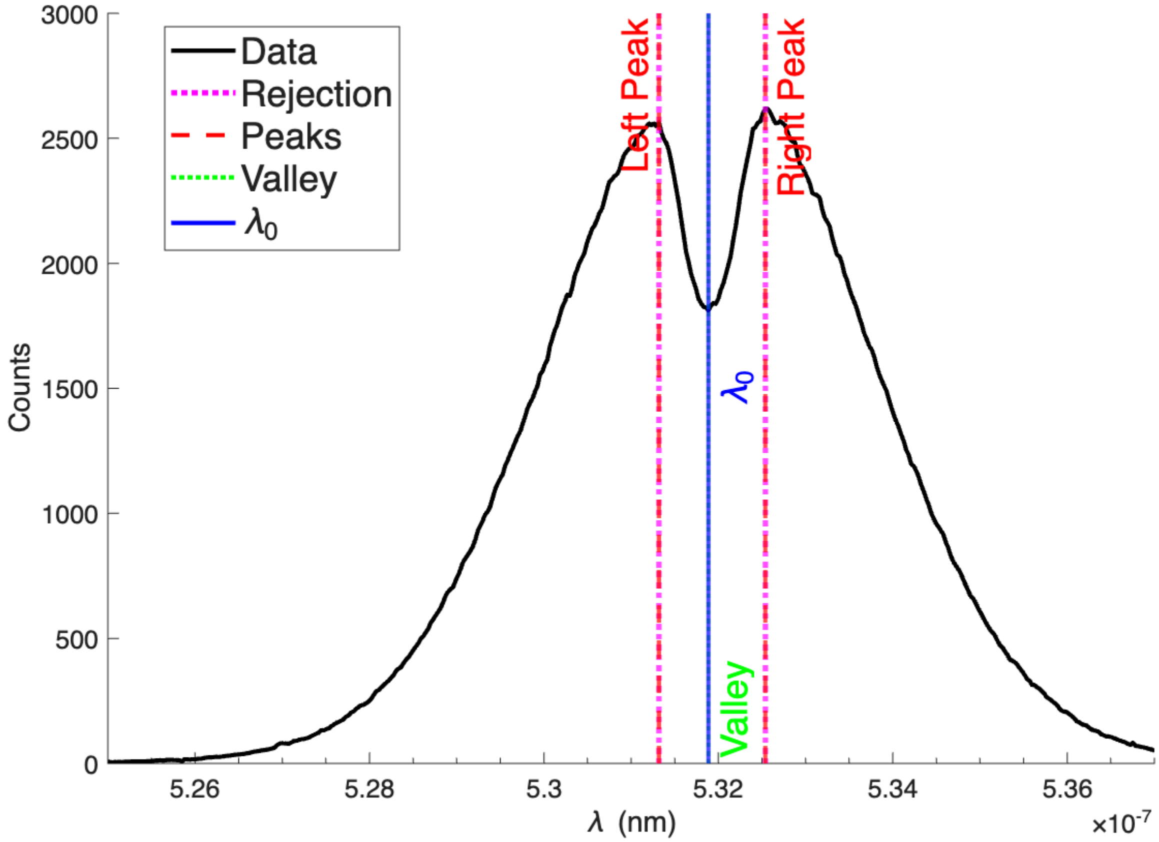

Figure 8: Automatic exclusion factor determination illustrated for representative condition.

2.6.3.4 Uncertainty

Parameter uncertainties were quantified using the covariance matrix from the nonlinear least-squares fit. Upon convergence of the optimization algorithm, the Jacobian matrix **J** that represents the sensitivity of the fitted model to each parameter was computed. The parameter covariance matrix was then calculated as:

$$\mathrm{Cov(p)} = \mathrm{MSE}(\mathrm{J^T J})^{-1} \qquad \text{Equation 33}$$

where MSE = Σ(residuals^2)/DoF is the residual variance and p = [A, V_d, T_e , n_e] are the fitted parameters. The one standard deviation, 1σ, uncertainties for each parameter were taken as the square root of the corresponding diagonal elements.

Electron density uncertainty was propagated from the amplitude uncertainty using standard error propagation:

$$\sigma_{n_e} = \left| \frac{\partial n_e}{\partial A} \right| \sigma_A \qquad \text{Equation 34}$$

Since $n_e \propto A \cdot \sqrt{T_e}$, the electron density uncertainty was further propagated, accounting for the covariance between the amplitude and temperature fit parameters via the off-diagonal covariance matrix element:

$$\left(\frac{\sigma_{n_e}}{n_e}\right)^2 = \left(\frac{\sigma_A}{A}\right)^2 + \left(\frac{\sigma_{T_e}}{2T_e}\right)^2 + \rho_{A,T_e} \cdot \left(\frac{\sigma_A}{A}\right) \cdot \left(\frac{\sigma_{T_e}}{T_e}\right) \qquad \text{Equation 35}$$

where $\rho_{A,\ T_e}$ = $\mathrm{Cov(p)}_{1,3}$ / ($\sigma_A \cdot \sigma\ T_e$) is the normalized correlation coefficient between the amplitude and temperature parameters extracted from the fit covariance matrix.

Electron temperature uncertainty was extracted directly from the diagonal elements of the parameter covariance matrix:

$$\sigma_{T_e} = \sqrt{\mathrm{Cov(p)}_{3,3}} \qquad \text{Equation 36}$$

Electron drift velocity uncertainty was similarly extracted directly from the covariance matrix diagonal:

$$\sigma_{V_d} = \sqrt{\mathrm{Cov}(p)_{2,2}} \qquad \text{Equation 37}$$

where the partial derivative accounts for the Raman calibration and scattering cross-section relationships. All reported uncertainties represent 1σ confidence intervals unless otherwise noted.

To provide a picture of what the average sample condition uncertainty was, Table 1 presents the extracted parameters and their uncertainties, which were calculated for a representative condition.

Table 1: Sample of extracted parameters and their uncertainties.

$\mathbf{A_{fit}}$	$2.848\times10^{3} \pm 1.88$
$\mathbf{V_{d,fit}}$	$-3.795\times10^{4} \pm 3.26\times10^{2}$ m/s
$\mathbf{T_{e,fit}}$	2.830 ± 0.003 eV ($3.284\times10^{4} \pm 3.91\times10^{1}$ K)
$\mathbf{n_{e,fit}}$	$4.120\times10^{21} \pm 2.08\times10^{18}$ m^{-3} (approximately 0.5% relative uncertainty)

These small relative uncertainties, approximately 0.5% for electron density and approximately 0.1% for electron temperature, reflect the high signal-to-noise ratio achieved at the 40 A, 150 V operating condition and validate the robustness of the forward convolution fitting procedure. Uncertainty information for all conditions was systematically saved to text files for subsequent analysis and error propagation through derived quantities such as electron pressure.

CHAPTER 3: INITIAL EXPERIMENTAL INVESTIGATION

This chapter outlines the initial experiments and diagnostic validation efforts undertaken to establish the foundation for the subsequent investigation. First, the experimental setup, including the HET, diagnostic tools, and electrical measurement setups, is described in detail. Next, the preliminary data collected under floating, cathode-tied, and grounded thruster body electrical configurations are presented. These initial measurements provide a foundational characterization of the electron density and temperature profiles in the near-field region downstream of the cathode. The preliminary findings illustrate how electron density and temperature profiles vary spatially with thruster bias conditions, highlighting early indications of how sheath structure, and thus potential distributions near critical surfaces, can be influenced by operational adjustments.

3.1 Introduction, Background, and Experimental Goals

HETs are a cornerstone of modern EP systems, widely utilized in commercial space missions because of their high specific impulse of over 1,000 s, high thrust-to-power ratio, and high reliability [59]. To date, ion thrusters have been the primary EP technology baselined for science missions by NASA, JAXA, and ESA [[60]], though HETs have seen limited science mission use, notably the SPT-140 on NASA's Psyche mission 61 and ESA's SMART-1 62. Advances in magnetic shielding are expected to extend

HET operational lifetimes, further enabling their adoption for long-duration science applications. Magnetically-shielded HET's utilize a transverse magnetic field to trap electrons, creating a high-density plasma region at the thruster exit plane. In this region, the high-temperature, >20 eV, electrons ionize the propellant gas while an applied electric field accelerates the ions through the thruster's exit [9]. The resulting ion beam generates thrust, while the electrons neutralize the ion beam to maintain plasma plume charge neutrality. This method offers high efficiency and exit velocity, making HETs ideal for long-duration space missions and satellite station-keeping. Various institutions have sought to optimize and increase their suitability for said mission applications through several design considerations, including but not limited to magnetic field optimization, e.g., magnetic shielding, [63], flight-like ground-based testing environments, and simulations that allow ground testing results to be accurately extrapolated to performance in space.

In ground-based testing, understanding and mitigating facility interactions is crucial as this technology continues to develop for more challenging mission applications. These interactions yield information about how the thruster will not only perform in space but also interact with the spacecraft. Studies in the last decade have identified a facility interaction, outside of the thoroughly investigated elevated pressure effects [64, 65, 66], that involves the electrical interaction of the conducting vacuum facility with the HET plume [67, 68].

The electrical configuration of the thruster, or how the thruster electrodes and chassis are connected, plays a major role in this. Peterson et al. [69] completed detailed performance maps of NASA's 12.5-kW Hall Effect Rocket with Magnetic Shielding (HERMeS) Technology Demonstration Unit-1 (TDU-1) with the thruster in several ground-based electrical configurations. The study assessed the best electrical configuration to conduct development and qualification testing for flight missions. An additional facet of the study was varying the exit plane boundary condition between a dielectric and conducting surface. This was employed using dielectric and conducting pole covers. While grounding the thruster body by electrically connecting it to the conducting vacuum chamber yielded the highest performance in this study, this configuration was not ideal since it created a low-resistance electron pathway through the conducting chamber. Such a pathway allows electrons to recombine with plume ions at the chamber walls which is a condition not representative of the space environment [67]. Peterson et al. confirmed this electron pathway, with 10% of the discharge current flowing through the thruster body to ground in this configuration [69].

Another electrical configuration for the HET is to isolate the thruster body from the vacuum chamber, allowing it to float electrically. This configuration was employed by HETs in flight on the ESA SMART-1 spacecraft [70]. However, in space, the thruster was electrically connected to the spacecraft, which also floated relative to the local plasma potential. While the floating configuration is more representative of the flight environment for ground-based testing, it does result in very negative floating potentials of the thruster body [71]. The resultant plasma sheaths accelerate ions toward components at the thruster body potential. These ions increase the erosion of the plasma-facing thruster components at the thruster body potential.

The final configuration examined by the author was electrically connecting the thruster body to the cathode common to limit the floating potential of the thruster body, thus mitigating possible erosion due to energetic ions [72]. It was found that this configuration provided negligible decay in performance from the grounded configuration, while still being representative of the flight environment. The power spectral density (PSD) plots in the study showed variance in the discharge current oscillation characteristics that may influence the near-field thruster plume physics [73]; however, no near-field measurements were taken. It has been postulated and measured in Ref. [74] that the electrons collected by the plasma-facing thruster components are conducted and re-emitted through the cathode. These parameters have not been definitively measured. Understanding the electron properties in the near field of HETs, immediately adjacent to the thruster exit plane, is difficult because the environment consists of complex plasma phenomena that significantly influence thruster operation.

The primary objective of this study is to characterize and understand how the near-field plasma properties, electron temperature, and electron density, change downstream of the cathode centerline in each of the three electrical configurations described above. An incoherent LTS diagnostic is employed to make these measurements. LTS is a noninvasive diagnostic technique used to measure electron properties in plasmas. The method involves directing a laser beam into the plasma, where the photons scatter off the free electrons. The scattered spectrum allows inference of key electron properties (such as density, velocity distribution, and temperature) if we assume that the velocity distribution is a Maxwellian distribution [75]. The noninvasive nature of LTS makes it particularly valuable for detailed studies of dynamic plasma behaviors in various applications. Recently, advances in hardware have enabled the necessary sensitivity for LTS to be applied to the low-temperature, low-density plasmas present in HETs [76, 77]. This manuscript presents measurements of near-field electron properties with the HET in three different electrical configurations, body grounded, body floating, and body tied to the cathode common. The axial electron number density and temperature profiles are compared. Additionally, power spectral density profiles of the thruster discharge current are also presented for each configuration.

3.2 Experimental Setup and Methodology

This section describes the vacuum facility in which the experiment was conducted, the H9 HET setup and operation, the LTS diagnostic setup, and the theory used to infer the electron parameters of interest. The combined experimental configuration allows for simultaneous investigation of thruster operation and plasma properties under controlled vacuum conditions.

3.2.1 Facility

The experiment was carried out in Vacuum Test Facility 2 (VTF-2) at Georgia Tech's High Power-Electric Propulsion Laboratory (HPEPL). VTF-2 measures 9.2 meters in length and 4.9 meters in diameter. The chamber is then evacuated to a moderate vacuum of approximately 10 mTorr measured with an Agilent Varian 531 Thermocouple Vacuum gauge. This rough vacuum was achieved through one 3800 CFM blower and one 495 CFM rotary-vane pump. To reach high vacuum, the facility utilizes 10 LN_2-cooled CVI TMI reentrant cryopumps that provide a pumping speed of approximately 400,000 l/s on krypton. The pressure in the high-vacuum phase of operation is measured in three locations: two internal and one externally mounted on a chamber flange. All three locations employ Agilent Bayard-Alpert 571 hot-filament ion gauges. Averaging over the three measurements provides a base pressure of 9.1×10^{-8} Torr and an operational pressure of 7.7×10^{-6} Torr-Kr at a krypton anode flow rate of 230 sccm (14.37 mg/s) during this experiment.

Understanding the electron current pathways in a Hall effect thruster is essential context for interpreting the experimental results presented in this work. The total current emitted by the cathode is distributed among several parallel paths. A portion of the emitted electrons undergo azimuthal drift in the discharge channel, constituting the Hall current. Electrons also diffuse cross-field from the cathode plume through the channel to the anode, closing the discharge circuit and forming the anode return current. A fraction of emitted electrons travels downstream to neutralize the ion beam, which is required to prevent spacecraft charging in flight. Finally, electrons must replenish the ionization zone near the channel exit to sustain the discharge. The relative partitioning of current among these pathways is sensitive to the local electric and magnetic field environment, and therefore to the electrical boundary conditions imposed on the thruster body. This sensitivity is the physical basis for the body bias investigation described in the following sections.

3.2.2 Hall Effect Thruster and Operating Conditions

The H9 is a 9 kW magnetically-shielded Hall thruster designed by JPL in collaboration with the University of Michigan and AFRL 78. The H9 has been described as a sub-scale cousin of the 12.5 kW Hall Effect Rocket with Magnetic Shielding (HERMeS) thruster [79], which served as the basis for the Advanced Electric Propulsion System (AEPS) [80, 81]. AEPS is the primary propulsion system for the Power and Propulsion Element of NASA's Lunar Gateway. The shared magnetically-shielded design philosophy between the H9 and HERMeS/AEPS makes findings on the H9 relevant to understanding the physics of this class of flight-qualified Hall thruster. The electrical configuration testing performed on HERMeS [3] further motivates the investigation of electrical configuration effects on electron behavior conducted in this work. The H9 anode and cathode were supplied with a mass flow of krypton with a purity of 99.999% measured by MKS GE50A mass flow controllers (MFCs). The MFCs were calibrated at the test article using a MesaLabs DryCal 800-10 volumetric flow meter, and a linear fit was generated between the commanded and measured propellant flow rates. Table 2 presents the performance parameters at the 6-kW operating condition.

Table 2: Thruster Performance

Operating Condition (kW)	**Thrust (mN)**	**I_{sp} (s)**	**Anode Efficiency**	**Background Pressure (μTorr-Kr)**
6	250	2000	0.56	5.93

The thruster is powered by multiple power supplies. The thruster discharge power is supplied by a Magna-Power TSA800-54 power supply in series with a 95-μF capacitor and 1.3-Ω resistor to prevent discharge current oscillations of above 1.4 kHz. The discharge filter is present in both experimental phases but is not included in the circuit diagrams shown in Figure 9, Figure 10, or Figure 11. The cathode heater, cathode keeper, and inner and outer magnet coils are powered by TDK-Lambda GEN60-25, GEN600-2.6, GEN40-38, and GEN80-42 power supplies, respectively. Time-resolved thruster telemetry is measured with a Teledyne LeCroy HDO6104 oscilloscope with a 1 MS/s sampling rate. Thruster telemetry recorded includes time-resolved measurements of the discharge current, discharge voltage, thruster body-to-ground voltage, and the cathode body-to-ground voltage. The discharge voltage is measured with a Powertek DP25 differential voltage probe rated up to 25 MHz. The discharge current is measured on the anode electrical line in the control room using a Teledyne Lecroy CP150 current clamp. Additionally, the oscilloscope records the discharge current data for the generation of PSD plots of the three electrical configurations.

The thruster is run at the same operating condition in all three electrical configurations. The thruster is run at one of the nominal H9 operating conditions of 6 kW with a discharge voltage of 300 V, a discharge current of 20 A, measured on the cathode electrical line, and a magnetic field 87.5% of the nominal magnetic field setting. The anode flow rate was 229.6 ± 1.89 sccm-Kr (14.35 mg/s) with a cathode flow rate of 20.17 ± 0.45 sccm-Kr (1.26 mg/s). The discharge peak-to-peak values for the floating, grounded, and tied configurations were 17.10 A, 9.70 A, and 15.92 A, respectively.

The electrical configuration of the thruster is varied at a breakout box in the control room. Figure 9, Figure 10, and Figure 11 show the associated circuit diagrams for the floating thruster body, grounded thruster body, and cathode-tied thruster body, respectively. The discharge voltage, V_d, is measured across the anode-cathode terminals at the breakout box in the control room using a differential voltage probe. The discharge current, I_d, is measured on the cathode electrical line at the breakout box using a CP150 current clamp. The floating thruster body configuration, further referred to as the "floating configuration," is where the thruster body is electrically isolated from the conducting vacuum chamber and floats at a potential determined by the local plasma environment. Because the thruster body is not tied to the cathode or the anode, its potential is driven by a net-zero collection of current: the surface receives both a flux of ions and a flux of electrons, and it tends to float negative because the electrons are more mobile and have higher thermal velocity. The resulting electron-repelling sheath limits the electron current to the body, establishing a self-regulating charge balance.

The cathode-tied thruster body configuration, further referred to as the "tied configuration," is where the thruster body is electrically tied to the cathode common. In this configuration, emitted electrons from the cathode act as collected current at the body surface, and the net flux of charge is no longer sheath-limited in the same manner as the floating case. The removal of sheath limitation tends to increase the total current to the thruster body relative to the floating configuration.

The grounded thruster body configuration, further referred to as the "grounded configuration," is where the thruster body is electrically tied to the vacuum chamber at facility ground. The electron collection mechanism in this configuration differs from the other two. It is unlikely that electrons emitted from the cathode flow directly to the thruster body; instead, the ambient plasma self-regulates the electron current to the grounded surfaces through ambipolar diffusion. The grounded surfaces are also free to supply electrons to the beam neutralization process, which can produce efficient thruster operation in ground testing but is not representative of the flight environment and may be problematic in flight. Each configuration produces a different transition from the thruster plume to the ambient plasma, which can affect the local plasma potential and potentially the beam divergence. The floating and cathode-tied configurations should also yield different secondary electron temperatures in the ambient plasma, which may or may not facilitate beam neutralization. The coupling between the configuration and the discharge is best characterized by the frequency and magnitude of the thruster oscillations.

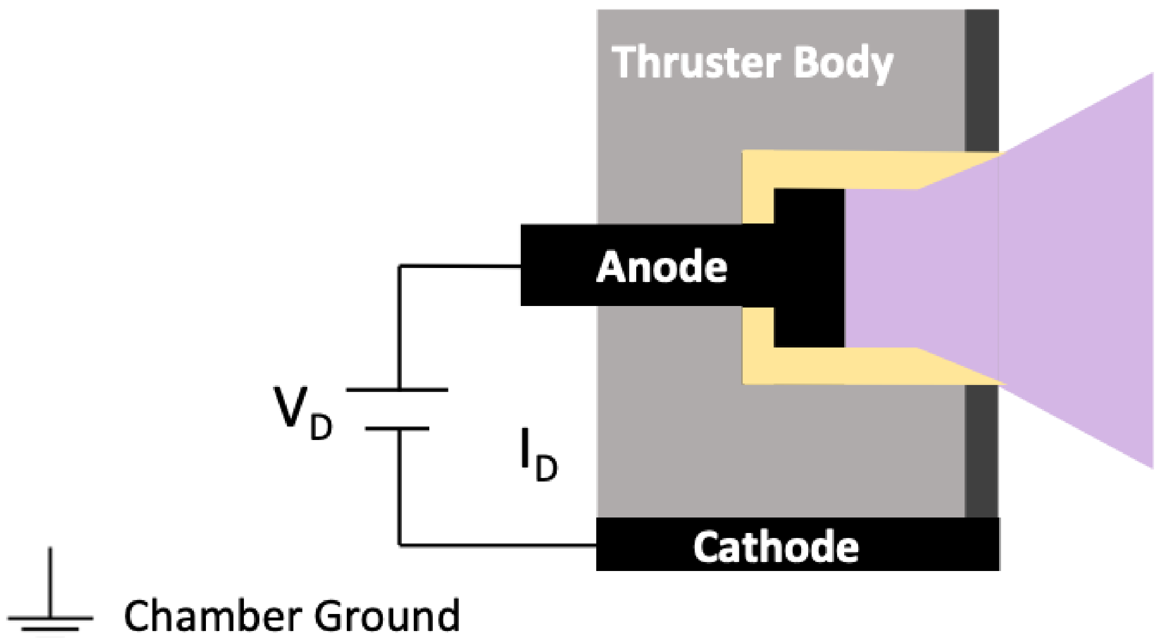

Figure 9: Circuit for the floating electrical configuration.

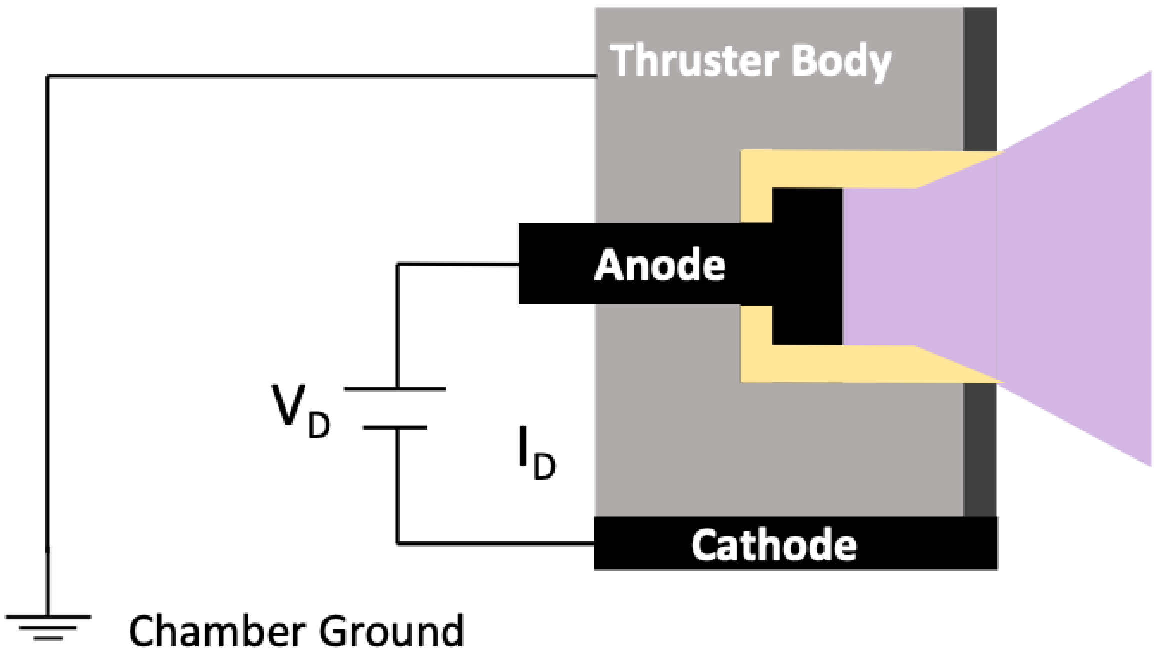

Figure 10: Circuit for the grounded electrical configuration.

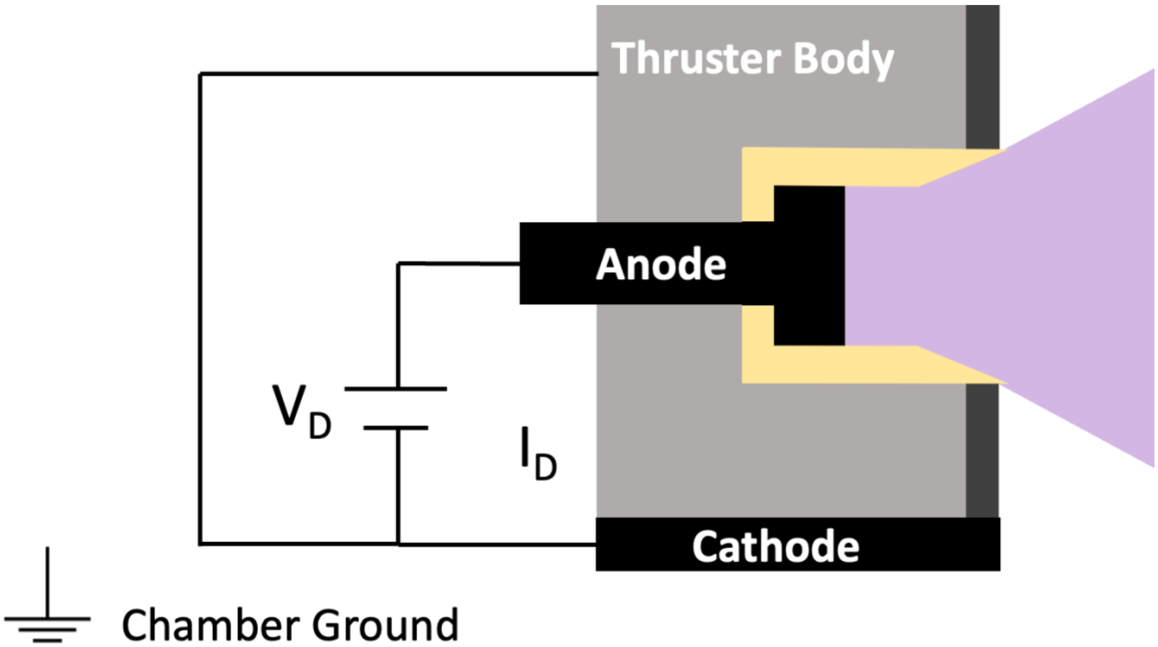

Figure 11: Circuit for the tied electrical configuration.

To produce the spatially resolved electron properties in the near field of the thruster, the H9 was translated relative to the stationary LTS interrogation beam and collection optics using two Parker 4062000XR motion stages with ± 8 μm positional accuracy. Figure 12 shows the coordinate system with the (x) along the direction of the interrogation laser propagation, (z) being the axial direction on which the measurements are taken, and y being the vertical direction on which the collection optics sit. Figure 12 also shows the thruster on the stages that enable probing of the near field of the thruster in the axial (z) and radial (x) directions. Figure 13 shows the total length over which the measurements are taken, as well as their spatial resolution.

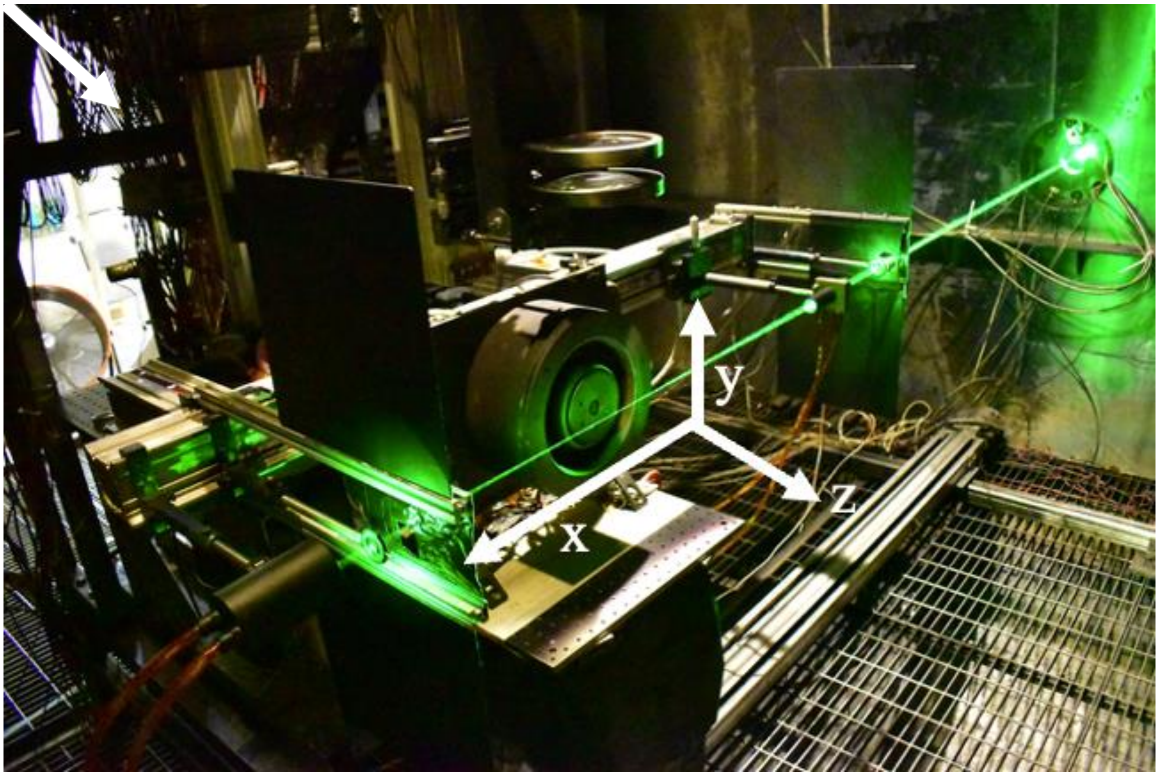

Figure 12: H9 Thruster on motion stages.

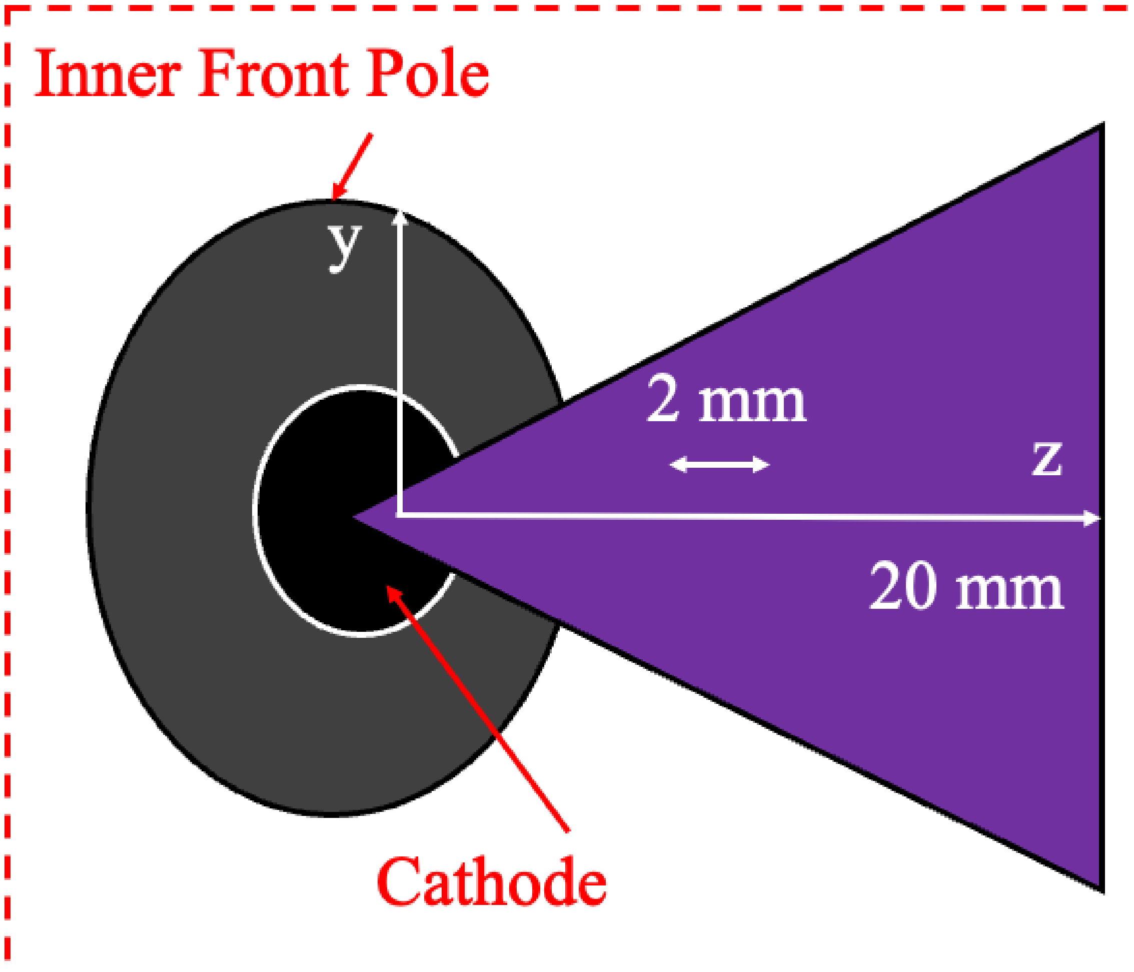

Figure 13: Measurement coordinate system and H9 on motion stages.

The three electrical configurations examined in this study were selected because they impose fundamentally different boundary conditions on electron current pathways to the thruster body. These distinct electrical environments are expected to produce measurable differences in both electron density and electron temperature in the near-field cathode plume, motivating the spatially resolved LTS measurements described in the following section.

3.2.3 Laser Thomson Scattering System

As previously mentioned, LTS in low-density plasmas involves laser photons scattering off free electrons in the plasma, collecting that scattered light, and performing spectral analysis that enables the inference of electron properties. The LTS system design is depicted in Figure 14 and is described in detail in Ref. [82]. To calibrate the LTS diagnostic absolute electron number-density measurements, a laser rotational Raman scattering (LRS) measurement was taken at 5 Torr. This pressure was measured with a Kurt J. Lesker XCG-BT-FB-1 capacitance manometer chosen for its accuracy of ± 0.5%.

An Amplitude DLS Powerlite 9010 injection-seeded Nd:YAG laser, operating at the second harmonic wavelength of 532 nm, delivered a beam diameter of 9 mm. The laser pulse duration ranged between 5 and 8 ns, with a maximum energy output of 1.15 J per pulse with a 10 Hz repetition rate. However, due to internal misalignments with the laser, the maximum laser output is approximately 670 mJ/pulse. The optical beam path depicted in Figure 14 is as follows: the beam exits the laser, intersects a mirror, turns into a beam expander assembly, and then into a half-wave plate and polarizing beam splitter cube so that the laser energy can be modulated without changing the timing settings internal to the laser. From there, the laser energy is measured using a power meter on a flip mount, allowing quick, unobtrusive energy measurements between LTS acquisitions. The energy is averaged over the 2.5-minute acquisition duration and measured by a Gentec UP52N-50S-QED-D0 power meter, which corresponds to PM in Figure 14. The beam turns again and goes through another half-wave plate that determines the final polarity of the beam before it enters the vacuum chamber through the periscope and Brewster window. The beam waist of about 100 μm intersects with the observation volume 2 mm downstream of the thruster face through a 600-mm focal length lens inside the chamber. The scattered light is collected and transmitted through two custom Thorlabs FG200LEA-FBUNDLE fiber bundles that contain seven 200-μm FG200LEA multimode fibers. The two fiber bundles are connected in series through a flange, allowing the collected light at the thruster to be relayed out of the chamber and into the external collection system. The light relayed through the bundles is spectrally filtered through two Optigrate OD-4 Bragg Notch Filters (BNFs) and then delivered to the spectrograph. The spectrograph consists of a Princeton Instruments ISOPLANE-320A spectrometer and a PM4-1024i-HB-FG-18-P46 PIMAX4 camera [83]. The collection fibers are delicately aligned to account for the chamber compression from the atmosphere to high vacuum. To enable this, the internal fiber bundle is placed on three motorized stages. Fine alignments at the axial location nearest to the cathode centerline are also made between each measurement to ensure that the maximum signal at the start of the experiment can be recovered throughout. For further details on the optical system design and alignment, refer to Ref. [82].

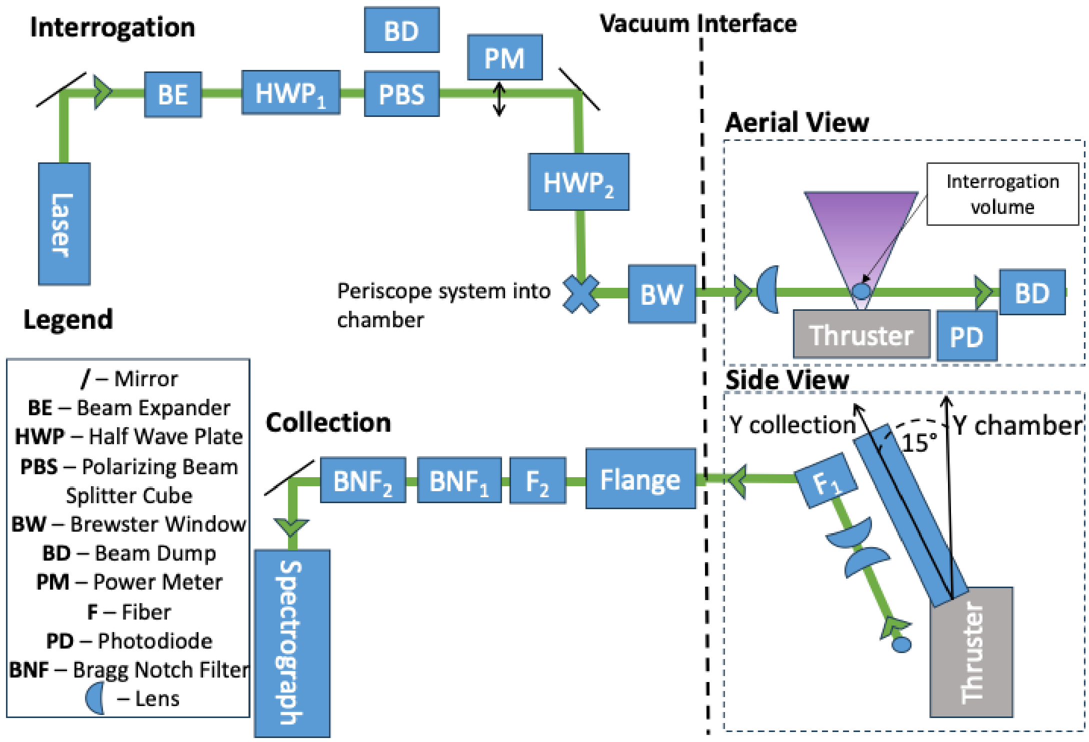

Figure 14: Master optical diagram for the interrogation, collection, and detection systems

3.3 Experimental Results and Discussion

The primary focus of this study is the axial characterization of the electron number density and temperature of the cathode plasma with the thruster body in three electrical configurations and, thus, potentials. A secondary objective is to characterize how the power spectral density distribution changes in the different electrical configurations. The goal is to understand the impact of the electrical configurations on the near-field plasma characteristics.

3.3.1 Electron Property Comparisons

The sheath potentials on the inner front pole surface of the HET regulate downstream electron propagation by determining whether electrons are attracted to or repelled from the surface. The polarity of the sheath (electron-attracting or repelling) dictates whether electrons remain near the pole or propagate downstream, while the strength of the sheath potential governs the gradient of potentials experienced by electrons as they are attracted or repelled to the surface.

Figure 15 presents the notional potential profiles (not drawn to scale) along the axial distance for three distinct electrical configurations of the thruster: cathode-tied (blue line), grounded (red line), and floating (black line). The light blue trapezoid is a notional illustration of the radially expanding sheath on the inner front pole. The sheath thickness, λ_D, is assumed to be increasing radially outward from the cathode centerline to the inner front pole cover. This trend aligns with the inverse relationship between electron density and sheath thickness ($\lambda_D \propto \frac{1}{\sqrt{n_e}}$), as the electron density is expected to decrease by orders of magnitude moving from the cathode centerline to the inner front pole. The figure is not drawn to scale, nor is the sheath expected to be linearly increasing; it is drawn this way for simplicity and to illustrate our conclusions. The figure aims to illustrate the comparative potential drops associated with each configuration relative to the plasma potential. Although the plasma potential was not measured during this experiment, it is assumed to remain independent of the thruster body potential. This assumption is supported by the convergence of electron properties observed beyond 15 mm axially downstream and the consistent cathode-to-ground voltage measured. Due to the non-uniform sheath thickness, the potential profiles exhibit a gradient. Consequently, configurations with larger total potential drops at the thruster body exit, primarily in the region of the inner front pole, correspond to steeper potential gradients, which influence the distribution of electron energies as they are either attracted or repelled.

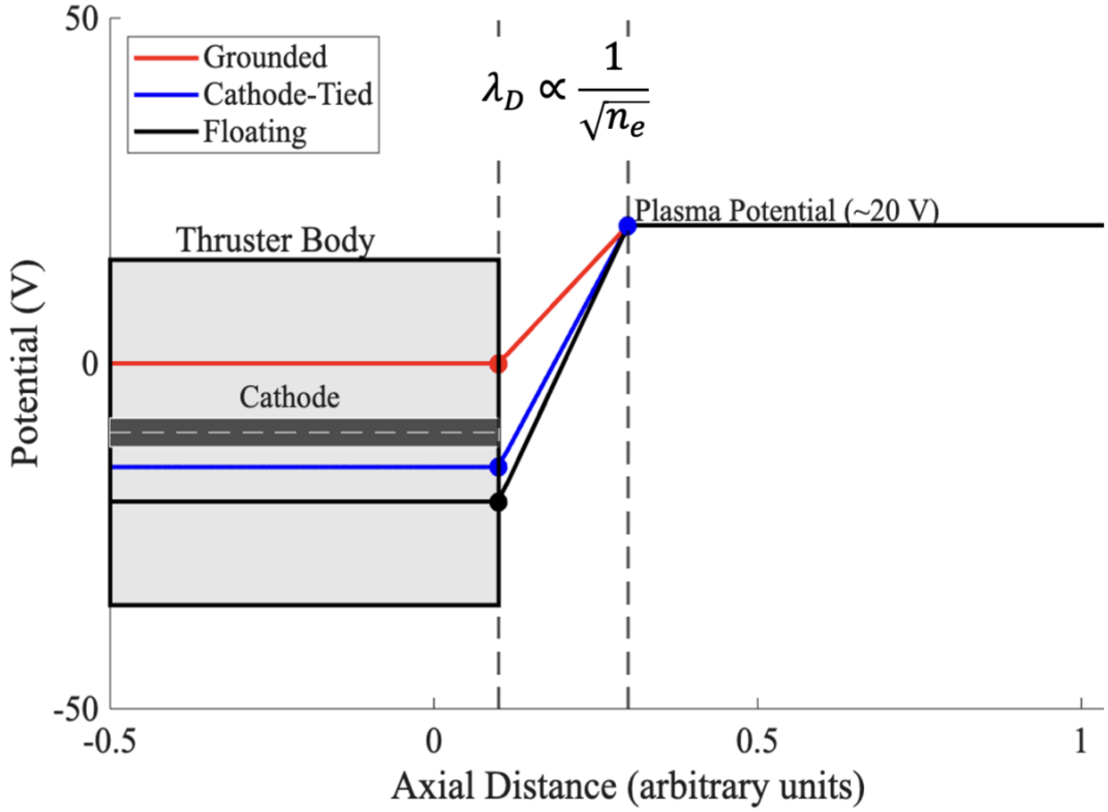

Figure 15: Notional potential profiles experienced by electrons emanating from the cathode exit (x = 0) for the three electrical configurations

Electron pressure measurements were previously measured to reach a minimum in the inner front pole region [1]. The observation of an electron pressure minimum in the inner front pole region reinforces this qualitative interpretation that the thruster body configuration actively drives a localized potential drop. Because the thruster body is a conducting element held at its own potential, it sets a boundary condition that influences the nearby plasma. According to the electron momentum equation, the electron pressure gradient serves as a proxy for the electrostatic potential gradient; hence, a minimum in electron pressure implies a corresponding local drop in potential. This potential drop not only creates an electrostatic pathway that accelerates ions toward the inner front pole (a mechanism that can contribute to pole erosion) but it also has important implications for electron behavior.

3.3.1.1 Electron Number Density

Figure 16 shows the electron number density, n_e, as a function of axial position for all three electrical configurations. As expected, the electron number density exponentially decays as the axial distance downstream of the cathode exit increases [55,1]. All three electrical configurations have a maximum electron density of an order of magnitude of 1×10^{19} m^{-3}, which is consistent with expected values at the cathode centerline based on measurements reported in other literature [1]. Neutral density simulation results for the HERMeS thruster operating at nominal conditions in [84] showed that the neutral density stays above 1×10^{19} m^{-3} up to 15 mm downstream of the cathode centerline (and decreases below 1×10^{18} m^{-3} 60 mm downstream from the cathode), whereas the measurements in this study drop an order of magnitude approximately 5 mm downstream. This discrepancy between these measurements is likely attributed to the fact that the neutral flow simulation does not account for various plasma effects present in the experimental environment, e.g., charge exchange collisions and ionization.

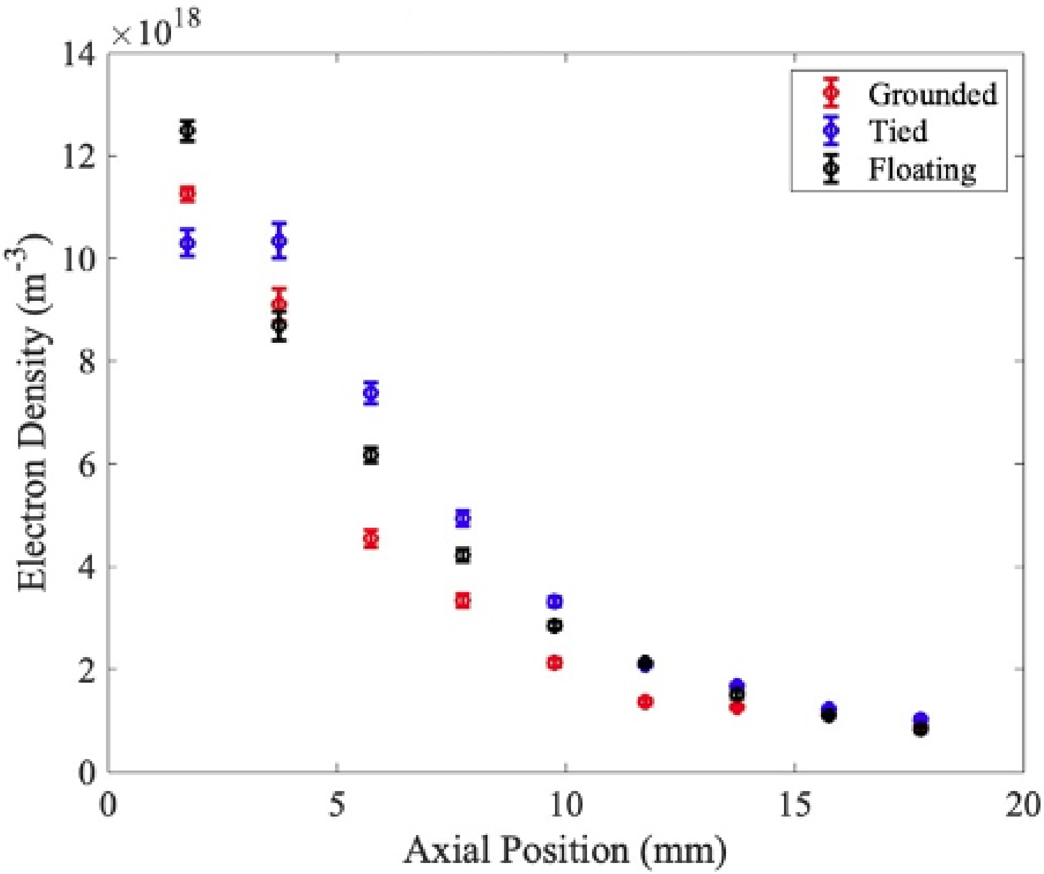

Figure 16: Electron number density as a function of axial position in the grounded, cathode-tied, and floating configurations inferred from the LTS spectrum as a function of distance from the cathode taken at a radial location of the cathode centerline.

The electron density exhibits a significant decrease of approximately two orders of magnitude over the 17 mm axial distance consistently across all electrical configurations before converging. Previous studies by Betancourt-Suazo et al. in Ref. 1 measure the same two orders of magnitude decrease over a similar axial distance. This convergence in the far-field plume suggests that electron density measurements taken far from the thruster face may not effectively differentiate between electrical configurations. The central mounting of the cathode combined with the conducting pole covers of the H9 thruster creates a specific plasma-surface interaction geometry, where the inner front pole cover, being the nearest conducting surface to the cathode exit, is likely to have some influence on the cathode plasma. The thruster face's direct contact with the plasma leads to stronger sheath formation compared to the circumferential thruster body components. These effects would likely be minimal with an externally mounted cathode configuration, as thruster body potential changes would have a limited influence on local cathode plasma density.

In the cathode-tied configuration, the observed increase in electron density downstream of the cathode can be explained by sheath dynamics under the assumption of constant plasma potential. Since the thruster body is electrically tied to the cathode (which is negatively biased relative to the plasma), the inner front pole cover adopts the cathode's potential. This creates a fixed sheath potential difference, $V_{Plasma} - V_{Thruster\ Body}$ that is electron-repelling, reflecting electrons away from the pole cover and confining them. The resulting reduction in electron-wall losses enhances electron retention in the plasma, thereby increasing the local electron density. The cathode's electron emission current, $I_{Cathode}$ must satisfy both the discharge current ($I_{Discharge}$) and any current collected by the thruster body, $I_{Thruster-Body}$: $I_{Cathode} = I_{Thruster-Body} + I_{Discharge}$. If the thruster body collects current, e.g., from CEX ions attracted to its negative potential), the LaB6 emitter must supply additional electrons to maintain current balance. This increased emission could further elevate downstream electron density. However, since $I_{Thruster-Body}$ was not directly measured, this hypothesis relies on indirect evidence. The electron-repelling sheath prevents emitted electrons from traveling to the thruster body to neutralize CEX ions collected by the thruster body. Instead, these electrons remain confined downstream, contributing to the observed density increase. This decoupling of the measurements and probably electron/ion pathways suggests that the elevated electron density arises from enhanced confinement rather than direct neutralization of thruster body currents. Further measurements, e.g., thruster body current, plasma potential maps, are needed to resolve the exact mechanism.

The grounded configuration exhibits the lowest electron density, as the electron-attracting sheath draws electrons to the pole surface, preventing significant downstream transport. Substantial electron collection occurs at the thruster body in the grounded configuration, with measurements from Peterson et al. showing up to 13% of discharge current can be collected by the thruster. The conducting, grounded inner front pole cover acts as an electron collector. In the floating configuration, electron collection occurs until the sheath establishes equilibrium, maintaining a zero net charge flux. While this configuration also results in an electron-repelling sheath, the magnitude of the sheath potential is lower than in the cathode-tied configuration. This difference could be attributed to the floating surface achieving a dynamic balance without the direct influence of the cathode potential.

The following three figures depict schematic cross-sections of the thruster body (gray) that surrounds the cathode (dark horizontal bar). The purple region on the right represents the downstream plasma plume. Red arrows illustrate expected electron paths: one arrow shows electrons flowing directly downstream from the cathode into the plume, while another indicates electrons that can travel toward or around the thruster body. The blue arrow at the bottom represents the ion or CEX flow that can interact with the thruster body.

In the Floating case, the thruster body is not electrically grounded and is free to float at a potential determined by the interaction of incoming ions and the emitted electrons. This configuration aims to balance the charge fluxes between the plasma and the body, so that the amount of positive charge collected by the thruster body from incoming ions is compensated by the flux of electrons emitted from the cathode. Consequently, electron collection by the body is self-regulating. Once the charge flux to the body reaches an equilibrium, further electron collection from the cathode is effectively halted. This charge neutrality is a critical feature of the Floating configuration, as any imbalance would result in a net charge build-up or depletion on the body, leading to a shift in the plasma potential and affecting electron flow downstream. As a result, the electron density measured downstream at the cathode centerline in this configuration will reflect a balance between the emitted electron flux and the electron loss to the body, producing an intermediate electron density compared to the grounded and cathode-tied configurations [85].

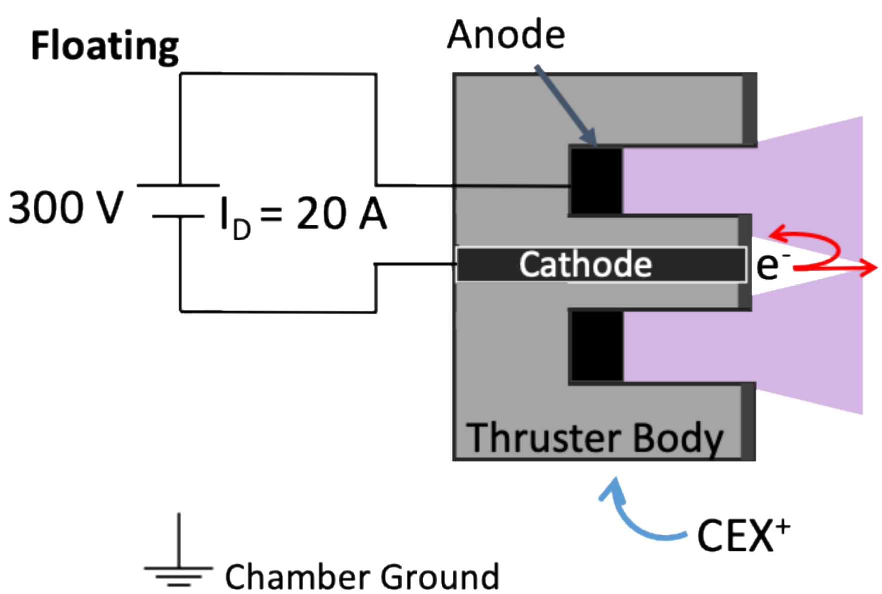

Figure 17: Schematic of the floating thruster configuration to depict electron pathways

In the grounded configuration, shown in Figure 18, the thruster body is connected to ground, meaning it has the same electrical potential as the surrounding environment. This sets up a potential difference between the cathode, which emits electrons, and the thruster body. The grounding of the body results in the attraction of electrons toward the thruster body, which reduces the number of electrons that travel downstream to the cathode centerline. The resulting effect is that fewer electrons from the cathode reach the centerline in comparison to the floating or cathode-tied configurations. As electrons accumulate on the thruster body, the discharge potential of the body becomes more favorable for attracting electrons, and thus, the body collects more electrons, diminishing the downstream electron density. This characteristic leads to a lower electron density in the grounded configuration, as the electron current is redistributed toward the body rather than allowing as many electrons to reach the downstream region. This behavior contrasts with the cathode-tied configuration, where the cathode and the body are at equal potential, allowing for a more direct flow of electrons downstream, and results in a higher electron density at the cathode centerline.

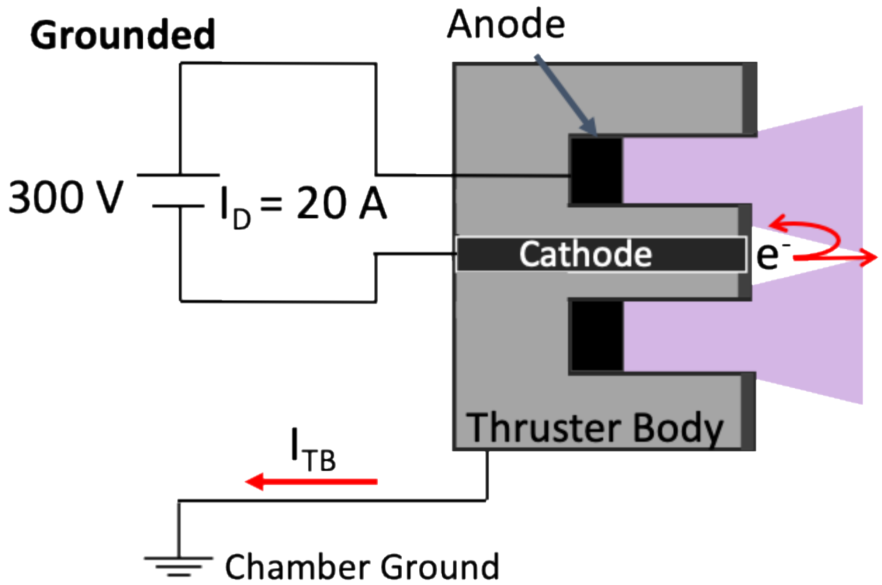

Figure 18: Schematic of the grounded thruster configuration to depict electron pathways

In the cathode-tied configuration, shown in Figure 19, the thruster body and the cathode share the same electrical potential. With no voltage difference between them, electrons emitted by the cathode are not pulled toward the body and instead flow freely downstream into the plasma plume. The curved arrows represent CEX flow entering and circulating through the thruster. While it does lead to enhanced current flowing back to the cathode common, it does not appear to necessitate additional electron emission from the cathode, as electrons would not be able to flow back to the body to complete the circuit. As a result, the electron density measured downstream is typically higher than in configurations where the thruster body is at a different potential. These configuration-dependent density orderings and the distinct electron pathways they imply motivate the expanded Phase II investigation, where spatially resolved electron temperature measurements further reveal how body bias modifies the energetics of near-field electron transport.

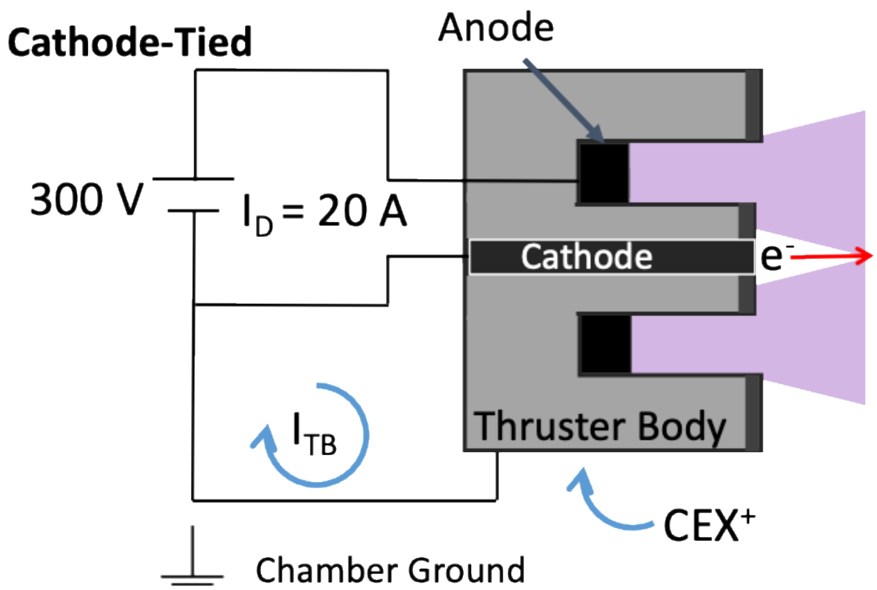

Figure 19: Schematic of the cathode-tied thruster configuration to depict electron pathways

3.3.1.2 Electron Temperature

The electron temperature trends depicted in Figure 20 show a temperature increase from approximately 2-4 eV as the axial downstream distance is increased from 2 mm to 17 mm. This linear increase in temperature is consistent with previous measurements [55,1]. Electron temperature measurements on the same thruster operating in the floating configuration downstream cathode centerline showed an increase from 3-6 eV1], consistent with measurements shown in Figure 20. Notably, both the electron density and temperature profiles converge across all three electrical configurations beyond approximately 15 mm downstream of the cathode exit. This coalescence suggests that thruster body bias effects on the cathode plume electrons are confined to the near-field region.

The potential difference across the sheath, φ_f, is dependent on the local electron temperature and is equal to $\varphi_f = \frac{k_B T_e}{e} \ln\left(\sqrt{\frac{2m_i}{\pi m_e}}\right)$, where $\frac{kT_e}{e}$ is the electron temperature in eV and $\frac{m_i}{m_e}$ is the ion-to-electron mass ratio. In the case of krypton propellant, the floating potential is approximately $5.75\frac{k_B T_e}{e}$. The electron temperature near the inner front pole region can be estimated by leveraging the convergence behavior of electron temperature profiles. Recent spatially resolved measurements demonstrated that axial profiles at radial locations r = 0 and 2 mm converge at z = 6 mm, suggesting minimal radial variation in electron temperature beyond this distance [55]. Given that the inner front pole is the nearest conducting surface to the cathode face, it is reasonable to expect that the electron temperature profile downstream of the inner front pole cover would similarly converge with the cathode centerline profile at the maximum measured axial distance of 17 mm. Reported electron temperatures across the inner front pole region are also found to range from 3-5 eV [1, 86, 87]. Based on this, using an estimated T_e of 3-4 eV at the inner front pole yields a sheath potential, φ_f, of approximately 20 V, which corresponds well with the measured thruster body-to-ground voltage in this experiment of approximately -19 V in the floating configuration.

The observation that the floating configuration exhibits the highest T_e among the three electrical configurations can be attributed to the gradient of sheath potentials experienced by the electrons. In the floating configuration, the thruster body potential is measured at approximately -18.8 V relative to ground, representing the most negative sheath potential in the inner front pole region. This value is more negative than the tied configuration, which is -14.9 V, and the grounded configuration, which is 0 V. The steepness of the sheath potential gradient affects the distribution of electron energies as they are repelled or attracted to the surface. A steeper potential gradient leads to broader electron energy distributions and, consequently, a higher T_e.

This interpretation aligns with the observed electron temperature trends across the three configurations. In the floating configuration, with the most negative thruster body potential, T_e is the highest. The tied configuration, with a less negative potential of -14.9

V, results in an intermediate T_e. Finally, in the grounded configuration, the sheath potential is weakest, leading to the narrowest electron energy distribution. As a result, the electron energy distribution remains closer to a Maxwellian state, producing the lowest measured T_e.

This observed ordering is also consistent with the framework of current-driven instabilities in hollow cathode plasmas. Hara and Treece [88] showed utilizing 1D Vlasov-Poisson simulations that the electron temperature at nonlinear saturation increases monotonically with the initial electron Mach number, $M_0 = u_e/v_{th,e}$. A higher initial electron Mach number produces a larger instability growth rate, which generates larger-amplitude plasma waves that trap electrons around the phase velocity, resulting in a higher saturated electron temperature. The grounded configuration, which exhibits the lowest T_e, is therefore consistent with the smallest instability growth rate and the smallest anomalous electron transport among the three configurations.

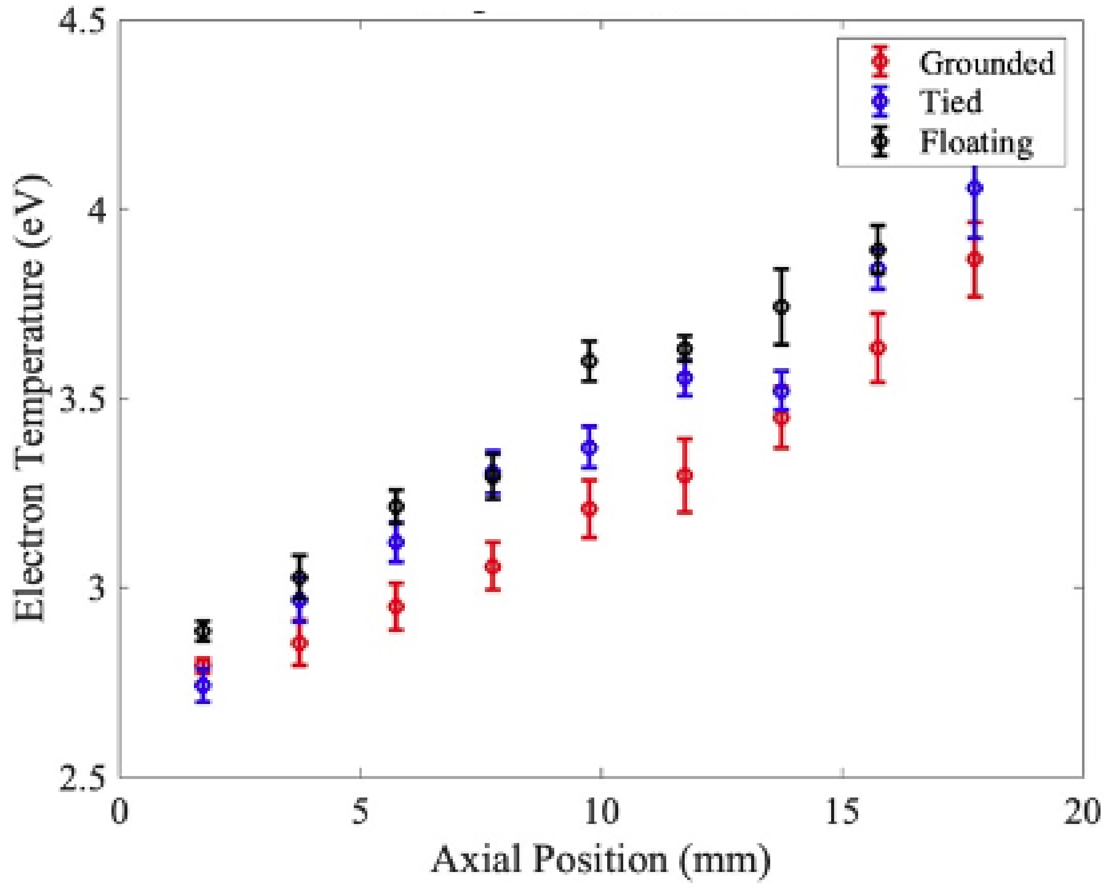

Figure 20: Electron temperature as a function of axial position in the grounded, cathode-tied, and floating configurations inferred from the LTS spectrum as a function of distance from the cathode, taken at a radial location of the cathode centerline.

3.3.2 Power Spectral Density Comparison

Peaks in the discharge current are attributed to the depletion of neutral populations in the discharge chamber because of ionization. The frequency content in the time-resolved discharge current gives information about the frequency at which that process is happening. The dominant or peak frequency is called the breathing mode [39] and can be found by performing power spectral density (PSD) analysis on the discharge current. PSD plots compared across the electrical configurations, as shown in Figure 21, reveal an increase in the frequency. The frequency shift was not expected, as similar PSD comparisons made for the HERMeS thruster in three electrical configurations from Peterson et al. show the opposite trend, with the main frequency increasing from the grounded to floating configurations. Both thrusters are magnetically shielded and in a comparable power class; however, the discrepancy is likely because the relationship between the thruster body potential and breathing mode frequency cannot be assumed to be linear, as shown in Walker et al. [89]. The plots therein depict the relationship for the T-140, with an externally-mounted cathode, and show more of a parabolic relationship between the thruster body potential and breathing mode frequency. Because of this, it is assumed that this relationship would need to be characterized for each individual thruster as it is likely dependent on the cathode position, pole cover material, and operating condition. To determine whether the same trend was present at higher discharge power levels, a comparative PSD plot was generated at the nominal 600 V, 9-kW operating condition as well. However, only the floating and tied configurations could be assessed. Without the grounded configuration, it is difficult to definitively say the trends match. The floating main frequency is still less than that of the tied configuration, which is true for both power levels.

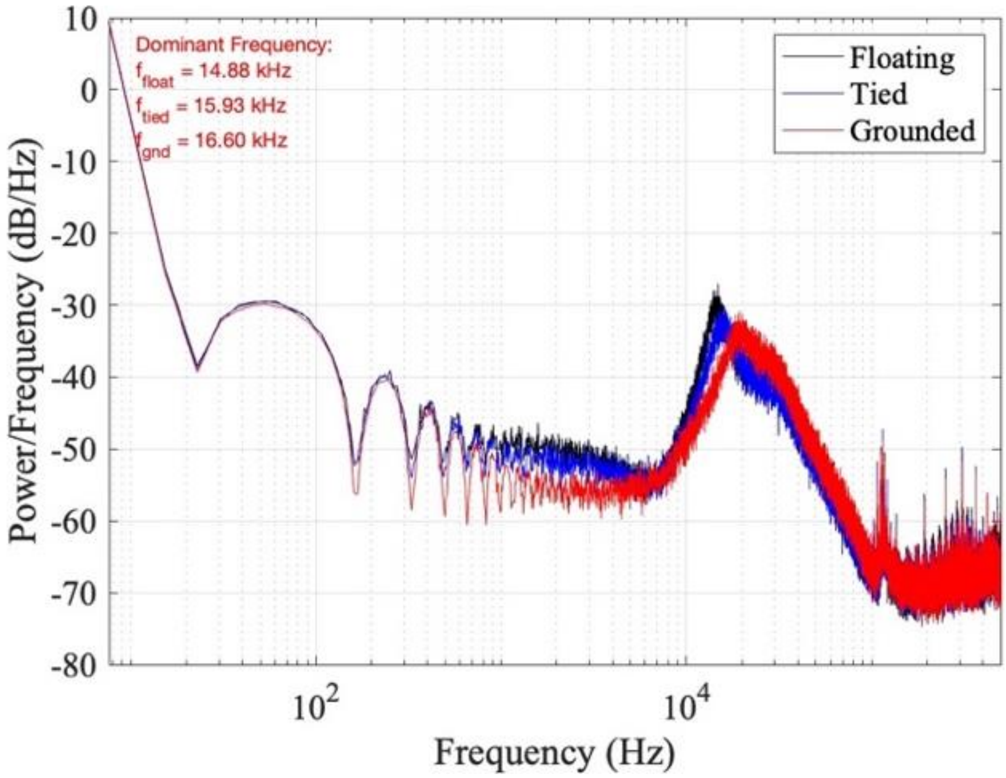

Figure 21: PSD plot as a function of electrical configuration at the 6-kW, 300 V operation condition.

Because the PSD plots of the various electrical configurations show a slight shift in primary oscillation frequency and amplitude, which is also found to be true in [69], there is a possibility that the acceleration and ionization region lengths vary due to the relation in Equation 38 [73].

$$L_{ion/accel} = \frac{\sqrt{V_{ion} V_n}}{2\pi f_i} \qquad \text{Equation 38}$$

Considering that magnetic shielding already shifts the acceleration region downstream toward the exit plane compared to unshielded HETs, there is more opportunity for cathode plume electrons to intersect and influence said region. It was also seen that these differences in oscillation characteristics are more drastic at higher power conditions. Figure 22 further shows that the bias-dependent effects on the discharge plasma are 31% more pronounced at 9 kW compared to 6 kW, suggesting that these effects are sensitive to the stability of the operating regime. It is known that this particular thruster is not as stable at high voltage when run on krypton compared to high current density power configurations. According to this relationship and the data presented in Figure 21, the floating configuration should have the longest acceleration region relative to the other configurations, and the grounded configuration should have the shortest. We postulate, especially in the case of magnetically-shielded thrusters, that the electrons repelled due to large negative thruster floating potentials are likely the reason for the downstream extension of the ionization front in this case. The strong electron repulsion is likely to make it more difficult for them to reach the ionization region [89]. Conversely, in the grounded configuration, the thruster body attracts electrons back toward its face, enabling them to enter the discharge chamber more readily.

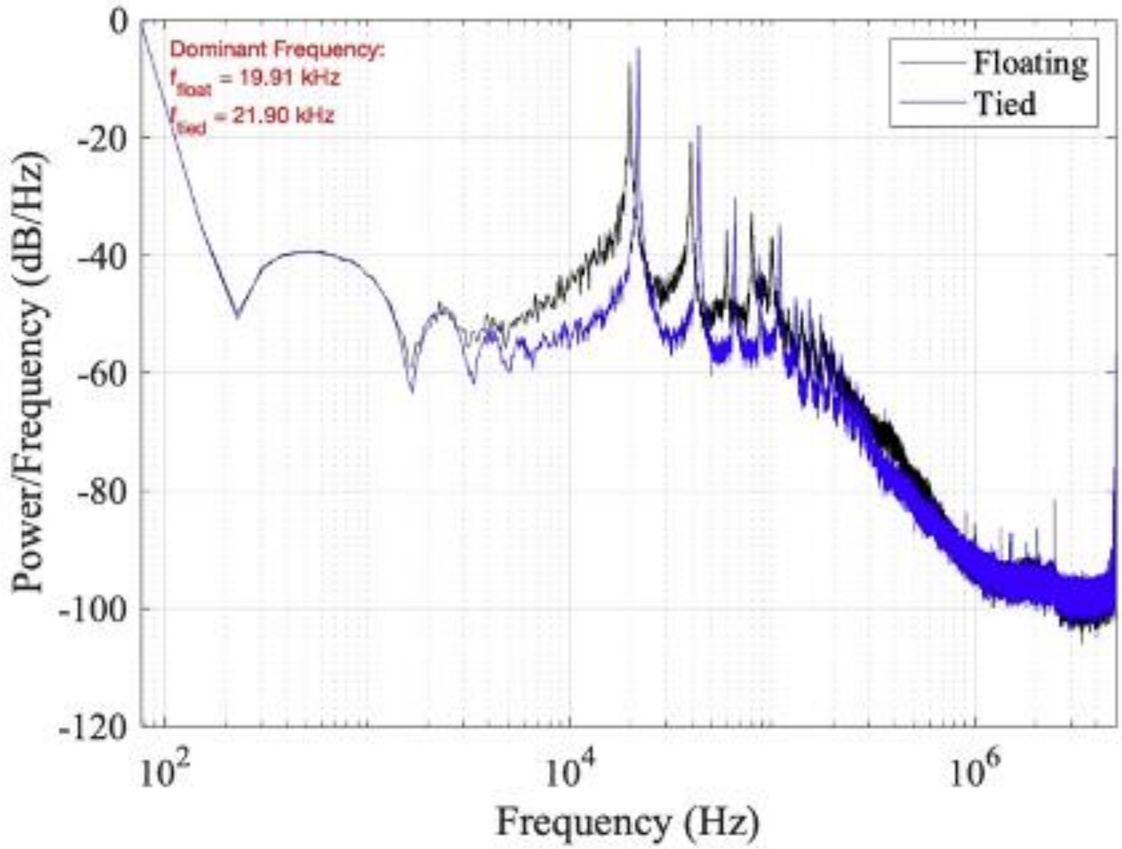

Figure 22: PSD plot as a function of electrical configuration at the 9-kW operating condition.

3.3.3 Thruster Body Current

A natural approach for analyzing thruster body current collection is to model the electron and ion currents under the assumption of a Maxwellian electron population near the thruster surface. While direct measurements of thruster body current were not taken during this experiment, theoretical calculations can provide insight into current collection behavior as a function of body-to-cathode potential and electron temperature. Figure 23 shows the simulated net current into the thruster body inner front pole surface area as a function of body-to-cathode voltage.

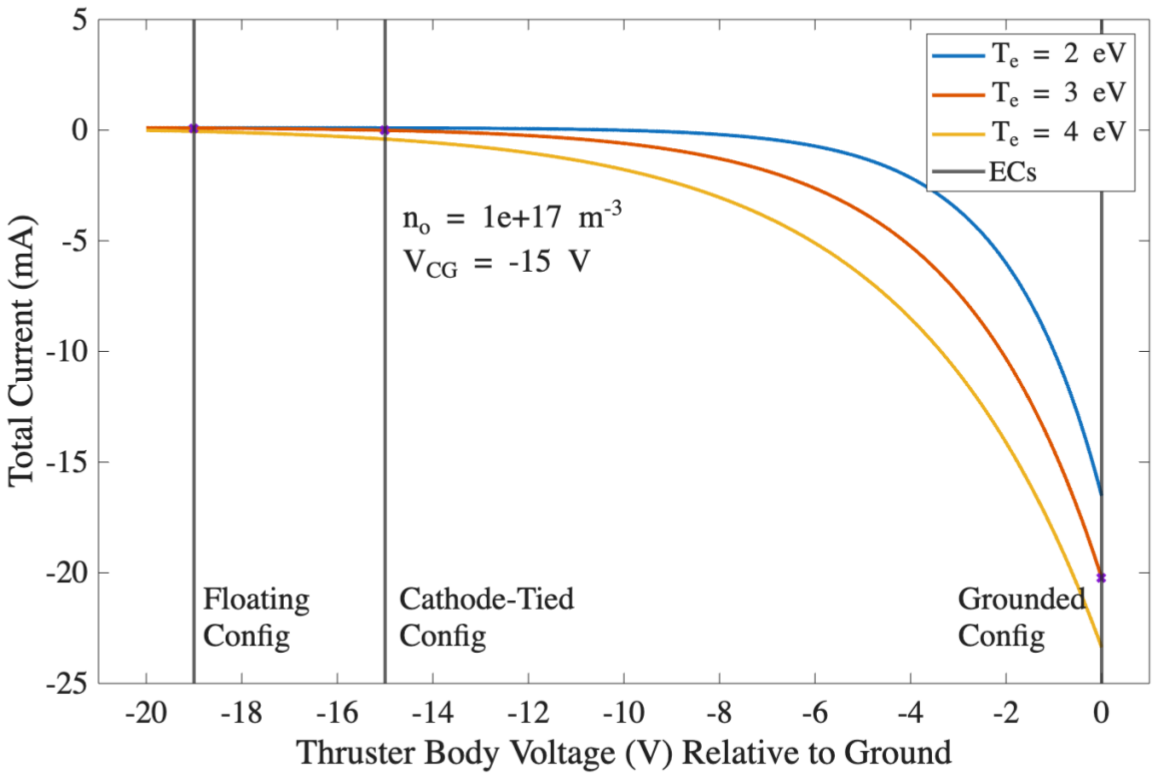

Figure 23: Simulated total current through thruster body as a function of body-to-cathode voltage for electron temperatures in the range of 2-4 eV, assuming a neutral density of 1×10^{17} m^{-3} and a measured cathode-to-ground voltage of -15 V. The black lines represent body voltages corresponding to each of the electrical configurations (ECs).

The current collected by the thruster body was not measured during this experiment, but under the assumption that electrons near the thruster surface are Maxwellian, the electron current, I_e, into the thruster body through the inner front pole can be calculated using $I_e = A_s e \sqrt{\frac{kT_e}{m_i}}\, 0.606 n_o \exp -\frac{e\Delta\emptyset}{kT_e}$. Equation 39,

$$I_e = A_s e \sqrt{\frac{kT_e}{m_i}}\, 0.606 n_o \exp\left(-\frac{e\Delta\emptyset}{kT_e}\right). \qquad \text{Equation 39}$$

A_s is the surface area of the inner front pole, $\sqrt{\frac{8kT_e}{\pi m_e}}$ is the mean electron thermal velocity, n_o is the local plasma density, and $\Delta\phi$ is the potential difference between the plasma and the thruster body. The density measurements that were made were not close enough the pole to use as n_o. The local plasma density in front of the front pole is assumed to be 1×10^{17} m^{-3} based on neutral flow simulation results for the HERMeS thruster operating at nominal conditions in VF-5 and [84] and previous measurements immediately downstream of the inner front pole of the H9 thruster operating at 150 V and 6 kW [1]. The collected ion current, I_i, can be calculated with $I_i = A_s e \sqrt{\frac{kT_e}{m_i}}\, 0.606 n_o$

Equation 40 ,

$$I_i = A_s e \sqrt{\frac{kT_e}{m_i}}\, 0.606 n_o \qquad \text{Equation 40}$$

where $\sqrt{\frac{kT_e}{m_i}}$ is the ion Bohm velocity [89]. Using the convention that ion current is positive, and electron current is negative, the same approach to plotting the collected current to the witness plate applied by Walker et al. [89] is applied and shown in Figure 23. While the simulated collected current cannot be validated by measurements, the data for an electron temperature of 4 eV shows the switch in sheath polarity at the expected body-to-cathode voltage of 0 V. The simulated results lend further credence that at body voltages positive relative to the cathode potential, and especially when grounded, significant electron current is collected through the body, resulting in a reduced number of electrons capable of propagating downstream.

3.4 Pathway to Enhanced Mapping of Thruster Body Potentials and Electron Dynamics

Building on the insights gained from the preliminary work, which demonstrated that thruster body bias produces measurable changes in near-field electron density and temperature along the cathode centerline, the main experimental campaign aimed to extend this investigation through a two-phase approach. While the preliminary study established that electrical configuration affects electron properties, it examined only a single axial line emanating from the cathode and tested three discrete and typical electrical configurations. The proposed work seeks to achieve higher spatial resolution of bias effects by employing the inner front pole cover as an electrically isolated current probe to systematically scan thruster body voltage from 0 to 2 V (Phase I), followed by spatially-resolved laser Thomson scattering measurements at three selected configurations: Float, Tied, and, originally, a transitional bias identified from Phase I current measurements (Phase II). This refined approach provides both current-voltage characterization to identify regions where dominant charge carriers change, and detailed spatial mapping of electron properties in the near-field plume region, thereby enhancing understanding of how electron pathways respond to applied body bias.

CHAPTER 4: EXPERIMENTAL SETUP

Building on the preliminary measurements presented in Chapter 3, which established that thruster body bias produces measurable changes in near-field electron properties, this chapter describes the experimental campaign designed to systematically investigate bias-dependent electron behavior through a two-phase diagnostic approach. The investigation employs the same H9 HET and facility infrastructure used in the preliminary work, but implements a strategically divided measurement strategy: Phase I uses the inner front pole cover as an electrically isolated witness plate to map body current response across a continuous voltage scan from 0 to 2 V, thereby inferring the global behavior of electron and ion fluxes to the surface from the sign and magnitude of the collected current, while Phase II employs laser Thomson scattering to obtain spatially-resolved electron property measurements at three discrete electrical configurations identified as Float, Tied, and +2 V. This division prevents diagnostic interference and ensures that each phase independently addresses specific aspects of how body bias influences electron transport in the cathode plume region.

This chapter first describes the experimental facilities and equipment common to both phases, including the vacuum test facility, thruster configuration, and power supply architecture. Subsequent sections then detail the phase-specific diagnostic implementations, measurement procedures, and operating conditions employed throughout the campaign. The experimental campaign is divided into two sequential phases, each employing distinct diagnostics to evaluate the influence of thruster body bias on near-field plasma behavior. The test plan is structured to avoid diagnostic interference and to ensure that each phase independently addresses a specific aspect of the central research question outlined in section 1.2.1.

4.1 Experimental Facility and Shared Diagnostics

4.1.1 Thruster, Test Facility, and Vacuum Environment

The experiment was performed using the H9 HET, shown in Figure 13. All details about the H9 thruster, except for the heaterless H9 cathode, are discussed in Section 3.2.2. The H9 anode and cathode were supplied with a mass flow of krypton with a purity of 99.999% measured by MKS GE50A MFCs. The MFCs were calibrated at the test article using a MesaLabs DryCal 800-10 volumetric flow meter, and a linear fit was generated between the commanded and measured flow rates.

The thruster was powered by multiple power supplies. The thruster discharge power was supplied by an EMI/TDK-Lambda EMHP 600 Vdc, 100 Adc power supply in series with a 95-μF capacitor and 1.3-Ω resistor to prevent discharge current oscillations of above 1.4 kHz. The cathode heater, and inner and outer magnet coils are powered by TDK-Lambda GEN60-25GEN40-38, and GEN80-42 power supplies, respectively. The heaterless H9 cathode utilized is discussed in Section 4.1.1.1.

Both phases operated the H9 HET at a discharge power of 6 kW with the magnetic field set to 87.5% of the nominal field setting [90], maintaining consistent magnetic shielding topology. However, the phases employed different combinations of discharge voltage and current to address competing experimental requirements: Phase I operated at lower current (20 A, 300 V) to protect flight hardware during IFPC electrical isolation, while Phase II operated at higher current (40 A, 150 V) to achieve sufficient electron density for adequate laser Thomson scattering signal quality. This setting has been previously demonstrated to yield sufficient electron density in the IFPC region for discernible LTS signal quality [1]. The differing operating conditions prevented direct quantitative comparison between phases but enabled complementary demonstrations of bias effects across different plasma density regimes.

Detailed operating conditions, flow rates, and electrical configurations and circuits for Phase I and Phase II are presented in Sections 4.2.3. and 4.3.3, respectively. Both experiments were conducted in Vacuum Test Facility 2 (VTF-2) at the Georgia Tech High-Power Electric Propulsion Laboratory, as described in Section 3.2.1.

4.1.1.1 H9 Heaterless Cathode

A heaterless version of the H9 hollow cathode was employed throughout all experiments in Chapter 0. This cathode retains the same critical geometric dimensions as the original heated design used in Chapter 0, including the cathode orifice diameter, keeper orifice diameter, and LaB_6 emitter material. The modification eliminates the external heater coil, which represents a primary failure mode in conventional heated hollow cathodes, thereby improving reliability while reducing power consumption and system complexity.

4.1.1.1.1 Cathode Design and Configuration

The heaterless H9 cathode implements the High Emission Current Cathode with Tube-Radiator (HECCTR) design concept. The modification replaces the sheathed heater cable coiled around the cathode body in the original design with a 3.3-mm diameter tantalum (Ta) tube that extends the gas feed line 0.5 inches into the hollow insert region. This tantalum tube serves dual purposes: it acts as the propellant feed structure and, when resistively heated during ignition, provides radiative heating to the LaB_6 emitter. This configuration prevents the inefficient coupling of the high-voltage discharge to upstream components that limited earlier heaterless cathode designs.

4.1.1.1.2 Keeper Power Supply Circuit

The cathode keeper circuit, shown in Figure 24, was specifically designed to accommodate the voltage and current requirements of heaterless ignition while protecting against discharge instabilities. The keeper is powered by two parallel power supplies, each protected by a series diode. The first supply is a Magna-Power SLC1000-1.5/UI DC power supply rated for 1000 V at 1.5 A, providing the high voltage necessary for initial Paschen breakdown. The second supply is a TDK-Lambda GEN600-2.6 rated for 600 V at 2.6 A, which sustains the keeper discharge during the thermionic emission phase after breakdown.

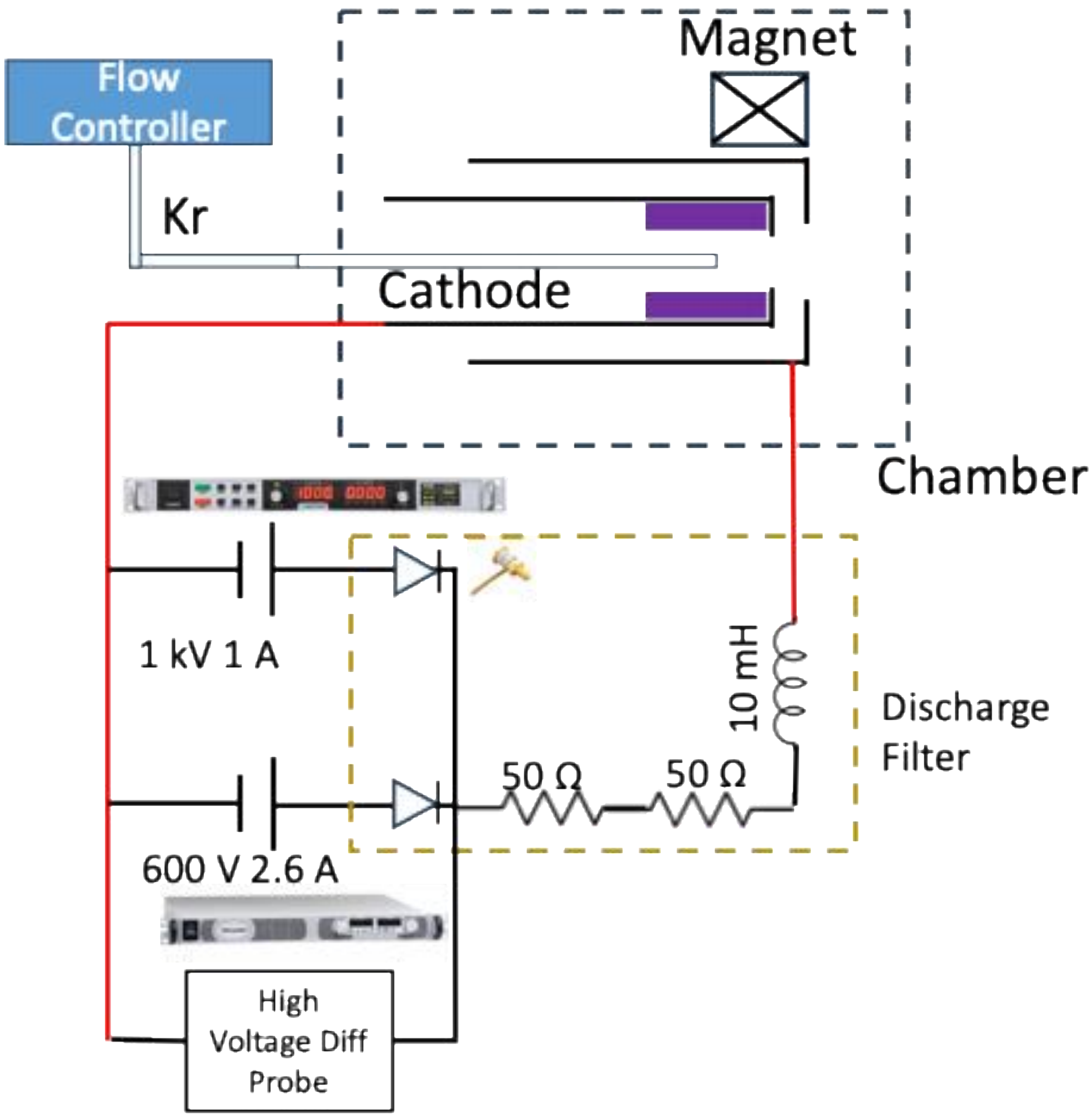

Figure 24: Heaterless H9 cathode circuit.

The Keeper discharge filter circuit incorporates two 50-Ω power resistors and a 10-mH inductor in series between the power supplies and the keeper electrode. These components serve to limit both current and voltage oscillations arising from keeper discharge instabilities during ignition. The series resistors provide current limiting during breakdown transients, while the inductor dampens high-frequency voltage oscillations. This filtering is critical for preventing destructive arcing and ensuring controlled transitions between ignition phases.

4.1.1.1.3 Heaterless Ignition Process

Heaterless ignition eliminates thermal preheating of the emitter, instead relying on a three-stage process where successive plasma discharges progressively heat the cathode components to operational temperatures. The H9 heaterless cathode employs the High Emission Current Cathode with Tube-Radiator (HECCTR) design concept developed by Payman and Goebel [91], which extends a 3.3-mm diameter tantalum tube 0.5 inches into the insert region to provide efficient radiative heating. Figure 25 illustrates the characteristic time-resolved voltage and current behavior during a typical heaterless ignition sequence, showing three distinct heating modes: high-voltage Paschen breakdown, intermediate-voltage tantalum thermionic discharge, and low-voltage LaB_6 thermionic discharge.

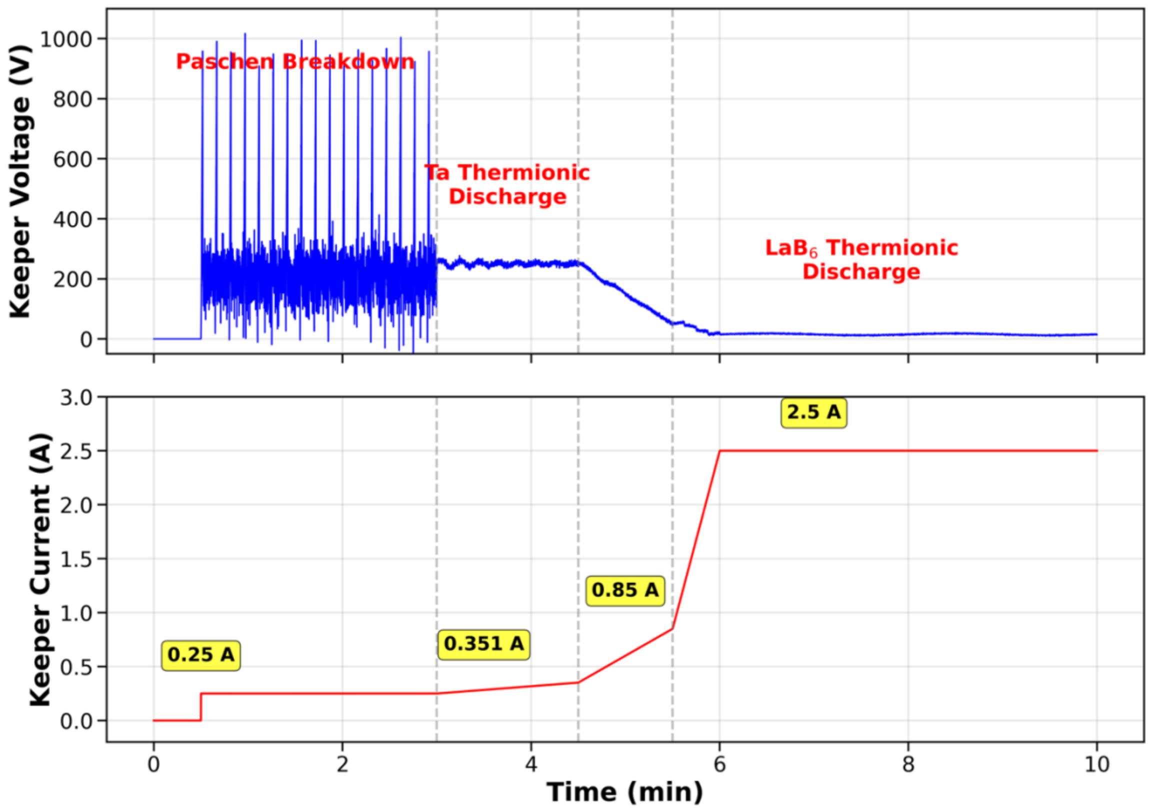

Figure 25: H9 Heaterless cathode ignition phase diagram (example).

During the initial Paschen breakdown phase, propellant is supplied at the ignition flow rate, which is typically 40-80 sccm-Kr, and the high-voltage keeper supply is activated to approximately 1000 V. The discharge current is limited to 0.7 A by the power supply and series resistors. As shown in Figure 25, the cathode exhibits characteristic relaxation oscillations during the first 2-3 minutes, manifesting as a repeating sawtooth pattern where voltage rapidly rises to the breakdown threshold, then collapses. These oscillations occur due to cyclic neutral depletion: electrons ionize the gas, creating a conductive plasma channel that rapidly depletes local neutrals, causing the discharge to collapse and the cycle to repeat [92]. The frequency ranges from a few Hz to tens of Hz, with voltage spike amplitudes exceeding 900 V. Higher ignition flow rates reduce both frequency and severity of oscillations by enabling faster neutral replenishment. After a successful breakdown, the keeper voltage falls to the Paschen minimum of 200-250 V for krypton.

In the intermediate tantalum thermionic phase, keeper current is gradually increased from 0.25 A to 1.5 A over approximately 1 to 1.5 minutes. The tantalum tube reaches temperatures exceeding 2600 °C, providing over 125 W of radiative heating power to the LaB_6 insert. The keeper voltage smoothly decays from approximately 250 V to below 45 V as thermionic emission from the heated tantalum surface begins to dominate the discharge. The HECCTR design confines the discharge to the tantalum tube in a hollow cathode mode, preventing inefficient coupling to upstream components [91]. Voltage oscillations continue with reduced amplitude (±8-15 V) that progressively dampen.

The final LaB_6 thermionic phase is achieved by increasing keeper current to 2.6 A, requiring 1-1.5 minutes as the insert heats to 1400-1700 K through radiative transfer. The keeper voltage exhibits step-like reductions with brief oscillation periods at each step, suggesting thermionic emission initiates at localized hot spots and then spreads across the emitting surface. Final stabilization occurs when the keeper voltage drops below 20 V with minimal oscillations (±1-3 V). The cathode becomes self-heating at anode discharge currents above 6 A; below this, approximately 1 A of keeper current is required for stable operation [91].

The complete ignition process typically requires 10-20 minutes from initial gas flow to stable LaB_6 emission. The heaterless approach eliminates the primary failure mode of conventional heated cathodes, which is electrical breakdown of heater coil insulators due to thermal fatigue [93].

The heaterless operation approach provided several advantages for the present experiments. Elimination of the heater power supply reduces electrical complexity and removes a documented failure mode associated with thermal cycling of heater assemblies. Additionally, the absence of heater power consumption simplified thermal management of the cathode assembly and surrounding thruster components. However, heaterless ignition requires careful control of the keeper voltage ramp rate and exhibits greater shot-to-shot variability in breakdown voltage compared to heated ignition, necessitating the robust power supply and filtering configuration described above.

4.1.2 Time-Resolved Telemetry Diagnostics

Time-resolved thruster telemetry was measured with Teledyne LeCroy HDO6104 and WaveSurfer 3054 oscilloscopes. Both oscilloscopes were configured with 1 MS (mega-sample) record length, 5 MS/s (mega-samples per second) sample rate, and 20 ms/div timebase to capture time-resolved plasma oscillations over extended measurement intervals. Thruster telemetry recorded includes time-resolved measurements of the discharge current, discharge voltage, keeper voltage, thruster body current, thruster body-to-ground voltage, and the cathode body-to-ground voltage. The discharge voltage was measured with a Powertek DP25 differential voltage probe rated up to 25 MHz. The discharge current is measured on the cathode electrical line in the control room using a Teledyne LeCroy CP150 current clamp. The remaining relevant telemetry channels and their associated measurement techniques are detailed in the respective sections for Phase I (Section 4.2.3) and Phase II (Section 4.3.3), including probe specifications, circuit locations, and data acquisition parameters specific to each experimental phase.

The reason a current clamp will be placed on the electrical line connected to the cathode common is to verify the presence of recirculating current through the thruster body in the cathode-tied configuration. This setup allows for direct measurement of the total current flowing back to the cathode, including current that recirculates through the thruster body before returning to the cathode. By isolating the cathode current from the anode discharge current, this method provides a clear quantification of the additional current sourced by the cathode in response to recirculation, specifically in the cathode-tied configuration.

4.2 Phase 1: Isolated IFPC Probe Current Collection

As introduced in Section 1.2.2.1, Phase I was originally designed to employ three discrete stainless steel witness plates mounted to the IFPC to measure localized current collection as a function of thruster body bias, as shown in Figure 26. The scientific rationale for this approach was to obtain spatially-resolved measurements of plasma-surface interactions at critical erosion sites with some spatial resolution, which would provide more targeted insight than integrated thruster body current measurements that aggregate contributions from all chassis surfaces, as is represented in the thruster body current.

The original experimental plan called for:

- Three 316 stainless steel witness plates positioned azimuthally around the IFPC
- Electrical isolation from the thruster chassis using ceramic coating (Aremco Ceramadip) and ceramic adhesive (Aremco Ceramabond)
- Biasing synchronized with the thruster body across a range from -15 V to +20 V relative to facility ground
- Independent current monitoring for each plate to enable spatial mapping of current collection

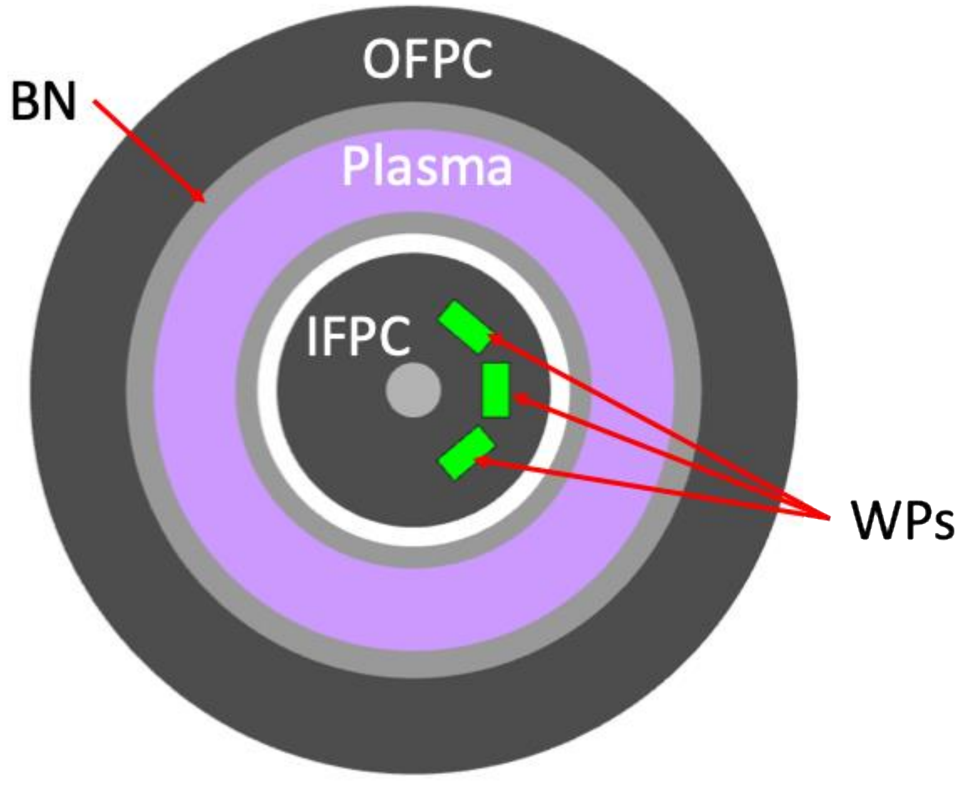

Figure 26: Spatial configuration of three witness plates shown as neon green boxes mounted on the inner front pole cover.

These measurements were intended to inform Phase II bias selection by identifying bias conditions where the dominant charge carrier transitions from electron to ion collection (or the alternative) indicated by inflection points in the current-voltage characteristic.

4.2.1.1 Witness Plate Challenges

Implementation of the discrete witness plate configuration was attempted but proved infeasible due to critical engineering constraints. The primary failure mode stemmed from the electrical isolation technique required to separate the witness plates from the metallic IFPC structure.

The proposed isolation method relied on ceramic coating (Ceramadip) and ceramic adhesive (Ceramabond) to electrically insulate the stainless-steel plates from the IFPC mounting surface. However, Ceramabond has a history of reliability issues in high-temperature, high-flux plasma environments, including outgassing, mechanical failure under thermal cycling, and degradation of isolation properties over time. Given the criticality of preserving the IFPC hardware for subsequent testing phases, the use of Ceramabond presented unacceptable risk.

Alternative isolation methods using ceramic spacers, e.g., alumina washers or standoffs, were evaluated but introduced a different set of problems. Ceramic spacers of sufficient thickness to guarantee electrical isolation would cause the witness plates to protrude several millimeters in front of the IFPC surface. This geometric perturbation would alter the local plasma environment, invalidating the assumption that the witness plates measure a current collection representative of the IFPC surface itself. Additionally, protruding plates would be exposed to enhanced ion bombardment and thermal loading from the discharge channel beam, accelerating erosion and risking permanent damage.

Due to these combined constraints, the discrete witness plate approach was deemed impractical for Phase I execution. The decision was made to revise the Phase I experimental objectives to use the IFPC cover itself as a surrogate current collection probe, eliminating the need for discrete witness plates while preserving the core scientific goal of measuring localized current as a function of bias.

4.2.2 IFPC as an Isolated Current Collection Probe

In place of discrete witness plates, Phase I was restructured to use the IFPC cover as a large-area, electrically isolated current collection probe, hereafter referred to as the "isolated IFPC probe". This approach preserved the fundamental measurement goal of characterizing localized current collection at a critical erosion site as a function of thruster body bias while circumventing the engineering challenges that precluded the discrete witness plate configuration.

Unlike integrated thruster body current measurements, which aggregate contributions from all chassis surfaces exposed to different plasma environments, the isolated IFPC probe provides localized current measurements at a specific, well-defined surface. This localization enables direct characterization of plasma-surface interactions at the inner front pole, a region of known erosion concern in magnetically-shielded HETs.

By isolating the IFPC electrically from the thruster body, the current collected by the IFPC surface can be independently monitored and correlated with applied bias voltage. This configuration avoids the spatial ambiguity inherent in thruster body current measurements, where contributions from distant surfaces, e.g., the circumferential chassis versus the exit plane surfaces, are indistinguishable.

Given the constraints imposed by hardware protection requirements and the transition to the isolated IFPC probe configuration, the objectives of Phase I evolved to:

1. Demonstrate the feasibility of using the IFPC as a current collection probe by verifying that measurable, bias-dependent currents can be obtained from the isolated IFPC surface.
2. Characterize local current collection (ion versus electron) as a function of body bias to identify inflection points or transitions in the current-voltage characteristic that indicate changes in the dominant charge carrier.
3. Assess whether body bias can modulate current flux to the IFPC surface, with implications for erosion mitigation strategies in future thruster designs.

These objectives preserved the scientific intent of the original witness plate plan which was to map bias-dependent current collection at erosion-critical surfaces while adapting the experimental implementation to accommodate hardware protection constraints and isolation technique limitations.

4.2.2.1 Isolated IFPC Structural Configuration

The Isolated IFPC Probe approach utilized the inner front pole cover itself as a large-area current collection surface to characterize near-surface particle flux under varying body bias conditions. The IFPC was electrically isolated from the thruster body using ceramic screws and washers fabricated from alumina, Al_2O_3, with a maximum operating temperature of 3000 °F. This isolation enabled independent bias control while preserving the flight-representative IFPC geometry and distance from the surface, shown in Figure 27.

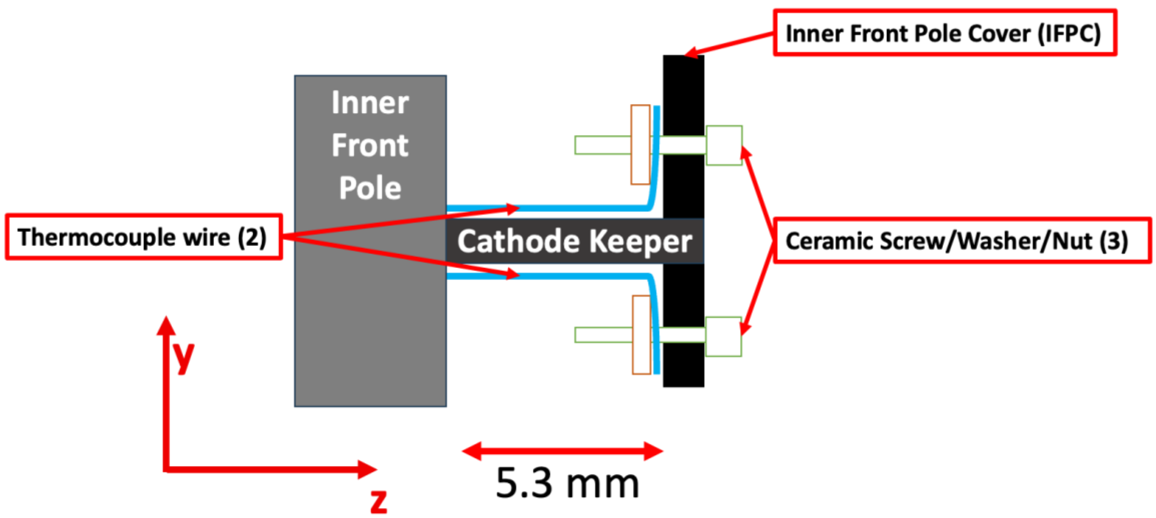

Figure 27: Diagram of IFPC in the isolated configuration. Not drawn to scale.

Current collection from the isolated IFPC was achieved using two McMaster-Carr 24-gauge, Type KK solid thermocouple wires that utilize ceramic fiber insulation and have a maximum temperature rating of 2200 °F and routing them through the center bore of the H9 thruster. The small wire diameter enabled feeding through the confined annular gap between the inner bore wall and the cathode keeper assembly. One conductor from each thermocouple wire was utilized for current collection, while the center conductor of the complementary wire was removed to prevent circuit formation. The ceramic fiber insulation jacket provided electrical isolation from the cathode keeper, with additional Kapton tape wrapping applied at bend locations. Each wire was approximately 10 feet long to reach from the IFPC to external instrumentation, with the wires positioned on either side of the keeper to maintain its centered alignment. The upstream ends of the wire were terminated together using a Supercon connector to complete the current collection path. The downstream end of the wires was terminated with ring terminals that interfaced with the backside of the IFPC and were isolated from the inner front pole using ceramic nuts. The distance that the IFPC protruded from the inner front pole was limited by the thermocouple wire that sat behind the pole cover. The cathode mounting plate was modified to accommodate wire feedthrough while maintaining electrical isolation from the plate structure, as shown in Figure 29. Both the alumina ceramic screws, with a maximum temperature of 3000 °F, and Type KK thermocouple wire were selected specifically for their high-temperature ratings to withstand the thermal environment of the inner bore and IFPC region during thruster operation.

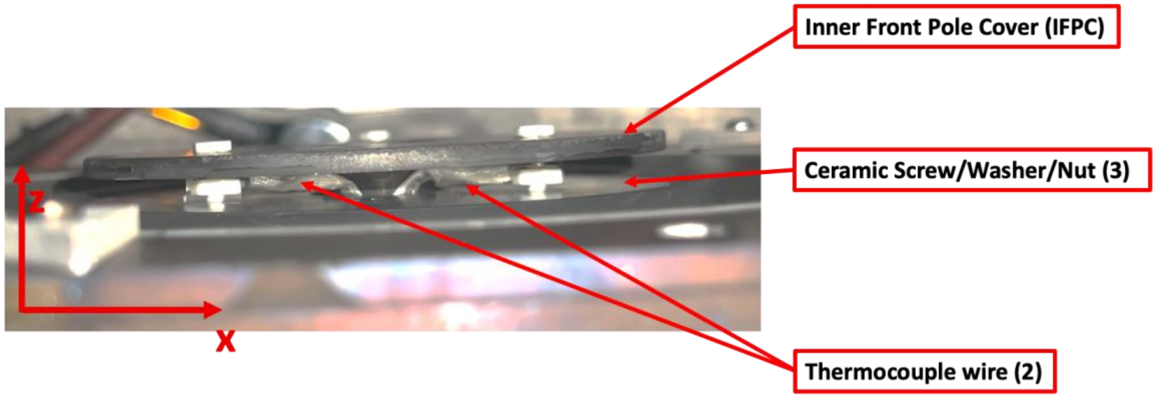

Figure 28: Isolated IFPC final configuration.

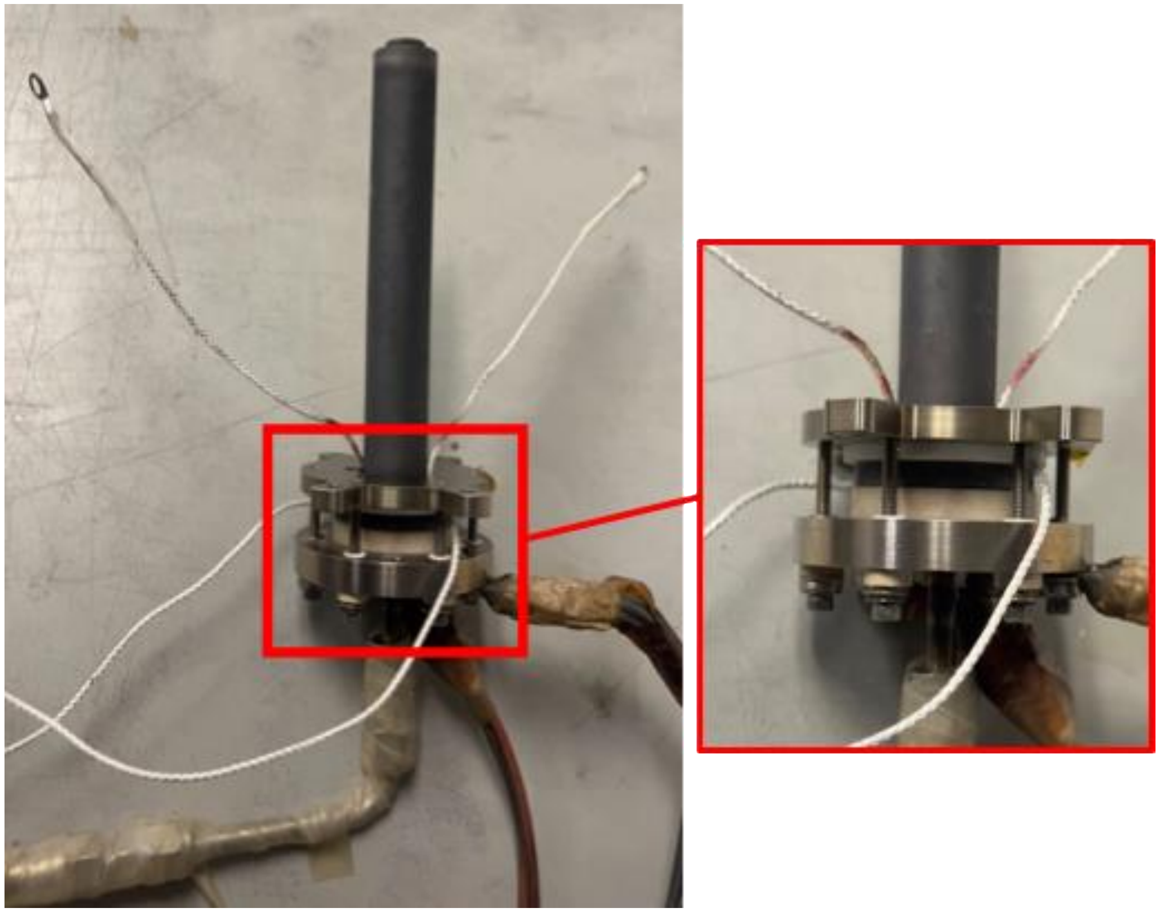

Figure 29: Isolated IFPC wire routed through the cathode mounting plate.

This dual-supply configuration was necessary because initial attempts to bias both the IFPC and thruster body from a single supply were unsuccessful, particularly when attempting to establish negative bias voltages. The plasma between the IFPC and thruster body created a conductive path that prevented the single supply from establishing independent potentials at the two surfaces. With separate supplies, each could independently regulate its output voltage relative to facility ground despite plasma-mediated current flow between the biased surfaces. Measurements with the dual-supply configuration showed inter-surface current averaged over all bias setpoints of 2.4 mA, confirming effective electrical isolation through the ceramic hardware while allowing plasma coupling.

This configuration provided spatially integrated current measurements capturing the net effect of azimuthally-varying plasma structures such as rotating spokes and cathode coupling asymmetries. The witness plate approach eliminated uncertainties associated with probe-plasma interactions or non-representative geometries by measuring directly at the erosion-experiencing surface, where local magnetic field topology, plasma density gradients, and sheath structure are very relevant to erosion mechanisms.

4.2.2.2 IFPC Current Probe Experimental Challenges and Operational Constraints

While the isolated IFPC probe approach circumvented the limitations of the discrete witness plate configuration, it introduced its own set of experimental challenges that shaped the Phase I test matrix, operational constraints, and data interpretation. The most critical limitation was the requirement to operate at a reduced power condition of 20 A discharge current and 300 V discharge voltage (6 kW), rather than the Phase II condition of 40 A, 150 V. This constraint was necessitated by hardware protection requirements stemming from the electrical isolation technique itself.

Electrically isolating the IFPC from the thruster body using ceramic mounting screws exposed portions of the metallic inner front pole surface directly to ion bombardment from the discharge channel. For magnetically-shielded HETs like the H9, ion flux to near-anode surfaces is expected to be elevated compared to unshielded configurations [63]. Preliminary testing at 40 A in the isolated IFPC configuration revealed a faster rate of increase in magnet coil resistance compared to nominal (non-isolated) operation. Since magnet resistance serves as a proxy for coil temperature, this accelerated resistance growth indicated excessive thermal loading of the magnetic circuit.

This accelerated heating raised dual concerns: (1) thermal damage to the magnetic circuit, potentially leading to permanent magnet demagnetization or structural failure, and (2) accelerated sputtering erosion of the IFPC hardware due to sustained high-flux ion bombardment. To preserve the integrity of the hardware and prevent damage during the Phase I campaign, operation was restricted to the 20 A, 300 V condition, and the original test matrix was heavily truncated.

Although the 20 A restriction represented a pragmatic compromise for equipment protection, it created a fundamental constraint: Phase I witness plate current measurements at 20 A, 300 V could not be directly compared with Phase II laser Thomson scattering electron property measurements at 40 A, 150 V. The different current densities, plasma densities, and sheath structures between these operating conditions precluded quantitative correlation of witness plate currents with measured electron properties.

The test matrix was further truncated by limiting the bias range to 0 V to +2 V relative to facility ground in discrete variable resolution steps, omitting the negative bias conditions originally planned (-15 V to 0 V). This restriction was driven by equipment protection priorities: biasing the isolated IFPC negative with respect to ground while maintaining electrical isolation proved impractical with available power supply configurations and introduced additional risk of arcing or breakdown through the ceramic isolation hardware. The selected bias range (0 to +2 V) reflects the positive limit of the bias ranges ultimately used in Phase II. The upper limit of +2 V was selected to minimize the risk of drawing excessive ion current to the isolated IFPC surface while still spanning a range sufficient to observe transitions in current collection behavior.

Additionally, the isolated IFPC configuration perturbed the thruster's electrical environment from its operational state by introducing a new electrical boundary within the main plasma discharge. For this reason, the thruster was not operated in a floating condition in the modified configuration, since a fully floating IFPC in front of the discharge could have produced a floating-probe condition and undesirable inter-surface currents between the IFPC and thruster body.

Although the inner front pole cover served as a large-area current collector rather than discrete witness plates in this modified configuration, it still fulfilled the Phase I objective of characterizing bias-dependent current collection. By electrically isolating the IFPC and measuring its current over the 0–2 V bias range, the collected current provided a measure of net particle flux (electron versus ion collection) to the inner front pole region as a function of applied bias. This approach traded spatial resolution for a different advantage: by integrating current over the entire IFPC surface, the measurement inherently averaged over any azimuthal non-uniformities in the plasma or magnetic field structure that might be present. While discrete witness plates would have provided point measurements at specific locations, the integrated IFPC measurement captured the net behavior of the entire inner front pole surface exposed to the discharge channel plasma.

4.2.3 Thruster Circuit and Operating Conditions

The thruster circuit diagram, shown in Figure 30, illustrates how the thruster body and witness plate were electrically configured to maintain a low-impedance path to their shared bias voltage while minimizing perturbation to the local plasma environment. In this schematic, green lines represent the connections to the IFPC/witness plate, blue lines denote wiring that connects the power supply to the thruster body chassis, and red lines correspond to conventional high-current EP system connections [9], e.g., discharge supply to the anode and cathode.

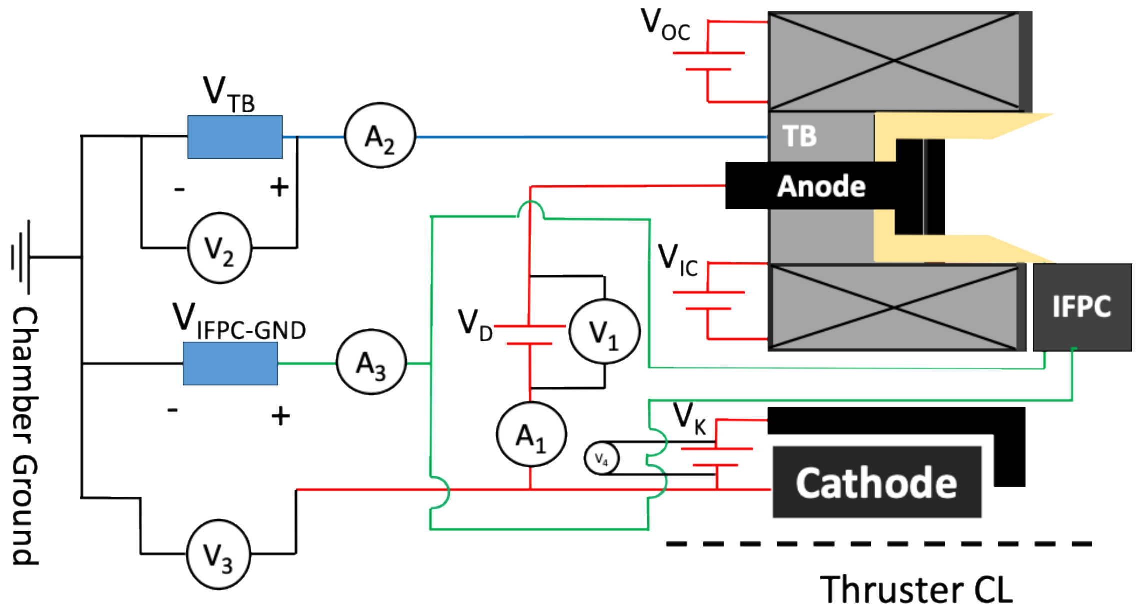

Figure 30: Thruster electrical circuit diagram in Phase I. Image not drawn to scale.

To avoid the presence of unintended ground loops, two separate programmable power supplies bias the thruster body, V_{TB}, and IFPC, $V_{IFPC\text{-}GND}$, witness plate relative to facility ground, allowing systematic control from +0.5 V to +2.0 V with a resolution rate of 1 voltage setpoint per minute, as shown in Figure 30. The individual bias setpoints can be found in Table 4. The thruster body was biased with a TDK Lambda GEN 80-42 power supply, and the measured voltage standard deviation was approximately 0.5 V across all bias conditions, ranging from 0.48 V to 0.52 V, which was measured with a Tektronix 10× probe. This consistency indicates that the primary source of error was primarily driven by instrumental factors like the 10× voltage probe resolution as opposed to bias-dependent plasma effects or the error associated with the power supply. Therefore, a constant uncertainty of ± 0.5 V is applied to all V_{TB} measurements in the I-V plots. The Isolated IFPC Probe is electrically isolated from the thruster body and is biased using a TDK lambda GEN 60-12.5 power supply with an applied bias uncertainty of ± 0.03 V. Due to equipment availability constraints, time-resolved voltage measurements of the witness plate were not acquired during the experiment. Instead, the applied bias accuracy of the GEN 60-12.5 supply was characterized through pre-experimental calibration using the Tektronix 10× high-voltage probe. The power supply was to deliver voltages spanning the experimental range of 0 to 2 V, and the actual output voltage was measured at each set point. The calibration data revealed a mean voltage offset of .03 V. The circuit includes floating and biased configurations as test points. The cathode, anode, and discharge supply were connected conventionally as described in Section 4.1.1. This design ensures that the biasing scheme affects only the intended surfaces without introducing stray currents or alternative return paths that could perturb the plasma or obscure measurements.

Table 3 details the electrical measurements acquired using two Teledyne LeCroy oscilloscopes with distributed channel assignments. Both oscilloscopes were configured with a 1 MS record length, 5 MS/s sample rate, 20 ms/div timebase. Both the thruster body and IFPC power supplies were referenced to facility ground. The symbol column in

Table 3 refers to the labels in Figure 30. The dual-oscilloscope configuration provided simultaneous time-resolved monitoring of all critical electrical parameters during bias sweeps. All current and voltage monitoring diagnostics were located inside the control room at the breakout box. The collected current sign conventions for each current probe are also notated. They are determined by the orientation of the arrow marking on each current probe, which indicates the direction defined as positive current flow. Current flowing in the direction of the arrow produces a positive output from the probe, while current in the opposite direction produces a negative output. A positive current reading corresponds to conventional current in the arrow direction, which represents electron flow opposite to the arrow, as shown in Figure 31.

Table 3: Phase I Electrical Instrumentation Configuration

Parameter	Symbol	Probe Sign Convention	Specifications	Oscilloscope
Discharge current	A_1	CP150 current probe Positive current is toward the cathode return	±150 A, 10 mV/A, 50 MHz	HDO6104[1]
Discharge voltage	V_1	PowerTek DP-25	×100, 6 kV max, 100 MHz	HDO6104
Witness plate current	A_3	CP150 current probe Positive current is toward the WP	±150 A, 10 mV/A, 50 MHz	HDO6104
Body-to-ground voltage	V_2	Tektronix 10× probe	×10, 300 V max, 300 MHz	HDO6104
Body current	A_2	CP030 current probe Positive current is toward the WP	±30 A, 100 mV/A, 50 MHz	WaveSurfer[2]
Cathode-to-ground voltage	V_3	Pintek CT-4024	×1000, 40 kV max, 120 MHz	WaveSurfer
Keeper voltage	V_4	Power Tek DP-25	×20, 300 V caution[3], 100 MHz	WaveSurfer

[1]Teledyne LeCroy HDO6104: 1 GHz bandwidth, 2.5 GS/s max sample rate
[2]Teledyne LeCroy WaveSurfer 3054: 500 MHz bandwidth, 4 GS/s max sample rate
[3]Probe connected only after V_k decreased below 300 V to avoid exceeding voltage rating

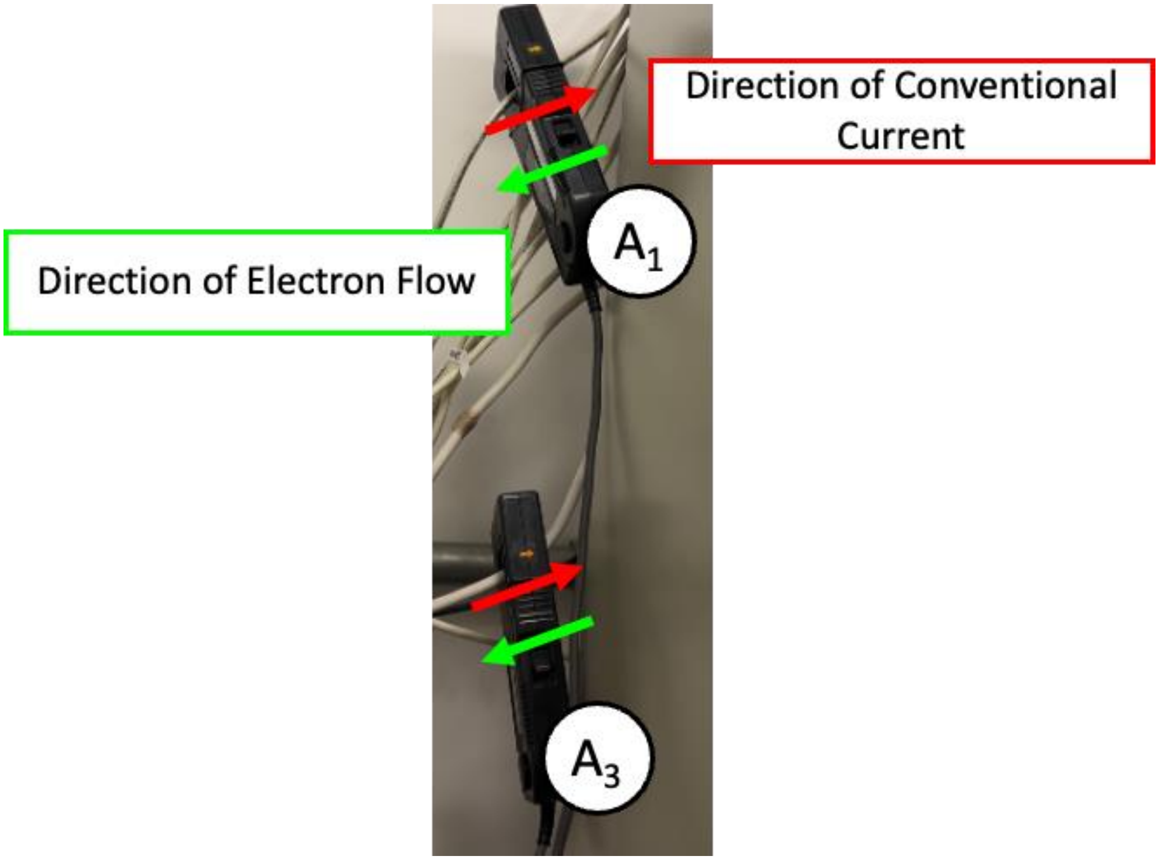

Figure 31: Current probe polarity.

Phase I operated at the nominal H9 condition of 6 kW with a discharge voltage of 300 V and a discharge current of 20 A at 87.5% of the nominal magnetic field setting [27] for all bias conditions. This lower-current operating condition was necessitated by equipment protection constraints: electrically isolating the IFPC for witness plate measurements exposed metallic surfaces to direct ion bombardment, and preliminary testing at the Phase II 40 A current revealed accelerated magnet resistance growth, indicating excessive thermal loading (see Section 4.2.2.2 for a detailed discussion of the equipment protection rationale). The mean Phase I discharge conditions at each applied thruster body bias can be found in Table 4. The 1σ (one standard deviation) uncertainty values are also reported and are calculated from the temporal fluctuations in each measured quantity over the sampling window. The standard deviation captures the typical deviation from the mean value during steady-state operation and corresponds to a 68% confidence interval under the assumption of normally distributed fluctuations. Anode and cathode flow rates were maintained across all bias setpoints. At the 20 A, 300 V operating condition, the cathode-to-ground voltage was averaged across all bias setpoints to be approximately -14 V.

Table 4: Phase I operating conditions.

Bias Condition (V)	**Discharge Current (A)**	**Discharge Voltage (V)**	**Body Voltage (V)**	**Anode Flow (sccm-Kr)**	**Cathode Flow (sccm-Kr)**	**Background Pressure (µTorr-Kr)**
0.5+	20.1 ± 5.84	300 ± 0.64	0.54 ± 0.5	229.6 ± 6.5	20.17 ± 0.31	4.2
0.65+	20.0 ± 5.84	300 ± 0.63	0.67 ± 0.5	229.6 ± 6.5	20.17 ± 0.31	4.2
0.75+	20.0 ± 5.84	300 ± 0.61	0.86 ± 0.5	229.6 ± 6.5	20.17 ± 0.31	4.2
1+	20.0 ± 5.84	300 ± 0.59	1.00 ± 0.5	229.6 ± 6.5	20.17 ± 0.31	4.1
1.5+	20.0 ± 5.84	300 ± 0.61	1.48 ± 0.5	229.6 ± 6.5	20.17 ± 0.31	4.2

2+	20.0 ± 5.84	300 ± 0.59	1.92 ± 0.5	229.6 ± 6.5	20.17 ± 0.31	4.2

Phase I current collection measurements were conducted independently from Phase II optical diagnostics to prevent experimental interference between the two measurement techniques. Operating the isolated IFPC probe configuration simultaneously with laser Thomson scattering would have introduced several complications: stray laser light could have interfered with electrical diagnostics, the optical access requirements and alignment constraints for the laser system were incompatible with the witness plate hardware configuration, and the physical presence of optical components would have obstructed diagnostic access to the IFPC region. By conducting Phase I and Phase II as sequential campaigns rather than concurrent measurements, each diagnostic technique could be optimized for its specific measurement objectives without compromise.

4.3 Phase 2: LTS Measurements

While Phase I provided global electrical characterization of body current across bias conditions, it could not reveal the local plasma mechanisms driving configuration-dependent electron transport. Phase II employs high-resolution LTS to obtain spatially-resolved measurements of electron density, electron temperature, and radial electron drift velocity in the cathode plume region. These measurements enable computation of electron pressure and its gradients, which can serve as a proxy for variations in the local electric potential landscape, as well as calculation of radial electron flux to quantify cross-field electron transport perpendicular to the thruster axis.

The radial electron flux can reveal configuration-dependent transport pathways, identify radial flow reversals indicating changes in confinement mechanisms, and illuminate whether electrons flow inward toward the thruster body or outward into the plume. Integration of the local radial flux over the measurement volume enables comparison with the global body current measurements from Phase I, potentially connecting local plasma physics to macroscopic electrical behavior.

Three discrete electrical configurations were investigated, representing distinct thruster body bias conditions:

1. Floating: IFPC electrically isolated, representing natural sheath behavior.
2. Cathode-tied: IFPC at cathode potential (approximately -10V relative to facility ground), corresponding to a known low-erosion configuration [30].
3. +2 V: IFPC biased +2 V above cathode potential, identified from exploratory campaigns as a bias where a transition in thruster body current collection occurs, as shown in Figure 32.

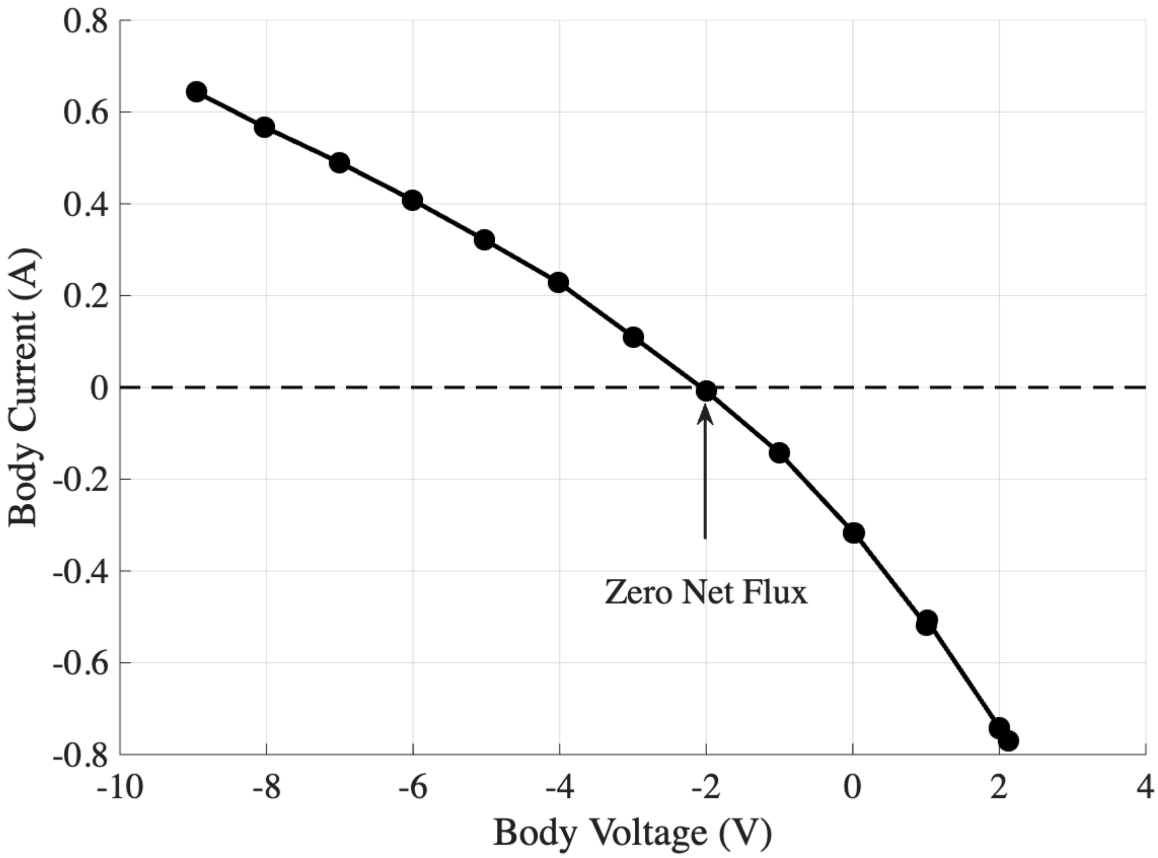

Figure 32: Phase II current collected by the thruster body while biased with different values relative to ground.

The +2 V relative to ground bias was selected as the third thruster body bias to explore in this campaign because it represented a bias at which current, opposite in polarity but comparable in magnitude to the -9 V bias case which was representative of the cathode-tied configuration, was collected as seen in Figure 32. The thruster body bias was swept from -9 V to +2.37 V ± 0.03 V. relative to facility ground in discrete 1V steps, as detailed in Figure 32.

4.3.1 Measurement Locations

Measurements were taken in two primary regions of interest:

a. Cathode centerline ($r/r_o = 0$): Initially intended to confirm repeatability of prior measurements from Chapter 0, these measurements were ultimately conducted at a different, high-current density operating condition due to LTS signal optimization requirements. While direct quantitative comparison is not possible due to the operating condition difference, the cathode centerline measurements provide valuable context for understanding radial variations of electron properties measured from the cathode plume region to the IFPC.

b. Radial-axial grid spanning the IFPC face from cathode centerline to the channel centerline ($r/r_o = 0.4$): to capture how plasma structure varies with bias across the region most sensitive to erosion in the magnetically-shielded HETs.

The probing locations are shown in Figure 34, where each blue circle represents a distinct LTS interrogation point. Spatial spacing is selected to exceed both the motion stage resolution (>150 µm) and interrogation volume size (approximately 1.4 mm axial × 100 µm radial), ensuring statistically independent measurements.

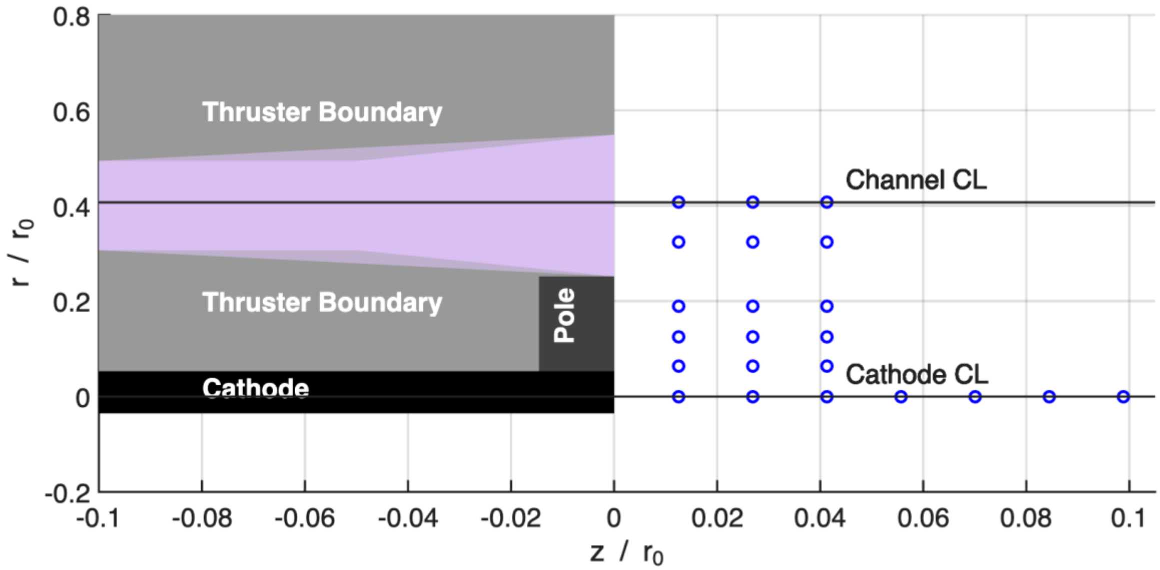

Figure 33: Spatial r, z map of LTS probing points for each thruster body bias condition

The cathode centerline measurements employed a spatial resolution of 2-mm axial spacing, traversing from $z/r_o = 0.13$ downstream of the cathode exit to over an axial extent of approximately 18 mm downstream of the cathode exit plane. This grid spacing was selected to exceed the LTS interrogation volume size of approximately 1.4 mm × 100 µm (axial × radial), ensuring statistically independent measurements at each spatial location with minimal overlap between adjacent measurement volumes.

The grid resolution is sufficient to resolve the key physical length scales relevant to understanding configuration-dependent electron transport. Analysis of the Chapter 0 centerline measurements reveals that the electron number density exhibits an exponential decay with a characteristic length scale $L_n/r_o \approx 0.027$, dropping two orders of magnitude over 17 mm from approximately 10^{19} m^{-3} to approximately 10^{17} m^{-3}. The electron temperature gradient scale is longer, with $L_T/r_o \approx 0.086$, as T_e increases from approximately 2.8 eV to approximately 4.1 eV over the same axial extent.

Critically, this spacing enables resolution of the configuration-dependent differences that emerge in the near-field cathode plume region ($z < 15$ mm), where body bias effects are most pronounced. Beyond approximately 15 mm axially, all three electrical configurations converge to nearly identical electron properties, indicating that the far-field plume does not effectively differentiate between configurations [52].

The radial measurement grid spans from the cathode centerline ($r/r_o = 0$) to the discharge channel centerline ($r/r_o = 0.4$) with a spacing of ≥ 1 mm, which was selected to exceed the interrogation volume radial dimension, approximately 100 μm, while providing sufficient resolution to capture configuration-dependent radial gradients in electron pressure. The measurement grid was designed to sample four radial locations across the IFPC face region (approximately $r/r_o = 0$ to 0.2) and two locations within the discharge channel ($r/r_o = 0.3, 0.4$), based on the electron pressure distribution observed by Suazo Betancourt et al. in the same H9 thruster and at the same operating condition [1]. This relatively sparse radial grid is appropriate for several reasons.

First, prior measurements by Suazo Betancourt et al. found that electron temperatures across the IFPC region remained relatively constant, ranging from 3-5 eV [1], with electron pressure varying by less than a factor of two across the entire IFPC and gap span

($r/r_0 \approx 0.2$-0.3), before rising by nearly an order of magnitude within the channel. Because of this, the measurement spacing at the IFPC is commensurate with the local gradient length scale, while the channel locations together resolve the dominant channel-boundary gradient where the steepest variation is concentrated. These prior results also indicate that the electron property fields in the pole region exhibit minimal axial variation except for in the discharge channel, where electron pressure appeared to increase with axial distance. This is expected as the electron temperature should increase as the acceleration region, which is shifted downstream at low discharge voltages, is approached [50]. This indicated that the smooth radial structure does not require as fine a spatial resolution.

Second, measurement locations in the intermediate radial range ($r/r_0 \approx 0.2$-0.3) were intentionally avoided due to increased stray light from reflections off thruster surfaces, which could skew electron property determination through contamination of the Thomson scattering signal. This region corresponds to the geometric interface between the IFPC surface edge and the boron nitride discharge channel, where laser-induced fluorescence from metallic surfaces is maximized. By concentrating measurements at radial locations with minimal stray light contamination, the grid prioritizes measurement accuracy over uniform spatial coverage.

These locations, as pictured in Figure 34, within the LTS probe volume in this work was positioned at an azimuth angle of 45° relative to the horizontal centerline, while the reference data from [1] was acquired at the horizontal centerline (azimuth angle of 0°).

This azimuthal positioning aligns the scattering wave vector with the radial direction (see Figure 35), enabling isolation of the radial components of electron temperature and drift velocity.

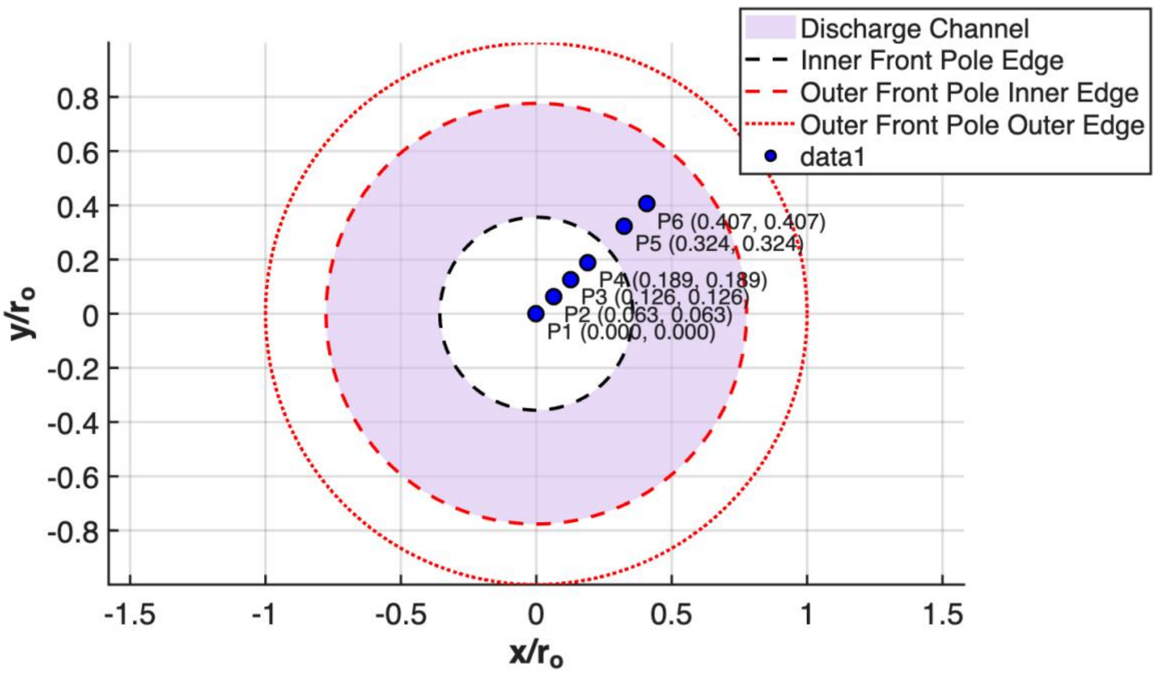

Figure 34: Front face view of LTS probing points for each thruster body bias condition.

The LTS scattering geometry, shown in Figure 35, employed a laser injection direction perpendicular to the observation direction. For measurements along the cathode centerline, which extends radially outward from the cathode orifice on the right side of the thruster ($x/r_o > 0$), the scattering vector is oriented such that the measured drift velocity corresponds primarily to the radial component of electron bulk motion. Positive drift velocities indicate net electron flow radially inward from the channel centerline axis, while negative velocities indicate net radial flow outward toward the channel. The measured temperature is also the radial component of the temperature.

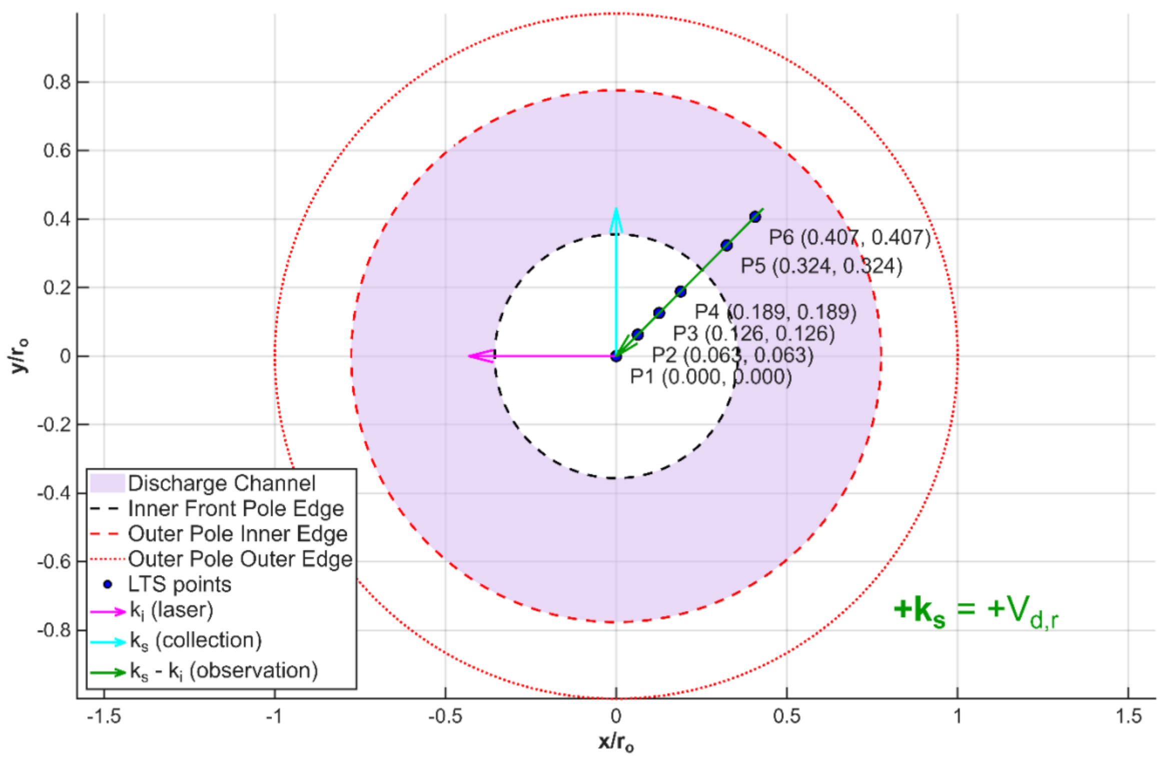

Figure 35: H9 thruster geometry and coordinate system definition. LTS measurements were performed at θ = 45° azimuthal angle (shown in green), while reference measurements from Betancourt et al. were at θ is measured from the horizontal centerline.

Positive electron radial drift velocities correspond to the positive direction of the scattering angle, $\overrightarrow{k_s}$.

4.3.2 LTS System

The LTS system, detailed in 3.2.3, is a critical component of our diagnostic suite. It employs a focused laser beam to probe the plasma, capturing scattered light that is analyzed to determine electron density and temperature with high spatial and temporal resolution. This precision enables us to resolve rapid changes in electron dynamics and provides essential insights into the effects of thruster body biasing. Minor updates made to the LTS system Figure 36 include,

- Replaced the focusing lenses on the collection optical axis internal to the vacuum chamber because the larger diameter collection optics suffered from spherical aberrations, where rays passing through the lens periphery focused differently than paraxial rays. This degraded the spatial localization of the measurement volume and increased susceptibility to stray light collection from regions outside the intended scattering volume. Smaller diameter lenses were installed to mitigate these aberrations.

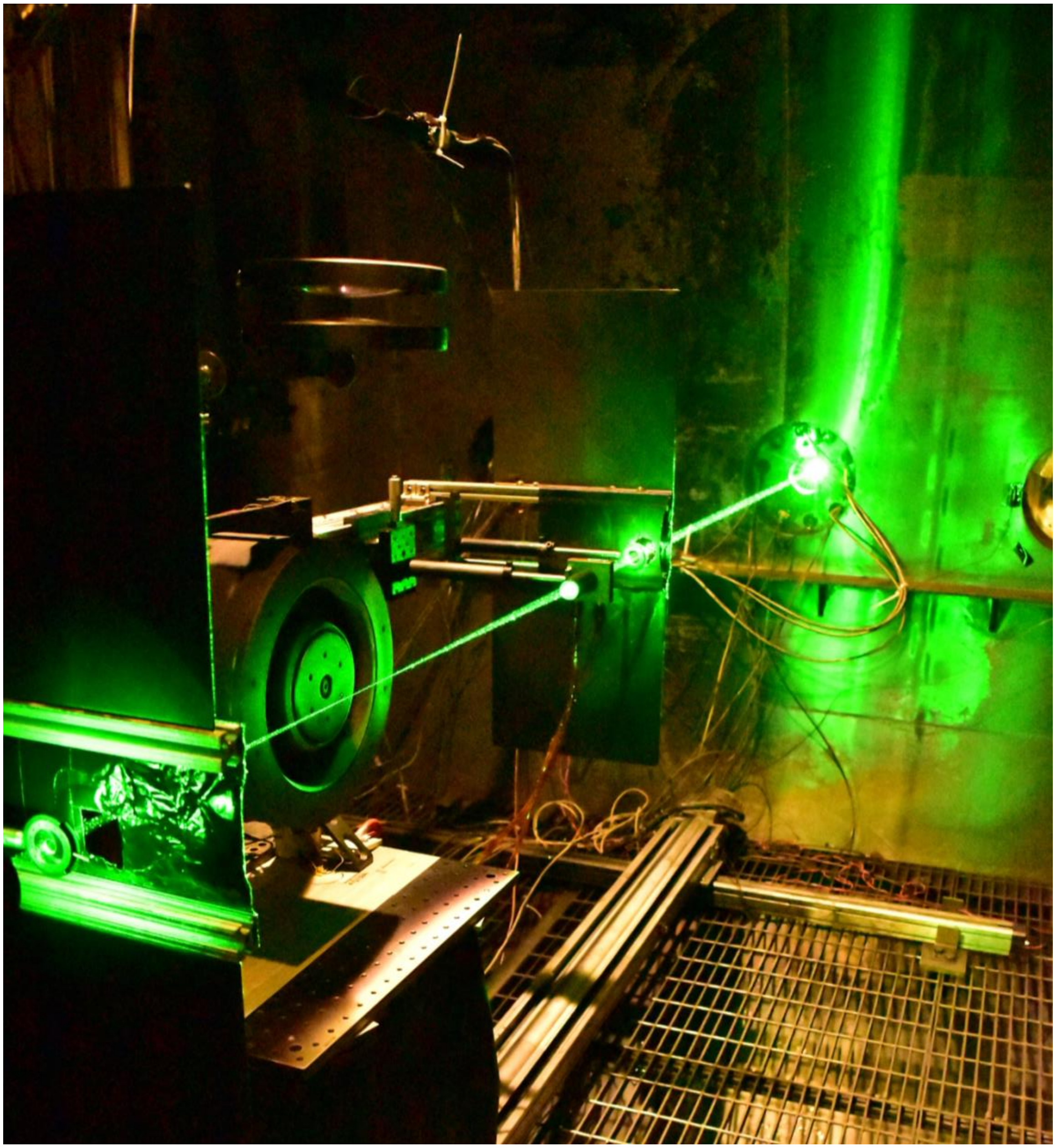

Figure 36: LTS system internal to the vacuum chamber and H9 thruster on r, z motion stages.

4.3.3 Thruster Circuit and Operating Conditions

Figure 37 illustrates the thruster electrical circuit. In this schematic, blue lines represent the connections to the thruster body which vary between biased, floating, and cathode-tied. Red lines correspond to conventional high-current EP system connections [9], e.g., discharge supply to the anode and cathode. The current and voltage measurement instrument locations, denoted by A_n, and V_n, respectively, are detailed in Table 5.

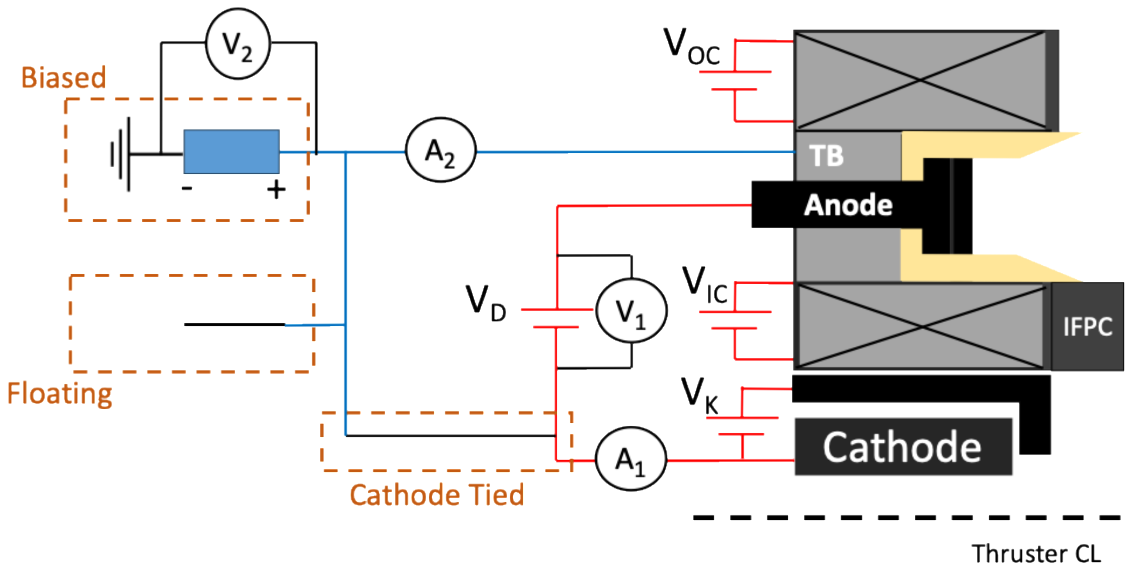

Figure 37: Phase II electrical circuit diagram.

Table 5: Phase II Electrical Instrumentation Configuration

Parameter	Symbol	Probe	Specifications	Oscilloscope
Discharge current	A_1	CP150 current probe	±150 A, 10 mV/A, 50 MHz	HDO6104[1]
Discharge voltage	V_1	Power Tek DP-25	×100, 6 kV max, 100 MHz	HDO6104
Body current	A_2	CP150 current probe	±150 A, 10 mV/A, 50 MHz	HDO6104
Body-to-ground voltage	V_2	Power Tek DP-25	×100, 6 kV max, 100 MHz	HDO6104

Phase II measurements were conducted at a 40 A discharge current and 150 V discharge voltage, maintaining the same 6 kW power level as Phase I but at a higher current density. At this condition, the cathode-to-ground voltage was approximately -10 V (±0.5 V). Three electrical configurations were tested: thruster body floating, cathode-tied, and biased +2 V relative to ground.

The selection of the 40 A, 150 V condition was driven by signal-to-noise requirements for LTS diagnostics. The region in front of the IFPC exhibits low electron density (10^{17} m^{-3} [1]) when run at nominal operating conditions. This results in a weak Thomson scattering signal. Operating at 40 A increases the electron density compared to the 20 A condition, improving the signal-to-noise ratio of LTS measurements. The lower discharge voltage of 150 V, as opposed to 300 V, reduces ion energies throughout the discharge channel, which combined with magnetic shielding topology, ensures that ions reaching the IFPC have substantially lower erosion potential than in Phase I. This made the 40 A operation thermally and mechanically acceptable for the extended run times required for spatial mapping with LTS. The average cathode body to ground voltages for the floating, tied, and +2 V biased configurations were 10.6 V ± .22 V, 10.5 V ± 0.09 V, and 10.0 ± 0.06 V, respectively. The rest of the operating conditions can be found in Table 6, and average operational values over the duration of the experiment can be found in Section 5.1.2.1.

Table 6: Phase II operating conditions

Bias Condition	**Body Voltage (V)**	**Discharge Current (A)**	**Discharge Voltage (V)**	**Anode Flow (sccm-Kr)**	**Cathode Flow (sccm-Kr)**	**Background Pressure (µTorr-Kr)**
Floating	-1.54 ± 2.92	40.2 ± 0.17	150 ± 0.16	402 ± 4.0	28 ± 0.31	7.73
Cathode Tied	-10.4 ± 0.09	39.6 ± 0.11	150 ± 0.05	402 ± 4.0	28 ± 0.31	7.73
Biased +2 V	1.89 ± 0.29	39.4 ± 0.12	150 ± 0.08	402 ± 4.0	28 ± 0.31	7.73

The operational stability and time-averaged characteristics of these bias configurations throughout the Phase II campaign are presented below in Figure 38, demonstrating that despite instantaneous oscillations associated with discharge dynamics, the electrical boundary conditions remained well-defined and reproducible across all LTS measurement sessions.

Figure 38 shows the complete thruster body current-voltage (I-V) characteristics measured throughout the Phase II experimental campaign at the nominal operating condition of 150 V discharge voltage and 40 A discharge current. Unlike Phase I, where the IFPC served as an electrically isolated witness plate, Phase II measurements were conducted with the thruster body directly connected to the bias power supply, resulting in body currents representative of the actual electron collection to the thruster structure during laser Thomson scattering measurements.

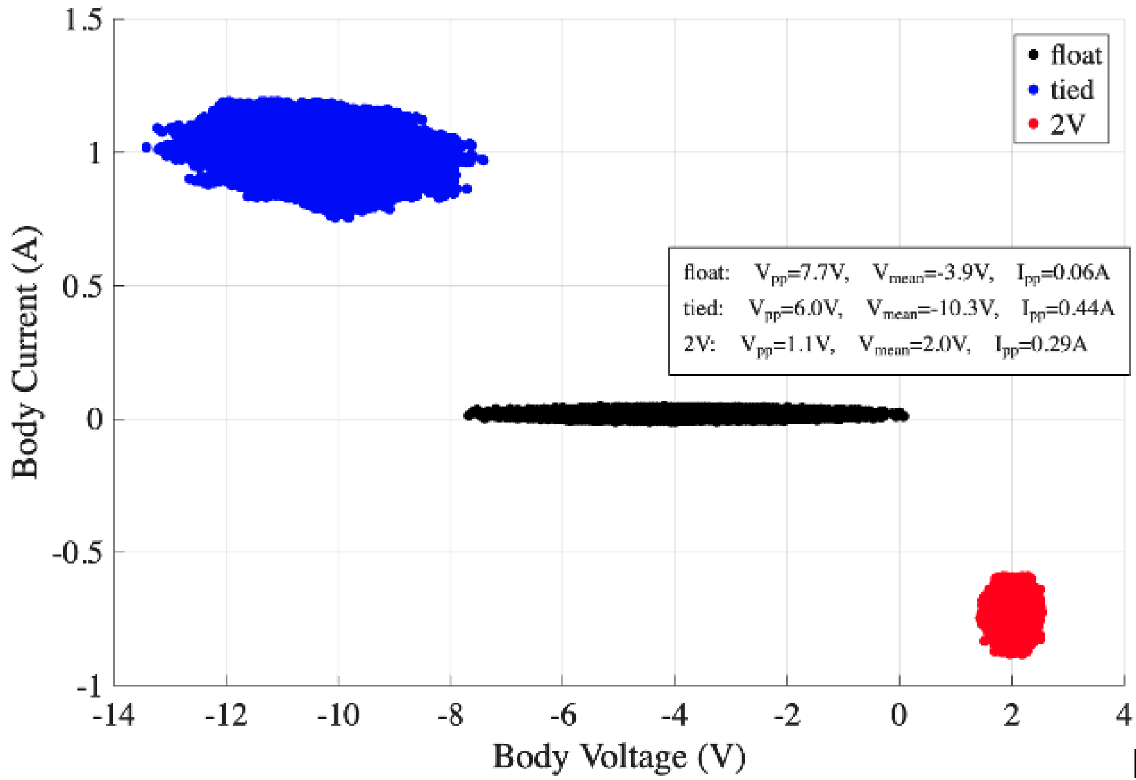

Figure 38: Phase II operational bias uncertainty associated with biasing in the various electrical configurations.

The three electrical configurations exhibit distinctly different I-V behaviors that reflect their fundamental electron collection mechanisms. The Float configuration (black) shows the thruster body naturally settling to approximately -4 V with respect to cathode common, drawing a body current of approximately 6 mA and a very low peak-to-peak value as expected. The substantial voltage spread ($\Delta V_{body} \approx 8$ V) observed across the campaign reflects the sensitivity of the floating potential to plasma conditions, cathode coupling efficiency, and minor variations in operating point stability. This floating voltage represents the self-consistent potential required to balance electron and ion collection currents to the thruster body when electrically isolated.

The Tied configuration (blue) actively forces the thruster body to cathode common potential which was averaged across all three bias conditions to a value of approximately -10.3 V. This resulted in body currents from 0.75 to 1.2 A. The cathode body potential's lack of sensitivity to body bias indicates that it is not affected by downstream boundary conditions imposed by the thruster body.

The +2 V configuration (red) applies a positive 2 V bias relative to cathode common, drawing approximately -0.8 A of body current. The negative sign indicates electron collection, as expected when the thruster body is biased positively with respect to the surrounding plasma. The observed voltage spread ($\Delta V_{body} \approx 0.5$ V) is significantly smaller than the other configurations, suggesting more stable operation under active bias control. The tight clustering of this configuration around the origin demonstrates the stability of this forced electrical boundary condition and validates the power supply control loop performance. This configuration represents an intermediate case where the body potential is elevated above ground but remains well below typical plasma potentials in the discharge channel.

4.4 Measurement Uncertainty Summary

This section consolidates the primary sources of measurement uncertainty affecting the experimental data reported in this investigation. Table 7 summarizes each source, its classification, and the treatment or mitigation strategy employed. Detailed derivations of the LTS fitting uncertainty and error propagation formulas are provided in the LTS methodology chapter. The uncertainty sources span both Phase I current collection measurements and Phase II spatially resolved LTS diagnostics.

Table 7: Consolidated measurement uncertainty sources.

Uncertainty Source	Phase	Classification	Treatment / Mitigation
LTS spectral fitting (parameter covariance matrix)	II	Random	Nonlinear least-squares with Jacobian-based covariance; typical uncertainties ~0.5% for n_e, ~0.1% for T_e
Instrument function spectral broadening	II	Systematic	Forward convolution fitting with measured instrument function for affected spectra
Raman calibration coefficient	II	Systematic	Synthetic Raman spectrum fitting at known pressure (±0.5% capacitance manometer accuracy)
Laser plasma perturbation	II	Systematic	Power density ratio verified below perturbation threshold at all measurement locations
Power supply bias setpoint accuracy	I, II	Systematic	Calibrated Tektronix probe measurement (±0.01 V resolution)

Breathing mode current oscillations	I	Random	Time-averaged over multiple breathing cycles; large residual variance reflected in error bars
Time-averaged density bias from oscillations	II	Systematic	Nonlinear averaging of oscillatory density is acknowledged; density measurements are particularly susceptible
Dynamic vs. static pressure in T_e	II	Systematic	Unresolved in time-averaged LTS; thermal and oscillatory contributions are inseparable without time-resolved diagnostics

The Phase I IFPC current measurements are subject to substantial oscillatory uncertainty arising from breathing mode instabilities in the discharge. Time-averaging over multiple breathing cycles captures the mean current behavior but does not fully resolve the underlying variance. These uncertainties are reflected in the error bars presented in the Phase I results and should be considered when interpreting current collection trends across the bias voltage sweep.

For Phase II LTS measurements, the dominant random uncertainty originates from the spectral fitting procedure and is quantified through the parameter covariance matrix. Systematic contributions from instrument function broadening were addressed through a forward convolution fitting approach for data acquired when the measured instrument function deviated from theoretical predictions. The laser power density at the measurement volume was verified to remain below the threshold for plasma perturbation, confirming that the diagnostic does not appreciably alter the electron properties under measurement. Absolute density calibration relies on rotational Raman scattering from air at a known pressure, with the capacitance manometer contributing a systematic uncertainty of approximately 0.5%.

Two systematic effects remain unresolved in the time-averaged measurements. First, because electron density oscillates at the breathing mode frequency with amplitudes comparable to the mean value, time-averaged density measurements are susceptible to nonlinear averaging bias. Second, the measured electron temperature from time-averaged LTS contains contributions from both thermal (static) and oscillatory (dynamic) pressure components, which cannot be separated without time-resolved diagnostics. Both limitations are acknowledged and discussed further in the context of the Phase II results.

CHAPTER 5: RESULTS

This chapter presents the experimental data collected during both phases of the investigation into thruster body bias effects on electron transport in the H9 magnetically-shielded HET. The analysis is organized to systematically build understanding from global electrical measurements to spatially-resolved plasma diagnostics, ultimately revealing the configuration-dependent nature of electron behavior in the cathode plume region.

Phase I employed the IFPC as an electrically isolated witness plate to characterize body current collection across a continuous range of applied voltages. These measurements establish the electrical operating space of the thruster-cathode system and identify discrete bias configurations of particular interest: electrically floating (Float), cathode-tied (Tied, approximately -10 V), and positively biased (+2 V). Power spectral density analysis of the body current reveals how global oscillatory modes respond to changes in thruster body potential. Together, these electrical diagnostics provide context for understanding the plasma-surface interactions that govern electron collection.

Phase II transitions to LTS diagnostics, which provide spatially-resolved measurements of electron number density, temperature, and radial drift velocity at the three discrete configurations identified in Phase I. Time-resolved telemetry and corresponding PSD analysis confirm the operating conditions during each optical measurement campaign and establish the relationship between stable versus unstable discharge regimes and the magnitude of configuration-dependent effects. The data processing techniques section details the forward convolution fitting methodology, uncertainty quantification procedures, and instrument function characterization necessary to extract reliable plasma parameters from the Thomson scattering spectra.

The spatial investigation focuses on three critical locations: the cathode centerline, where electron emission and near-field plasma dynamics directly influence the electron population; the inner front pole cover region, where plasma-surface interactions occur, and the witness plate measurements were obtained; and the channel centerline, which represents the primary ionization and acceleration zone of the thruster. At each location, electron properties are examined across the measurement volume to reveal how body bias modulates density, temperature, and flow patterns. Finally, the relative properties between biases section synthesizes these findings to identify configuration-dependent trends and quantify the extent to which thruster body potential influences electron transport pathways.

5.1.1 Phase I Results

Phase I of this experimental campaign investigated the effects of thruster body bias on plasma dynamics and current collection by performing voltage sweeps from 0 V to 2 V above ground potential for both the isolated IFPC and the thruster body. This section presents the analysis of three key measurement types collected during these bias sweeps: averaged thruster telemetry data to demonstrate stable thruster operation across all bias configurations, current-voltage characteristics for both the isolated IFPC and thruster body to quantify electron collection as a function of applied bias, and power spectral density analysis to characterize the oscillatory behavior of the plasma discharge. Together, these measurements provide a comprehensive picture of how thruster body bias influences both local current collection at the IFPC surface and global current redistribution throughout the thruster system.

5.1.1.1 Phase I Thruster Telemetry

Figure 39 shows the thruster telemetry measurements, which were averaged over the duration of the measurement, as a function of IFPC bias voltage, spanning the range from 0.5 V to 2.0 V. These measurements include discharge voltage, discharge current, thruster body-to-ground voltage, keeper voltage, and cathode body-to-ground voltage. The purpose of these measurements is to demonstrate that thruster operating conditions remained stable across all bias configurations, with telemetry values not changing appreciably as a function of IFPC bias. This stability isolates the observed current collection differences to the electrical configuration itself rather than to variations in thruster operating state. Error bars represent the standard deviation of each telemetry value over the measurement period. The magnitude of these uncertainties is primarily attributed to the oscillatory nature of Hall effect thruster plasma, particularly the breathing mode oscillation that causes periodic variations in discharge current and other plasma parameters.

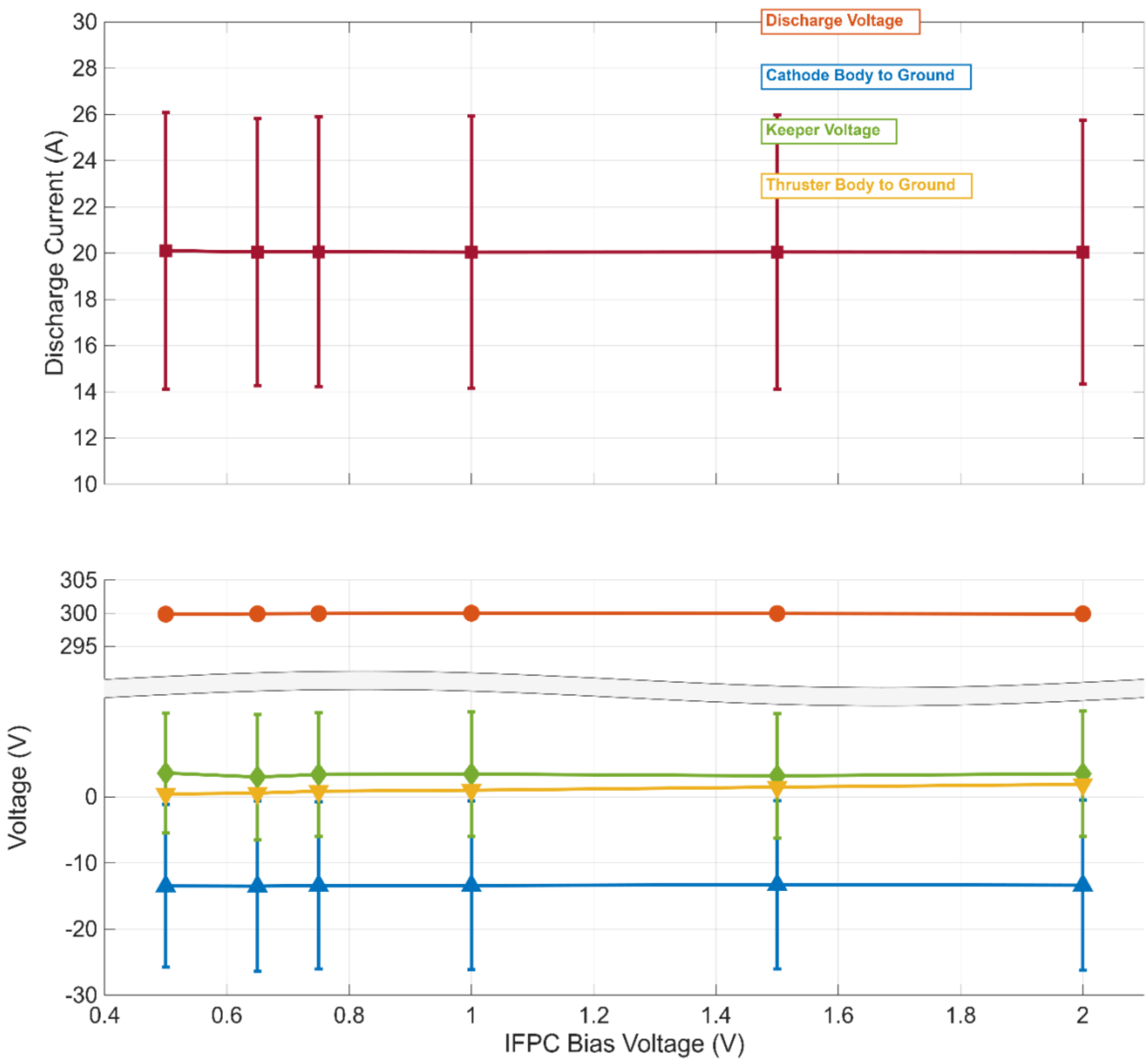

Figure 39: Phase I discharge telemetry evolution with IFPC bias operating at 300 V, 20 A. Error bars represent 1σ standard deviation of time-resolved measurements.

5.1.1.2 Phase I Collected Current

Figure 40 compares the thruster body current and IFPC current as a function of IFPC bias voltage. Both currents are negative, indicating electron collection in the sign convention used throughout this work. The thruster body current (red) varies between approximately -0.55 A and -0.75 A across the bias range, while the IFPC current (green) remains much smaller in magnitude, ranging from approximately -0.05 A to +0.15 A. The limited bias range of 0.5 V to 2.0 V was constrained by operational considerations described in Section X. While the variations are small and potentially within the applied bias voltage resolution, both measurements exhibit a discernible downward trend with increasing IFPC bias voltage, indicating enhanced electron collection at higher bias values. This trend is observed both locally at the IFPC surface and globally at the thruster body, confirming that increasingly positive thruster body voltages draw additional electron current from the plasma. The error bars, particularly evident on the thruster body current measurements, reflect the temporal variations in current collection driven by the breathing mode oscillations inherent to HET operation.

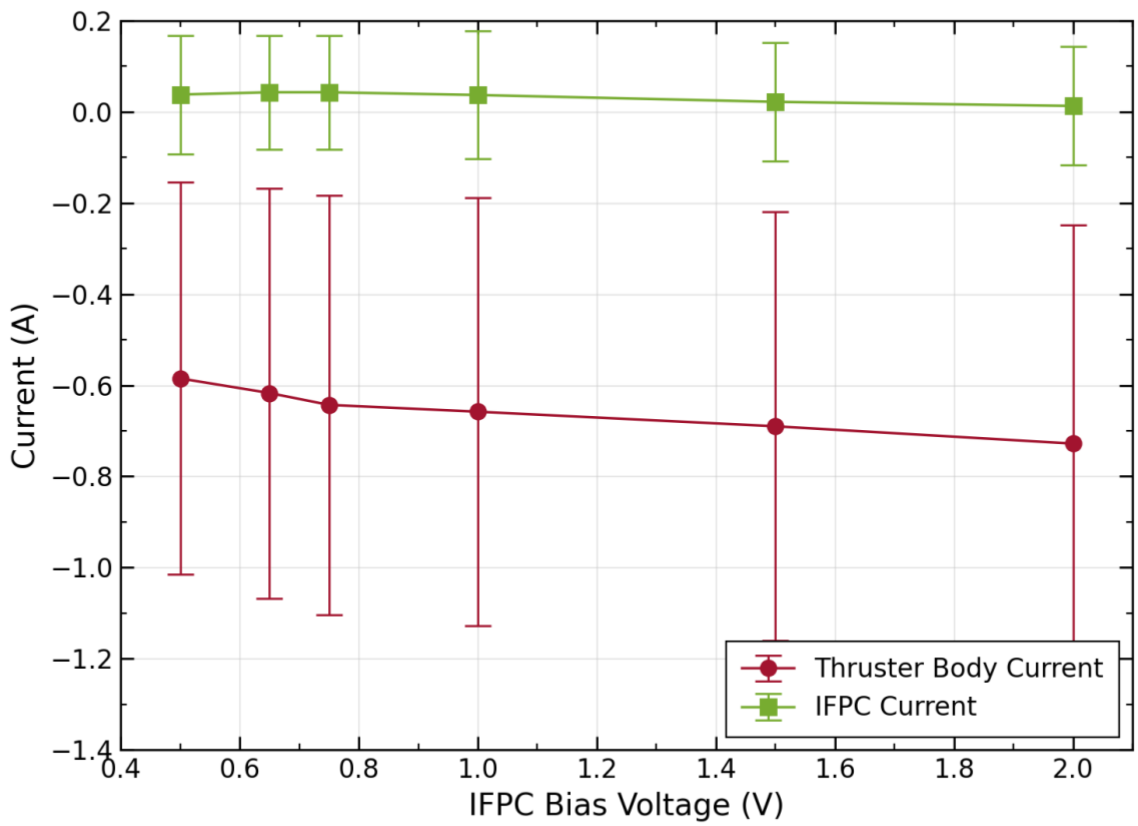

Figure 40: Phase I collected current by the Isolated IFPC Probe (green) and thruster body (red) as a function of mean thruster body voltage operating at 300 V, 20 A. Error bars represent 1σ standard deviation of time-resolved measurements.

5.1.1.3 Power Spectral Density Plots

Power spectral density (PSD) analysis was performed on the discharge current time-series data to identify the breathing mode frequency for each electrical configuration. The instrumentation and associated specifications used to acquire this data are discussed in

Section 4.1.2. The discharge current signals were sampled at a frequency of 1 MHz. For each electrical configuration, three separate measurements were collected and averaged in the time domain to reduce the influence of random fluctuations and confirm repeatability.

Prior to PSD computation, the DC component was removed from each averaged signal by subtracting the mean value. This step is critical for accurate spectral analysis as the DC offset can dominate the low-frequency portion of the spectrum and obscure the breathing mode peak [94]. The PSD was computed using Welch's method [95] which reduces variance in spectral estimates by averaging modified periodograms. Welch's method divides the signal into overlapping segments, applies a window function to each segment, computes the periodogram of each windowed segment and averages the result. A Hann window with a length determined by dividing the total signal length by the window division parameter was used. One was selected for its good frequency resolution and low spectral leakage properties [96]. MATLAB's "pwelch" function was used to perform the Welch periodogram calculation with the specified parameters. The dominant peak was identified as the peak in the PSD within 10-20 kHz frequency range which was selected based on typical reported breathing mode frequencies observed in HETs [39, 97]. Also, while excluding lower frequencies. To reduce the influence of noise spikes on peak identification, a 5-point moving average filter was applied to the PSD before locating the maximum value. The frequency corresponding to this maximum was recorded as the breathing mode frequency. The resulting PSD curves were plotted on a decibel scale

(10×$\log_{10}$(PSD)) to better visualize the dynamic range of the spectral content, with the frequency axis also plotted on a log scale to focus on the breathing mode and its harmonics.

Time-resolved measurements of discharge current, IFPC current, thruster body current, and keeper voltage revealed breathing mode oscillations across all bias conditions tested, with a harmonic appearing in some cases. Figure 41 through Figure 46 show the power spectral density for these measurements at IFPC bias set points of +0.50 V, +0.65 V, +0.75 V, +1.00 V, +1.50 V, and +2.00 V relative to ground, respectively.

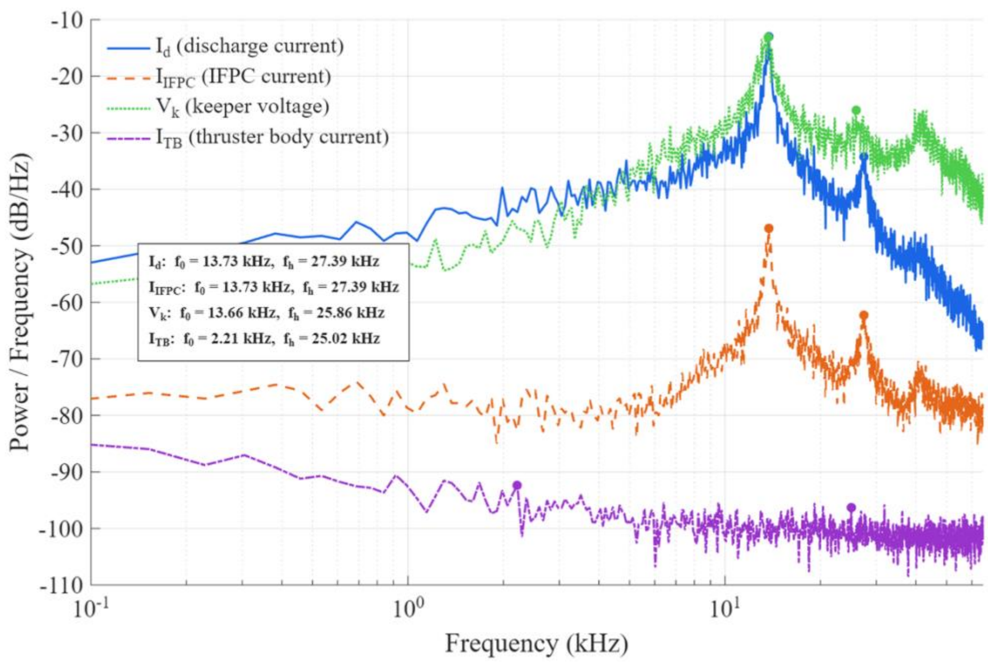

Figure 41: Power spectral density plot at +0.5 V bias setpoint.

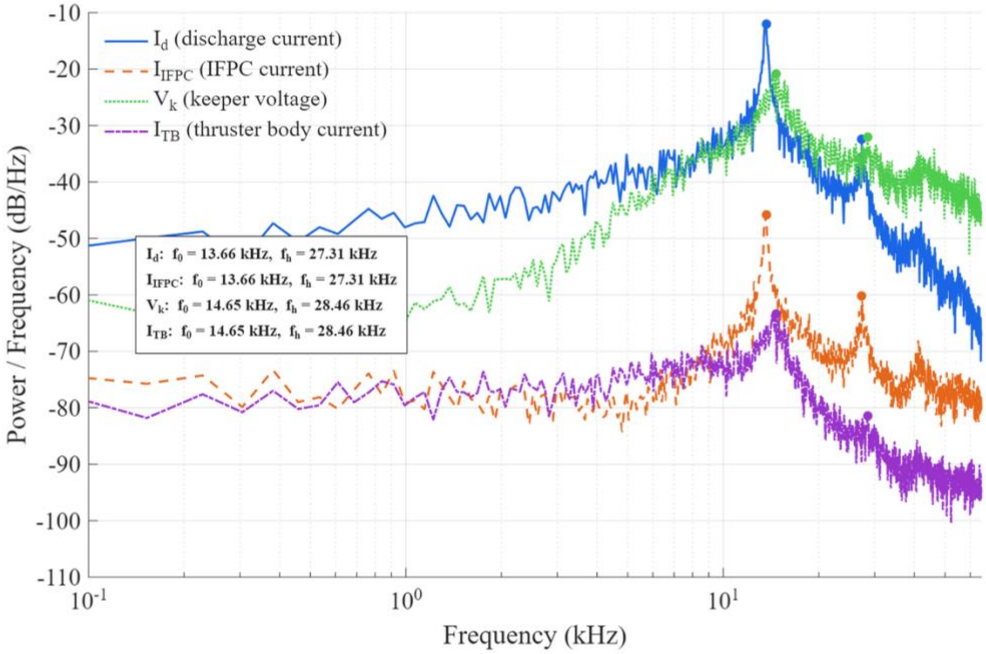

Figure 42: Power spectral density plot at +0.65 V bias setpoint.

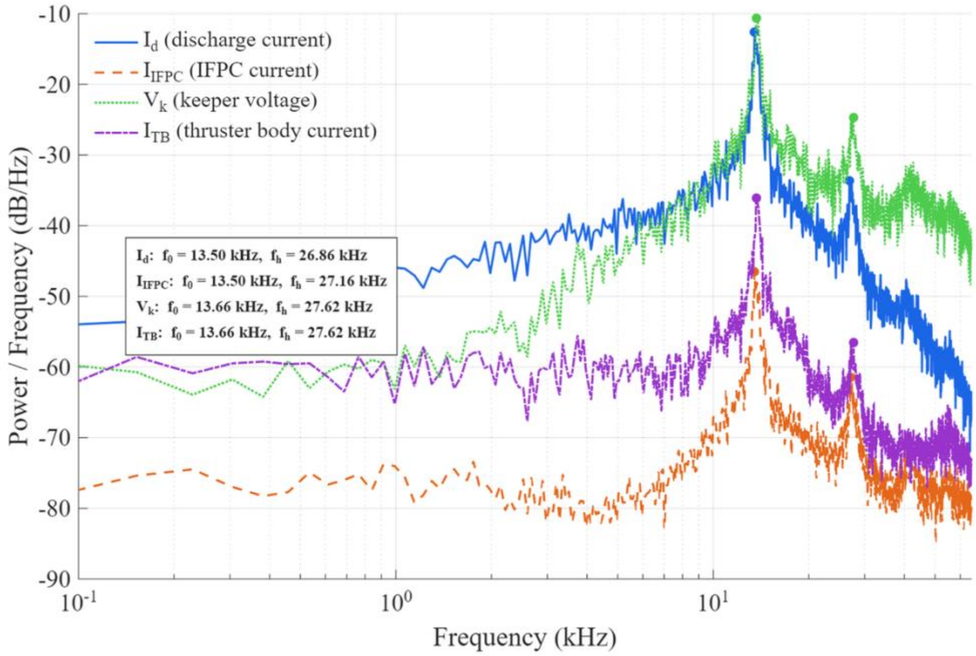

Figure 43: Power spectral density plot at +0.75 V bias setpoint.

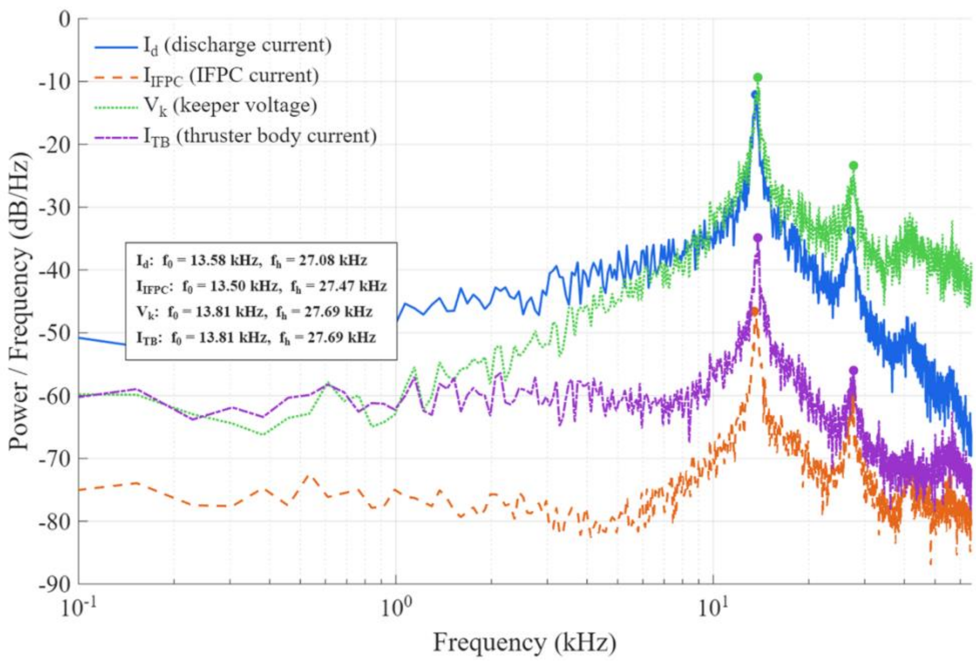

Figure 44: Power spectral density plot at +1 V bias setpoint.

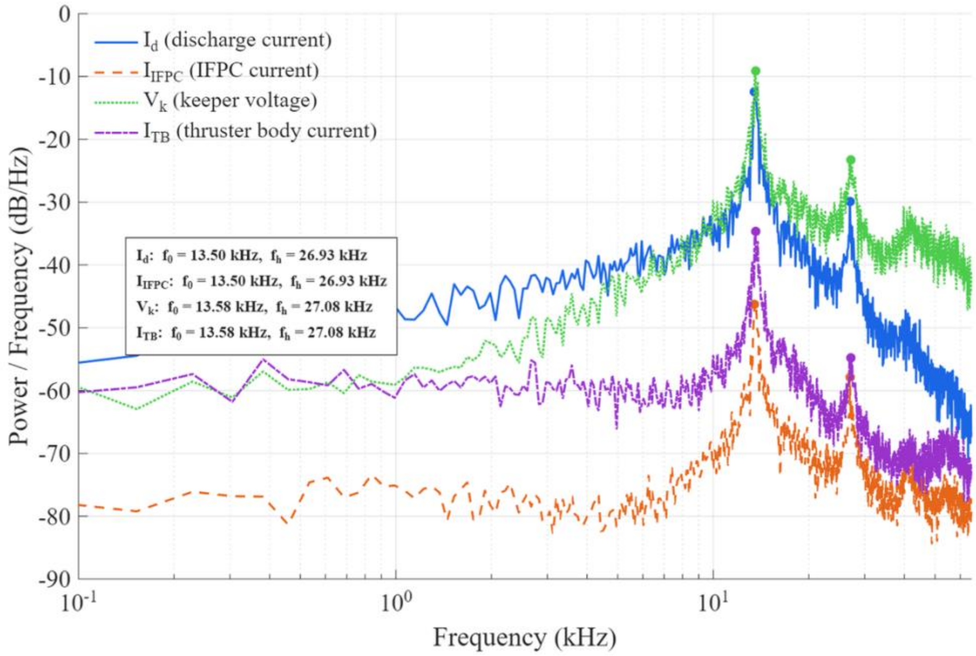

Figure 45: Power spectral density plot at +1.5 V bias setpoint.

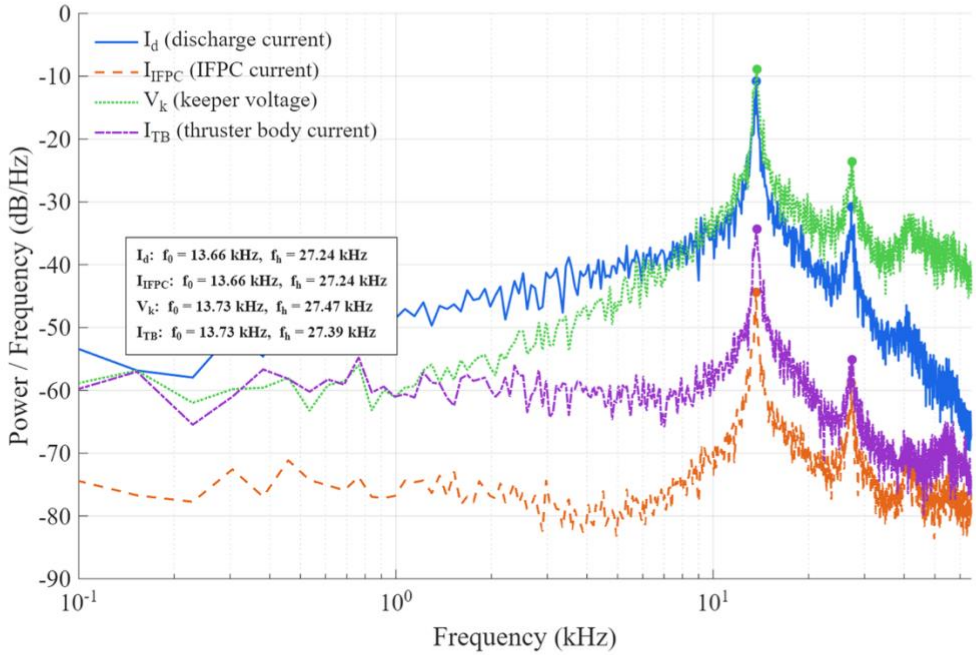

Figure 46: Power spectral density plot at +2 V bias setpoint.

The breathing mode exhibits nominal behavior with an average fundamental frequency of 13.6 kHz, ranging from 13.5 kHz to 13.7 kHz across bias conditions. This indicates that the applied bias, at least over this 1.5 V range, had no discernible effect on the global oscillatory characteristics of the discharge. The breathing mode frequency in the biased configuration varies only slightly from the nominal frequency for this thruster at this operating condition, which was 16.6 kHz in the grounded configuration, as shown in Figure 21, representing an 18% decrease.

However, which electrodes responded to these global oscillatory characteristics varied with bias voltage. At the lowest bias voltage of +0.50 V above ground, as shown in Figure 41, discharge current, IFPC current, and keeper voltage all exhibit clear breathing mode peaks, while the thruster body current spectrum remains relatively flat with no discernible fundamental frequency. A harmonic between 25 kHz and 30 kHz appears in all channels except the thruster body current.

At +0.65 V above ground, as shown in Figure 42, the thruster body current begins to respond to the breathing mode, registering a slightly elevated fundamental frequency of 14.7 kHz that also appears in the keeper voltage spectrum. As the IFPC bias voltage increases beyond +0.65 V, all electrodes display increasingly uniform spectral responses, with fundamental frequencies and harmonic frequencies agreeing to within 5% across channels, though with varying amplitudes.

5.1.2 Phase II Results

Phase II of this experimental campaign employed laser Thomson scattering diagnostics to obtain spatially-resolved measurements of electron properties at three electrical configurations: Float, cathode-tied (Tied), and +2 V above ground (+2 V). This section presents the analysis of several complementary datasets collected during these measurements. First, time-resolved thruster telemetry is examined to document any variations in operating conditions that may be responsible for configuration-dependent differences in the plasma. Power spectral density analysis is then performed at each bias configuration to characterize the breathing mode oscillations and assess plasma stability. The primary focus of this section is the presentation of electron properties measured along two regions of interest (ROIs): the cathode centerline and a radial traverse from the IFPC to the channel centerline. The data-processing techniques employed to extract these properties from the raw Thomson scattering spectra are detailed. Electron pressure profiles are compared against previous measurements by [1] to validate the experimental approach, while electron current density derived from the measured electron drift velocity is presented to quantify radial electron transport. Throughout this analysis, relative changes in electron properties between configurations are highlighted to elucidate the physical mechanisms by which thruster body bias influences electron dynamics.

5.1.2.1 Phase II Time Resolved Telemetry

Thruster telemetry was monitored for the duration of the experiment for the purpose of ensuring that any changes in electron properties are associated with the varied bias and not any other sources, like changes in the discharge behavior. Each figure presents a triplot comprising three panels: the top panel shows the thruster body-to-ground voltage (blue, left axis) and cathode-to-ground voltage (orange, right axis), the middle panel shows the discharge voltage (green dashed, left axis) and discharge current (black, right axis), and the bottom panel shows the per-acquisition mean discharge current (blue, left axis) and thruster body current (orange, right axis) over the full experiment duration. Red horizontal lines in all panels represent the overall mean value of each signal over the experiment duration. All panels were generated by reading the wall-clock timestamp from each oscilloscope CSV file header, computing the mean and standard deviation of the discharge current and thruster body current within each approximately 0.2 s acquisition at 5 MHz, and plotting these values against elapsed time in hours. Error bars on all panels represent the within-acquisition standard deviation, capturing the instantaneous oscillation amplitude at each measurement point, and red lines indicate the overall mean of each signal as described above. Figure 47 through Figure 49 depict these averaged discharge characteristics in each thruster body bias/electrical configuration over the duration of the Phase II experimental campaign.

5.1.2.1.1 Floating Time-Resolved Results

The floating configuration shown in Figure 47 exhibits distinct temporal evolution in both ground voltage relationships and discharge characteristics. In the top panel, the thruster body-to-ground voltage (blue) begins near 0 V, drifts downward to approximately −4 V over the first four hours, then rises sharply and stabilizes around +2 V for the remainder of the test. This polarity reversal from negative to positive is a notable feature of the floating configuration telemetry. The cathode-to-ground voltage (orange) starts at approximately +11 V and gradually decreases to approximately 10.3 V over the test duration. The middle panel shows the discharge voltage (green, dashed) starting near 149.8 V, dropping to approximately 149.6 V during the mid-test period, then rising back to approximately 150.2 V by test completion. The discharge current (black) remains relatively stable around 40.15 A throughout, with minor fluctuations corresponding to the voltage variations. The abrupt transition in thruster body-to-ground voltage at approximately four hours into the floating configuration represents anomalous behavior inconsistent with expected floating potential temporal evolution. Possible explanations for this discontinuity include instrumentation issues rather than genuine plasma physics changes. Specifically, the BNC cable connection for the oscilloscope measurement channel was discovered to be loose during the floating configuration test and was subsequently replaced before the cathode-tied and +2 V configurations. The loose connection likely introduced intermittent contact resistance and signal integrity issues, potentially explaining both the sudden voltage transition in the thruster body-to-ground signal. Post-repair measurements in subsequent configurations showed significantly more stable voltage readings, supporting the hypothesis that the oscilloscope measurements of this telemetry point were compromised by faulty instrumentation.

The bottom panel presents the per-acquisition mean discharge current (blue, left axis) and thruster body current (orange, right axis) over the full experiment duration. The thruster body current remained near zero for the entire experiment duration, with a mean value (red line) on the order of 0.01 A and within acquisition standard deviations of approximately ±0.02 A. The zero-body current magnitude is consistent with the electrically isolated floating body, where no external current path exists to sustain a net DC current through the body.

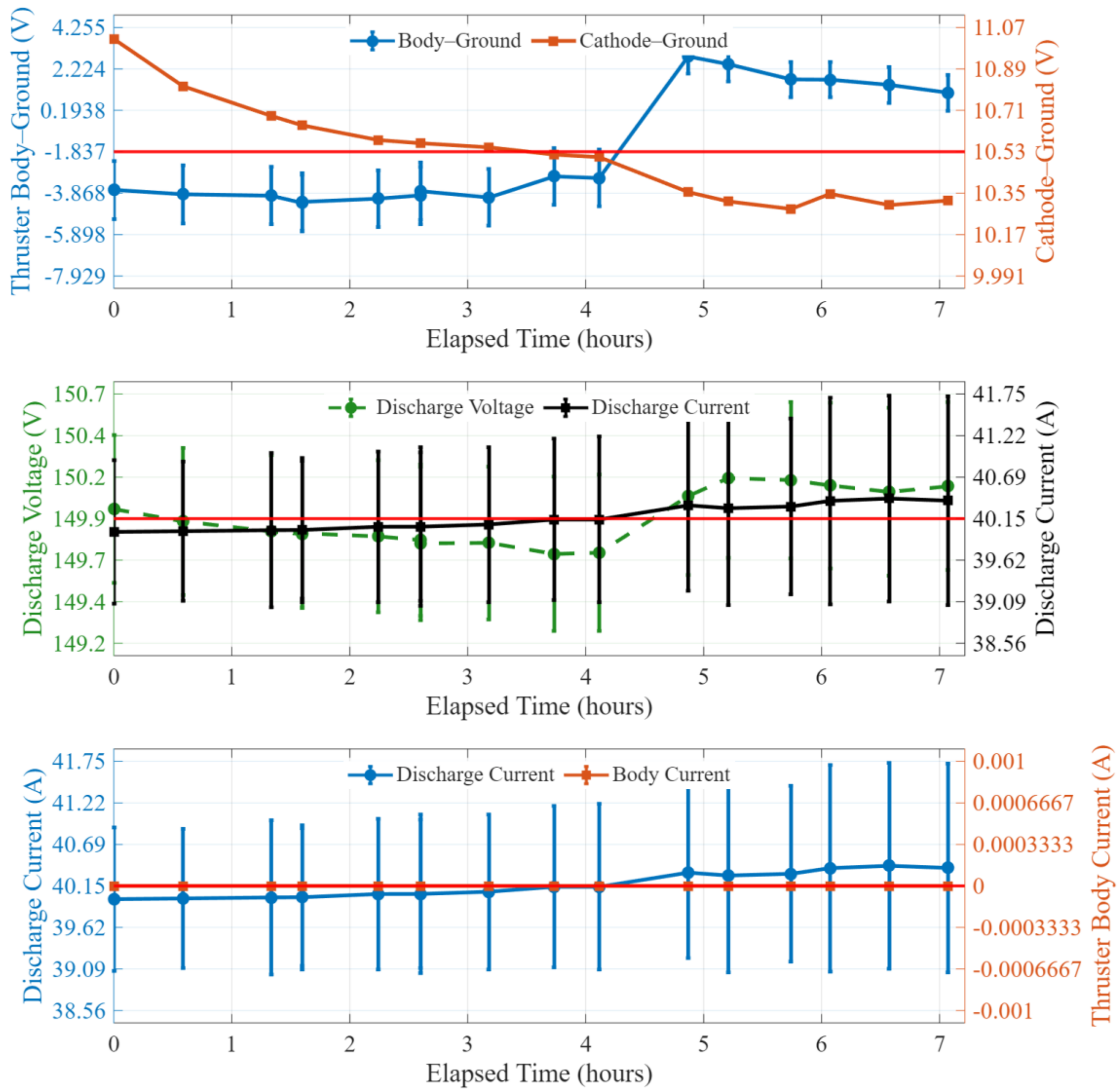

Figure 47: Phase II floating configuration thruster telemetry and current comparison over experiment duration operating at 150 V, 40 A. Top: thruster body-to-ground voltage (blue) and cathode-to-ground voltage (orange). Middle: discharge voltage (green, dashed) and discharge current (black). Bottom: per-acquisition mean discharge current (blue) and

thruster body current (orange) with 1σ within-acquisition standard deviation error bars and overall mean lines (red).

5.1.2.1.2 Cathode Tied Time-Resolved Results

Figure 48 shows the thruster telemetry for the cathode-tied configuration. In the top panel, the body-to-ground voltage (blue) maintains a nominal baseline of approximately −10.5 V, consistent with the body being electrically tied to the cathode at its negative potential relative to ground. The cathode-to-ground voltage (orange) was stable, starting at approximately 10.4 V, rising to a peak of approximately 10.7 V at $t \approx 250$ minutes, then settling to approximately 10.5 V for the remainder of the test. The middle panel confirms that the discharge characteristics exhibit very low variability, with the discharge voltage (green dashed) stable near 150 V and the discharge current (black) steady at approximately 39.6 A throughout the experiment. The body and cathode voltages in this configuration track each other more closely than in the floating case, consistent with their electrical connection through cathode common.

The top panel also reveals several intermittent negative voltage spikes in the thruster body-to-ground signal, with excursions reaching values below −13 V compared to the nominal −10.5 V baseline. These transient excursions do not correspond to any visible perturbation in the cathode-to-ground voltage or in the discharge telemetry shown in the middle panel, suggesting they are localized transient events on the body voltage sensing line rather than bulk discharge perturbations. The bottom panel shows the per-acquisition mean discharge current (blue, left axis) stable at approximately 39.6 A (red mean line) throughout the experiment. The thruster body current (orange, right axis) in this configuration is positive, with a mean value (red line) of approximately 0.78 A and individual acquisition means ranging from approximately 0.5 to 1.0 A, indicating a sustained net current flow through the thruster body consistent with the direct electrical connection between the body and cathode common.

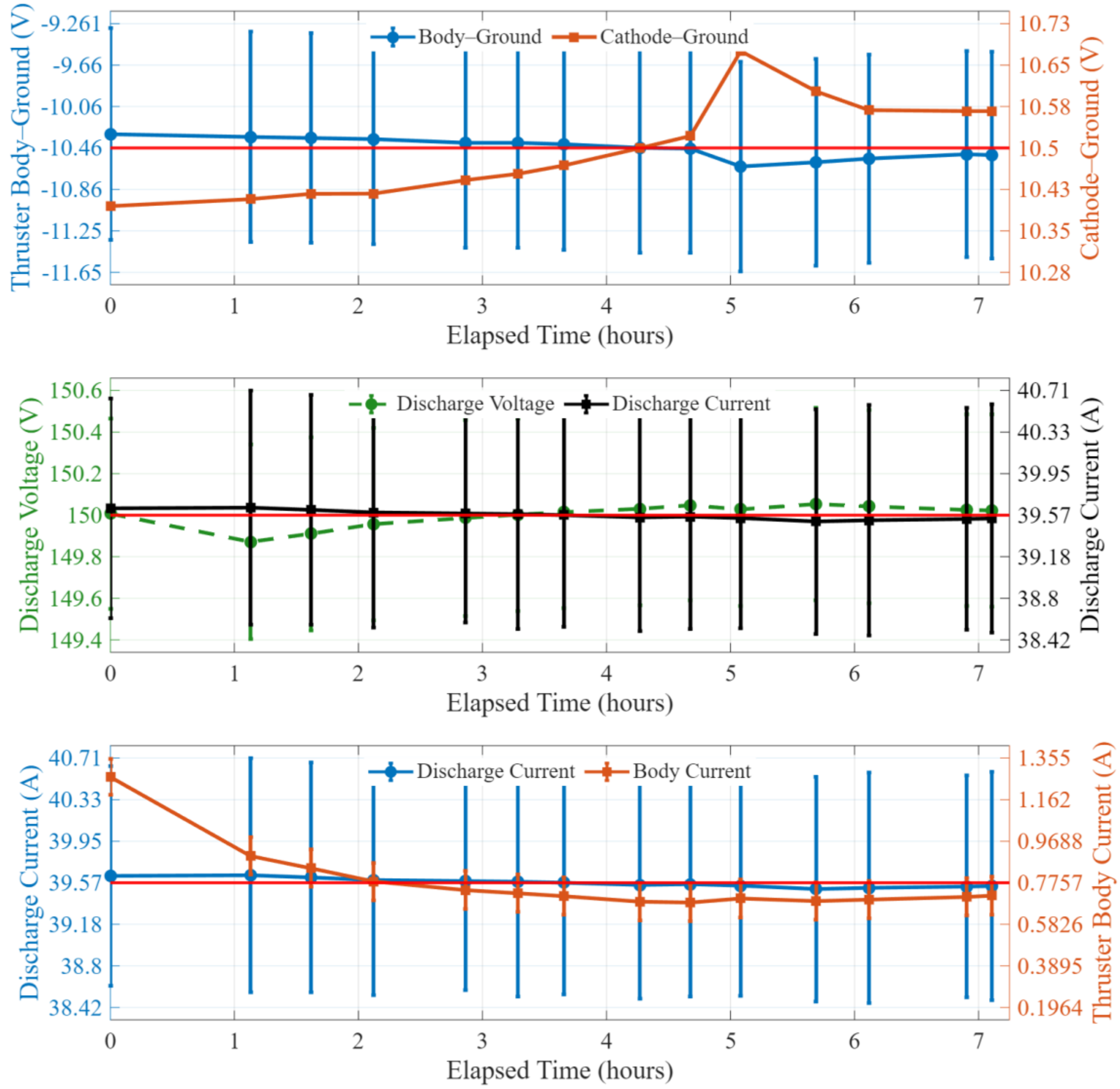

Figure 48: Phase II cathode-tied configuration thruster telemetry and current comparison over experiment duration operating at 150 V, 40 A. Top: thruster body-to-ground voltage (blue) and cathode-to-ground voltage (orange). Middle: discharge voltage (green, dashed) and discharge current (black). Bottom: per-acquisition mean discharge current (blue) and

thruster body current (orange) with 1σ within-acquisition standard deviation error bars and overall mean lines (red).

5.1.2.1.3 +2 V Bias Time-Resolved Results

Figure 49 shows the thruster telemetry for the +2 V bias relative to the ground configuration. The top panel demonstrates the most stable body-to-ground voltage behavior of all three configurations, maintaining a consistent value of approximately +2.0 V throughout the test duration with minimal temporal drift. This stability was observed through the operational bias uncertainty in Figure 38. The cathode-to-ground voltage (orange) shows an initial value near +10.1 V, then gradually decreases to approximately 9.95 V by test completion. The middle panel shows the discharge characteristics remained relatively constant, with the discharge voltage (green dashed) near 149.9 V and the discharge current (black) around 39.5 A. The consistent body bias relative to ground in this configuration, enforced by the external power supply, produces the most stable electrical conditions as reflected in the reduced variability of both ground voltages and discharge telemetry. The cathode-to-ground voltage remained stable throughout the experiment, regardless of electrical configuration, though all three configurations exhibited the same gradual decreasing trend.

The bottom panel shows the per-acquisition mean discharge current (blue, left axis) is stable at approximately 40.1 A (red mean line), with within-acquisition standard deviations comparable to those of the other configurations. The thruster body current (orange, right axis) in the +2 V bias configuration is negative, with a mean value (red line) of approximately −0.85 A. This represents a reversal in the sign of the body current relative to the cathode-tied configuration, where the body current was positive at approximately +0.78 A.

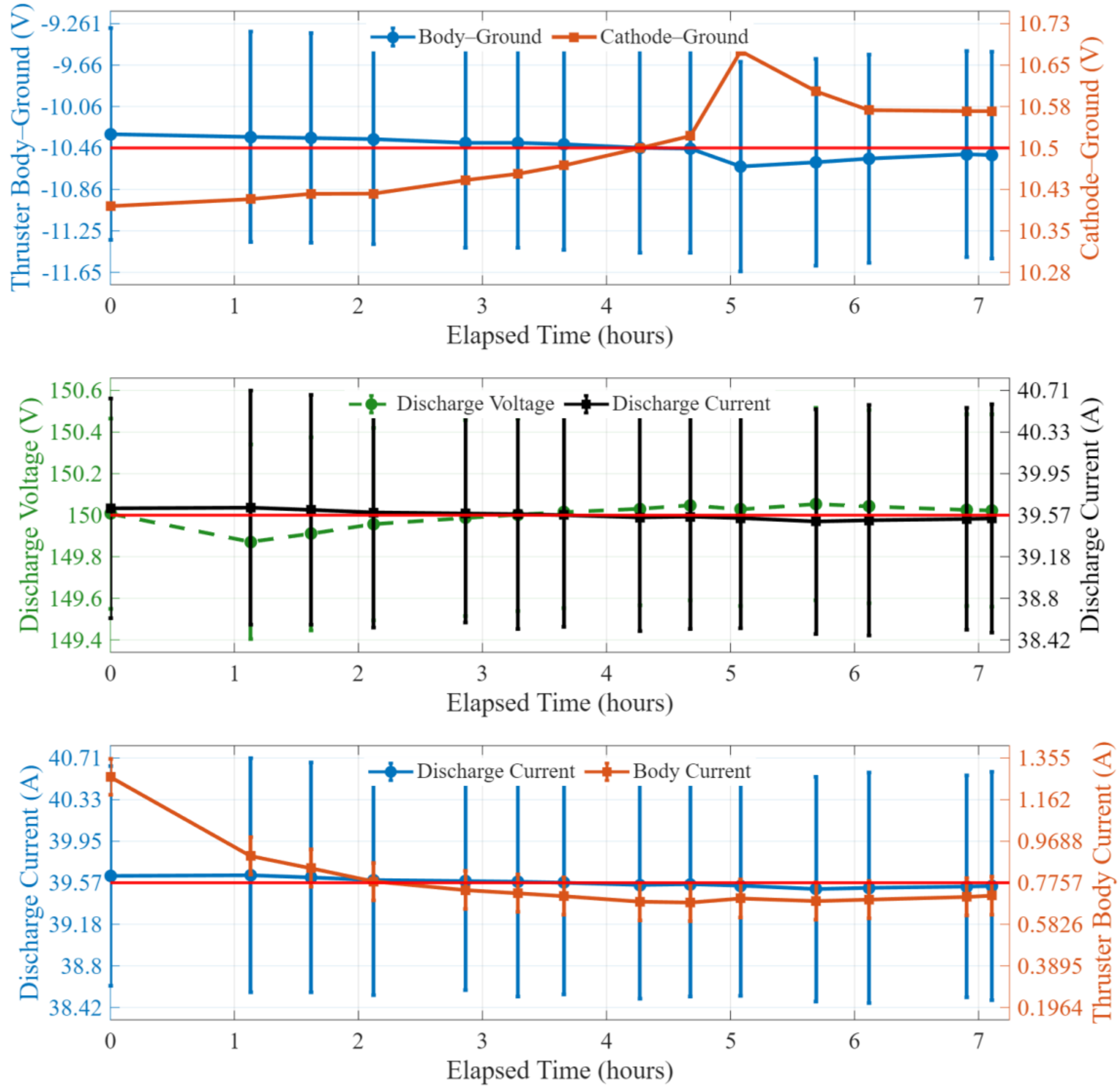

Figure 49: Phase II +2 V bias relative to ground configuration thruster telemetry and current comparison over experiment duration operating at 150 V, 40 A. Top: thruster body-to-ground voltage (blue) and cathode-to-ground voltage (orange). Middle: discharge voltage (green, dashed) and discharge current (black). Bottom: per-acquisition

mean discharge current (blue) and thruster body current (orange) with 1σ within-acquisition standard deviation error bars and overall mean lines (red).

5.1.2.2 Power Spectral Density Plots

Figure 50 shows the PSD of the discharge current for the three electrical configurations at the 40 A, 6 kW operating condition. A description of the method of generating these PSD plots can be found in Section 5.1.1.3. The breathing mode frequencies are 6.24 kHz, 6.37 kHz, and 6.29 kHz for the floating, tied, and +2 V configurations, respectively. This represents a decrease from the breathing mode frequency of approximately 14.5 kHz observed at the nominal 20 A, 6 kW operating condition documented in Butler-Craig et al. [47], which is a reduction of approximately 57% between the two operating points.

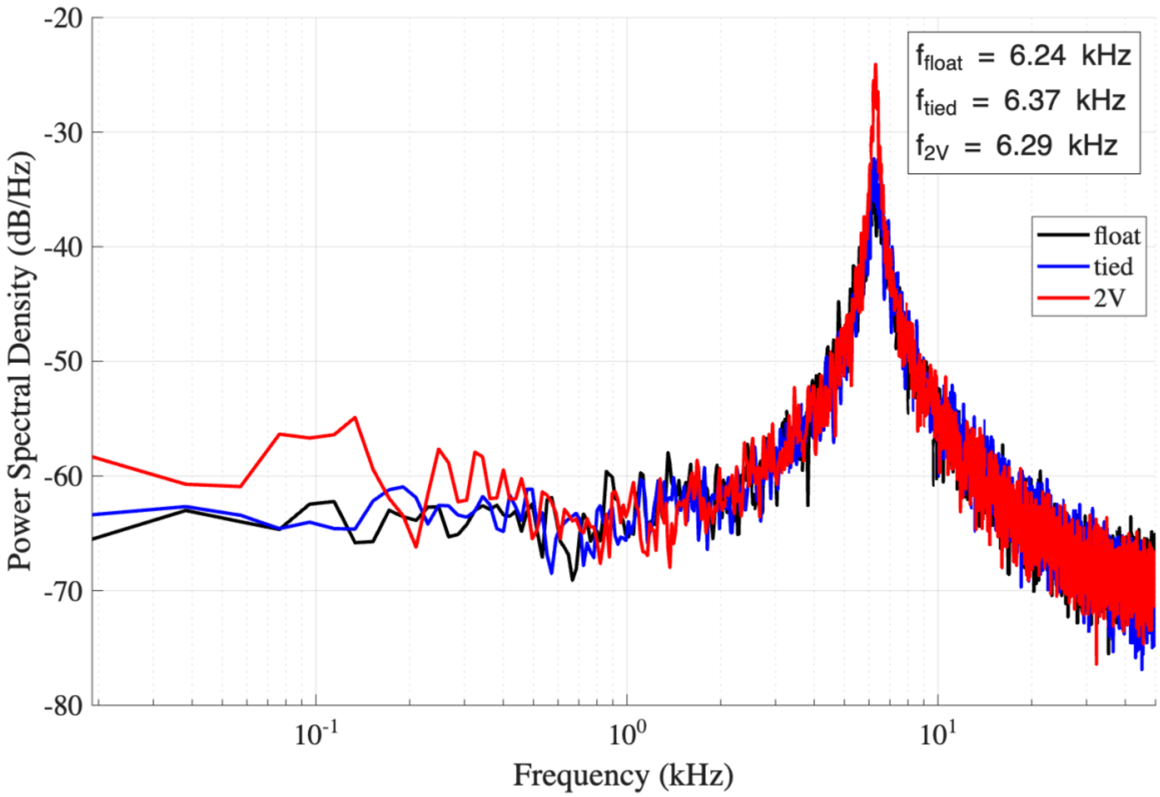

Figure 50: PSD of the I_d of the thruster in three electrical configurations: floating (black), tied (blue), and biased 2 V above ground (red) operating at 150 V, 40 A.

5.1.2.3 Phase II Electron Property Estimation

The following sections present the spatially resolved electron density, temperature, and drift velocity measurements as well as the data processing methods.

Refer to section 2.6.3.1 for the method utilized for electron property estimation.

5.1.2.3.1 Radial Measurement Locations

Figure 51 illustrates the radial measurement locations used in the subsequent plots illustrating the radial variation of electron properties at three axial locations downstream of the thruster exit plane. Six discrete radial stations, labeled L1 through L6, span from the cathode centerline to the discharge channel centerline. L1, cathode centerline data, is presented separately as it has a longer axial scan and in the case of electron density, presents values that eclipse the resolution at the lower density regions. The data labels in the subsequent radial variation plots of electron density, electron temperature, and radial drift velocity correspond to these positions. Here are the definitions for the radial locations.

- L1: Cathode centerline
- L2: Inner side of IFPC
- L3: Mid IFPC
- L4: Outer edge of IFPC
- L5: Inner channel
- L6: Channel centerline

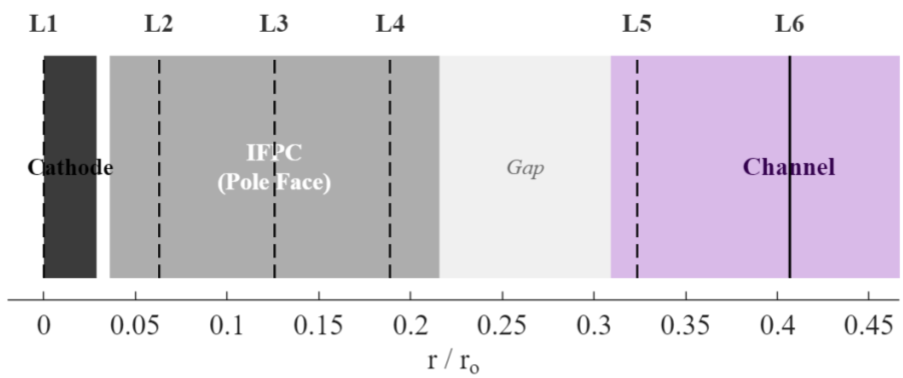

Figure 51: Radial measurement locations L1 through L6 in normalized coordinates r/r_o, spanning from the cathode centerline to the discharge channel centerline. The IFPC (pole face) region is shaded, and dashed lines indicate each measurement station.

5.1.2.3.2 Electron Density

Figure 52 presents spatially-resolved electron density measurements in the cathode plume region of the H9 HET across three body bias configurations (Tied, +2 V, and Float), obtained using laser Thomson scattering. The measurements span the radial range of r/r_o 0.08 to 0.42 and axial range of 0.017 to 0.04, capturing the near-field plasma environment. All three configurations exhibit qualitatively similar electron density distributions, with densities ranging from approximately 10^{18} m^{-3} near the cathode to above 10^{17} m^{-3} at the outer radial positions. In all three cases, n_e is highest near the axis (L1, approximately 10^{19} m^{-3}) and decreases radially outward, consistent with previous measurements by Betancourt et al [1]. A pronounced local density depletion is observed near L4 ($r/r_o \approx 0.18$), most markedly under the +2 V bias condition, where densities fall below 5×10^{16} m^{-3}. The tied and floating cases exhibit qualitatively similar density distributions, with modest differences at L4 and in the outer radial region (L5–L6). The floating-configuration cathode centerline peak density of 6.6×10^{19} m^{-3} is 2.6 × higher than the 2.6×10^{19} m^{-3} value reported by Suazo Betancourt et al. [1] for the same thruster and operating condition at the 0° azimuthal position, attributable to the different azimuthal sampling angle (45° versus 0°). At the channel stations (L5–L6), the present measurements of $5–12 \times 10^{17}$ m^{-3} are consistent with the Suazo Betancourt channel region values when accounting for the different angular slices of the thruster, confirming the same qualitative trend of decreasing n_e with axial and radial distance from the cathode. As in the initial investigation, the cathode centerline electron density and temperature profiles for the three bias configurations coalesce beyond the near-field region, reinforcing the conclusion that body bias effects on the cathode plume are a near-field phenomenon. This convergence is consistent across both operating conditions and both phases of testing.

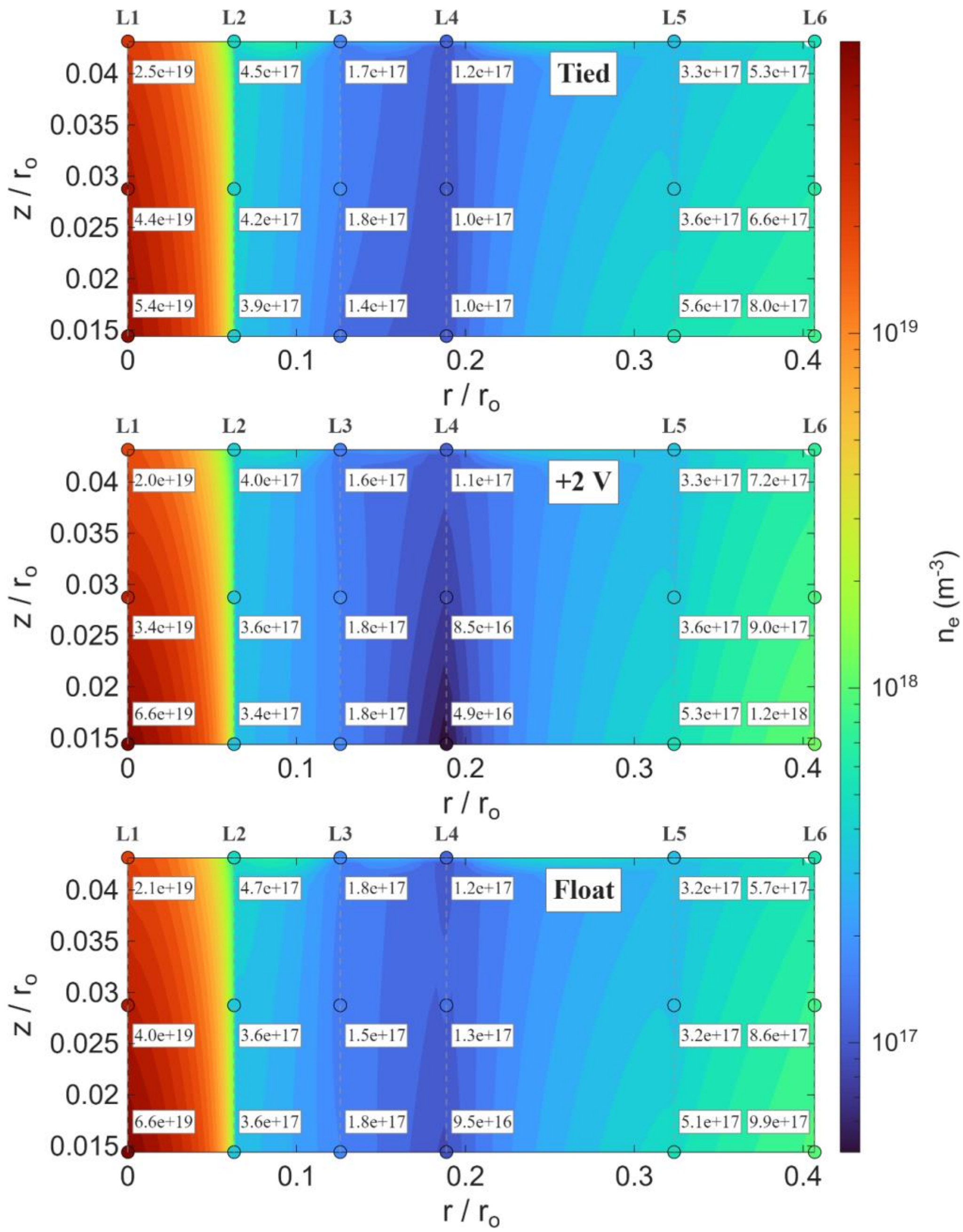

Figure 52: Spatially-resolved electron number density (n_e, m^{-3}) in the near-field region for the Tied (top), +2 V (middle), and Float (bottom) body bias configurations. Thruster operated at 150 V discharge voltage and 40 A discharge current.

The configuration-dependent ordering of cathode-centerline (L1) density observed here is consistent with the trend established in the preliminary study at 300 V and 20 A as shown in Section 3.3.1.1. In that study, the cathode-tied configuration exceeded the floating configuration by approximately 23% and exceeded the grounded configuration by up to 67% at mid-axial positions along the cathode centerline. In the present Phase II measurements at $z/r_0 = 0.025$, the cathode-tied configuration again produces the highest cathode-centerline density at 4.4×10^{19} m^{-3}, followed by floating at 4.0×10^{19} m^{-3} and the +2 V configuration at 3.4×10^{19} m^{-3}. The trend is preserved, though the maximum spread between any two configurations narrows to approximately 26% at the 150 V, 40 A operating condition.

5.1.2.3.3 Electron Temperature

Figure 53 presents spatially-resolved electron temperature measurements across the three body bias configurations (Tied, +2 V, and Float) in the cathode plume region of the H9 HET. All three configurations display qualitatively similar temperature distributions, with electrons ranging from approximately 3–5 eV near the cathode to 25–32 eV at the outer radial positions approaching the discharge channel. The temperature gradient increases with radial distance from the cathode, reflecting the transition from the cathode plume to the higher-energy discharge channel plasma. The Tied and +2 V configurations reach peak temperatures above 30 eV in the outer radial region despite their opposite body current polarities. The Float configuration shows a comparable overall temperature range with different spatial structure in the intermediate region ($r/r_o \approx 0.15$–0.25). A localized cooler region appears in the +2 V and Float configurations near $r/r_o \approx 0.15$–0.20 and $z/r_o \approx 0.025$–0.030, corresponding spatially with the density depression observed in Figure 52. The spatial co-location of these correlated density and temperature depressions across two configurations is noted; quantitative interpretation is deferred to the relative difference analysis in Section 6.2.2.

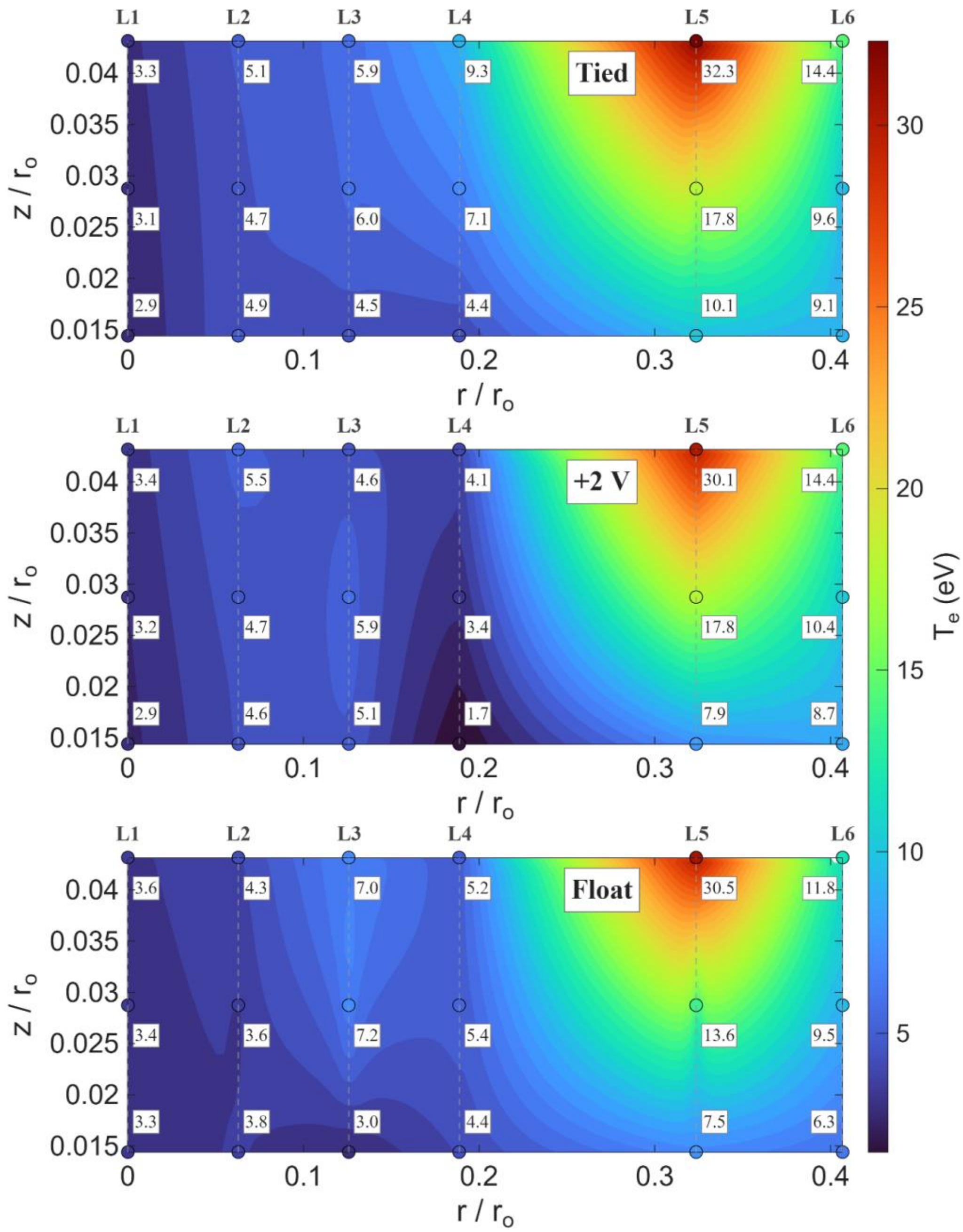

Figure 53: Spatially-resolved electron temperature (T_e, eV) in the near-field region for the Tied (top), +2 V (middle), and Float (bottom) body bias configurations. Thruster operated at 150 V discharge voltage and 40 A discharge current.

The cathode centerline temperatures are consistent with Suazo Betancourt et al. [1], who reported 2–3 eV near the cathode orifice increasing to 5–7 eV by $z/r_o \approx 0.06$–0.08 in the floating configuration at the same operating condition. The present channel station values of 25–32 eV (Float, L5) are consistent with the 25–40 eV range reported in the near-field channel region of the reference work, providing independent validation of the present T_e extraction.

5.1.2.3.4 Radial Electron Drift Velocity

Before reporting the radial electron drift velocity ($V_{drift,r}$) results, two measurement constraints must be noted. First, the spectral resolution of the LTS system limits velocity sensitivity to approximately 18 km/s per detector pixel at 532 nm using the 1200 lines/mm grating corresponding to a reciprocal linear dispersion of approximately 2.55 nm/mm; this sets the practical floor below which radial drift cannot be resolved from the spectral line center. Second, during floating-configuration data acquisition, the LTS instrument function exhibited an asymmetric spectral distortion. Although the processing corrections described in Section 0 attempt to mitigate this effect, the floating-configuration $V_{drift,r}$ results retain a larger systematic uncertainty than those from the biased configurations. The cathode-tied and +2 V drift velocity measurements are therefore the more reliably resolved results in this section.

The radial drift velocity component $V_{drift,r}$ is isolated by orienting the LTS scattering wave vector along the radial direction at the 45° azimuthal measurement position. Negative values indicate radially outward drift toward the discharge channel; positive values indicate radially inward drift toward the cathode centerline.

Figure 54 presents the spatially resolved radial electron drift velocity ($V_{drift,r}$) measured using LTS at the six radial stations (L1–L6) and three axial planes ($z/r_o \approx 0.015$, 0.025, and 0.04) for the three thruster body electrical configurations. Numerical annotations give $V_{drift,r}$ in m/s at each measurement location; arrows indicate the local drift direction, and the background contour is interpolated from these sparse and discrete points. In the Tied and +2 V configurations, the largest magnitudes occur near the channel centerline (L3–L4) at $z/r_o \approx 0.015$, reaching 2.97×10^5 m/s and 1.97×10^5 m/s, respectively, with the midplane ($z/r_o \approx 0.025$) drift directed predominantly inward. The Float configuration reverses this pattern: drift at $z/r_o \approx 0.025$ is directed outward across L3–L6, with magnitudes up to 1.48×10^5 m/s at L5, and the peak at L4, $z/r_o \approx 0.015$ reaches 2.14×10^5 m/s. The outer-radial-station magnitudes of up to 3.5×10^5 m/s (350 km/s) fall within the range reported by Vincent et al. [98], who measured $V_{drift,r}$ along the ISCT200 channel centerline from 2–40 mm downstream and observed values from −500 to +600 km/s depending on operating condition. The primary distinction is that the present measurements span the IFPC region at the 45° azimuthal position rather than the acceleration zone channel centerline. Suazo Betancourt et al. [1] did not report drift velocity measurements in their H9 LTS campaign.

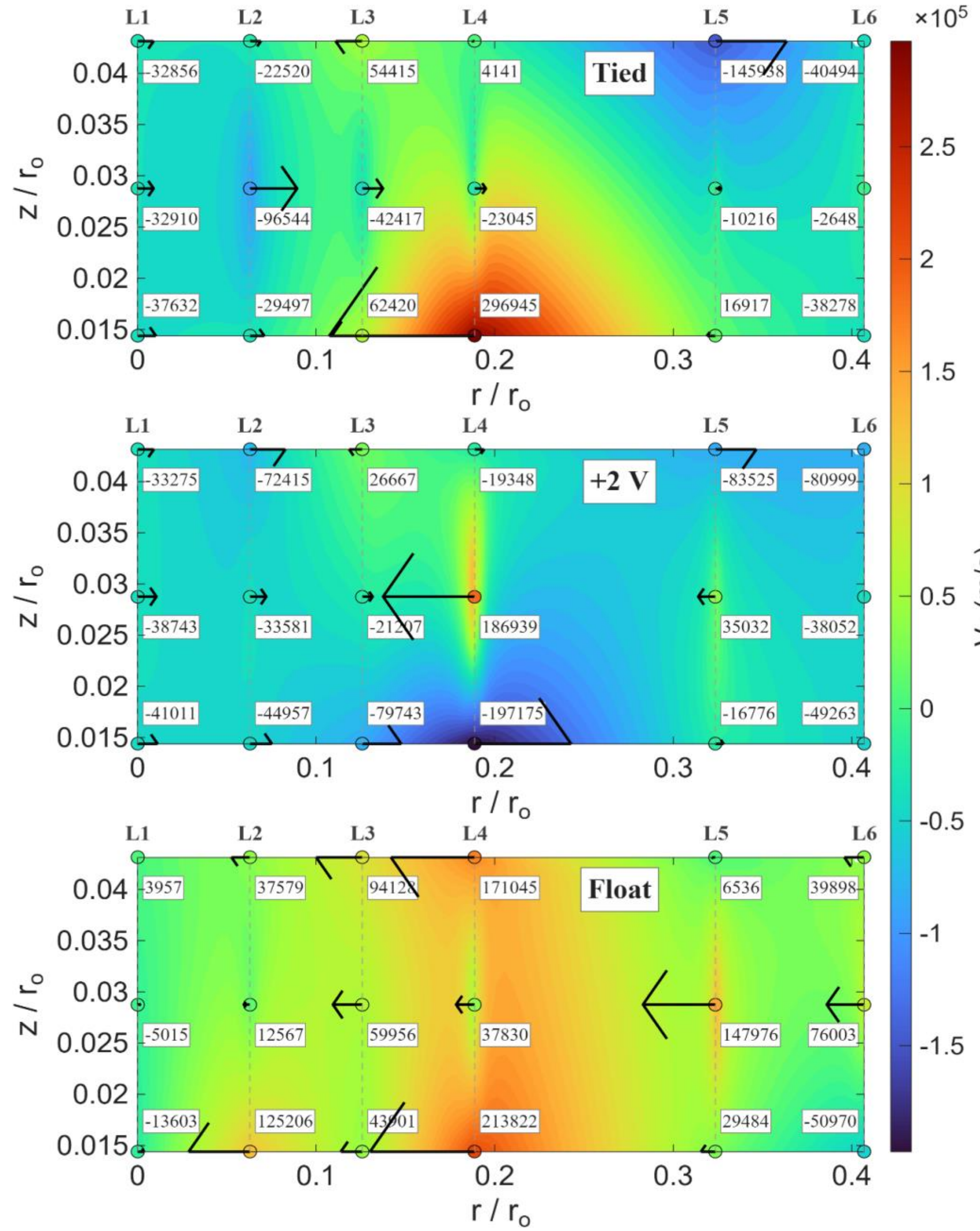

Figure 54: Spatially-resolved radial electron drift velocity ($V_{drift,r}$, km/s) in the near-field region for the Tied (top), +2 V (middle), and Float (bottom) body bias configurations. Positive values indicate radially inward drift toward the cathode centerline; negative

values indicate radially outward drift toward the discharge channel. Thruster operated at 150 V discharge voltage and 40 A discharge current.

5.1.2.3.5 Floating Configuration Data Processing

Unless otherwise stated, electron properties for the cathode-tied, and biased configurations were obtained using the standard LTS analysis procedure described in Chapter 0. In both cases, the measured spectra were convolved with the theoretical instrument function and the method outlined in Section 2.6.3.1. For the floating condition, however, the standard procedure was not sufficient because the measured instrument function exhibited a noticeable asymmetry that deviated from the assumed theoretical shape. To accurately recover the electron properties in this case, the measured spectra were convolved with the measured (rather than theoretical) instrument function and the analysis was repeated using this experimentally determined response.

All floating-configuration results presented in Section 5.1.2.3 were processed using the following corrected method. The floating LTS spectra were analyzed using a forward convolution fitting procedure to extract T_e , V_d, and n_e. The standard approach for LTS analysis, as described in Section 2.6.3.1, employs a theoretical IF based on the assumption that the spectrometer's spectral response can be approximated as a Gaussian profile with width determined by the FWHM of the system. The theoretical spectral redistribution function for a drifting Maxwellian plasma convolved with a Gaussian instrument function is given by:

$$f_{conv}(\lambda) = A \cdot \exp\left[-\frac{(v-V_d)^2}{2(k_B T_e/m_e)}\right] \otimes IF_{theory} + bg \qquad \text{Equation 41}$$

where the drifting Maxwellian is expressed in velocity space and mapped to wavelength space by using the transformation in Step 2 before convolution, and the theoretical instrument function is:

$$IF_{theory}(\lambda) = \frac{1}{\sqrt{2\pi\sigma_{IF}}} \exp\left[\frac{-1}{2}\left(\frac{\lambda-\lambda_0}{\sigma_{IF}}\right)^2\right] \qquad \text{Equation 42}$$

with $\sigma_{IF} = \frac{\tau}{2\sqrt{2\ln(2)}}$ where τ is the system FWHM.

However, periodic validation of the spectrometer's instrument function through Raman scattering measurements revealed that the measured IF deviated from the ideal Gaussian profile for the first half of the floating portion of the experimental campaign. Specifically, Raman calibration scans acquired on October 7, 2025 (10/07) exhibited asymmetric instrument functions with broadened wings and irregular peak shapes. After background subtraction, this structure was substantially reduced, but a pronounced asymmetry persisted, as shown in Figure 55. The IF measured on 10/07 showed noticeable asymmetry and departure from the theoretical IF (red dashed line).

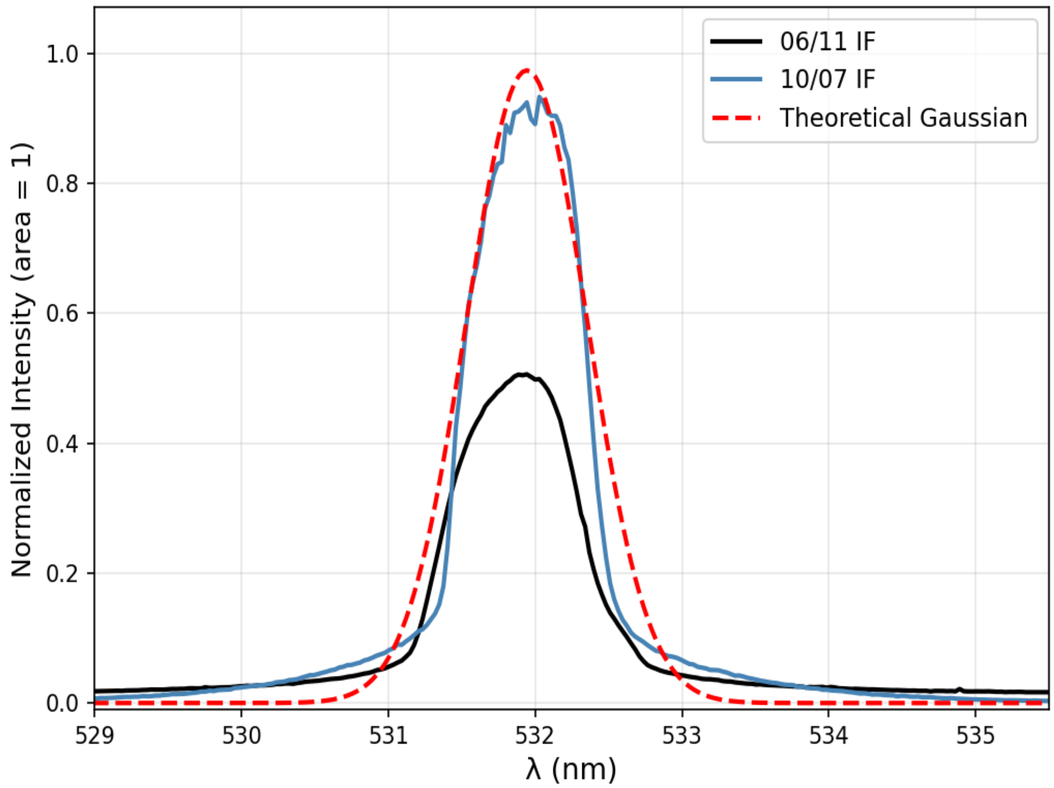

Figure 55: Instrument function comparison.

This asymmetry in the measured IF manifested as anomalous spectral features in the Thomson scattering data itself. Initial analysis of several spectral acquisitions revealed an unusual broadening centered around the laser line wavelength ($\lambda_0 \approx 532$ nm) that was inconsistent with expected plasma physics. Upon comparing these suspect spectra with the measured instrument function from the same experimental session, it was observed that the measured IF exhibited the same asymmetric character observed in the anomalous

Thomson spectra, indicating that spectrometer optical alignment or internal stray light conditions had shifted from their nominal calibrated state. The anomaly spontaneously repaired on its own before the source of the abnormality could be identified. Concurrent with this IF stabilization, the Thomson signal at the cathode centerline increased from approximately 35,000 counts to the previously acquired 45,000 counts at the same spatial location and operating condition, confirming improved optical throughput. The author postulates that this was a result of the thermal stabilization of the optics after extended operation, including the thermal stabilization of the focusing lens by way of a chiller with a 10 °C coolant temperature.

However, to account for this, the following forward convolution approach using the measured instrument function was implemented for all data acquired during periods when the measured IF deviated from theoretical predictions. The affected data were acquired while in the floating configuration. The measured IF was acquired by way of acquiring in a location with strong reflections and dropping the Bragg-Notch filters. The analysis procedure consisted of the following steps:

1. The measured instrument function was loaded from the corresponding calibration file. It was then normalized to unit area and recentered at the laser line wavelength λ_0 to ensure proper alignment with the Thomson spectrum.
2. A theoretical drifting Maxwellian Thomson spectrum was generated in velocity space based on the scattering geometry, then mapped to wavelength space

following the standard transformation: $\nu = \frac{c(\lambda - \lambda_0)}{\lambda_0 \cos\frac{\theta}{2}}$, where θ is the scattering angle and c is the speed of light.

3. The isolated Thomson spectrum was convolved with the measured instrument function on the same wavelength sampling grid: $S_{\text{model}}(\lambda) = S_{\text{theory}}(\nu \to \lambda) \otimes IF_{\text{measured}}(\lambda) + bg$. This forward convolution inherently accounts for the actual spectral broadening and asymmetry introduced by the spectrometer hardware.
4. Model parameters [A, V_d, T_e , n_e] were optimized using MATLAB's `lsqcurvefit` function with the Levenberg-Marquardt algorithm [99] to minimize the residual between the measured Thomson spectrum and the forward-convolved model.
5. Electron density was computed from the fitted A using the calibrated Raman scattering cross-section relationship [Section 2.6.3.1] with propagated uncertainties.

The following presents a comparison between fits using the theoretical IF (Figure 56) and the measured IF (Figure 57) for a representative condition. Although the theoretical IF fit appears to track the data points more closely, this visual agreement is misleading because the symmetric theoretical IF cannot account for the instrumental asymmetry, so the fitting algorithm is forced to compensate by distorting the physical parameters. This produces artificial agreement with the data and yields incorrect physics. The measured IF forward convolution fit (right) properly separates instrumental effects from plasma physics by way of convolution with the measured data, allowing the asymmetric instrument response to be captured in the instrument function rather than incorrectly absorbed into the velocity distribution parameters. While the measured IF fit may show slightly larger residuals, these residuals are random rather than systematic, and the extracted physical parameters are physically meaningful. For data acquired when the measured IF was symmetric and matched theoretical expectations, the standard theoretical IF approach was employed as described in Section 2.6.3.1, allowing for computational efficiency without loss of accuracy.

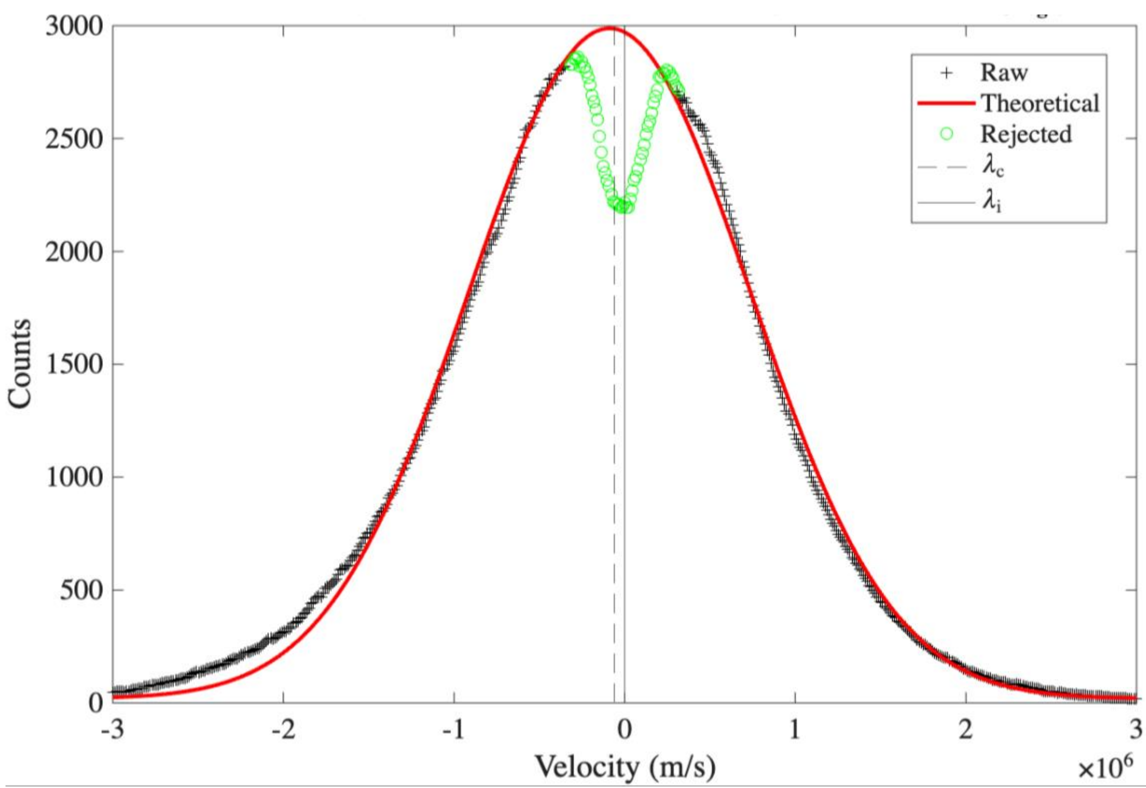

Figure 56: Data processing on affected data using convolution with the theoretical IF.

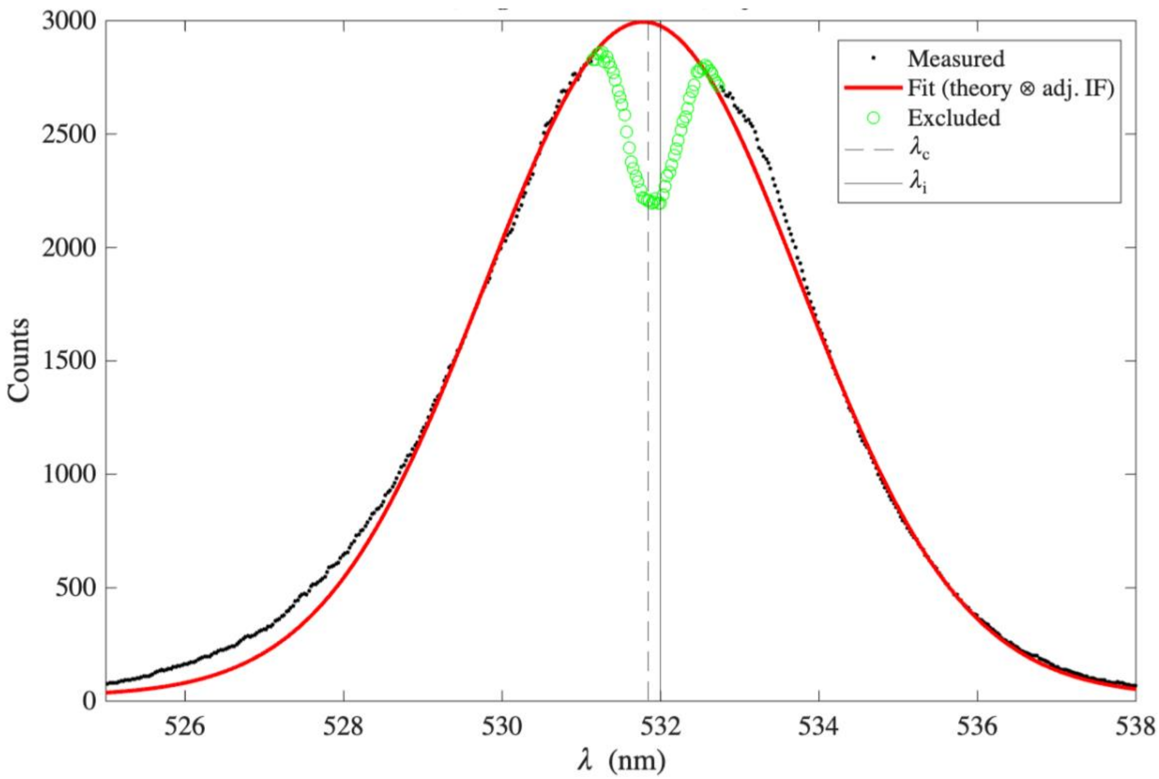

Figure 57: Data processing on affected data using convolution with the measured IF.

CHAPTER 6: DISCUSSION

This chapter uses the data presented in Chapter 5 to answer the central dissertation question posed in Chapter 1:

> Does varying the thruster body bias affect the electron behavior in the near-field of a magnetically-shielded Hall effect thruster?

The answer is yes. The argument proceeds in three parts. First, Phase I current collection measurements at the electrically isolated IFPC demonstrate that net electron flux to the thruster body surfaces varies monotonically with applied bias voltage. This result follows from the foundational principle that the current collected by a surface immersed in plasma is governed by the local electron density, electron temperature, and the potential difference between the surface and the surrounding plasma [100]. Because the IFPC geometry and plasma-facing area are fixed, changes in the collected current require changes in at least one of these local plasma quantities. Second, spatially resolved laser Thomson scattering measurements of electron density, temperature, and radial drift velocity across three electrical configurations (Float, Tied, and +2 V) localize where and how the electron population redistributes in response to each imposed boundary condition. Third, the radial electron current density $J_{e,r}$, computed from the measured density and drift velocity, provides direct evidence of configuration-dependent electron transport pathways in the near-field.

6.1 Local Electron Current Collection at the Inner Front Pole Cover

6.1.1 Observed Changes in Collected Current

Phase I employed the electrically isolated IFPC as a current collection probe while scanning the applied IFPC bias from 0.5 V to 2.0 V above ground at the 300 V, 20 A operating condition. Figure 58 presents the current collected by both the IFPC (green) and the thruster body (red) as a function of IFPC bias voltage. The thruster body current varies from approximately −0.58 A at 0.5 V to −0.75 A at 2.0 V, while the IFPC current ranges from approximately +0.04 A to 0.0 A over the same range. Linear fits to the raw current-voltage data yield slopes of −0.088 A/V ($R^2 = 0.93$) for the thruster body current and −0.020 A/V ($R^2 = 0.95$) for the IFPC current. Both currents exhibit a monotonic trend with increasing bias, with the thruster body collecting increasingly negative (electron) current as the IFPC bias increases, and the IFPC current decreasing correspondingly toward zero. This anticorrelated behavior suggests a redistribution of collected current between the two surfaces rather than a net change in total current to the thruster.

The high R^2 values and apparent linearity of the I-V traces initially motivated a semi-logarithmic analysis to determine whether the current-voltage behavior could be interpreted within the framework of Langmuir probe theory, in which a linear relationship between ln(I) and applied voltage in the electron retardation region enables extraction of the electron temperature [Merlino, 2007; Chen, 2003]. However, the 1.5 V bias range explored here is far narrower than the gap between the applied surface potentials and the estimated plasma potential (~20 V relative to ground at this operating condition), making it insufficient to traverse the retardation region or to meaningfully identify the collection regime. A broader voltage sweep extending through the plasma potential would be required for such analysis..

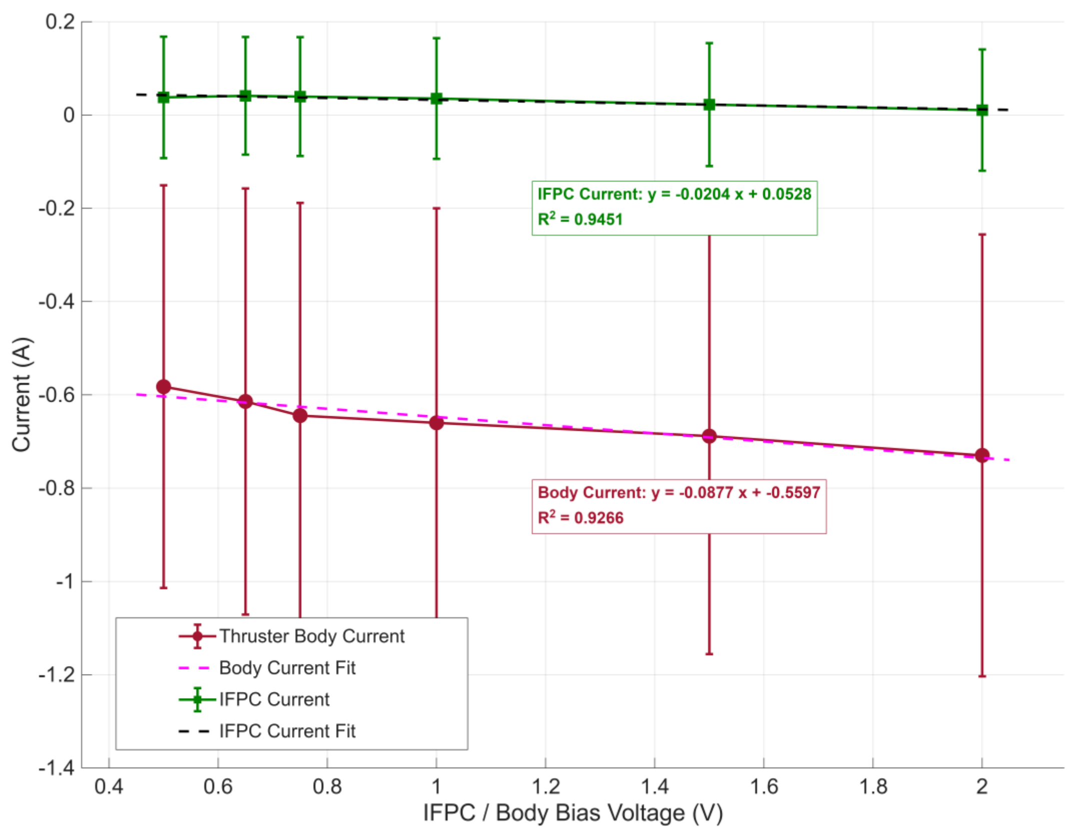

Figure 58: Phase I collected current by the isolated IFPC (green) and thruster body (red) as a function of mean body bias voltage at 300 V, 20 A. Linear fits with R^2 values are shown.

6.1.2 Implications for the Near-Field Plasma

The systematic increase in collected electron current with increasing body bias voltage demonstrates that even small changes in the body potential (spanning 1.5 V total) measurably alter the net particle flux to both the IFPC and thruster body surfaces. Both the IFPC and thruster body respond with increasingly negative current with increasing positive bias, confirming that the effect is systematic.

This establishes first-order evidence that the answer to the thesis question is affirmative: varying the thruster body bias does affect electron behavior in the near field. When the electrical boundary condition at the body surface is changed, the amount of electron current that can be collected changes in a predictable fashion. This motivates the spatially resolved investigation in the following sections.

It is noted that the Phase I current collection sweep was performed at 300 V, 20 A, while the Phase II LTS measurements were obtained at 150 V, 40 A. The three Phase II configurations (Float at approximately −2 V, Tied at −10 V, and +2 V relative to ground) span a much wider voltage range (approximately 12 V) than the Phase I sweep (1.5 V). Direct quantitative comparison of collected currents between the two phases is not possible due to the different operating conditions and the different bias ranges. However, the Phase I data establishes the principle that body bias systematically modulates electron collection, providing physical context for interpreting the configuration-dependent differences observed in Phase II.

6.2 Spatially Resolved Near-Field Electron Behavior

This section presents the Phase II spatially resolved electron measurements and their physical interpretation. Before examining configuration-dependent differences in electron properties, Section 6.2.1 first establishes that electrons are magnetized throughout the measurement domain which a necessary prerequisite for interpreting the kinematic measurements that follow. The subsequent subsections characterize how electron density, temperature, pressure, and radial drift velocity each respond to the three body bias configurations across the cathode centerline, IFPC pole region, and discharge channel, building toward an integrated picture of near-field electron pathways under each electrical boundary condition.

6.2.1 Electron Magnetization in the Measurement Domain

Before interpreting the spatial distribution of electron properties, it is necessary to establish that electrons are magnetized throughout the measurement domain. The primary magnetization criterion is the normalized electron gyroradius r_{ce}/r_o, the electron gyroradius normalized by the channel outer radius. Electrons are considered magnetized when $r_{ce}/r_o \ll 1$, meaning electron gyro-orbits are tightly confined relative to the characteristic scale of the thruster geometry. The Hall parameter $\Omega_e = \omega_{ce}/\nu_{ei} \gg 1$ provides supplementary confirmation that electron–ion collisions are rare relative to the cyclotron frequency, further establishing that the magnetic field governs electron motion rather than collisional diffusion.

Figure 59 presents the normalized electron gyroradius r_{ce}/r_o computed at every measurement location using the measured electron temperature and the known magnetic field strength from simulation. At typical conditions in the measurement domain ($T_e \approx 3$ eV, $B/B_{max} \approx 0.02$–0.06), r_{ce}/w_{chan} ranges from approximately 0.03 to 0.10 across all measurement locations. The largest gyroradii occur near downstream axial locations in the discharge channel, where the electron temperature is highest; even there, r_{ce}/w_{chan} remains below 1, confirming that electron gyro-orbits are confined to a small fraction of the thruster's outer radius throughout the entire domain. The Hall parameter, computed from the same measured quantities, ranges from approximately 10–50 at the outermost stations to greater than 10^3 near the channel, exceeding unity everywhere and providing supplementary confirmation of magnetization.

The gyroradius criterion is satisfied throughout the entire measurement domain: r_{ce}/r_o remains well below 0.1 at every measurement location, confirming that electron gyro-orbits are tightly confined relative to the thruster outer radius. The Hall parameter $\Omega_e \gg 1$ everywhere provides supplementary confirmation. Together, these results establish that the magnetic field topology governs electron motion throughout the measurement domain which makes trends in the electron radial drift velocity difficult to resolve.

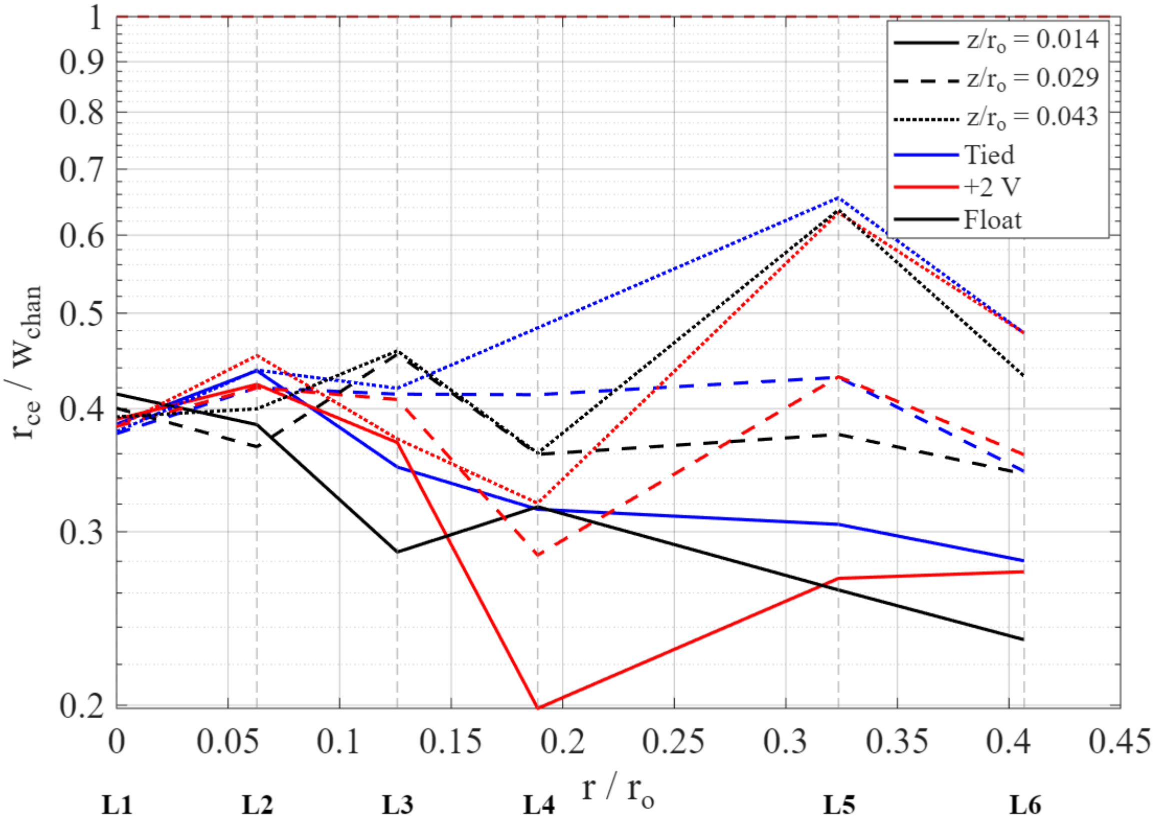

Figure 59: Normalized gyroradius r_{ce}/w_{chan} as a function of radial location shown for all three configurations at three axial stations (z/r_o = 0.014, 0.029, and 0.043). Labels 1-6 indicate radial measurement locations.

6.2.2 Relative Difference Analysis

This section presents the configuration-dependent differences in n_e, T_e, and $V_{drift,r}$ analyzed by spatial region: the cathode centerline ($r/r_o = 0$), the pole/IFPC region (r/r_o = 0.13–0.25; L2–L4), and the discharge channel ($r/r_o > 0.30$; L5–L6). Differences are reported only where they exceed the measurement uncertainty. The following data are presented as line plots rather than contour maps (Section 5.1.2.3) because the sparse measurement grid makes configuration-dependent differences easier to resolve in this format.

6.2.2.1 Electron Density

Figure 60 presents the cathode centerline electron density as a function of z/r_o for all three configurations. All three show decreasing n_e with axial distance. Configuration differences outside measurement uncertainty are confined to $z/r_o \approx 0.03$–0.08. At z/r_o = 0.015, the floating and +2 V configurations produce equal cathode-centerline densities of approximately 6.65×10^{19} m^{-3}, while the cathode-tied configuration is approximately 18% lower at 5.45×10^{19} m^{-3}. Moving downstream to z/r_o = 0.025, the ordering reverses: the cathode-tied configuration produces the highest cathode-centerline density at 4.4×10^{19} m^{-3}, followed by floating at 4.0×10^{19} m^{-3} and the +2 V configuration at 3.5×10^{19} m^{-3}, a spread of approximately 26%. At z/r_o = 0.040, the cathode-tied configuration remains highest at 2.45×10^{19} m^{-3} while floating and +2 V are equal at approximately 2.05×10^{19} m^{-3}, roughly 19% lower.

The density inversion at the nearest cathode axial station in the cathode-tied configuration, where tied exhibits the lowest density before crossing over to the highest density at subsequent stations, is reproduced from the initial investigation at 300 V, 20 A to the Phase II data at 150 V, 40 A and does not appear in the floating or +2 V configurations. In the cathode-tied configuration, the inner front pole cover, cathode body, and cathode orifice are all held at the same electrical potential, forming a set of concentric equipotential surfaces. The keeper face, however, floats to its own potential relative to the cathode body. This geometry may produce an unusual near-orifice potential landscape in which the floating keeper introduces a local potential hill or radial electric field structure between the orifice exit and the surrounding equipotential surfaces, depressing the local electron density at the closest measurement station. The mechanism has not been isolated, but the configuration specificity and cross-campaign reproducibility point to the tied-configuration potential topology rather than a diagnostic artifact.

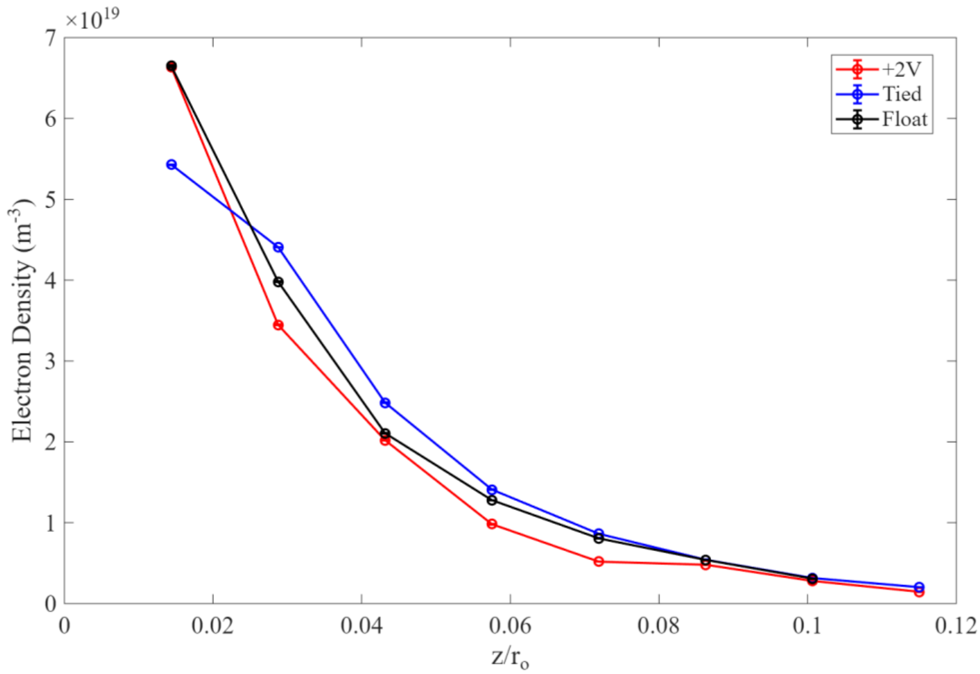

Figure 60: Cathode centerline (r = 0) electron density as a function of normalized axial distance z/r_o for the Float (black), Tied (blue), and +2 V (red) body bias configurations. The H9 was operated at 150 V discharge voltage and 40 A discharge current.

Figure 61 presents the radial profiles at three axial stations, excluding the cathode centerline, on a logarithmic scale to resolve the differences in the pole region. Figure 62 presents the radial n_e profiles at three axial stations excluding the cathode centerline on a linear scale to resolve the differences in the channel region. At all stations, density falls by approximately two orders of magnitude from L2 to a minimum near L4 (outer IFPC face), then recovers by one order of magnitude toward L5–L6 (channel region).

Configuration-dependent differences outside measurement uncertainty are observed only at $z/r_o = 0.014$ in the pole region (L4): the +2 V configuration is a factor of 2–3 below Float and Tied at this station. And at channel centerline, the +2 V configuration has the highest n_e, followed by the floating configuration, with the cathode-tied configuration presenting the lowest n_e. At $z/r_o = 0.043$, all three configurations overlap within error bars at every radial station, indicating that body bias has no resolvable effect on the radial n_e distribution beyond the $z/r_o = 0.029$ axial measurement plane.

The pronounced electron density depletion at L4 in the +2 V configuration warrants particular attention. L4 sits at the outer edge of the inner front pole cover, where the magnetic field topology transitions from the closed field lines threading the IFPC to the open field lines of the discharge channel. This transition region, the magnetic separatrix, features field lines that connect the inner and outer front pole covers across the channel. In the +2 V configuration, the body potential is the least negative relative to the local plasma potential of the three configurations tested, producing the shallowest electron-repelling sheath at the pole surface. Electrons confined along the separatrix field lines, which have a direct magnetic line of sight to the IFPC, encounter the weakest sheath barrier in this configuration and are therefore most readily collected at the body surface. This produces the observed density depletion, which is most severe at the closest axial station where the field line curvature is tightest and proximity to the body surface is greatest. The coincident depression of electron temperature at L4 is consistent with energy-selective collection: the reduced sheath barrier in the +2 V case permits a broader portion of the electron energy distribution to reach the surface, depleting the population and lowering both density and temperature simultaneously. This separatrix-mediated depletion mechanism is unique to the +2 V configuration because it is the only tested case in which the sheath barrier is sufficiently shallow for substantial electron collection along field lines with a direct line of sight to the pole surface. Resolving whether this localized depletion modifies beam divergence through electrostatic lensing at the channel boundary would require higher spatial resolution measurements tracing individual field lines through the separatrix region.

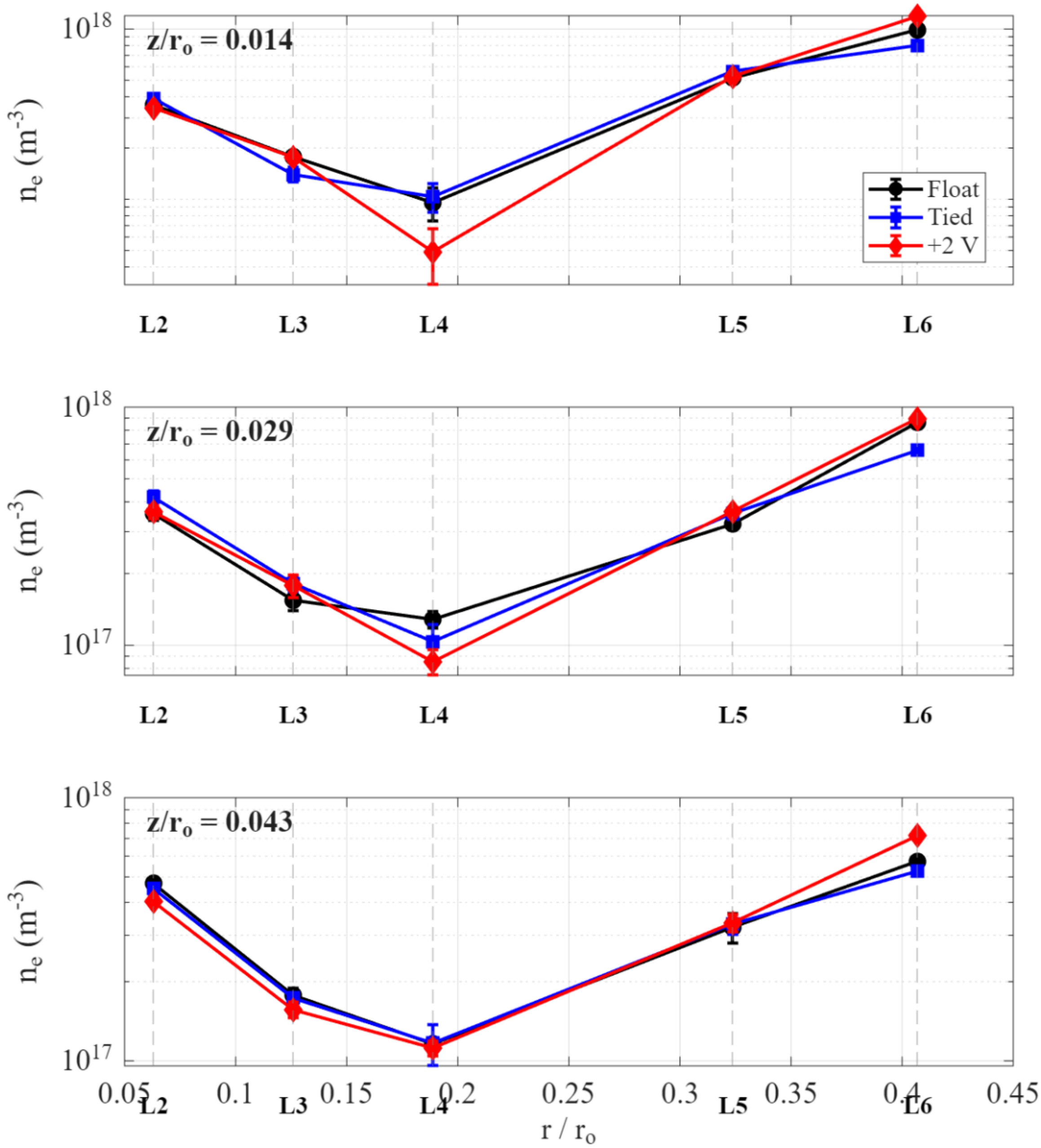

Figure 61: Electron density as a function of radial position on a logarithmic scale to resolve differences in pole region at three axial stations (z/r_o = 0.014, 0.029, and 0.043) for the Float (black), Tied (blue), and +2 V (red) body bias configurations. Radial stations

L1–L6 are indicated. The H9 was operated at 150 V discharge voltage and 40 A discharge current.

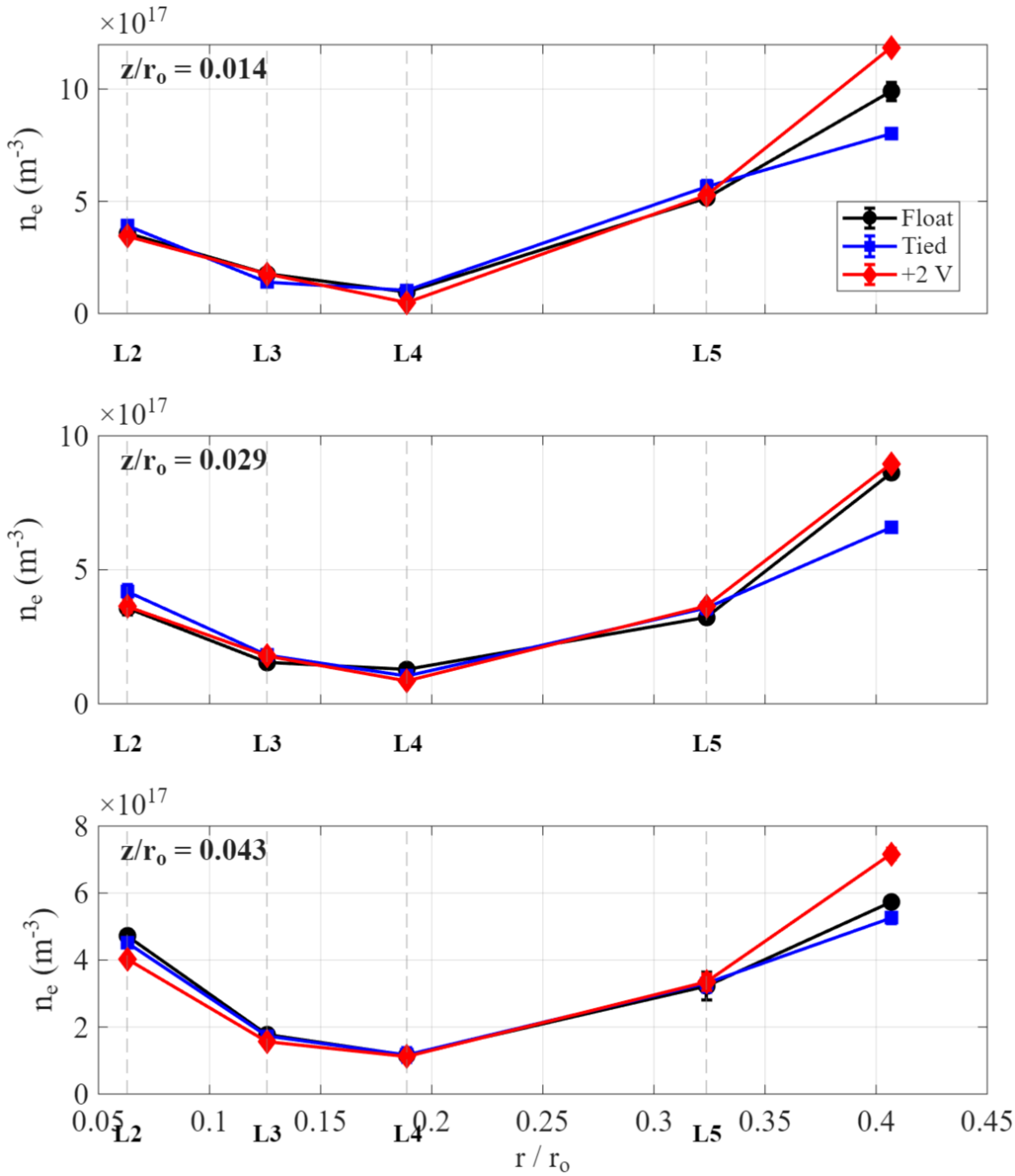

Figure 62: Electron density as a function of radial position on a linear scale to resolve differences in channel region at three axial stations (z/r_o = 0.014, 0.029, and 0.043) for

the Float (black), Tied (blue), and +2 V (red) body bias configurations. Radial stations L1– L6 are indicated. The H9 was operated at 150 V discharge voltage and 40 A discharge current.

The cathode-tied configuration produces the highest cathode-centerline density but the lowest channel-centerline density; the +2 V configuration produces the opposite. At z/r_0 = 0.025, the cathode-tied configuration exhibits a cathode-centerline density of 4.4×10^{19} m^{-3} and a channel-centerline density of 6.6×10^{17} m^{-3}, a factor of approximately 67× across the measurement domain, while the +2 V configuration shows a cathode-centerline density of 3.4×10^{19} m^{-3} and a channel-centerline density of 9.0×10^{17} m^{-3}, a shallower gradient of approximately 38×. The floating configuration occupies an intermediate density magnitude at both locations, with values of 4.0×10^{19} m^{-3} and 8.6×10^{17} m^{-3} respectively (~47×). This spatial inversion, a steeper cathode-to-channel gradient in the tied case and a flatter one in the +2 V case, reflects the redistribution of electrons in response to the differing electrical boundary conditions at the thruster body, as is developed in Section 6.2.3.

6.2.3 Configuration-Dependent Electron Pathways

The relative property differences described in Section 6.2.2.1, interpreted through the circuit topology of each configuration, define distinct electron transport pathways through the near field. Figure 63 presents the mean discharge current and thruster body current across all three Phase II configurations, establishing the global current balance context for the pathway analysis in the following subsections. Each data point represents an independent thruster electrical configuration, and the values are time-averaged from the telemetry presented in Section 5.1.2.1. This campaign was conducted at fixed anode and cathode mass flow rates.

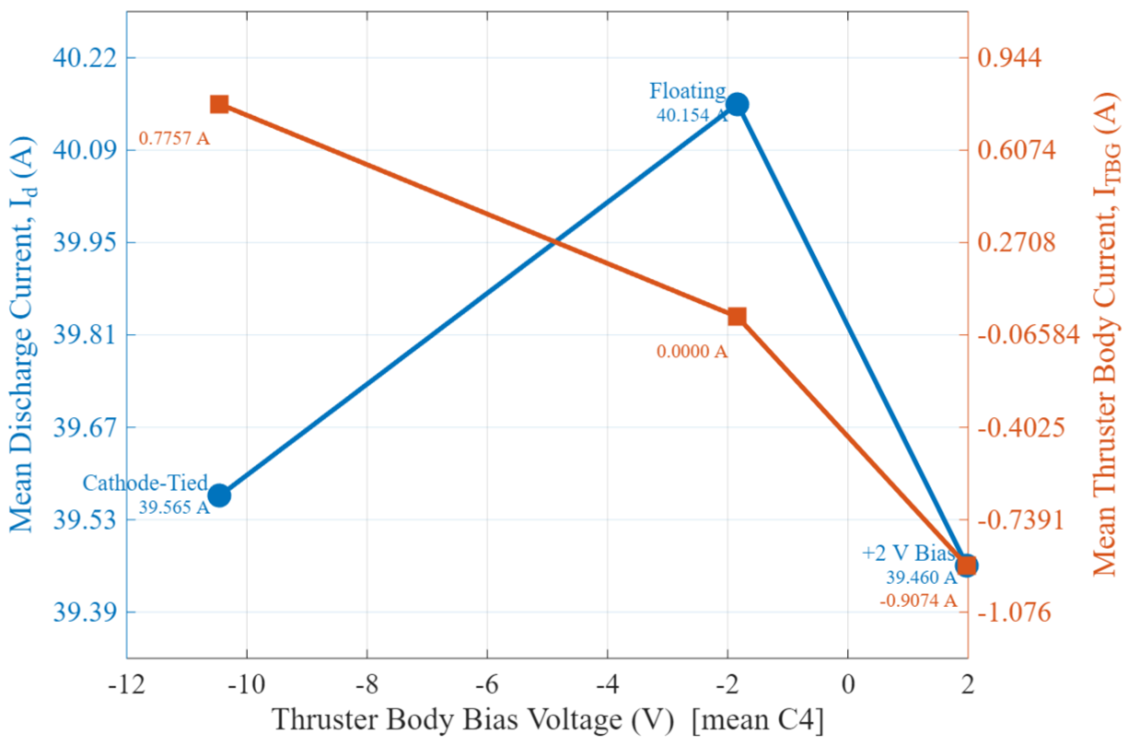

Figure 63: Phase II mean discharge current (blue, left axis) and mean thruster body current (orange, right axis) as a function of thruster body bias voltage for the three configurations operating at 150 V, 40 A.

This section interprets the configuration-dependent spatial electron property differences identified in Section 6.2.2.1 through the lens of each configuration's circuit topology. Throughout this section, the floating configuration is treated as the nominal baseline, that is the state in which the thruster body imposes no active boundary condition on the discharge. Figure 68 establishes the global current balance: each configuration produces a distinct combination of discharge current and thruster body current, reflecting the available electron collection pathways at the body surface. The following subsections examine each configuration in turn, linking the measured spatial distributions of electron density, temperature, and drift velocity to the transport pathway implied by the circuit topology.

The cathode-tied configuration, where the cathode and thruster body-to-ground voltages were equal and averaged approximately −10.3 V, presents an average discharge current of approximately 39.6 A and a thruster body current of approximately +0.78 A. The +2 V bias configuration presents an average discharge current of approximately 39.5 A and a thruster body current of approximately −0.90 A. In both biased configurations, the discharge current is reduced by approximately 0.5–0.6 A relative to the floating baseline of 40.1 A, yet the mechanism by which the discharge self-adjusts differs. In the cathode-tied case, the reduction is circuit-level: the body is electrically connected to the cathode, sharing the same electrical node (the cathode node, which is the common point connecting the negative terminal of the discharge supply, the cathode neutralizer, and, in this configuration, the thruster body chassis). The body, therefore, shares the cathode node with the discharge supply, so the +0.78 A collected at the body surface completes the circuit through the external body-to-cathode connection rather than through the full plasma transport pathway. The charge is returned to the shared node through the wire, but the cathode must emit additional electrons to meet the combined discharge and body collection demand. In the +2 V case, the body circuit is electrically independent of the discharge loop, so the reduction instead occurs at the plasma level: the positively-biased body intercepts approximately 0.85 A of electrons from the discharge plasma before they complete the cathode-to-anode transport cycle, and the discharge current self-adjusts downward at fixed mass flow rate to reflect this loss. This behavior is consistent with the findings of Peterson et al. [30], who operated the HERMeS thruster at fixed discharge current and observed that the floating configuration required less propellant mass flow than the grounded configuration to sustain the same discharge current which was a result they attributed to the floating configuration having lower current utilization efficiency. In Peterson's framework, “leakage current” is the electron current that flows from the cathode, through the plasma, to the anode without having contributed to ionization of a propellant neutral along the way. Specifically, electrons that close the discharge circuit without being consumed in an ionization event. A configuration with lower current utilization efficiency could therefore appear to carry a larger fraction of its discharge current through this non-ionizing pathway. However, Peterson did not directly measure ion production rates; his result reflects how current is tracked in the discharge circuit, not a direct measurement of ionization. At fixed mass flow rate, as in this study, a higher floating-configuration discharge current is consistent with more electrons completing the circuit consistent with Peterson's framework characterizing this as lower apparent current utilization efficiency. When an electrical connection to the body is introduced, whether through the cathode electrical connection or through an independent bias circuit, a portion of those electrons is intercepted or redirected through the body pathway, reducing the net discharge current measured on the anode line.

Although body current collection might appear to reduce cathode workload by offloading a portion of the discharge current demand, the data indicate otherwise. In the cathode-tied configuration, the cathode must increase its total emission to service both the discharge and body collection demand simultaneously, as the shared cathode node requires current for both paths. In the +2 V configuration, the body intercepts electrons that have already entered the discharge plasma, so the cathode emission adjusts only to the self-reduced discharge demand rather than being relieved of an emission obligation. In neither case does body current collection reduce the fundamental cathode emission requirement; instead, it redistributes where the emitted electrons ultimately terminate within the circuit.

6.2.3.1 Modified Electron Pathways

The circuit topologies described above predict distinct spatial distributions in the near-field electron density, and the measurements in Section 6.2.2 confirm them directly. In the cathode-tied configuration, the cathode node services both the discharge and body neutralization paths. The electrons needed to neutralize ion impingement on the body are provided through cathode-thruster body electrical connection, not through the plasma. However, the shared node means fewer electrons complete the full discharge transit to the anode, reducing the electron density at the channel that should close the discharge circuit. At the same time, the cathode drives increased emission to meet the combined current demand, elevating electron density along the cathode centerline. In the +2 V configuration, the body draws directly from the plasma near the thruster exit plane (including the IFPC), reducing the cathode-region electron population, while the independent discharge loop leaves the electron pathway for closing the discharge circuit intact. This elevated channel electron density is consistent with what the framework of Peterson et al. [30] would predict for a configuration in which fewer electrons close the circuit through non-ionizing pathways, though this reflects a circuit interpretation, not a direct measurement of ionization rates. In the floating configuration, with no externally imposed electron collection pathway active at the body surface in either region, there are no additional loss mechanisms active on either pathway, and electron densities remain intermediate across both regions. The result is a clear spatial inversion between the two biased configurations: cathode-tied is increased at the cathode centerline and depleted at the channel, +2 V, the opposite, which is a direct reflection of where each circuit topology draws from and where it leaves the electron population undisturbed.

6.2.3.1.1 Cathode-tied Configuration

In the cathode-tied configuration shown in Figure 64, the thruster body is electrically connected to the cathode common node, placing it at approximately −10.3 V relative to facility ground. At this potential, the body lies below the local plasma potential by approximately the cathode coupling voltage, attracting low-energy charge-exchange (CEX) ions from the near-field plume. The measured body current of +0.78 A (approximately 2% of the 40 A discharge current) represents this net CEX ion collection. These ions are neutralized at the body surface by electrons sourced through the tie wire from the cathode common node. Because the body shares the cathode node with the discharge supply, the thruster body is a participant in the discharge current loop: the cathode supplies electrons for both the primary discharge path (denoted as the discharge circuit pathway, e_{DC}^-) and the body neutralization path through the node, and the total current drawn from the cathode node is $I_D + I_{TBG} \approx 39.6 + 0.78 = 40.4$ A. This shared-node topology is consistent with the cathode-tied behavior reported by Peterson et al. [30] for the HERMeS thruster, where sustained body currents were collected. The attribution of that collected current to CEX ion collection at the cathode-potential body surface is a unique feature of this work but is supported by the erosion by CEX ion that happens as a result of negative potential on the body relative to the plasma [71].

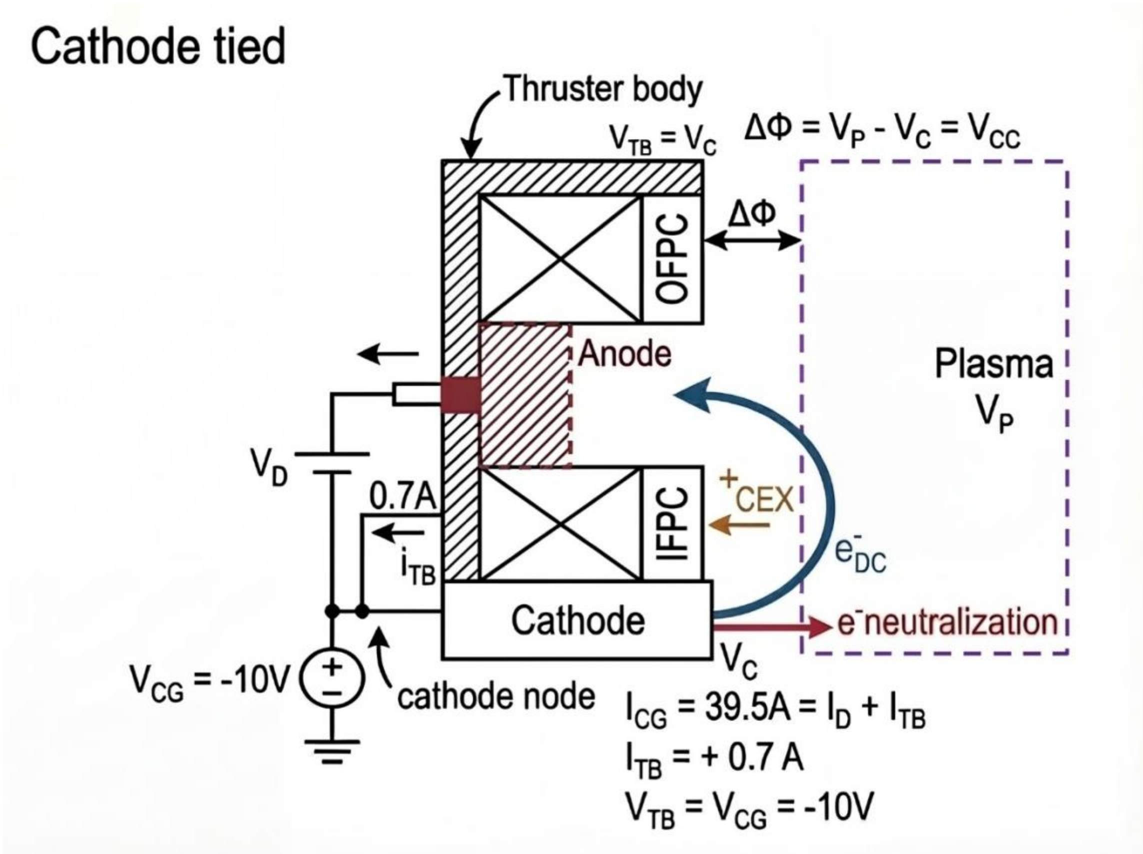

Figure 64: Circuit pathway diagram for the cathode-tied body bias configuration. The thruster body is connected to the cathode node (the common electrical point connecting the negative terminal of the discharge supply, the cathode neutralizer, and the thruster body chassis) at approximately −10.3 V relative to facility ground. CEX ions are attracted to the body; electrons are supplied from the cathode node to neutralize them. I_D denotes the discharge current.

6.2.3.1.2 +2 V Bias Configuration

In the +2 V bias configuration shown in Figure 65, the thruster body is connected to an external bias supply referenced to facility ground and is electrically isolated from the cathode node. At +2 V relative to ground, the body sits at a negative potential relative to the surrounding plasma, drawing electrons from the near-field plasma through body pathways denoted by e_B^-. The measured body current of −0.90 A represents this net electron collection. These electrons flow through the body and through the external bias supply to facility ground, completing a circuit loop that is entirely independent of the discharge circuit: the cathode node and discharge power supply play no role in this pathway. The +2 V configuration, therefore, operates two independent circuit loops: the discharge loop (e_{DC}^-) and the bias loop (plasma to body to ground, e_B^-). The body current therefore operates independently of the discharge current. The approximately 0.6 A reduction in discharge current from the approximately 40.1 A setpoint occurs because the body intercepts electrons from the plasma and cathode that would otherwise complete the cathode-to-anode pathway, diverting them through the bias supply before they reach the anode. Those electrons are then effectively returned to the plasma environment through neutralization of the ion current hitting the grounded facility surfaces, like the chamber wall. The +2 V bias loop is therefore a ground-test artifact as opposed to a result of any specific thruster body bias relative to ground that could not be replicated in space.

An additional consequence of the +2 V body potential is modification of the sheath character at the pole cover surfaces. Because the body is biased positively relative to ground but remains negative relative to the local plasma potential, the resulting sheath is weakly electron-repelling. Relative to the floating and cathode-tied configurations, this represents the shallowest electron-repelling barrier at the pole surfaces, which simultaneously produces the strongest ion-repelling component. An ion-repelling sheath at the inner and outer front pole covers could, in principle, redirect low-energy ions away from these surfaces and toward the channel centerline, effectively focusing the beam and concentrating plasma density in the discharge channel. This mechanism would be consistent with the elevated channel electron density observed in the +2 V configuration. However, this hypothesis is tempered by observations from long-duration wear testing, where IFPC erosion striation patterns exhibited minimal sensitivity to background pressure variations that are known to alter beam divergence angles. If beam focusing were the dominant driver of ion flux to the IFPC, erosion patterns would be expected to correlate with divergence changes, which was not observed. The density redistribution measured in the +2 V configuration may therefore reflect local sheath-driven transport effects at the pole surfaces rather than a global change in beam divergence geometry.

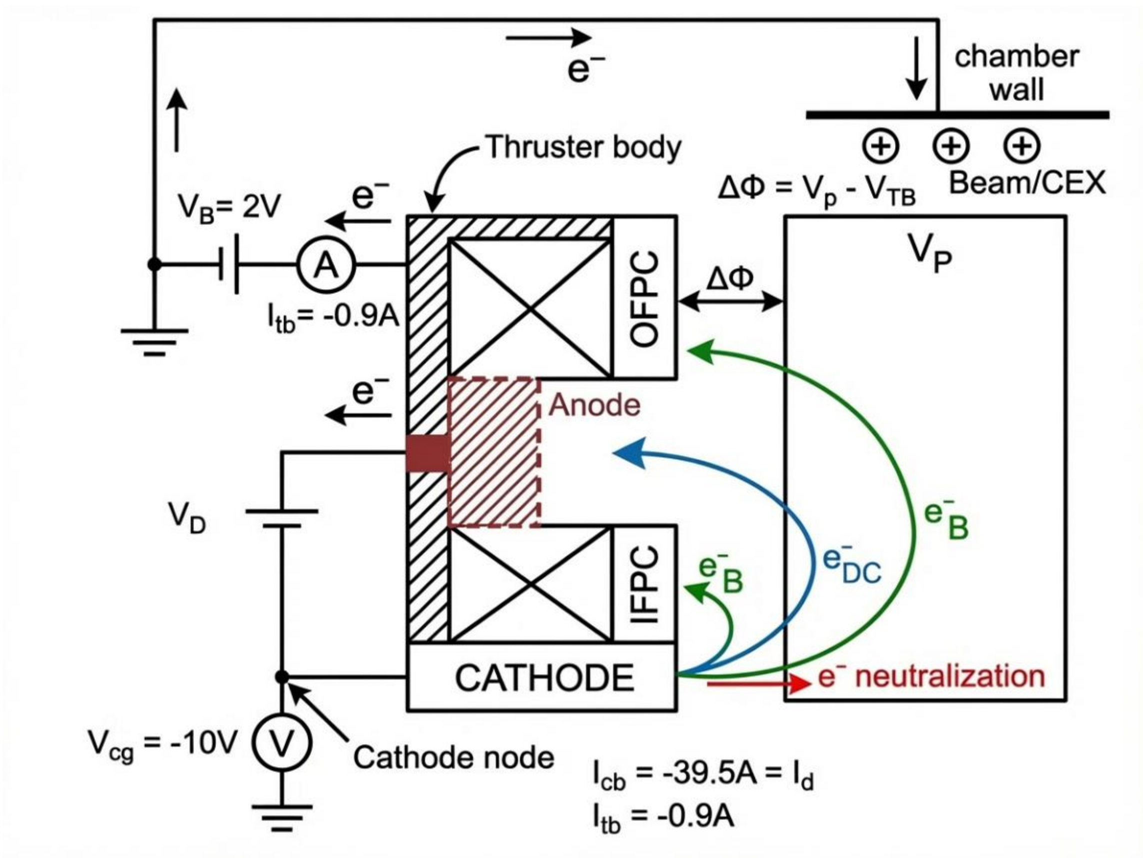

Figure 65: Circuit pathway diagram for the +2 V body bias configuration. The thruster body is connected to an external supply at +2 V relative to facility ground, electrically isolated from the cathode node. At this potential, the body is modestly negative relative to the local plasma potential, drawing net electron current from the near-field plasma. I_D denotes the discharge current.

6.2.3.1.3 Floating Configuration

In the floating configuration, as shown in Figure 66, the thruster body is electrically isolated and reaches a self-consistent floating potential (approximately −2 V relative to ground) at which the electron and ion fluxes to the body surface balance, producing zero net current. Although electron and ion fluxes to the body surface are always present, no external circuit pathway connects the body to the discharge supply or cathode node so the floating potential adjusts so that these fluxes balance without any net current flowing through an external connection. The discharge operates in its baseline unperturbed state, with the 40.1 A discharge current flowing uninterrupted between cathode and anode.

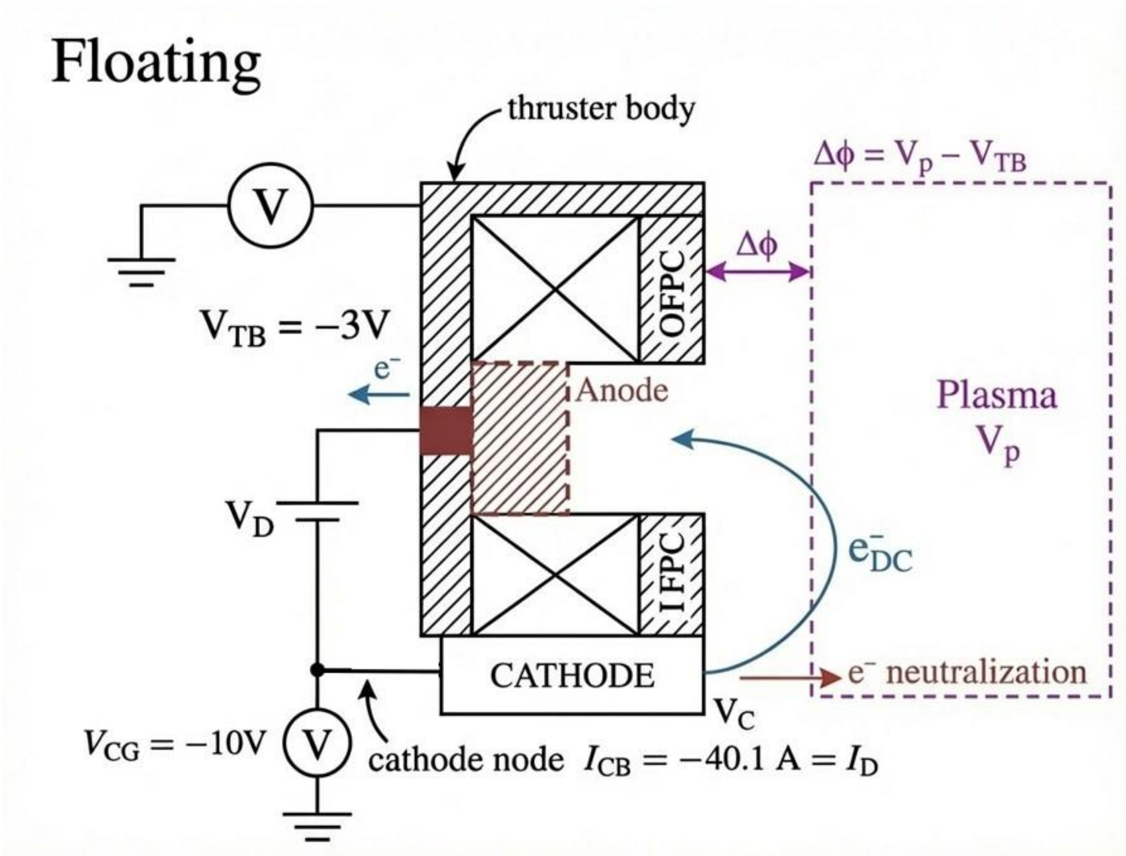

Figure 66: Circuit pathway diagram for the floating body bias configuration. The thruster body is electrically isolated with no external circuit connection. I_D denotes the discharge current flowing uninterrupted between cathode and anode.

With no externally imposed collection pathway active at the body surface, electrons in the IFPC vicinity are not actively drawn from the discharge circuit away by a bias circuit.

The local electron density near the pole in the floating configuration matches the cathode-tied magnitude, both exceeding the +2 V result, consistent with a longer effective electron residence time in the pole region, compared to the +2 V case, in the absence of an external body collection pathway.

The central finding across all three configurations is that body bias effects on near-field electron behavior are spatially and circuit dependent. In the cathode region ($r/r_o \lesssim 0.13$), the cathode-tied configuration elevates n_e by 25–50% relative to the other configurations in the intermediate near-field, reflecting the direct connection between body CEX ion collection and cathode-node electron supply. In the channel region ($r/r_o > 0.30$), the trend inverts. These distinct spatial signatures arise from the distinct circuit topologies described above and cannot be explained by body voltage alone.

6.2.4 Electron Temperature

Figure 67 presents the cathode centerline electron temperature as a function of z/r_o for all three configurations. Near the cathode orifice ($z/r_o \approx 0.015$), the floating configuration is 0.35–0.4 eV (12–14%) above Tied and +2 V (3.3 eV versus 2.85–2.95 eV). Across $z/r_o \approx$ 0.04–0.06, all three profiles converge within a 0.4 eV band near 3.5–3.75 eV, within measurement uncertainty. Beyond $z/r_o \approx 0.06$, Tied and +2 V exceed Float by up to 0.9 eV (16%) at $z/r_o \approx 0.10$. Compared to the electron temperature results reported in Section 3.3.1.2 where all electrical configurations exhibited the same downstream trend, the clear deviation of the float configuration suggests that the measurements were impacted by the asymmetric instrument function as opposed to a result of a physical mechanism introduced by the floating circuit.

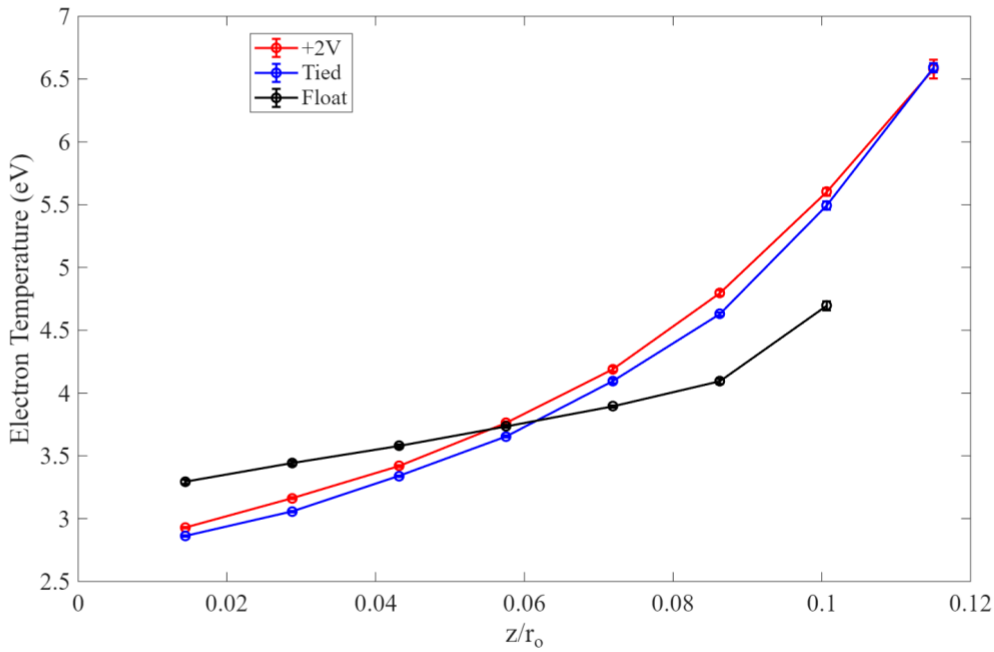

Figure 67: Cathode centerline (r = 0) electron temperature as a function of normalized axial distance z/r_o for the Float (black), Tied (blue), and +2 V (red) body bias configurations. The H9 was operated at 150 V discharge voltage and 40 A discharge current.

Figure 68 presents the radial electron temperature variation at three axial stations. T_e increases with radial distance from cathode to channel at all stations. At $z/r_o = 0.014$, differences across configurations are within 2 eV at all locations and are not consistently outside measurement uncertainty. At z/r_o = 0.029, the primary outside-uncertainty difference occurs at L5: Tied and +2 V both measure 17–18 eV versus 13.5 eV for Float, a deficit of 3.5–4.5 eV. At z/r_o = 0.043, this spread widens to 5–7 eV across L5–L6 (25–32 eV range). The most spatially reproducible configuration-dependent T_e signature is the +2 V depression at L4, which shows 2–3 eV across all axial stations versus 4.5–7 eV for Float and Tied.

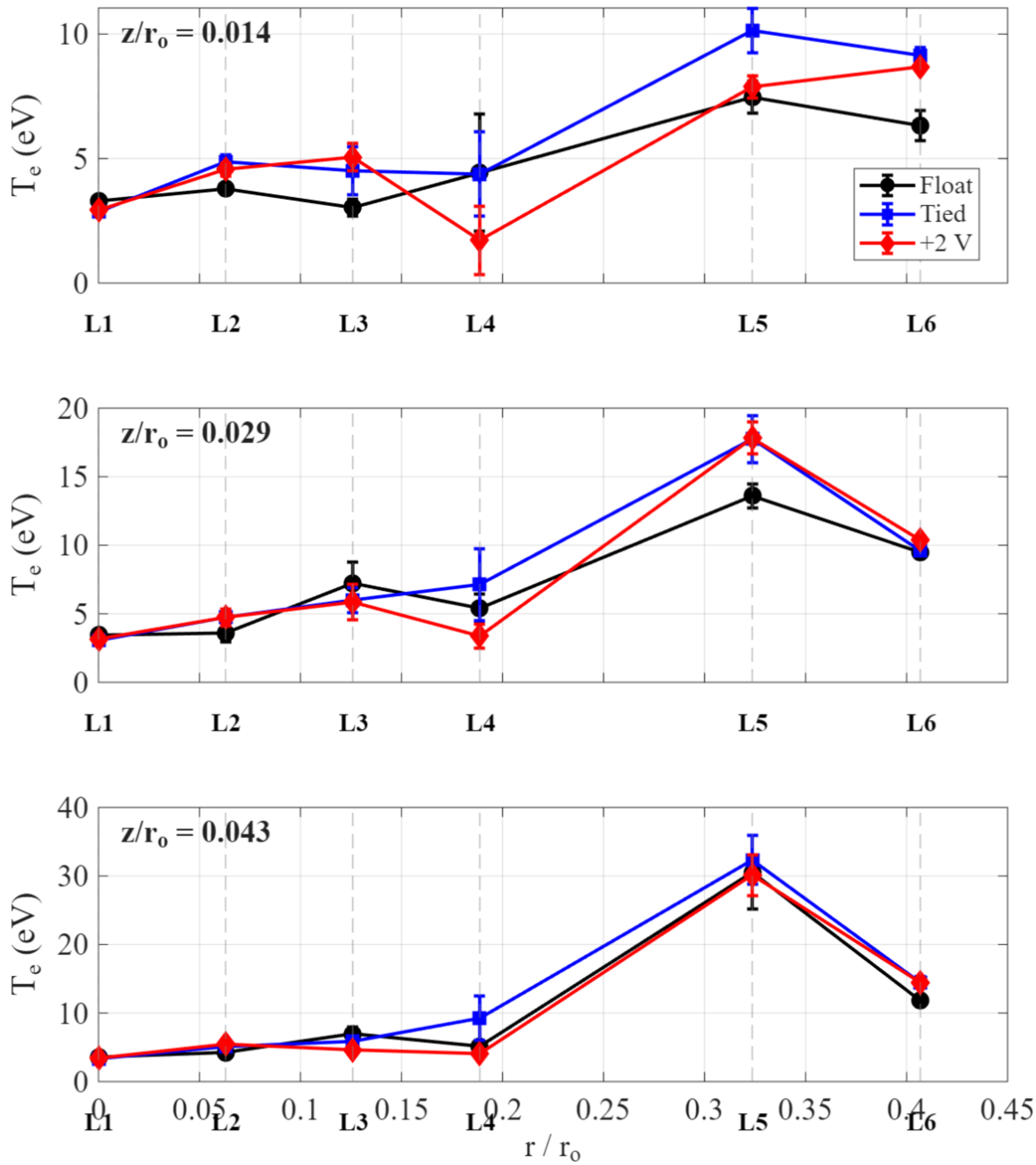

Figure 68: Electron temperature as a function of radial position at three axial stations (z/r_o = 0.014, 0.029, and 0.043) for the Float (black), Tied (blue), and +2 V (red) body bias

configurations. Radial stations L1–L6 are indicated. The H9 was operated at 150 V discharge voltage and 40 A discharge current.

Although the majority of configuration-dependent electron temperature differences fell within or near measurement uncertainty, the trends that are present are consistent with the modified electron pathway mechanism. The +2 V configuration in particular consistently demonstrates the lowest electron temperature across the pole region (L4) at all three axial stations.

This is physically consistent with selective electron absorption at the body surface. Only electrons with sufficient energy to overcome the repelling body sheath potential reach and are collected by the IFPC. This preferentially depletes the high-energy tail of the electron energy distribution, thereby reducing the average temperature measured in that region.

The floating-case electron temperature at the IFPC-adjacent locations L2–L4 is approximately 3.8 eV. Combined with the measured floating body potential of 1.35 V, the local plasma potential is estimated at approximately 21.4 V. The fraction of a Maxwellian EVDF with sufficient energy to reach the body is given by $F = \exp(-\Delta V/T_e)$. For the cathode-tied configuration, ΔV is approximately 31.7 V, yielding $F \approx 0.02\%$. For the +2 V bias case, ΔV is approximately 19.4 V, yielding $F \approx 0.6\%$. The substantially lower collection fraction in the cathode-tied case is consistent with its much deeper potential below V_p. These estimates apply specifically to electrons in the near-IFPC measurement volume at L2–L4, as circumferential body locations with differing plasma environments may exhibit distinct collection characteristics.

This energy-selective collection mechanism is distinct from the circuit-level effects seen in the cathode-tied configuration and represents the body acting as a partial energy filter in the +2 V bias case.

The electron temperature and bulk drift velocity measurements reported here are five-minute time averages acquired over many breathing mode cycles. Time-averaging over a non-Maxwellian EVDF that oscillates at the breathing mode frequency can produce a Gaussian-appearing photon count distribution even when the instantaneous distribution is non-Maxwellian. The second-order EVDF moments, electron pressure and temperature, are particularly susceptible to this effect because they involve the integral of velocity squared times the distribution function, introducing a nonlinear correlation term that does not vanish under time averaging. Consequently, the reported T_e values represent the time-averaged total energy (static plus dynamic pressure) divided by the time-averaged density, which may overestimate or underestimate the instantaneous thermal temperature depending on the oscillation amplitude and phase. This limitation does not invalidate the configuration-dependent trends, which are observed consistently across all measurement locations, but it does constrain the quantitative interpretation of absolute T_e values in the near field where oscillatory behavior is most pronounced.

Time-resolved near-field plume measurements by Lobbia [101] demonstrated that the breathing mode drives large-amplitude oscillations in electron density while electron temperature remains comparatively stable over the oscillation cycle. This decoupling between density and temperature oscillations has implications for interpreting the present time-averaged LTS data: the reported electron density values represent the mean over many breathing cycles and may mask oscillatory structure, but the electron temperature values are less susceptible to this averaging effect. If the breathing mode amplitude is configuration-dependent, as suggested by the PSD analysis in the preliminary data, the time-averaged density at a given location could be biased differently across configurations, though the direction and magnitude of such bias cannot be determined without time-resolved diagnostics. Future time-resolved LTS implementations at matched operating conditions would enable direct assessment of whether configuration-dependent oscillatory electron behavior exists that is obscured in the present dataset.

To directly assess whether the configuration-dependent oscillation characteristics correlate with the observed electron temperature differences, the peak breathing mode PSD amplitude for each configuration was compared against the mean electron temperature at each radial measurement location, averaged across the three axial stations presented in Figure 69.

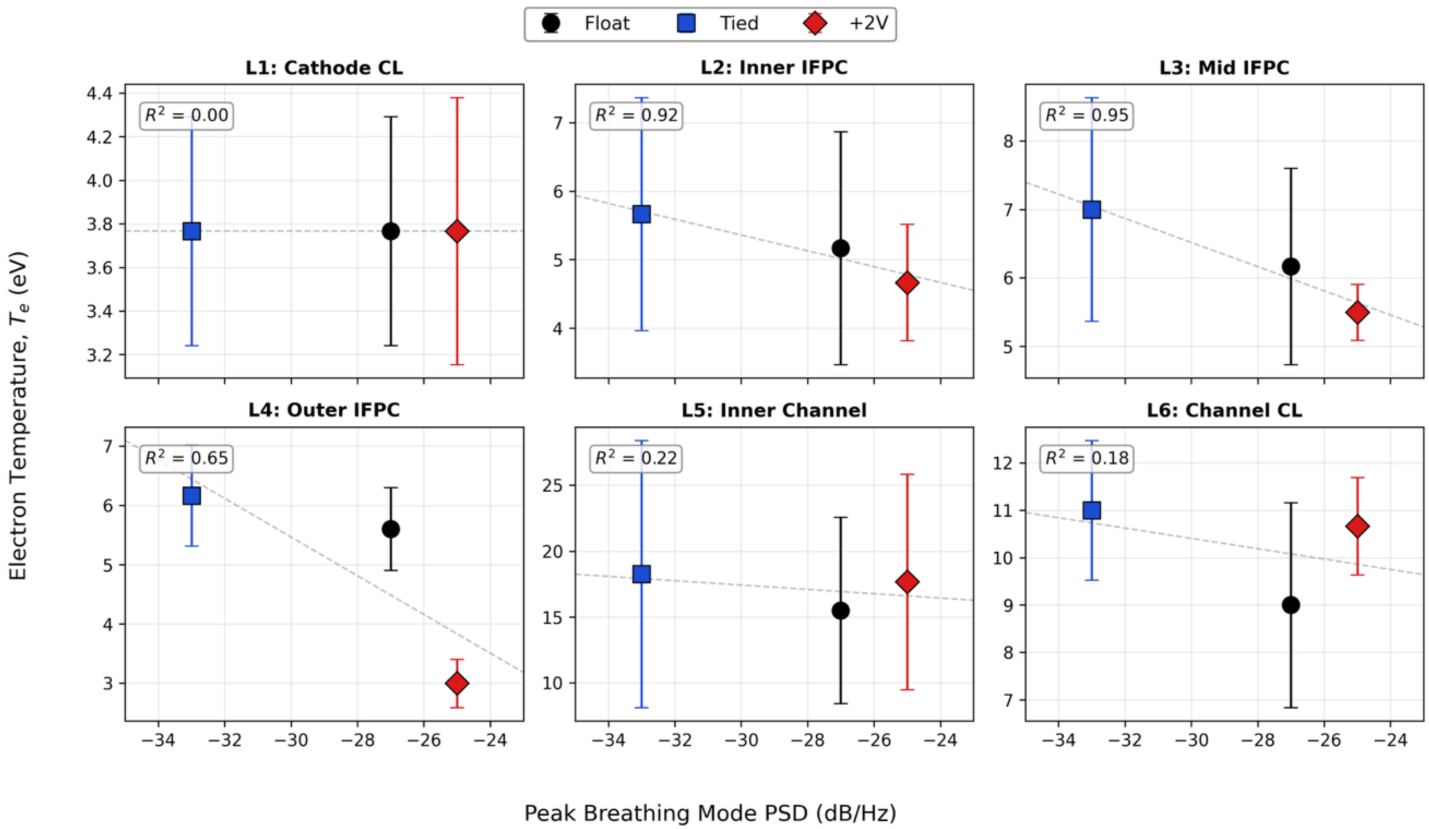

Figure 69: Electron temperature and peak oscillation frequency correlation plots for each of the electrical configurations at radial measurement locations L1-6.

The peak PSD values at the breathing mode frequency are approximately -25 dB/Hz (+2 V), -27 dB/Hz (Float), and -33 dB/Hz (Tied), indicating that the +2 V configuration exhibits the strongest discharge current oscillations while the Tied configuration exhibits the weakest. If oscillation-induced broadening of the electron energy distribution dominated the time-averaged electron temperature differences, a positive correlation between oscillation amplitude and electron temperature would be expected. At the IFPC locations (L2, L3, L4), the correlation is strong but negative (R-squared > 0.65): the +2 V configuration, despite having the strongest oscillations, consistently exhibits the lowest electron temperature. This effect is most pronounced at L4, where the +2 V electron temperature depression of 2-3 eV persists across all axial stations. At the cathode centerline (L1), no correlation exists (R-squared approximately 0). At the channel locations (L5, L6), the correlation is weak (R-squared < 0.25) with large scatter. These results indicate that the configuration-dependent electron temperature signatures observed in this work are not primarily attributable to oscillation-induced measurement bias. The spatial structure of the differences is instead consistent with the distinct electron transport pathways imposed by each configuration's circuit topology, as discussed in Section 6.2.3.

6.2.5 Electron Pressure: Measurements and Limitations as a Potential Proxy

The electron pressure is computed at every measurement location from the directly measured density and temperature. It was initially hoped that electron pressure could serve as a proxy for local potential structure and thereby confirm the presence of a potential well at the IFPC that could drive ion impingement thereon. Figure 70 presents the radial electron pressure profiles at three axial stations. At all stations, P_e reaches a minimum in the IFPC region ($r/r_o \approx 0.15$–0.20) and increases monotonically toward the channel centerline, consistent with the transition from the low-density, moderate-temperature pole region to the high-density, high-temperature channel plasma.

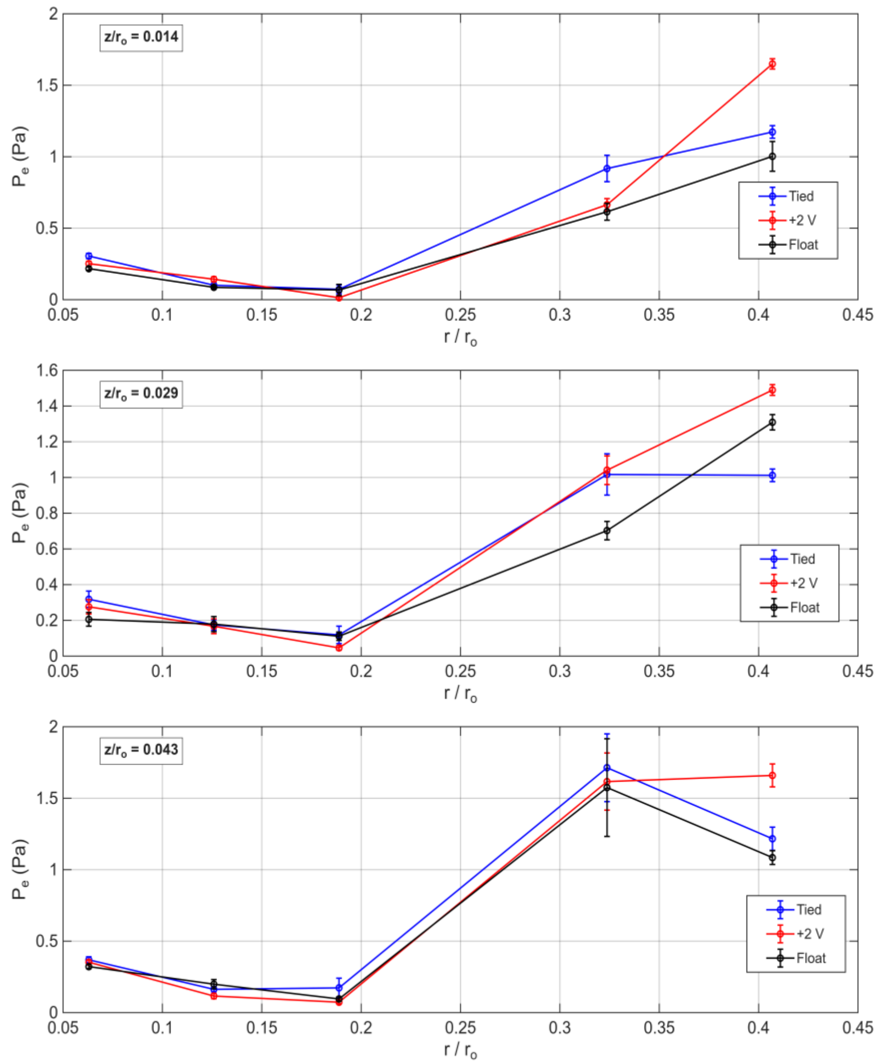

Figure 70: Electron pressure as a function of radial position for three axial stations for the Tied (blue), +2 V (red), and Float (black) configurations.

Figure 71 compares the present Float-configuration electron pressure profile at $z/r_o \approx 0.043$ with reference measurements by Suazo Betancourt et al. [1] at $z/r_o = 0.040$ in the same H9 thruster at the same operating condition (150 V, 40 A) but at the 0° azimuthal position. The qualitative agreement is strong: both datasets show a pressure minimum in the IFPC region with monotonically increasing pressure toward the channel centerline. The lack of perfect quantitative agreement could be attributed to the potential azimuthal asymmetry. However, the order of magnitude agreement provides confidence in the pressure measurements and confirms the presence of a radial pressure gradient directed from the channel toward the IFPC, a structure identified by Suazo Betancourt et al. as potentially relevant to electrostatic erosion pathways [1].

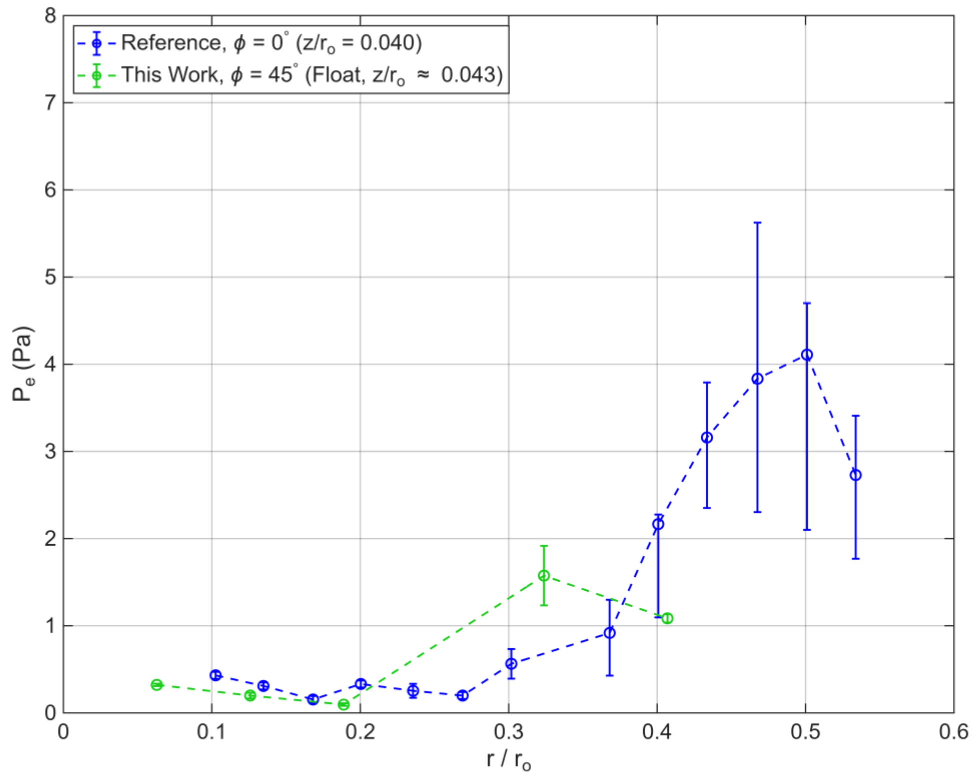

Figure 71: Electron pressure as a function of radial position for the reference work (blue, $\phi = 0°$, $z/r_o = 0.040$ [1]) and this work (green, $\phi = 45°$, Float, $z/r_o \approx 0.043$).

However, the electron pressure gradient alone cannot serve as a reliable proxy for the local electrostatic potential in this region. The electron momentum equation relates the electric field to the pressure gradient and collisional/anomalous transport terms: $E = (1/neqe)[\nabla Pe - \Sigma veime(ue - ui)]$. In the near-field of a magnetically-shielded HET, the measurement domain is strongly magnetized (Ω_e >> 1 everywhere, as shown in Section 6.2.1), and instabilities such as the modified two-stream instability (MTSI), electron cyclotron drift instability (ECDI), and lower-hybrid drift instability (LHDI) may contribute to anomalous transport. Under these conditions, the collisional/anomalous term cannot be neglected. The electron pressure was therefore examined as a potential proxy for local potential structure, but this approach was not decisive: while the pressure data confirm the expected qualitative geometry of a minimum in the IFPC region consistent with the proposed ion impingement pathway, the unmeasured transport and collisional contributions prevent a quantitative determination of the local electric field from pressure gradients alone.

This inconsistency between the pressure gradient direction and the observed radial drift underscores the role of collisional and anomalous transport in governing near-field electron dynamics. In the strongly magnetized IFPC region, cross-field electron transport is mediated not by the pressure gradient alone but by the balance of the pressure force, the Lorentz force, and the collisional or anomalous drag. Anomalous transport arising from instabilities such as the MTSI, ECDI, or LHDI can drive electron fluxes that oppose the pressure gradient direction, producing the observed sign reversal. The present measurements therefore demonstrate that characterizing IFPC electron transport requires either direct measurement of the anomalous collision frequency or computational closure of the momentum equation. The pressure gradient alone is not a sufficient diagnostic of the local electrostatic environment.

6.2.6 Electron Radial Drift Velocity

The radial electron drift velocity was measured to directly observe how body-bias conditions modify electron transport pathways in the near-field. In principle, a net radial drift toward the thruster body in the cathode-tied or +2 V configurations would provide direct kinematic evidence supporting the modified electron pathway mechanism. However, as stated in Section 6.2.1, because the measurements span a highly magnetized region, the drift velocity trends are difficult to interpret. The drift velocity results are therefore presented as supplementary context rather than as primary evidence for the proposed transport mechanism.

Figure 72 presents the cathode centerline $V_{drift,r}$ as a function of z/r_o. The cathode-tied configuration maintains +20 to +37 km/s (radially inward) across the full domain. The +2 V configuration is similarly inward at +40 to +42 km/s through $z/r_o \approx 0.07$, transitioning to +5 km/s at $z/r_o \approx 0.115$. The floating configuration departs from this pattern, transitioning from +15 km/s (radially inward) near $z/r_o = 0.015$ to −65 km/s (radially outward) at $z/r_o \approx 0.10$.

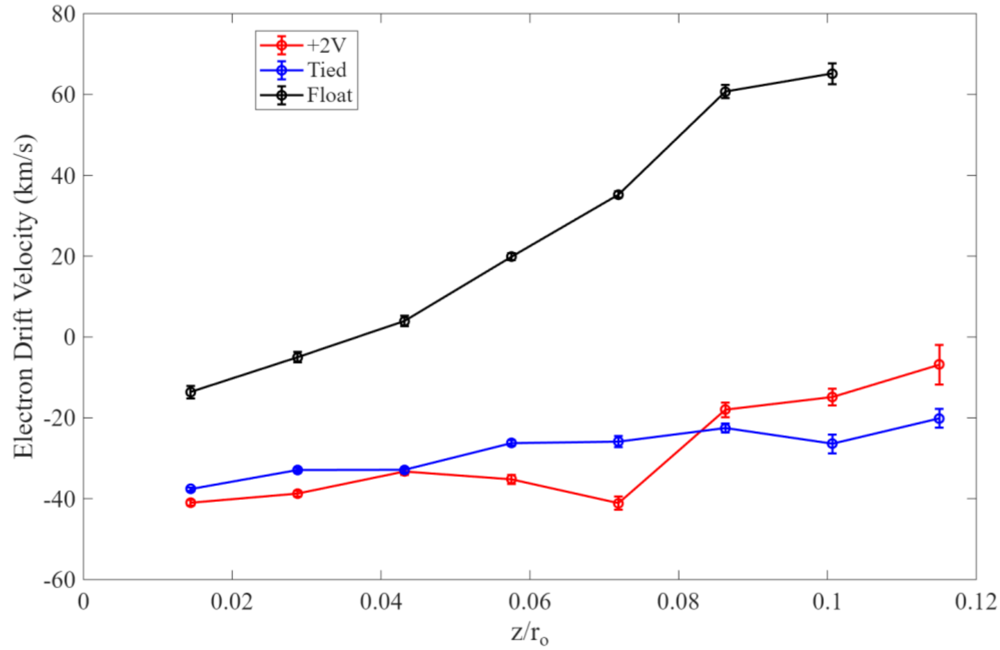

Figure 72: Cathode centerline (r = 0) radial component of the electron drift velocity as a function of normalized axial distance z/r_o for the Float (black), Tied (blue), and +2 V (red) body bias configurations. Positive values indicate radially inward drift toward the cathode centerline; negative values indicate radially outward drift toward the discharge channel. The H9 was operated at 150 V discharge voltage and 40 A discharge current.

Figure 73 presents the cathode centerline $V_{drift,r}$ data as a vector arrow diagram enabling simultaneous comparison of direction and relative magnitude across all three configurations and all axial stations. Arrow direction indicates sign (leftward = radially inward, rightward = radially outward) and arrow length is proportional to magnitude on a scale normalized by the maximum measured value. The most physically significant feature of the plot is the behavior of the +2 V configuration at upstream axial stations ($z/r_o \leq 0.07$): the +2 V arrows are consistently the largest inward-directed vectors of any configuration at these stations. This upstream inward drift in the +2 V configuration is consistent with the modified electron pathway mechanism: at +2 V relative to ground, the body acts as an electron-attracting surface, and the radially-inward drift reflects electrons being drawn toward it, consistent with the measured body current of −0.90 A. The arrow diagram makes this argument visually unambiguous: the +2 V inward arrows are largest precisely in the near-orifice upstream region where emitted cathode electrons first enter the near-field, and they diminish at downstream stations as the electrons that survive past the body's collection zone continue into the discharge channel. By contrast, the cathode-tied configuration's inward arrows are smaller in magnitude at the same upstream stations, consistent with that body collecting positive ions (CEX) rather than electrons. The floating-configuration arrows at upstream stations are the smallest of the three, consistent with no net current pathway at the body. This also supports the interpretation of additional thermionic electron emission from the cathode in the tied configuration, because the cathode-tied centerline density is greater than floating beyond $z/r_o = 0.02$ in spite of the magnitude of inward drift at the centerline that could otherwise inhibit downstream propagation of electrons.

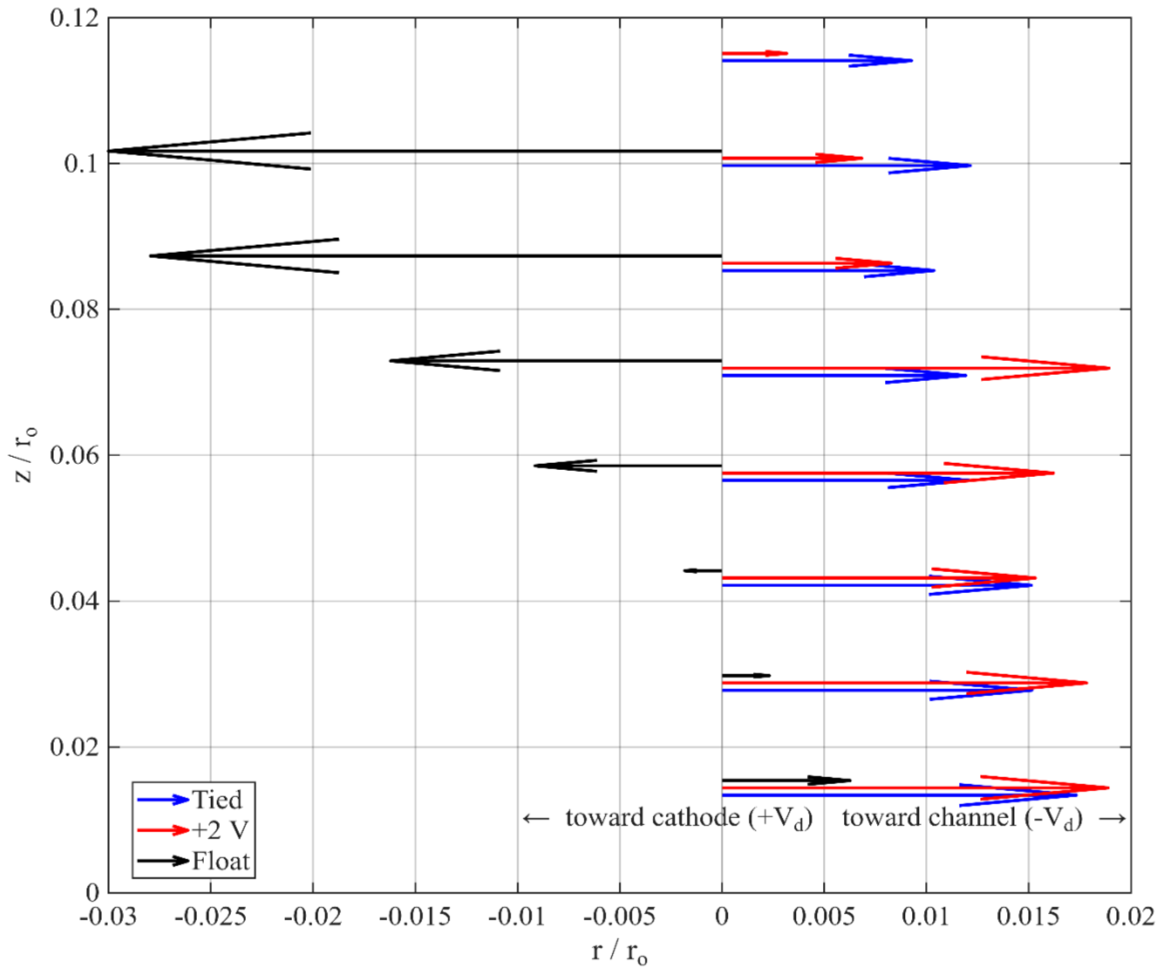

Figure 73: Cathode centerline (r = 0) radial drift velocity vector arrow diagram for the Float (black), Tied (blue), and +2 V (red) body bias configurations as a function of normalized axial distance z/r_o. Arrow direction indicates the sign of $V_{drift,r}$: leftward arrows correspond to positive values (radially inward, toward the cathode centerline) and rightward arrows correspond to negative values (radially outward, toward the discharge channel). Arrow lengths are normalized to the maximum drift velocity magnitude across all configurations, with the largest arrow scaled to approximately 20% of the z-axis

range; all other arrows are proportional via V_d multiplied by this common scale factor, enabling direct magnitude comparison across configurations and axial stations. The H9 was operated at 150 V discharge voltage and 40 A discharge current.

Figure 74 presents the radial variation of $V_{drift,r}$ at three axial stations: $z/r_o = 0.014$, 0.029, and 0.043. At the cathode centerline (L1), all configurations are near zero at all stations, consistent with the near-axial magnetic field geometry there. At $z/r_o = 0.014$, the most prominent difference is at L4, where Float and Tied show outward drift of -2.5 to -3.0×10^5 m/s, while +2 V shows inward drift of $+2 \times 10^5$ m/s, which produces a separation of $\sim 5 \times 10^5$ m/s outside measurement uncertainty. At $z/r_o = 0.029$, the L4 pattern shifts: +2 V becomes strongly outward (approximately -2×10^5 m/s) while Tied moves weakly inward. At $z/r_o = 0.043$, Float is predominantly outward across the IFPC region (L3–L4), while +2 V shows inward drift at L5 and L6, consistent with the configuration-dependent pathway behavior.

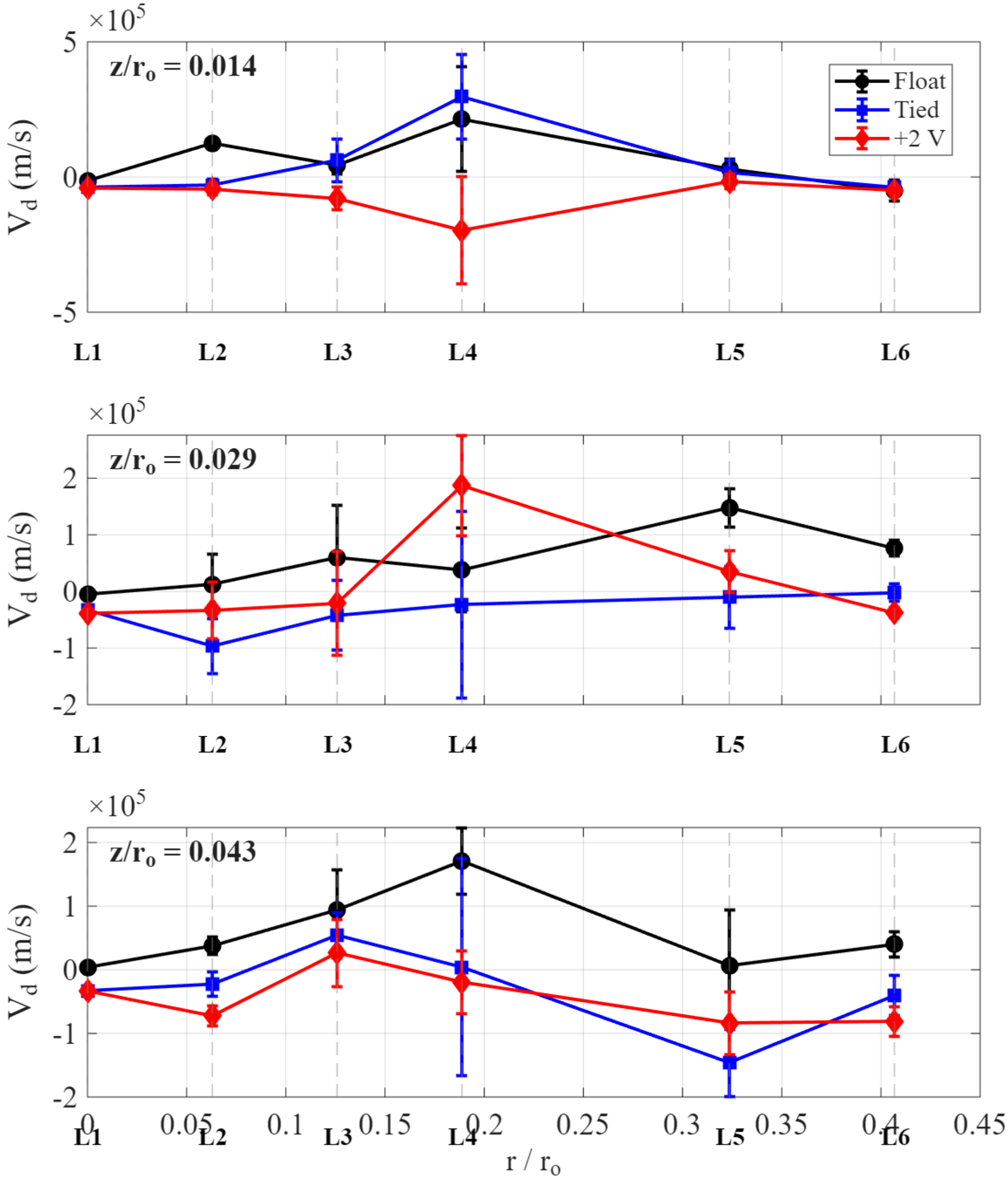

Figure 74: Radial variation of the radial component of the electron drift velocity at three axial stations (z/r_o = 0.014, 0.029, and 0.043) for the Float (black), Tied (blue), and +2 V

(red) body bias configurations. Positive values indicate radially inward drift toward the cathode centerline; negative values indicate radially outward drift toward the discharge channel. Radial stations L1–L6 are indicated. The H9 was operated at 150 V discharge voltage and 40 A discharge current.

Figure 75 presents quiver plots of $V_{drift,r}$ across the full two-dimensional measurement domain for all three configurations simultaneously. At outer radii ($r/r_o \approx 0.35$–0.40), the floating configuration displays the largest vectors, and they are uniformly outward-directed, which is a qualitatively different spatial pattern from the cathode-tied and +2 V configurations, whose outer-radii vectors are mixed or weakly inward. This apparent unidirectional outward drift in the floating configuration across the outer measurement domain is physically consistent with its circuit topology: with no current pathway available at the thruster body, the unperturbed discharge drives electrons radially through the near-channel region toward the anode as a portion of the nominal discharge current path. The floating-configuration vectors carry the systematic instrument function uncertainty (Section 5.1.2.3), which also could be shifting all floating-configuration estimates outward, so it is unknown whether this is a true physical measurement or an instrumentation artifact. The cathode-tied and +2 V quivers do not carry this uncertainty and are more quantitatively reliable.

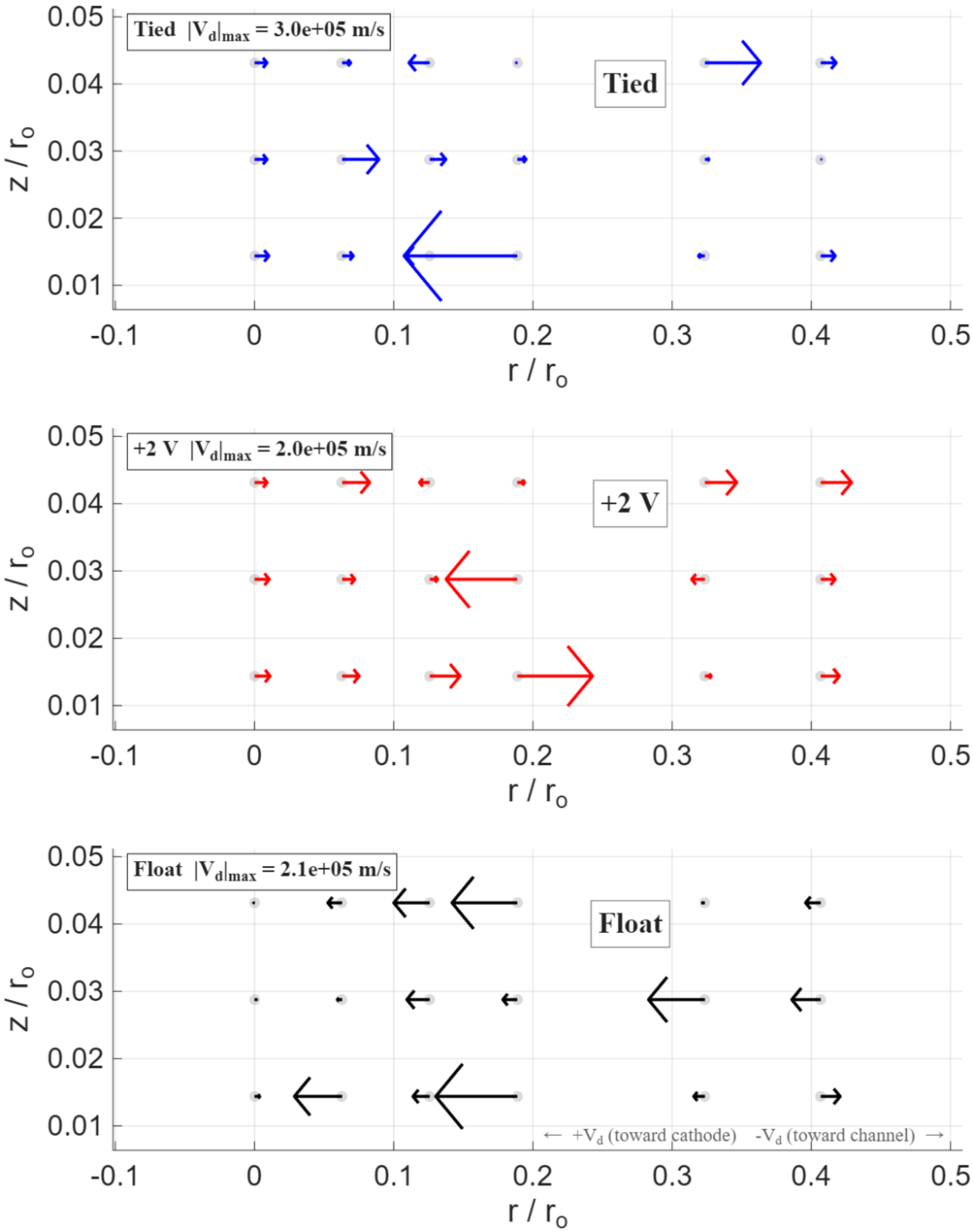
Tied |V_d|max = 3.0e+05 m/s
Tied
+2 V |V_d|max = 2.0e+05 m/s
+2 V
Float |V_d|max = 2.1e+05 m/s
Float
← +V_d (toward cathode)
-V_d (toward channel) →
z / r_o
r / r_o

Figure 75: Quiver plots of the radial component of the electron drift velocity across the measurement domain in normalized coordinates for the Tied (top), +2 V (middle), and Float (bottom) configurations. Arrow length is proportional to the local radial drift velocity magnitude normalized by the maximum; rightward arrows indicate radially outward drift. The H9 was operated at 150 V discharge voltage and 40 A discharge current.

The measurements presented in this chapter are time-averaged, and Hall thruster plasmas are inherently oscillatory. Breathing mode and higher-frequency instabilities drive time-dependent electron transport that the present LTS measurements average over. Future computational modeling of the near-field region under different body bias conditions would complement these measurements by resolving the oscillatory electron dynamics that time-averaged diagnostics cannot capture. Such models could decompose the measured transport into its steady and oscillatory components, clarify whether bias-dependent differences in electron properties arise from changes in the mean transport, the oscillation amplitude, or both, and provide the directional current density information needed to close the gap between scalar pressure measurements and the full vector current closure picture. Coupling the experimental constraints from this work with validated simulations would enable a more complete characterization of how body bias modifies electron current closure in the near-field.

6.3 Practical Considerations for Configuration Selection

The following tables (Table 8, Table 9, Table 10) summarize practical considerations for each electrical configuration investigated in this work. These observations are drawn from the Phase I current collection measurements, Phase II spatially resolved LTS diagnostics, and telemetry characterization presented in Chapters 5 and 6. They are intended to inform ground-test configuration selection rather than prescribe flight design, as the present data were collected in a ground-test environment.

Table 8: Floating configuration pros and cons comparison

Floating	
Pros	Simplest implementation. No additional power supply or wiring required for the thruster body. Represents the default flight configuration for most heritage HETs. No body current (zero). No additional power draw or thermal load on body surfaces from electron collection.
Cons	Floating potential sensitive to plasma conditions and drifts over time (8 V spread observed in Phase II telemetry). Less predictable boundary condition. Electron temperature scales with discharge voltage [85], which drives the floating voltage low and could make the body highly ion-attractive, increasing erosion risk.

Table 9: Cathode-tied configuration pros and cons comparison

Cathode-Tied	
Pros	Widely used heritage ground-test configuration. Eliminates one degree of freedom by tying body to cathode common. Produces measurable body current (~0.78 A), lower than the grounded configuration, through a well-defined circuit pathway. Stable, predictable boundary condition.
Cons	Drops electron density at the channel centerline relative to the other configurations, which could result in lower ionization efficiency measured in this region.

Table 10: Ground relative configuration pros and cons comparison

Ground Relative	
Pros	Most stable voltage boundary condition (0.5 V spread vs 8 V for floating). Clean, controllable. Highest oscillation amplitude. If oscillatory behavior is representative of flight, this configuration may better preserve flight-like discharge dynamics.
Cons	Requires an independent bias supply, adding mass, complexity, and a failure mode. Introduces a ground-test artifact: collected electrons complete their circuit through the chamber walls. The electron temperature depression and density depletion at L4 are features of this facility interaction, not necessarily flight-representative. Density redistribution at the IFPC may affect erosion qualification. NightX wear test data showed IFPC erosion striations insensitive to background pressure variations (which altered beam divergence), tempering but not eliminating concerns about divergence-mediated erosion changes.

CHAPTER 7: CONCLUSIONS

This dissertation investigated the influence of thruster body bias configuration on electron behavior in the near-field of a magnetically-shielded Hall effect thruster through a two-phase experimental campaign on the 9-kW H9 thruster. Phase I combined body current and IFPC current measurements with a body bias sweep to characterize macroscopic current collection; Phase II deployed spatially-resolved laser Thomson scattering (LTS) to measure electron density, electron temperature, and radial drift velocity at 15 locations spanning the near-field from the cathode centerline to the channel centerline under three bias conditions: floating, cathode-tied, and +2 V.

The first principal finding is that electrons are magnetized throughout the near-field measurement domain under all three body bias configurations. The normalized electron gyroradius r_{ce}/r_o remains below 0.1 at every measurement location which is well within the criterion for strong magnetization, and the corresponding electron Hall parameter Ω_e exceeds unity by at least an order of magnitude across the domain. This result validates the assumption of magnetized electron transport throughout the measurement region and establishes that the applied magnetic field, rather than collisional diffusion, plays a key role in governing the electron trajectories. All subsequent configuration-dependent results are therefore interpreted in the context of electron transport in a strongly magnetized plasma.

The second principal finding is that the thruster body bias systematically and measurably modulates electron current collection. Phase I demonstrated a monotonic, linear response: scanning the body bias from 0.5 to 2.0 V produces a proportional increase in collected electron current magnitude (slope = −0.088 A/V, R^2 = 0.93 for the body; slope = −0.020 A/V, R^2 = 0.95 for the IFPC). The linear response is more consistent with operation in the saturation region of a Langmuir probe I-V characteristic than with the transition region; however, the bias range examined in this work does not provide enough data to definitively distinguish between the two regimes. In Phase II at the 150 V, 40 A operating condition, the cathode-tied configuration draws +0.78 A of body current and the +2 V configuration draws −0.85 A, while both reduce the discharge current by approximately 0.5 A relative to the floating baseline of 40.1 A. The Phase II laser Thomson scattering measurements show elevated electron density at the channel centerline in the +2 V configuration relative to both the floating and cathode-tied configurations, providing direct experimental evidence consistent with the higher current utilization efficiency Peterson et al. [30] reported for the ground-relative configuration of the HERMeS thruster.

The linear current-voltage response observed across the tested bias range raises the question of whether a saturation limit exists at higher bias voltages. Peterson et al. [3] demonstrated that the grounded configuration can collect up to 10% of the discharge current through the thruster body, indicating that ground-referenced configurations are particularly susceptible to large parasitic body currents. At some threshold, the collected current should asymptote as the body potential approaches the local plasma potential and the electron-attracting sheath transitions to space-charge-limited collection. The present data show no evidence of saturation onset within the tested range, where the body current remains below approximately 2% of the mean discharge current. Whether the linear trend persists, saturates, or exhibits a transition at higher body currents remains an open question, and the saturation limit is likely dependent on the circuit topology: the grounded and +2 V configurations route current through fundamentally different external circuits with distinct impedance characteristics. Identifying such a threshold has practical implications for ground-based testing configurations, where facility-mediated ground currents could constitute a significant fraction of the total discharge current and thereby affect thruster performance characterization.

The third principal finding is that the spatial distribution of near-field electron density undergoes a configuration-dependent inversion that directly reflects the distinct circuit topologies of each body bias condition. In the cathode-tied configuration, the thruster body shares the cathode node potential; charge-exchange ions produced near the body surface are neutralized by electrons supplied from the cathode node through an external wire connection, a loop that bypasses the local plasma. In the +2 V configuration, the positively biased body collects electrons directly from the near-field plasma through an independent circuit loop composed of facility ground, which is a pathway with no analog in the space environment and therefore a ground-test artifact. Consistent with these mechanisms, the cathode-tied configuration sustains elevated electron density at the cathode centerline ($r/r_o = 0.063$) while the +2 V configuration maintains higher density at the channel-adjacent stations ($r/r_o = 0.407$). This spatial inversion is reproduced across all three axial measurement stations and constitutes direct macroscopic evidence for the proposed circuit topology interpretation.

The fourth principal finding is that the electron temperature and radial drift velocity provide supplementary kinematic evidence consistent with the circuit topology mechanisms. Electron temperature differences across configurations were generally within or near measurement uncertainty; however, the +2 V configuration exhibits the lowest T_e at the inner pole region (L4 radial station, $r/r_o \approx 0.063$), which is consistent with preferential absorption of high-energy electrons by the positively biased surface. Radial drift velocity measurements provide the most direct kinematic evidence for configuration-dependent electron transport; however, trends were difficult to resolve in a region where the azimuthal electron drift dominates. Quantitative interpretation of the floating-configuration drift is limited by an estimated instrument-function systematic bias; however, floating-configuration vectors are consistent with the nominally unperturbed discharge.

The fifth principal finding is that electron pressure cannot serve as a reliable proxy for electrostatic potential in the near-field of a magnetically-shielded HET. Electron pressure was computed at each measurement location from the directly measured density and temperature. The electron momentum equation requires that the electrostatic potential gradient be balanced by both the pressure gradient and the anomalous transport term; in this strongly magnetized environment, the anomalous term is not negligible and was not independently characterized in this study. At certain locations, the sign of the measured pressure gradient and the measured radial drift direction are mutually inconsistent, confirming that pressure alone does not determine the local electron transport. Direct measurements of electron properties redistribution under the varied electrical configuration, therefore, provide more reliable evidence for electron pathway characterization than pressure-based inferences.

CHAPTER 8: FUTURE WORK

This chapter identifies four directions for extending the present investigation. The first addresses operating condition dependence, as the 150 V, 40 A condition used in Phase II was selected for diagnostic signal-to-noise rather than to maximize configuration-dependent effects. The second proposes improvements to the IFPC's current collection diagnostic that would enable direct correlation with spatially resolved electron measurements. The third addresses a fundamental limitation of the present experimental design: all three configurations biased the thruster body relative to facility ground, and the resulting electron transport modifications, while they are measurable and outside of experimental uncertainty, they reflect current pathways mediated by the grounded vacuum chamber that do not exist in the space environment. The fourth describes how the spatially resolved measurements obtained in this work can serve as inputs to computational models, enabling estimation of transport quantities that cannot be directly measured.

8.1 Extended Operating Conditions

The present investigation was conducted at the 150 V, 40 A (6 kW) operating condition, selected primarily for signal-to-noise considerations in the LTS diagnostic. Preliminary data presented in Chapter 0 at the nominal 300 V, 20 A (6 kW) condition showed larger configuration-dependent differences in cathode centerline electron properties, and the breathing mode frequency exhibited greater sensitivity to body bias at 600 V, 15 A (9 kW). Performing the full spatial mapping on krypton at a higher-voltage, more oscillatory operating condition is expected to reveal more pronounced bias-dependent behavior, since the high-voltage, low-current operating conditions on krypton have already been demonstrated to be highly oscillatory relative to high current density operation. Additionally, extending to higher power operating conditions, e.g., 600 V, 15 A, would determine whether the trends identified at 6 kW persist, saturate, or intensify at power levels more representative of mission-relevant operation.

The preliminary data at 300 V and 20 A showed configuration-dependent differences in cathode-centerline electron density as large as 67% between the cathode-tied and grounded configurations and approximately 23% between cathode-tied and floating at mid-axial positions [52]. At the 150 V, 40 A condition employed in Phase II, the maximum spread between any two configurations at the cathode centerline narrowed to approximately 26%. This compression of configuration-dependent differences at lower voltage and higher current suggests that operating conditions significantly modulate the sensitivity of near-field electron properties to body bias, and that higher-voltage conditions may amplify the configuration-dependent effects reported in this work.

8.2 Improvements to the IFPC Current Collection Diagnostic

This work demonstrated the first use of the IFPC itself as a large-area current collection surface in a magnetically-shielded HET. However, equipment protection concerns necessitated operation at 20 A, 300 V rather than the Phase II condition of 40 A, 150 V, preventing direct flux comparison between phases. Preliminary testing revealed that isolating the IFPC at 40 A caused accelerated magnet resistance growth, indicative of thermal loading from increased ion bombardment, and electrical isolation introduced plasma-mediated coupling between body and IFPC potentials that increased operational bias uncertainty.

Future implementations should address these limitations through erosion-resistant protective coatings on the IFPC surface to enable higher-power operation, a segmented IFPC design with independently instrumented annular sections to provide radial current density resolution comparable to the LTS measurements and coupled power supply control between the IFPC and thruster body bias to mitigate plasma-mediated coupling. Operating the IFPC current collection simultaneously with the LTS measurements at matched operating conditions would enable direct correlation between the spatially integrated current and local electron properties, closing the gap between Phase I and Phase II. High-bandwidth current measurements synchronized with discharge oscillations would further capture whether body bias affects the oscillatory component of electron transport in addition to the DC component.

8.3 Thruster Body Bias Relative to Cathode

The three configurations investigated in this work biased the thruster body relative to the facility ground. The resulting measurements revealed configuration-dependent modifications to electron density, temperature, drift velocity, and radial flux that exceeded experimental uncertainty across multiple spatial locations. However, when the thruster body is biased relative to ground, collected electrons complete their circuit through the grounded metallic chamber walls, which is a recombination pathway that has been shown to carry up to 10% of the discharge current [30] and that does not exist in the space environment [71, 30]. The ground-referenced bias, therefore, modulates electron pathways through a facility-mediated current return, not solely through the body-to-plasma potential difference.

Biasing the thruster body relative to the cathode common using a dedicated bias supply, while electrically isolating the thruster-cathode system from facility ground, would remove the chamber ground plane from the discharge circuit entirely. In this configuration, current collected by the thruster body is returned through the cathode rather than through facility surfaces, producing a closed thruster-cathode current loop. This is a flight-implementable configuration: no ground reference exists on orbit, and the thruster body is inherently referenced to cathode common and the spacecraft chassis. Sweeping the body-to-cathode bias would reveal how near-field electrons respond to the thruster body potential above and below cathode potential and would quantify the effect of modulating the circulatory current through the thruster body on the electron transport pathways measured in this work.

The observation that all three configurations coalesce to the same electron density and temperature along the cathode centerline beyond the near-field region, in both the initial investigation and Phase II, suggests that body bias effects are spatially confined. Complementary far-field Langmuir probe measurements would determine whether the plasma potential structure is also configuration-independent beyond this convergence point. Combined with the electron termination pathway framework of Walker et al. [89] and the current pathways model of Jovel et al.[102], which demonstrated that beam neutralization in ground-based facilities is predominantly mediated by chamber-wall electrons rather than cathode electrons, such measurements would help distinguish the cathode-sourced and facility-sourced electron populations in the far field and clarify whether body bias modifies only facility-mediated current pathways or also affects the flight-relevant cathode electron transport.

The measurements reported in this work are time-averaged over acquisition windows spanning many breathing mode oscillation cycles. Because the breathing mode frequency is itself configuration-dependent, as shown by the PSD analysis, the ionization region length and electron energy perturbations differ across configurations during each oscillation cycle [103]. Time-resolved laser diagnostic studies have demonstrated that electron density and plasma properties oscillate with amplitudes comparable to their mean values over the breathing cycle [104]. Consequently, the configuration-dependent differences reported here represent only the DC component of the body bias effect. Body-bias-induced modifications to electron transport that occur on timescales comparable to the breathing mode period would be averaged out, and second-order quantities such as electron temperature are particularly susceptible to this effect because they depend nonlinearly on the velocity distribution function moments. Time-resolved measurements at breathing mode frequencies would determine whether additional configuration-dependent structure exists in the oscillatory component of the electron properties.

In parallel with experimental extensions, the spatially resolved electron property measurements obtained in this work can serve as direct inputs to computational models of the near-field plasma. Yamashita et al. [85] demonstrated this approach by utilizing cathode centerline electron density and temperature data from the present H9 campaign as inputs to a one-dimensional plasma fluid model, estimating the effective cross-field electron mobility under each electrical configuration. This is significant because the electron pressure gradient, while measurable utilizing LTS, is only one contributing term in the electron momentum equation. The collision and resistivity terms, which depend on the cross-field electron mobility, must also be resolved to fully determine the local electric potential structure from the momentum balance. Because the cross-field mobility is directly related to the effective collision frequency, its estimation from measurement data provides the information needed to evaluate the otherwise inaccessible resistive term in the momentum equation. The model-data fusion framework thus represents a path toward closing the momentum equation and resolving features of the electron transport that the experimental measurements alone cannot capture. Extension to higher-dimensional models would further clarify how the electron pathways identified in this work relate to the underlying magnetic field structure.

REFERENCES

[1] Suazo Betancourt, J. L., Lopez-Uricoechea, J., Butler-Craig, N., Steinberg, A. M., & Walker, M. L. R. (2024). Bayesian-inverted laser Thomson scattering measurements indicate electrostatic erosion pathways in magnetically-shielded Hall effect thrusters. *Journal of Applied Physics*, *136*(12), 123301. https://doi.org/10.1063/5.0221547

[2] Roberts, P. J., Chaplin, V. H., & Jorns, B. A. (2024). Azimuthal ion dynamics at the inner pole of an axisymmetric Hall thruster. *Physics of Plasmas*, *31*(8), 083513. https://doi.org/10.1063/5.0214477

[3] Peterson, P. Y., Kamhawi, H., Huang, W., Williams, G., Gilland, J. H., Yim, J., & Herman, D. A. (2016). NASA's HERMeS Hall thruster electrical configuration characterization (AIAA Paper 2016-5027).

[4] Mikellides, I. G., Katz, I., Hofer, R. R., & Goebel, D. M. (2013). Magnetic shielding of walls from the unmagnetized ion beam in a Hall thruster. *Applied Physics Letters*, *102*(2).

[5] Huang, W., & Kamhawi, H. (2021). Experimental investigation of ionization and ion acceleration in the near-field plume of a 12.5-kW magnetically shielded Hall thruster. *Journal of Applied Physics*, *129*, 133304.

[6] Lieberman, M. A., & Lichtenberg, A. J. (2005). *Principles of plasma discharges and materials processing* (2nd ed.). Wiley.

[7] Cusson, S. E., Dale, E. T., Jorns, B. A., & Gallimore, A. D. (2019). Acceleration region dynamics in a magnetically shielded Hall thruster. *Physics of Plasmas*, *26*(2).

[8] Nikrant, A., & Switzer, Z. (2024). NGHT-1X pole cover erosion measurements on xenon and krypton. In *AIAA Sci Tech 2024 Forum* (p. 1140).

[9] Goebel, D. M., & Katz, I. (2008). *Fundamentals of electric propulsion: Ion and Hall thrusters*. John Wiley & Sons.

[10] Choueiri, E. Y. (2004). A critical history of electric propulsion: The first 50 years (1906-1956). *Journal of Propulsion and Power*, *20*(2), 193-203.

[11] Kim, V., Kozubsky, K. N., Murashko, V. M., & Semenkin, A. V. (2007, September). History of the Hall thrusters development in USSR. In *Proceedings of the 30th International Electric Propulsion Conference, Florence, Italy* (pp. 17-20).

[12] Patterson, M. J., & Sovey, J. S. (2013). History of electric propulsion at NASA Glenn Research Center: 1956 to present. *Journal of Aerospace Engineering*, *26*(2), 300-316.

[13] Goddard, R. H. (1906). *The green notebooks* (Vol. 1). The Dr. Robert H. Goddard Collection at Clark University Archives, Clark University, Worcester, MA.

[14] Mel'kumov, T. M. (Ed.). (1965). *Pioneers of rocket technology: Selected works*. National Aeronautics and Space Administration.

[15] Cybulski, R. J., Shellhammer, D. M., Lovell, R. R., Domino, E. J., Kotnik, J. T., Cybulski, J., & Loveli, R. R. (1965, March). Results from SERT I ion rocket flight test. In *Air Force Office of Scientific Research Proceedings* (Vol. 1, p. 21).

[16] Rayman, M. D., Varghese, P., Lehman, D. H., & Livesay, L. L. (2000). Results from the Deep Space 1 technology validation mission. *Acta Astronautica*, *47*(2-9), 475-487.

[17] Dudeck, M., Doveil, F., Arcis, N., & Zurbach, S. (2012, February). Plasma propulsion for geostationary satellites for telecommunication and interplanetary missions. In *IOP Conference Series: Materials Science and Engineering* (Vol. 29, No. 1, p. 012010). IOP Publishing.

[18] Jahn, R. G. (2006). *Physics of electric propulsion*. Courier Corporation.

[19] Choueiri, E. Y. (2001). Fundamental difference between the two Hall thruster variants. *Physics of Plasmas*, *8*(11), 5025-5033.

[20] Zhurin, V. V., Kaufman, H. R., & Robinson, R. S. (1999). Physics of closed drift thrusters. *Plasma Sources Science and Technology*, *8*(1), R1.

[21] Choueiri, E. Y. (2001). Fundamental difference between the two Hall thruster variants. *Physics of Plasmas*, *8*(11), 5025-5033. https://doi.org/10.1063/1.1407838

[22] Hofer, R. R., Goebel, D. M., Mikellides, I. G., & Katz, I. (2014). Magnetic shielding of a laboratory Hall thruster. II. Experiments. *Journal of Applied Physics*, *115*(4).

[23] Cusson, S. E., Jorns, B. A., & Gallimore, A. D. (2019). Non-invasive in situ measurement of the near-wall ion kinetic energy in a magnetically shielded Hall thruster. *Plasma Sources Science and Technology*, *28*(10), 105012.

[24] Jorns, B., Dodson, C. A., Anderson, J. R., Goebel, D. M., Hofer, R. R., Sekerak, M. J., & Mikellides, I. G. (2016). Mechanisms for pole piece erosion in a 6-kW magnetically-shielded Hall thruster. In *52nd AIAA/SAE/ASEE Joint Propulsion Conference* (p. 4839).

[25] Polk, J. E., Lobbia, R., Barriault, A., Guerrero, P., Mikellides, I., & Ortega, A. L. (2017, October). Inner front pole cover erosion in the 12.5 kW HERMeS Hall thruster over a range of operating conditions. In *35th International Electric Propulsion Conference, Atlanta, GA*.

[26] Mikellides, I. G., Lopez Ortega, A., & Jorns, B. (2014). Assessment of pole erosion in a magnetically shielded Hall thruster. In *50th AIAA/ASME/SAE/ASEE Joint Propulsion Conference* (Paper No. AIAA 2014-3897). https://doi.org/10.2514/6.2014-3897

[27] Cusson, S. E., Jorns, B. A., & Gallimore, A. D. (2019, September). Impact of neutral density on the magnetic shielding of Hall thrusters. In *Proceedings of the 36th International Electric Propulsion Conference, Vienna, Austria* (pp. 15-20).

[28] Frieman, J. D., King, S. T., Walker, M. L. R., Khayms, V., & King, D. (2014). Role of a conducting vacuum chamber in the Hall effect thruster electrical circuit. *Journal of Propulsion and Power*, *30*(6), 1471-1479.

[29] Walker, J. A., Langendorf, S. J., Walker, M. L. R., Khayms, V., King, D., & Peterson, P. (2016). Electrical facility effects on Hall current thrusters: Electron termination pathway manipulation. *Journal of Propulsion and Power*, *32*(6), 1365-1377. https://doi.org/10.2514/1.B35904

[30] Peterson, P. Y., Kamhawi, H., Huang, W., Williams, G., Gilland, J. H., Yim, J., & Herman, D. A. (2016). NASA's HERMeS Hall thruster electrical configuration characterization (AIAA Paper 2016-5027).

[31] Chen, F. F. (1984). *Introduction to plasma physics and controlled fusion* (Vol. 1, pp. 19-51). Plenum Press.

[32] Lieberman, M. A. (1994). *Principles of plasma discharges and materials processing* (pp. 117-138). John Wiley & Sons.

[33] Boeuf, J. P. (2017). Tutorial: Physics and modeling of Hall thrusters. *Journal of Applied Physics*, *121*(1).

[34] Sahu, R., Mansour, A. R., and Hara, K. (2020). Full fluid moment model for low-temperature magnetized plasmas. Physics of Plasmas, 27, 113505.

[35] Hara, K. (2019). An overview of discharge plasma modeling for Hall effect thrusters. *Plasma Sources Science and Technology*, *28*(4), 044001.

[36] Birdsall, C. K., & Langdon, A. B. (2018). *Plasma physics via computer simulation*. CRC Press.

[37] Hirakawa, M. U. U. (1997, August). Electron transport mechanism in a Hall thruster. In *26th International Electric Propulsion Conference, Cleveland, Ohio* (pp. 97-021).

[38] Hara, K., and Hanquist, K. M. (2018). Test cases for grid-based direct kinetic modeling of plasma flows. Plasma Sources Science and Technology, 27, 065004. AND Hara, K., Boyd, I. D., and Kolobov, V. I. (2012). One-dimensional hybrid-direct kinetic simulation of the discharge plasma in a Hall thruster. Physics of Plasmas, 19, 113508.

[39] Fife, J. M. (1998). *Hybrid-PIC modeling and electrostatic probe survey of Hall thrusters* [Doctoral dissertation, Massachusetts Institute of Technology].

[40] Mikellides, I. G., & Katz, I. (2012). Numerical simulations of Hall-effect plasma accelerators on a magnetic-field-aligned mesh. Physical Review E, 86(4), 046703. https://doi.org/10.1103/PhysRevE.86.046703

[41] Kaganovich, I. D., Smolyakov, A., Raitses, Y., Ahedo, E., Mikellides, I. G., Jorns, B., Taccogna, F., et al. (2020). Physics of E × B discharges relevant to plasma propulsion and similar technologies. *Physics of Plasmas*, *27*(12), 120601.

[42] Jackson, J. D. (1998). *Classical electrodynamics* (3rd ed., pp. 661-698). Wiley.

[43] Froula, D. H., Glenzer, S. H., Luhmann, N. C., & Sheffield, J. (2011). Scattered power spectrum. In *Plasma scattering of electromagnetic radiation* (pp. 31-44). Elsevier.

[44] Kempkens, H., & Uhlenbusch, J. (2000). Scattering diagnostics of low-temperature plasmas (Rayleigh scattering, Thomson scattering, CARS). *Plasma Sources Science and Technology*, *9*(4), 492.

[45] Vincent, B., Tsikata, S., Mazouffre, S., Minea, T., & Fils, J. (2018). A compact new incoherent Thomson scattering diagnostic for low-temperature plasma studies. *Plasma Sources Science and Technology*, *27*(5), 055002.

[46] Spektor, R., & Tighe, W. G. (2016). Laser induced fluorescence measurements in a Hall thruster as a function of background pressure. In *52nd AIAA/SAE/ASEE Joint Propulsion Conference* (Paper No. AIAA 2016-4839). https://doi.org/10.2514/6.2016-4839

[47] Chaplin, V. H., Byrne, M., Butler-Craig, N., Roberts, P. J., Lobbia, R. B., & Polk, J. E. (2024). Laser-induced fluorescence measurements of driven high-frequency electrostatic waves in a hollow cathode plume. In *AIAA SCITECH 2024 Forum* (p. 0924).

[48] Wegner, T., Friss, A., Dumitrache, C., & Yalin, A. (2019, September). Two-photon absorption laser induced fluorescence (TALIF) of ground state neutral xenon. In *36th International Electric Propulsion Conference, Vienna*.

[49] Williams, G., Soulas, G., & Kamhawi, H. (2012, July). Optical diagnostic characterization of high-power Hall thruster wear and operation. In *48th AIAA/ASME/SAE/ASEE Joint Propulsion Conference & Exhibit* (p. 4036).

[50] Vincent, B., Tsikata, S., & Mazouffre, S. (2020). Incoherent Thomson scattering measurements of electron properties in a conventional and magnetically-shielded Hall thruster. *Plasma Sources Science and Technology*, *29*(3), 035015.

[51] Washeleski, R., Meyer, E., & King, L. (2012). Laser Thomson scattering measurements of electron temperature and density in the near-field plume of a Hall-effect thruster. In *48th AIAA/ASME/SAE/ASEE Joint Propulsion Conference & Exhibit* (p. 4118).

[52] Butler-Craig, N. I., Suazo Betancourt, J. L., Lopez-Uricoechea, J., Lev, D., & Walker, M. L. (2025). Comparison of the near-field electron properties of the H9 Hall effect thruster in various electrical configurations with incoherent laser Thomson scattering. In *AIAA SCITECH 2025 Forum* (p. 1099).

[53] Shastry, R., Huang, W., Haag, T. W., & Kamhawi, H. (2013, December). Langmuir probe measurements within the discharge channel of the 20-kW NASA-300M and NASA-300MS Hall thrusters. In *International Electric Propulsion Conference (IEPC)* (No. GRC-E-DAA-TN11513).

[54] Roberts, P. J., & Jorns, B. (2024). Inferring electron heat flux in a high-power Hall thruster with incoherent Thomson scattering. In *AIAA SCITECH 2024 Forum* (p. 1957).

[55] Suazo Betancourt, J. L., Butler-Craig, N., Lopez-Uricoechea, J., Steinberg, A. M., & Walker, M. L. R. (2024). Laser Thomson scattering measurements indicate non-isothermal magnetic field lines in magnetically shielded Hall effect thrusters. *Physics of Plasmas*, *31*(11).

[56] Brick, D. G., & Jorns, B. (2025). Numerical investigation of electron energy transport in Hall thrusters. In *AIAA SCITECH 2025 Forum* (p. 0298).

[57] Thomas, S., Thomas, R., Zachariah, A. K., & Mishra, R. K. (Eds.). (2017). Raman spectroscopy. In *Spectroscopic methods for nanomaterials characterization* (Vol. 2, pp. 95-127). Elsevier.

[58] Bernath, P. F. (2020). *Spectra of atoms and molecules*. Oxford University Press.

[59] Smith, B. K., Nazario, M. L., & Cunningham, C. C. (2012). *Solar electric propulsion vehicle demonstration to support future space exploration missions* (No. E-18409).

[60] Brophy, J. R. (2011). The Dawn ion propulsion system. Space Science Reviews, 163, 251-261. https://doi.org/10.1007/s11214-011-9848-y

---

[61] Snyder, J. S., Goebel, D. M., Chaplin, V. H., Lopez Ortega, A., Mikellides, I. G., Aghazadeh, F., Johnson, I., Kerl, T., & Lenguito, G. (2019). Electric propulsion for the Psyche mission. *Proceedings of the 36th International Electric Propulsion Conference*, IEPC-2019-244, Vienna, Austria.

[62] Koppel, C. R., & Estublier, D. (2005, October). The SMART-1 Hall effect thruster around the Moon: In flight experience (IEPC 2005-119).

[63] Mikellides, I. G., Katz, I., Hofer, R. R., & Goebel, D. M. (2014). Magnetic shielding of a laboratory Hall thruster. I. Theory and validation. *Journal of Applied Physics*, *115*(4), 043303. https://doi.org/10.1063/1.4862313

[64] Walker, M., Gallimore, A., Cai, C., & Boyd, I. (2002). Pressure map of a facility as a function of flow rate to study facility effects. In *38th AIAA/ASME/SAE/ASEE Joint Propulsion Conference & Exhibit* (Paper No. AIAA 2002-3815). https://doi.org/10.2514/6.2002-3815

[65] Hofer, R. R., Peterson, P. Y., & Gallimore, A. D. (2001). Characterizing vacuum facility backpressure effects on the performance of a Hall thruster. In *27th International Electric Propulsion Conference, Pasadena, CA* (Paper No. IEPC-01-045).

[66] Walker, M. L. R. (2005). *Effects of facility backpressure on the performance and plume of a Hall thruster* [Doctoral dissertation, University of Michigan].

[67] Frieman, J. D., King, S. T., Walker, M. L. R., Khayms, V., & King, D. (2014). Role of a conducting vacuum chamber in the Hall effect thruster electrical circuit. *Journal of Propulsion and Power*, *30*(6), 1471-1479. https://doi.org/10.2514/1.B35308

[68] Walker, J. A., Langendorf, S. J., Walker, M. L. R., Khayms, V., King, D., & Peterson, P. (2016). Electrical facility effects on Hall current thrusters: Electron termination pathway manipulation. *Journal of Propulsion and Power*, *32*(6), 1365-1377. https://doi.org/10.2514/1.B35904

[69] Peterson, P. Y., Kamhawi, H., Huang, W., Williams, G., Gilland, J. H., Yim, J., & Herman, D. A. (2016). NASA's HERMeS Hall thruster electrical configuration characterization (AIAA Paper 2016-5027).

[70] Koppel, C. R., & Estublier, D. (2005, October). The SMART-1 Hall effect thruster around the Moon: In flight experience (IEPC 2005-119).

[71] McDonald, M. S. (2012). *Electron transport in Hall thrusters* [Doctoral dissertation, University of Michigan].

[72] Kamhawi, H., Huang, W., Gilland, J. H., Haag, T. W., Mackey, J., Yim, J., & Herman, D. (2017, October). Performance, stability, and plume characterization of the HERMeS thruster with boron nitride silica composite discharge channel (IEPC 2017-392).

[73] Fife, J., Martinez-Sanchez, M., & Szabo, J. (1997). A numerical study of low-frequency discharge oscillations in Hall thrusters (AIAA Paper 1997-3052).

[74] Hofer, R. R., Jorns, B. A., Katz, I., & Brophy, J. R. (2019). *U.S. Patent No. 10,480,493*. U.S. Patent and Trademark Office.

[75] van de Sande, M. J. (2002). *Laser scattering on low temperature plasmas: High resolution and stray light rejection* [Doctoral dissertation, Eindhoven University of Technology].

[76] Vincent, B. (2019). *Incoherent Thomson scattering investigations in Hall thruster, planar magnetron and ECR ion source plasmas* [Doctoral dissertation, Université d'Orléans].

[77] Washeleski, R., Meyer, E., & King, L. (2012). Laser Thomson scattering measurements of electron temperature and density in the near-field plume of a Hall-effect thruster. In *48th AIAA/ASME/SAE/ASEE Joint Propulsion Conference & Exhibit* (Paper No. AIAA 2012-4118). https://doi.org/10.2514/6.2012-4118

[78] Hofer, R. R., Cusson, S. E., Lobbia, R. B., & Gallimore, A. D. (2017). The H9 magnetically shielded Hall thruster. *Proceedings of the 35th International Electric Propulsion Conference*, IEPC-2017-232, Atlanta, Georgia.

[79] Hofer, R. R., Cusson, S. E., Lobbia, R. B., and Gallimore, A. D. (2017). The H9 magnetically shielded Hall thruster (IEPC-2017-232). Key quote: 'the H9 can also be described as a sub-scale cousin of HERMeS

[80] Kamhawi, H., Huang, W., Haag, T., Shastry, R., Thomas, R., Yim, J., et al. (2015). Development approach and status of the 12.5 kW HERMeS Hall thruster for the Solar Electric Propulsion Technology Demonstration Mission. *Proceedings of the 34th International Electric Propulsion Conference*, IEPC-2015-186, Kobe, Japan.

[81] Herman, D. A., Gray, T. G., Peterson, P. Y., Kamhawi, H., & Frieman, J. D. (2021). Advanced Electric Propulsion System (AEPS) enabling a sustainable return to the lunar surface through NASA Gateway. *NASA Technical Memorandum*, NASA/TM-20210022011.

[82] Suazo Betancourt, J. L., Butler-Craig, N., Lopez-Uricoechea, J., Bak, J., Lee, D., Steinberg, A. M., & Walker, M. L. R. (2024). Thomson scattering measurements in the krypton plume of a lanthanum hexaboride hollow cathode in a large vacuum test facility. *Journal of Applied Physics*, *135*(8), 083302. https://doi.org/10.1063/5.0180251

[83] Lopez-Uricoechea, J., Suazo Betancourt, J. L., Butler-Craig, N., & Walker, M. L. R. (2024). Spatially resolved Thomson scattering measurements of electron properties across the acceleration region of a high-power magnetically shielded Hall effect thruster. *Journal of Applied Physics*, *136*(11). https://doi.org/10.1063/5.0213928

[84] Hall, S. J., Gray, T. G., Yim, J. T., Choi, M., Mooney, M. M., Sarver-Verhey, T. R., & Kamhawi, H. (2019, September). The effect of anode position on operation of a 25-A class hollow cathode. In *International Electric Propulsion Conference* (No. GRC-E-DAA-TN72893).

[85] Yamashita, Y., Butler-Craig, N., Walker, M. L. R., & Hara, K. (2025). Estimation of near-field electron mobility in hollow cathode discharge with different electrical configurations of a Hall effect thruster. Manuscript submitted for publication to Journal of Applied Physics.

[86] Haas, J., & Gallimore, A. D. (2000, August). An investigation of internal ion number density and electron temperature profiles in a laboratory-model Hall thruster (AIAA 2000-3422).

[87] Herman, D., Shastry, R., Huang, W., Soulas, G., & Kamhawi, H. (2012). Plasma potential and Langmuir probe measurements in the near-field plume of the NASA-300M Hall thruster (AIAA Paper 2012-4115).

[88] Hara, K., & Treece, C. M. (2019). Ion kinetics and nonlinear saturation of current-driven instabilities relevant to hollow cathode plasmas. *Plasma Sources Science and Technology*, 28, 055013.

[89] Walker, J., Lev, D., Walker, M. L., Khayms, V., & King, D. (2022). Electrical characteristics of a Hall effect thruster body in a vacuum facility testing environment. *Journal of Electric Propulsion*, *1*(1), Article 18. https://doi.org/10.1007/s44205-022-00016-9

[90] Su, L. L., Vazsonyi, A. R., & Jorns, B. (2020). Performance of a 9-kW magnetically-shielded Hall thruster with krypton. In *AIAA Propulsion and Energy 2020 Forum* (p. 3617).

[91] Payman, A. R., & Goebel, D. M. (2022). Development of a 50-A heaterless hollow cathode for electric thrusters. *Review of Scientific Instruments*, *93*(11), 113543.

[92] Choueiri, E. Y. (2001). Plasma oscillations in Hall thrusters. *Physics of Plasmas*, *8*(4), 1411-1426.

[93] Goebel, D. M., Jameson, K. K., Watkins, R. M., Katz, I., & Mikellides, I. G. (2005). Hollow cathode theory and experiment. I. Plasma characterization using fast miniature scanning probes. *Journal of Applied Physics*, *98*(11), 113302. https://doi.org/10.1063/1.2135417

[94] Stoica, P., & Moses, R. (2005). *Spectral analysis of signals* (pp. 45-78). Prentice Hall.

[95] Welch, P. D. (1967). The use of fast Fourier transform for the estimation of power spectra: A method based on time averaging over short, modified periodograms. *IEEE Transactions on Audio and Electroacoustics*, *15*(2), 70-73. https://doi.org/10.1109/TAU.1967.1161901

[96] Harris, F. J. (1978). On the use of windows for harmonic analysis with the discrete Fourier transform. *Proceedings of the IEEE*, *66*(1), 51-83. https://doi.org/10.1109/PROC.1978.10837

[97] Lobbia, R. B., & Gallimore, A. D. (2008). A method of measuring transient plume properties. In *44th AIAA/ASME/SAE/ASEE Joint Propulsion Conference and Exhibit* (AIAA Paper 2008-4650).

[98] Vincent, B., Tsikata, S., Mazouffre, S., & Boniface, C. (2019, September). Thomson scattering investigations of a low-power Hall thruster in standard and magnetically-shielded configurations. In 36th International Electric Propulsion Conference.

[99] Marquardt, D. W. (1963). An algorithm for least-squares estimation of nonlinear parameters. *SIAM Journal on Applied Mathematics*, *11*(2), 431-441. https://doi.org/10.1137/0111030

[100] Mott-Smith, H. M., & Langmuir, I. (1926). The theory of collectors in gaseous discharges. *Physical Review*, *28*(4), 727–763. https://doi.org/10.1103/PhysRev.28.727

[101] Lobbia, R. B. (2010). A time-resolved investigation of the Hall thruster breathing mode (Doctoral dissertation, University of Michigan).

[102] Jovel, D. R., Cabrera, J. D., and Walker, M. L. R. (2024). Current pathways model for hall thruster plumes in ground-based vacuum test facilities: measurements and observations. Journal of Electric Propulsion, 3, 35.

[103] Hara, K. (2014). Perturbation analysis of ionization oscillations in Hall effect thrusters. Physics of Plasmas, 21(12), 122103.

[104] Dale, E. T. and Jorns, B. A. (2021). Experimental characterization of Hall thruster breathing mode dynamics. Journal of Applied Physics, 130(13), 133302.